Department of Chemistry

Modification of Electrode Surfaces for the Sensing of Toxic Gases

Ghulam Hussain

This thesis is presented for the Degree of
Doctor of Philosophy
of
Curtin University

August 2017

Declaration

To the best of my knowledge and belief, this thesis contains no material previously published by any other person except where due acknowledgement has been made.

Furthermore, this thesis contains no material which has been accepted for the award of any other degree or diploma in any university.

Ghulam Hussain

Date: 14 August, 2017

“A Father gives his Child nothing better than a Good Education”

Prophet Muhammad (صلى الله عليه وسلم)

This Work is dedicated to my Father, Mother, my Wife, my Daughter, all my Family Members and my Mentors (Dr. Debbie Silvester & Prof. Damien Arrigan).

Abstract

The work presented in this thesis demonstrates the modification of electrode surfaces for the sensing of toxic/flammable/ambient gases such as ammonia, hydrogen chloride, hydrogen, and oxygen in room temperature ionic liquids (RTILs). The electrode surfaces are modified with nanomaterials of different size and shape, such as platinum nanoparticles (PtNPs), 2D Pt nanostructures, 3D Pt cauliflower shaped nanostructures, and PtNP modified microchannels. These modified surfaces are employed as sensing surfaces for the detection of toxic gases using RTILs as non-volatile solvents. In the first half of this thesis, the electrochemical behaviour of gases is investigated in the RTIL 1-ethyl-3-methylimidazolium bis(trifluoromethylsulfonyl)imide [C_2mim][NTf_2] on different types of planar macrodisk and microdisk electrodes, (commercially available and modified surfaces) using cyclic voltammetry. To investigate the analytical utility and limit of detection for ammonia sensing, four different electrochemical techniques are employed: linear sweep voltammetry (LSV), differential pulse voltammetry (DPV), square wave voltammetry (SWV) and potential-step chronoamperometry (PSCA) over various concentration ranges. The results reveal what surface and which electrochemical technique is the best for a particular analyte. In the second half of this thesis, different analytes (with reversible, quasi-reversible and irreversible redox kinetics) are modelled using the simulation program Digi-Elch, to understand which electrochemical technique (LSV, DPV, and SWV) gives the highest current responses and why. Finally, all of the information reported in this thesis can used to help design improved sensors for gases, with a focus on producing low cost, miniaturized, fast responding gas sensors to detect low concentrations of gases with adequately high sensitivity and low limits of detection.

Acknowledgements

First and foremost, I would like to thank and express most sincere gratitude from the core of my heart to my supervisor Dr Debbie Silvester-Dean for welcoming me into her research group on a special request to work with her on her ARC DECRA research project and for letting me to attend many national and international conferences where I had such a great experience to express my expertise in front of great scientists from all over the world. It has been a great honour and pleasure for me to work under such a kind mentorship where she always provides an excellent guidance, both on an academic and personal level and boosts me enthusiastic encouragements when I feel down during my PhD.

I would also like to give special thanks to my co-supervisor Professor Damien Arrigan for his patient guidance, passionate inspiration, and his excellent mentorship that always motivated and encouraged me with great discussions when I knock on his office door at any time. While working in the lab, he always comes to see me and discuss what I am doing and gives me valuable suggestions.

It has been a great pleasure for me to work in such an excellent academic environment where I was welcomed into their research group (Electrochemistry & Sensors) and considered me always like a family member. I truly appreciated that they were always approachable and made themselves readily available to offer valuable scientific feedback and suggestions. I believe that, without their great supervision and encouragement, the completion of my PhD thesis would not have been possible.

I would like to thanks Dr Leigh Aldous from Kings College London (previously UNSW) for his great mentorship on simulation of voltammetric analysis. I had a great time under his kind supervision in UNSW, especially at PRiME 2016, Hawaii, USA where he spent his valuable time to teach me simulation of voltammetry which enabled me to visit UNSW for two weeks where I learnt a lot about modelling of redox reactions. I would also like to thanks Associate Professor Chuan Zhao and his student Jason from UNSW for the collaboration on hydrogen sensing at microchannels electrodes.

I would also like to give special thanks to Curtin University, the Department of Chemistry and the Curtin Institute of Functional Molecules and Interfaces (CIFMI) for my PhD scholarship (Curtin International Postgraduate Research Scholarship). In addition, I acknowledge the use of equipment, scientific and technical assistance of the Curtin University Electron Microscope Facility, which is partially funded by the University, State and Commonwealth Governments of Australia, and the use of the instruments of the Scanning Probe Microscopy facility of the CIFMI/Department of Chemistry at Curtin University. I would like to show special gratitude to Dr Thomas Becker for his patient guidance and great assistance for AFM analysis. It is great pleasure for me to acknowledge his precious time that he always spent with me to analyse my samples without any reward. I would also like to thank Ms Elaine Miller for her cooperation and assistance for SEM analysis throughout my PhD. I would also like to say special thanks to the Department administrative staff; Ms Harriet Wai, Ms Annie Burgos, and Miss Nicole Sing who always helped and cooperated during my PhD. I would also thank to technical staff of our department; Mr Peter Chapman, Dr Ching Yong Goh, and Mr Grant Cope for their assistance in experimental setup and chemicals ordering.

I would also gratitude to everyone in the Electrochemistry & Sensors Group (of past and present) who always behaved like a family member and I acknowledge them as both my colleagues and friends; Dr Junqiao Lee, Dr Krishnan Murugappan, Dr Eva Alvarez De Eulate, Dr Masniza Sairi, Bren Mark Felisilda, Benjamin Austen, David Jorritsma, Gazi Jahirul Islam, Nasibeh Kalaei, Colin Kang, Caitlyn Gibson, Gert Du Plessis, Salmah Abdul Aziz and Chandramalika Peiris for the gossip, scientific discussion, and conversations that we have shared during working together in the lab, at coffee-break time, and during group presentations and meetings.

Last but not least, I would like to show special gratitude to my father (Muhammad Ashraf), mother (Suryyia Bibi), my pretty daughter (Aiza Fatima) to whom, always I missed her, my wife (Najma Kousar), my lovely brother (Engineer Muhammad Rashid Minhas), my sister (Dr. Sumera Azmat) and all family members and relatives for their encouraging, loving, inspiring, friendly and convivial behaviour and for their prayers which always soothed and calmed me throughout my PhD. I would also like to show special gratitude to my uncles (Arshid Ali Nambardar and Professor Muhammad Shafi) who encouraged me at my 12^{th} year of education when I was

going to quit science education due to allergy from chemistry subject which seems difficult to understand, now that I am completing my **Doctor of Philosophy** in the same subject. I would also like to thank all my mentors in my bachelor and masters studies; Professor Paul Bartlett from University of Bristol, UK, Professor M.A Khan, Dr Zaib-Un-Nisa-Hussain, Dr Z. H. Farooqi from the University of Punjab, Lahore, Dr Mehmood-Ul-Hassan and Professor Malik Ajmad from Govt. SE College Bahawalpur, who all encouraged and guide me on my educational career. I would also like to thank all my friends from both Perth and Pakistan who helped me in anyway throughout my PhD.

Contents

Glossary

Table 1. List of symbols commonly used in this thesis

Symbol	Definition	Unit
E_{eq}	equilibrium potential	V
E^o	standard electrode potential	V
E	applied potential	V
E^o_f	Formal potential	V
ΔE_p	peak to peak separation	V
R	universal gas constant	$JK^{-1}mol^{-1}$
T	absolute temperature	K
n	number of electrons transferred	-
F	Faraday constant	$C\ mol^{-1}$
α	activity	-
Q	charge	C
Φ	electrostatic potential	V
Φ_M	electrostatic potential of the electrode	V
Φ_s	electrostatic potential of the solution	V
Φ_Δ	Variation in electrostatic potential	V
k_B	Boltzmann constant	$J\ K^{-1}$
z_i	charge on ionic specie	C
e	charge on proton	C
v	scan rate	mVs^{-1}
C_{dl}	double layer capacitance	Fcm^{-2}
J	flux	$mol.cm^{-2}s^{-1}$
D	diffusion coefficient	$cm^{-2}s^{-1}$
u	ionic mobility	$m^2\ s^{-1}\ V^{-1}$
η	viscosity	cP
i	current	A
i^o	standard exchange current	A
i_p	peak current	A
k^o	standard heterogeneous rate constant	$cm\ s^{-1}$
δ	thickness of diffusion layer	cm
α	electron transfer coefficient	-
a	activity	-
σ	conductivity	S/cm
t	time	s
Δt	time interval	s
x	direction	-
Δx	length interval	-
O	general specie undergoing one electron reduction	-
R	general specie undergoing one electron oxidation	-

Table 2. List of units commonly used in this thesis

Units	Definition
V	volt
K	Kelvin
C	coulomb
m	meter
A	ampere
cP	centipoise
mm	millimeter
cm	centimeter
mM	millimolar
μm	micrometer
s	second
ppm	parts per million
ppb	parts per billion
S/cm	Siemens per centimeter

Table 3. List of abbreviations commonly used in this thesis

Abbreviations	Definition
AgCl	silver chloride
LOD	limit of detection
CE	counter electrode
WE	working electrode
RE	reference electrode
TFE	thin film electrode
SPE	screen printed electrode
MATFE	microarrays thin film electrode
CV	cyclic voltammetry
LSV	linear sweep voltammetry
DPV	differential pulse voltammetry
SWV	square wave voltammetry
CPCA	constant potential chronoamperometry
RTIL	room temperature ionic liquid
Fc/Fc^+	ferrocene/ferrocenium
AFM	atomic force microscopy
SEM	scanning electron microscopy

Chapter 1

1. Introduction to Electrochemistry

The word electrochemistry is derived from two terms – **"electricity"** and **"chemistry"**. This term is often used in industry as well as in the scientific world. In a simple way, it can be defined as the science which describes the interactions between electricity and chemistry, where electrical energy is converted into chemical energy and chemical energy is converted into electrical energy. More precisely, it can be defined as, "the branch of physical chemistry which deals with the study of chemical species and reactions that takes place at the interface of an **"electron conductor"** (referred to as an *electrode*) and an **"ionic conductor"** (referred to as an *electrolyte*, which could be a solution, a liquid or a solid) where charge transfer occurs between the electrode and the electrolyte in solution. It analyses the transformation of matter (solid, liquid and gas) on the atomic level by transfer of an electric charge which can be controlled by means of an electric device. Such electronic transformations are called oxidation-reduction reactions.[1] Therefore these transformations (oxidation-reduction reactions) of matter are controlled by an electric current or with a voltage. One of the advantages of electrochemistry is its broadness, which lies in the additional, adjustable degrees of freedom offered by the voltage or current.[1] In fact, the field of electrochemistry has great applications in different phenomena such as electrophoresis and corrosion, a large number of practical devices where chemical energy is converted into electric energy (which includes electrochromic displays, electroanalytical sensors, batteries, and fuel cells), and technologies such as electroplating and electro-refinement to produce metals and chemicals.[2]

There are two main types of electrochemistry; *"equilibrium electrochemistry"* and *"dynamic electrochemistry"*. Equilibrium electrochemistry is concerned when the chemical and electrical gradients are equal in magnitude and the potential difference is established between the electrode and electrolyte resulting in no change in net current.[3] The potential between the electrode and electrolyte under equilibrium is described by the Nernst equation.[4]

$$E_{eq} = E^{o} + \frac{RT}{n\mathrm{F}} \ln \frac{[O]}{[R]} \qquad \textbf{(1.1)}$$

Where E_{eq} is equilibrium potential and E^{o} is the standard electrode potential for the redox reaction, R is the universal gas constant (8.314 $JK^{-1}mol^{-1}$), T is the absolute temperature (K), *n* is the number of electrons transferred in the redox reaction, F is Faraday's constant (96485.4 C mol^{-1}), and [O] and [R] are the concentrations of oxidized and reduced forms of the redox couple, usually expressed in term of activity (α). Equilibrium potential and standard electrode potential indicates weather the reaction is favourable or not and gives thermodynamic information of a redox reaction such as enthalpy, entropy or free energy of a reaction, the equilibrium constant and the pH of a solution.[3] The best example of the application of equilibrium electrochemistry is a *"galvanic cell"* where chemical energy is converted into electricity as a result of a spontaneous reaction occurring inside it. Another application is an *"electrolytic cell"* in which a non-spontaneous reaction proceeds as a result of an external source of current.[5]

"*Dynamic electrochemistry"* deals with the study of charge transfer between an **"electron conductor"** (an *electrode*) and an **"ionic conductor"** (an *electrolyte*) when a potential difference is applied between the interface of electrode and electrolyte and as a result the electrode potential, the current is monitored as a function of the applied potential.[2] The transfer of charge through the electrode is due to the movement of electrons. The most commonly used electrodes are solid metals (i.e. platinum, Pt and gold, Au), liquid metals (i.e. mercury, Hg), carbon materials (i.e. glassy carbon, GC and graphite), and semiconductors (i.e. indium-tin oxide and silicon). The charge transfer in the electrolyte is carried with the movement of ions. The commonly used electrolytes are liquids solutions of ionic species i.e. hydrogen ions (H^{+}), sodium ions (Na^{+}) chloride ions (Cl^{-}) etc. in aqueous or organic solvents.[2] In a "*dynamic electrochemical system"* the electrochemical cell usually employs a three electrode set-up. The "*working electrode"* (WE) where the potential is applied and the current is measured as a result of a redox reaction occurring. The WE is usually an inert material such as gold, platinum or glassy carbon. The second type of electrode is *"reference electrode"* (RE) used to measure the potential at the *"working electrode"*. The RE has a fixed potential and does not allow current to pass through it. Internationally accepted REs include the *"standard hydrogen electrode"*

(SHE) or *"normal hydrogen electrode"* (NHE) having unit activity (α) for every component. Commonly used REs are the "*saturated calomel electrode"* (SCE) and *"silver-silver chloride electrode"*. The third electrode is a *"counter electrode"* (CE, or auxiliary electrode) on which an opposite reaction of the same magnitude as the *"working electrode"* occurs. If oxidation occurs on a working electrode, it acts as an anode and the counter electrode acts as a cathode, to balance the reaction occurring at *"working electrode"*. The surface area of the CE is usually large compared to the WE to ensure that the reaction occurring at the CE is fast enough so that it does not limit the redox process at the WE.[2] In most electrochemical experiments, the *"counter electrode"* is usually act as the current source/sink and relatively inert material is used such as platinum or graphite.[3, 6]

Thus in an electrochemical cell, the potential of the working electrode is measured relative to the RE, which has a fixed potential, and the counter electrode reaction balances the redox process at the working electrode. In another sense, one can observe (in potentiometry) or control (in a potentiostatic measurement) the potential of the working electrode with respect to the reference electrode which is equivalent to observing or controlling the energy of the electrons within the working electrode.[2, 7] When a negative potential is applied at the working electrode, the energy of the electrons is raised. As a result, the electrons have large enough energy to reach the vacant electronic states on species in the electrolyte. In this case, the flow of electron from electrode into electrolyte is called a *"reduction".* Similarly, when a positive potential is applied at the working electrode, the energy of electrons is decreased. As a result, the electrons from species in the solution find a more favourable energy at the electrode and transfer towards the electrode. In this case, the flow of electrons from the electrolyte into the electrode is called an *"oxidation".*[2] All oxidation or reduction reactions on the working electrode are related to a specific potential for a particular species called the *"standard electrode potential, E^{o}"*. The number of electrons that pass through the interface are stoichiometrically related to the extent of redox reaction (the amount of reactant consumed on the surface of electrode and the amount of products generated that move away from the electrode surface). The number of electrons transfered is measured in terms of the total charge (*Q*), which is expressed in coulombs (C), where 1 C = 6.24×10^{24} electrons. The relationship between the consumed charge and products generated is given by *Faraday's Laws of*

electrolysis, which is stated as; the transfer of 96485.4 C of charge (*Q*) that can produce one equivalent of product (N) (e.g. the consumption of 1 mole of reactant to produce 1 mole of product as a result of 1 electron transfer).[2, 4]

$$Q = n\mathrm{FN} \qquad \textbf{(1.2)}$$

Where F is Faraday's constant (96485.4 C mol^{-1}), and n is the total number of electrons transferred per mole of product. The rate of charge transfer is equivalent to 1 ampere (C/t). A plot of current (*i*) as a function of applied potential is called a current-potential (*i* vs *E*) curve or *"voltammogram"* which provides both kinetic and thermodynamic information for the electron transfer process.[2]

In this thesis, the work presented is concerned with the second type of electrochemistry; "*dynamic electrochemistry"* to study the reactions occurring between a solid electrode and an electrolyte solution. Different electrochemical techniques such as voltammetry and amperometry are employed to study the sensing of toxic gases in room temperature ionic liquids in later chapters. In this chapter, an introduction and some fundamental concepts about electrochemical processes that are relevant to the work reported in this thesis will be discussed.

1.1 Structure of the Electrical Double Layer

In electrochemistry, an electrode is considered as a source or sink of electrons. When an electrode is immersed in an electrolyte solution, it is charged due to ionization, dissociation of ionic groups or ion-adsorption.[8] The development of charge on the surface of the electrode affects the distribution of ions in the electrolyte medium. As a result, a potential difference is established between the electrode and electrolyte interface. This potential difference causes the ions in the immediate vicinity of electrode surface to re-orientate themselves in order to achieve the most energetically stable arrangement. Thus, a positively charged electrode attracts a layer of negatively charged ions (*counter-ions*) toward its surface and the ions of similar charge (*co-ions*) are repelled from the surface. An increase in the concentration of counter-ions in the vicinity of the electrode results in the formation of an electric potential gradient which extends out toward the bulk solution. The electric field gradient due to the presence of oppositely charged ions at the interface of the electrode and electrolyte is called the "*electrical double layer"*.[8]

1.1.1 Helmholtz Model

The structure of the electrical double is very complicated with several distinct layers from the solution side. Various models have been proposed to describe the structure of the electrical double layer. The first compact model was proposed by Helmholtz in 1879, which consisted of two ridged layers of oppositely charged ions on the both sides of the interface to form a compact layer (*double layer*) that behaves like a capacitor.[9] A uniform distribution of counter ions opposite to the charge of the electrode forms a ridged and compact layer called the *Helmholtz layer* which is strongly held at the electrode and the locus of the center of these strongly attached counter-ions from the electrode is called the *outer Helmholtz plane* which is at a distance of x_H from the electrode.[2] The decay of electrostatic potential (Φ) from the metal electrode potential (Φ_M) to the solution or bulk potential (Φ_s) is linear as the distance (x) is increased from the electrode surface towards the bulk. The capacitance of the electrical double layer (C_d) remains constant with applied potential (E). This model has two defects: first it neglects the interactions associated with thermal motion of ions away from the electrode (OHP). Secondly this model disregards the dependence of electrolyte concentration.[2, 7, 10]

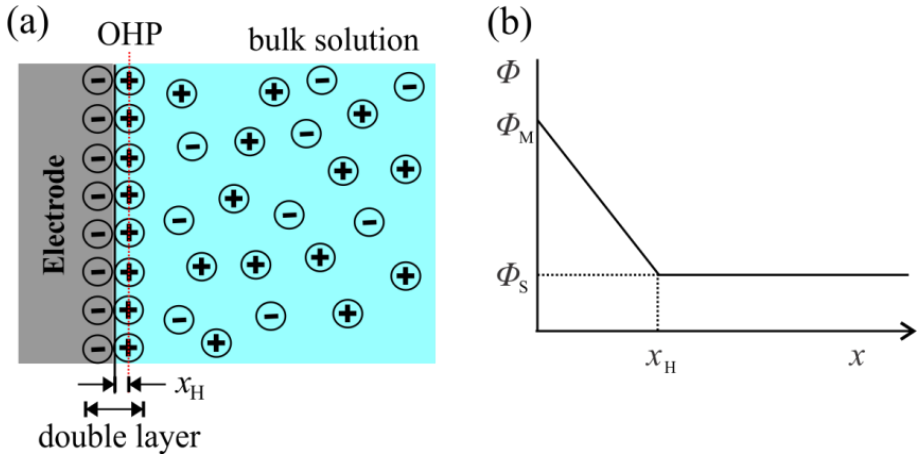

Figure 1.1: A schematic representation of the Helmholtz model of the electrical double layer. (a) Compact and rigid arrangement of ions, (b) Variation of the electrostatic potential (Φ) with distance (x) from the electrode surface.

1.1.2 Gouy-Chapman Model

Gouy [11] in 1910 and Chapman [12] in 1913 independently proposed their own model for the electrical double layer which is considered more realistic than the Helmholtz model. In this model the applied potential and ionic concentration of the electrolyte

both affect the thickness of the electrical double layer. They consider ions as point charges and the double layer is not compact like in the Helmholtz model. The counter ions which are non-specifically adsorbed, are distributed in a three dimensional region due to Brownian motion, extending from the OHP towards the bulk solution and form a layer called a "*diffuse layer"*. The solvated ions are attracted towards the electrode through long-range electrostatic forces. At low concentrations of electrolyte, there are few ionic species in the solution; therefore a thick layer of counter ions would be necessary to counterbalance the charge. Furthermore, the applied potential also has a great impact on the thickness of the electrical double layer; at higher potentials, the electrostatic forces become dominant, therefore the thickness of double layer is reduced. The applied potential tends to order the ionic species, and thermal motions disorder the distribution of ions in the diffuse layer. Thus there is equilibrium between these two opposite effects which indicates that the concentration of ionic species (n_i) at a given distance (x) decays exponentially with the ratio of electrostatic energy ($z_i e\Phi_\Delta$) and thermal energy ($k_B T$) in accordance with the Boltzmann law.[2, 7]

$$n_i = n^o exp\left[\frac{-z_i e\Phi_\Delta}{k_B T}\right] \qquad \textbf{(1.3)}$$

Where n^o is the bulk concentration, z_i is the charge on the ionic species, e is the charge on a proton, $\Phi_\Delta = \Phi - \Phi_s$ is variation in electrostatic potential and k_B is the Boltzmann constant.

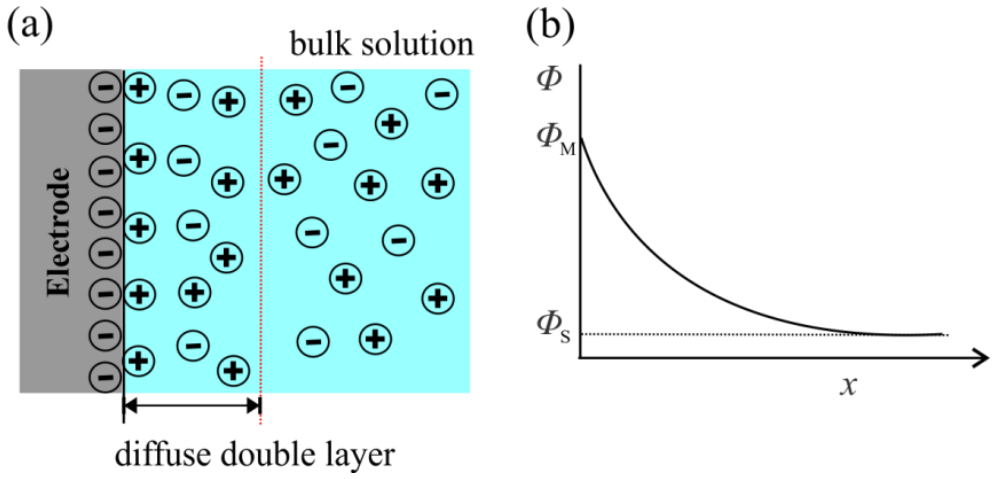

Figure 1.2: A schematic representation of the Gouy-Chapman model of the electrical double layer. (a) Distribution of ions in the diffuse layer, (b) Variation of the electrostatic potential (Φ) with distance (x) from the electrode surface.

The total charge on the electrode surface is equal in magnitude (with opposite sign) to the total charge of the diffuse layer. The potential decays exponentially within the diffuse layer from the surface of the electrode over a distance *x*.

1.1.3 Stern Model

Finally, Stern in 1924 [13] proposed a more realistic model which combines both the Helmholtz model and the Gouy-Chapman model. He considered that ions are not point charges but have a finite size that cannot reach the surface of electrode closer than the ionic radius.[2] He considered that the electrical double layer is formed by the combination of compact layer of ions near the surface of the electrode into the OHP and diffuse layer extending from the OHP towards the bulk solution. Figure 1.3 shows the schematic representation of the Stern model.

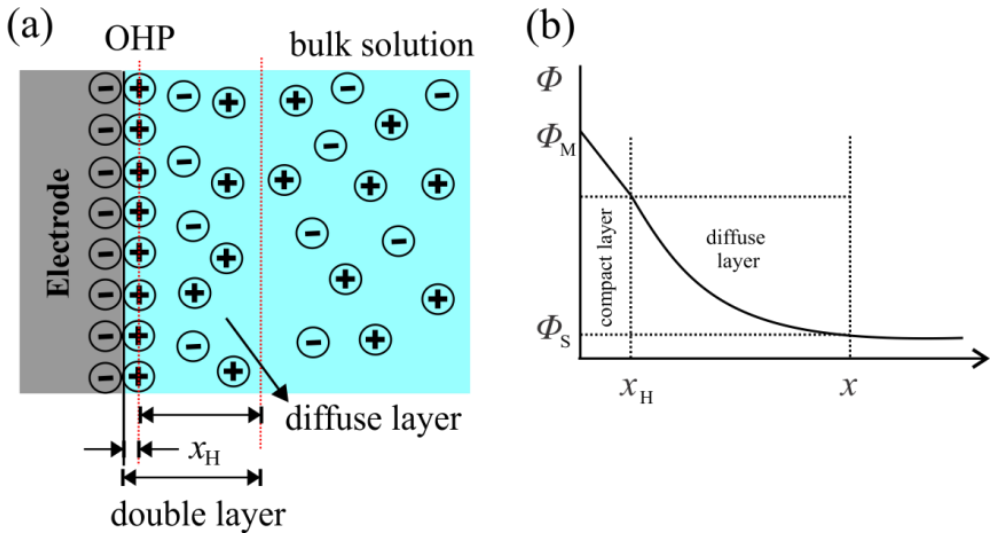

Figure 1.3: A schematic representation of the Stern model of the electrical double layer. (a) Distribution of ions in the Helmholtz layer and diffuse layer, (b) Variation of electrostatic potential (Φ) with distance (x) from the electrode surface.

The ions in the compact layer are rigidly attached to the electrode surface due to strong electrostatic forces and the ions in the diffuse layer have weak attractive forces. The total charge on the electrode surface is equal in magnitude (with opposite sign) to the total charge of the compact layer and diffuse layer. In the potential-distance profile, a linear decrease of potential drop from electrode surface to OHP at a given distance x_H followed by an exponential decay from the OHP to a distance x. The total capacitance of the electrical double layer (C) is a combination of the capacitance of the Helmholtz layer (C_H) with the capacitance of the diffuse layer (C_d) – like two capacitors in series – and is given by the following equation:[2, 7]

$$\frac{1}{C} = \frac{1}{C_H} + \frac{1}{C_d} \qquad \textbf{(1.4)}$$

C_d is strongly affected by electrolyte concentration while C_H is independent of concentration. For example, at high concentrations, most ionic species are confined in the Helmholtz layer with only a few ions in the diffuse layer; therefore the thickness of the diffuse layer is reduced. Thus in this case, the capacitance of the compact layer (C_H) is much higher than the capacitance of the diffuse layer (C_d), $1/C_H >> 1/C_d$, $1/C \approx 1/C_H$. On the other hand at low concentrations of electrolyte, C_d is much higher than C_H, $1/C_d >> 1/C_H$, $1/C \approx 1/C_d$.[7]

1.1.4 Grahame Model

Grahame in 1947 [14] proposed more sophisticated model, even though the Stern model is thought to provide an adequate information to explain the interfacial structure. In the Grahame model, the electrical double layer constitutes three regions. The first "*inner layer*", close to the electrode surface which contains solvent molecules and some ionic species (Cl^-, Br^-, or molecules which are not hydrolysed in aqueous solution) that are specifically adsorbed on the surface of the electrode is called the *compact, Helmholtz, Stern layer*. The locus of the center of the specifically adsorbed ions from the electrode is called the "*inner Helmholtz plane*" (IHP) which is at a distance of x_1 and the total charge density associated from specifically adsorbed ions (*inner layer*) is represented by σ^i ($\mu C/cm^2$).[2, 9] The second layer of oppositely charged ions to the *Helmholtz layer* is composed of non-specifically adsorbed solvated ions which are distributed in a three dimensional region, extending from the OHP towards the bulk solution, called the "*diffuse layer*". This layer is attracted towards the electrode surface through long-range electrostatic forces. The locus of the center of these solvated ions from the electrode is called the "*outer Helmholtz plane*" which is at a distance x_2 from the electrode and the total charge density associated with this layer is σ^d ($\mu C/cm^2$). Due to Brownian motion in the solution, the non-specifically adsorbed solvated ions are distributed into the diffuse layer and the total charge density associated from these ions is represented by σ^d ($\mu C/cm^2$). Thus the total charge density on the solution side σ^s ($\mu C/cm^2$) associated from the electrical double layer is given by the following equation.[2]

$$\sigma^s = \sigma^i + \sigma^d = -\sigma^M \qquad \textbf{(1.5)}$$

Where σ^M ($\mu C/cm^2$) is the total charge density on the electrode surface, and the –ve sign indicates the opposite charge with respect to the electrical double layer. In the potential-distance profile, similar to the Stern model, a linear decrease of potential occurs from the electrode surface to the OHP at a given distance x_2 and then an exponential decay within the diffuse layer to a distance x.

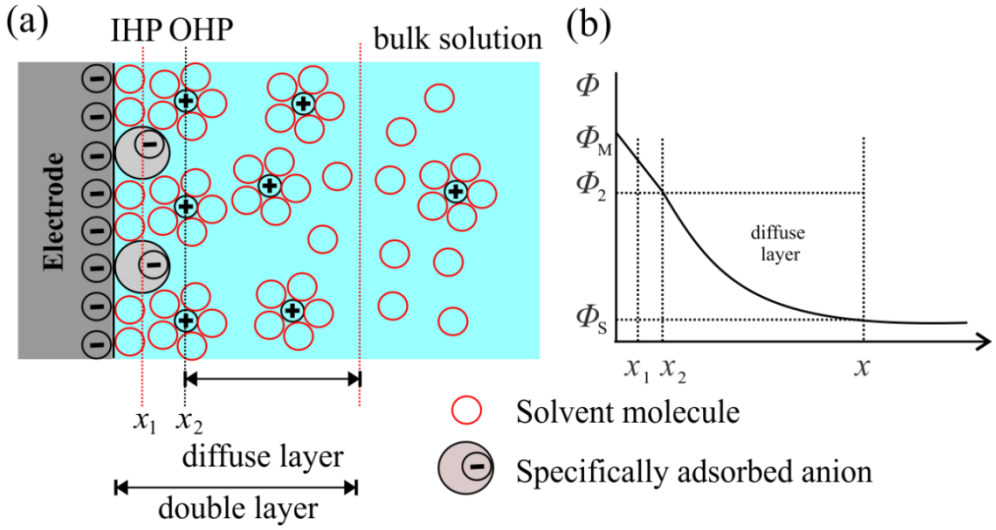

Figure 1.4: A schematic representation of the Grahame model of the electrical double layer. (a) Distribution of ions in the Helmholtz layer and diffuse layer, (b) Variation of electrostatic potential (Φ) with distance (x) from the electrode surface.

1.1.5 Electrical Double Layer in Room Temperature Ionic Liquids

The work presented in this thesis is performed in room temperature ionic liquids (RTILs) as an electrolyte. The electrical double layer (EDL) in RTILs is considered much more complicated compared to conventional aqueous or organic solvents.[15-18] Therefore, it is necessary to give a brief discussion on the EDL in RTILs. The Gouy-Chapman-Stern theory of dilute electrolytes cannot be applied for these dense ionic systems. Baldelli in 2005 proposed a model for the electrical double layer in ionic liquids at a metal interface and suggested that the double layer in ionic liquids is "one-ion-layer thick".[19] Later on Dogonadze–Chizmadjev proposed a double layer model for molten salts and suggested that the structure of the EDL in ionic liquids is much more complicated.[20] For the first time, Heyes and Clarke observed a multilayer structure with several layers extending toward the bulk to several nanometres from the interface when they performed molecular dynamics (MD) simulations on molten salts (KCl), placed between two uncharged parallel plates.[21, 22] They observed clear oscillations in the density $\rho(z)$ with a period of ca. 0.3 nm, which decay rapidly

toward the center of bulk. These oscillations indicated the layering of ions near the interface due to repulsive forces. When they applied a potential across the interface, they observed ordering of charges at the interface indicating "multilayers" with clear splitting of the density profile into a cation, $\rho_+(z)$ and an anion, $\rho_-(z)$ profile. The first simple theory to explain the structure of electrical double layer (EDL) on a flat interface was given by Kornyshev.[15, 17, 18] It was called "*mean-field theory*" and took into account the natural constraints on the ion packing in RTILs. The approach is simply based on the lattice gas model in which N_+ cations and N_- anions, are distributed with a fixed total number of both ions $\bar{N} = N_+ + N_-$, over N available lattice sites. The distribution of ions in the lattice is random except when a potential is applied. The electrode potential is determined by the polarization of cation and anion distributions near the electrode surfaces. In this model they predict maxima and minima depending on the compacity parameter (γ) which is given by the following equation.

$$\gamma = \frac{\bar{N}}{N} = \frac{2c^o}{c_{max}} \qquad \textbf{(1.6)}$$

Where γ is the ratio of the average salt concentration to the maximal possible local concentration of ions (both cations and anions) c_{max}. The physical explanation of this compacity parameter is described in figure 1.5.

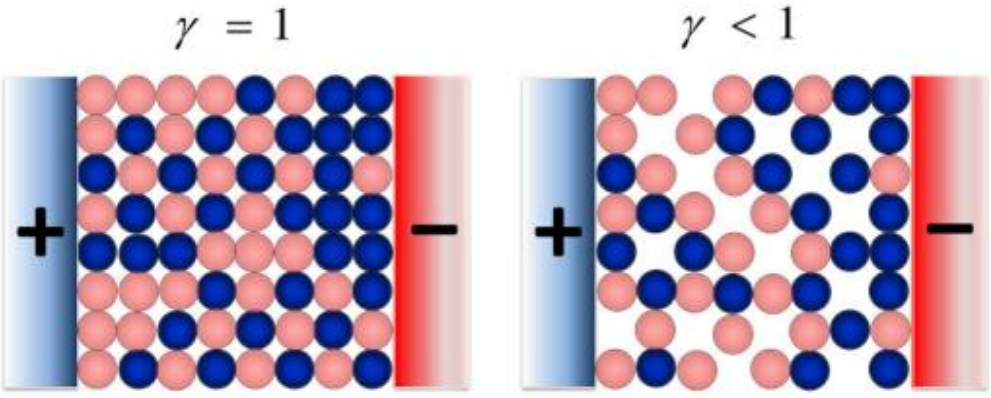

Figure 1.5: Schematic representation of an ionic liquid between two parallel electrodes showing the concept of compacity parameter γ. The red spheres represent anions and the blue spheres represent cations. Reproduced from Ref.[18]

In figure 1.5, γ = 1 corresponds to a very dense system with maximum packing of ions with no solvent in the RTIL. The value of γ is different for different RTILs but

mostly it lies around or above 0.5.[18] From mean field theory, Kornyshev gave the following conclusions for the electrical double layer in ionic liquids.

(1). The electrical double layer is not one-ion-layer thick, it is a combination of multiple layers.

(2). The electrical double layer in RTILs has strong oscillations of electrostatic potential near the electrode surfaces extending approximately several nanometres away from the electrode to the bulk of RTIL corresponding to multilayers of ions in which counter-ion rich layers alternate with co-ion rich layers.

(2). The capacitance curve for the EDL is not like the U-shape of the Gouy–Chapman model, it is a bell-shaped or camel shaped taking into account the effect of limited maximum packing of ions.

(4) The decrease in capacitance in the EDL is inversely proportional to the square root of the electrode potential.

(5). There is no diffuse layer in the electrical double layer of RTILs and the decay of electrode potential is characterized by the oscillation behaviour caused by layering or ordering of ions.

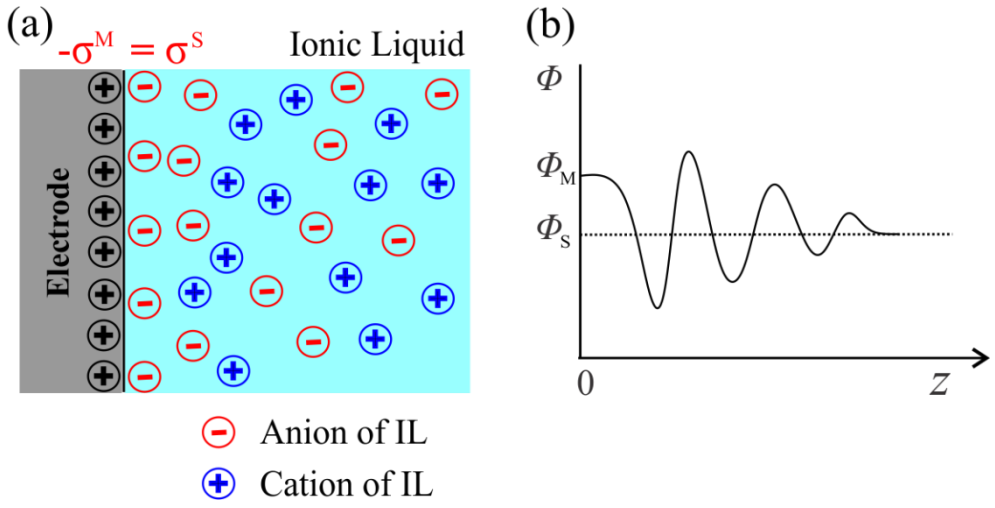

Figure 1.6: A schematic representation of the electrical double layer in RTILs in mean-field theory. (a) The structure of the ionic fluid near the charged electrode surface showing ordering or layering of anions and cations, (b) The decay of electrostatic potential (Φ) over several layers towards the bulk solution. Figure adapted from Ref. [22]

It is noted that mean-field theory still has limitations and cannot be applied to all RTILs due to the different geometry, symmetry and size of cations and anions.[15]

1.2 Faradaic and Non-Faradaic Processes

In an electrochemical cell, when a potential is applied, there are two types of processes that can occur on the electrode surface. One is called a "*faradaic process*" and the second is a "*non-faradaic process*". A faradaic process involves the transfer of charge (electron) across the electrode/electrolyte interface as a result of oxidation or reduction of an electroactive species of interest and is given by the Faraday law (the amount of product generated as a result of a redox reaction on the electrode surface is proportional to the amount of current passed).[2] At the electrode at which a faradaic process occurs is called an "*electron transfer electrode*". The current associated with a faradaic process is called faradaic current and is given by the following equation:[2]

$$\frac{dQ}{dt} = \frac{d}{dt}(nFN) = nF\frac{dN}{dt} \qquad \textbf{(1.7)}$$

Where Q is charge (in Coulombs), n is the number of electrons, F is Faraday's constant and N is the total number of moles of reactants converted into products. Faradaic processes occur in a potential region where electron transfer is thermodynamically or kinetically favourable.[2] But under some conditions, for a given electrode-electrolyte interface, there is a range of potential where there is no electron transfer reaction occuring because these reactions are not thermodynamically and kinetically favourable.[2]

The second process that occurs on the electrode surface is called a non-faradaic process. This is associated with the movement of electrolyte ions, reorientation of solvent molecules, adsorption/desorption of ions, etc. at the electrode-electrolyte interface. In a non-faradaic process, there is no electron transfer occurring, but instead charging of the electrical double layer (see section 1.1). The current associated with a non-faradaic process is called capacitive current/background current or charging current (i_C) given by the following equation.[2, 7]

$$i_C = AC_{dl}\frac{dE}{dt} = AC_{dl}v \qquad \textbf{(1.8)}$$

Where A is the area of the electrode (cm^2), C_{dl} is the double layer capacitance per unit area, usually in the range of tens of μFcm^{-2}, $\frac{dE}{dt}$ is the change in potential with time and v is the scan rate (Vs^{-1}). From the above equation, the C_{dl} is assumed to be independent to the electrode potential and the capacitive current is directly related to the scan rate. So when a fast scan rate is applied (*e.g.* kVs^{-1}), the capacitive current is undesirably large enough to swamp the faradaic current. In this case small size electrodes (microelectrodes) are used to reduce the effect of capacitive current.[2]

Although both faradaic and non-faradaic process occur when an electrode process takes place, faradaic processes are the primary interest in the investigation of redox reaction except those studies where the nature of electrode-electrolyte interface are under investigation. In an electrochemical measurement, the effect of a non-faradaic process must be taken into account to obtain complete information on the charge transfer and associated reactions. During an experiment, such conditions are usually designed so the contribution from non-faradaic process can be minimized. The magnitude of faradaic process mainly depends on the following three factors: the rate of mass transport to and from the electrode surface, heterogeneous electron transfer between electrode and electrolyte interface, and any homogeneous chemical reactions coupled with the electron transfer process.[2] These topics will be discussed in the following sections.

1.3 Mass Transport

Mass transport is the movement of electroactive species from the bulk solution towards the electrode surface as a result of a difference in applied potential or a concentration gradient. For an electrode process, it is necessary to provide a refresh supply of electroactive species from bulk solution towards the electrode surface which is achieved by mass transport through three different ways: diffusion, convection, and migration. In an electrochemical experiment, flux (J) is a measure of the rate of mass transport towards an electrode surface at a fixed point and can be defined as the number of an electroactive species (moles) passing through a unit area (cm^2) per unit time (sec), expressed in unit $mol.cm^{-2}s^{-1}$. The one dimensional total flux, $J_o(x)$ associated by diffusion, convection, and migration can be described mathematically by Nernst-Planck-equation.[4, 7]

$$\underbrace{J_o(x)}_{\textit{Total Flux}} = \underbrace{-D_o \frac{\partial C_o(x)}{\partial x}}_{\textit{diffusion}} - \underbrace{\frac{z_o F}{RT} D_o C_o \frac{\partial \Phi(x)}{\partial x}}_{\textit{migration}} + \underbrace{C_o v(x)}_{\textit{convection}} \quad \textbf{(1.9)}$$

Where $J_o(x)$ [mol.cm^{-2}s^{-1}] is the total flux of species (O) at a distance x from the electrode surface, D_o [cm^{-2}s^{-1}] is the diffusion coefficient, zo is the charge, C_o [mol.cm^{-3}] is the concentration of species (O). The term $\partial C_o(x)/\partial x$ is the concentration gradient, $\partial \Phi(x)/\partial x$ is the potential gradient, and $v(x)$ is the hydrodynamic velocity along the x-axis.

Thus the total current (I_T) produced as a result of a redox process is a combination of these three processes, given by the following equation:[23]

$$I_T = I_d + I_m + I_c \quad \textbf{(1.10)}$$

Where I_d is the current associated with diffusion process, I_m is the current associated with migration and I_c is the current due to convection process.

1.3.1 Diffusion

Diffusion is the spontaneous movement of electroactive species from a region of high concentration to a region of low concentration under the influence of a concentration gradient. In equation (1.9), the first term is concerned with the diffusion process and it defines Fick's first law.[4]

1.3.1.1 Fick's Laws

Fick's laws are the differential equations which describe the flux of specie (O) having concentration (C) as a function of time (t) and position (x). Fick's first law is defined as having the rate of diffusion/mass transfer (flux) directly proportional to the concentration gradient, $\partial C_o(x)/\partial x$ along the x-axis:

$$J_o(x,t) = -D_o \frac{\partial C_o(x,t)}{\partial x} \quad \textbf{(1.11)}$$

Where D_o [cm^{-2}s^{-1}] is the diffusion coefficient of species (O), a measure of the ease with which species (O) diffuses, and is given by the following equation:[4, 7, 24]

$$D_o = \frac{(\partial x)^2}{2\partial t} \quad \textbf{(1.12)}$$

Where ∂x is the distance travelled by species (O) over a time interval ∂t. The value of D_o in aqueous solutions typically varies between 10^{-5} to 10^{-6} cm^2s^{-1} at 298 K [24] and depends on the following factors: molecular size of diffusing species (O), viscosity of the solvent and temperature *T*. By rearranging equation (1.12), we can obtain the root mean square displacement which has great significant in voltammetry and enables us to determine the distance travelled by species (O) in time *t*:[24]

$$\sqrt{\langle x^2 \rangle} = \sqrt{2D_o t} \qquad \textbf{(1.13)}$$

Fick's second law is described as the change in concentration ∂c with time ∂t being directly related to the change in flux with position ∂x, given by the following relation:[4, 7, 24]

$$\frac{\partial C_o(x,t)}{\partial t} = D_o \frac{\partial^2 C_o(x,t)}{\partial x^2} \qquad \textbf{(1.14)}$$

Equation (1.14) is Fick's second law in one dimension. Fick's second law in three dimensions describing diffusion along the *x,y and z*-axes can be written by the following equation:[4, 24]

$$\frac{\partial C_o(x,y,z,t)}{\partial t} = D_o \left(\frac{\partial^2 C_o(x,t)}{\partial x^2} + \frac{\partial^2 C_o(y,t)}{\partial y^2} + \frac{\partial^2 C_o(z,t)}{\partial z^2} \right) \textbf{(1.15)}$$

This equation enables us to determine the change in concentration of electroactive species (O) close to the electrode surface.

The diffusion coefficient is a measure of the rate at which species (O) diffuses through a solution and can be expressed by the Stokes-Einstein equation:[24]

$$D_o = \frac{k_B T}{6\pi\eta a_o} \qquad \textbf{(1.16)}$$

Where k_B is the Boltzmann constant, T is the absolute temperature, η is the viscosity of solvent and a_o is the hydrodynamic radius of diffusing specie (O). The diffusion coefficient is strongly temperature sensitive according to the following Arrhenius relationship:[24]

$$D_o = D_\infty \exp\left(\frac{-E_a}{RT}\right) \qquad \textbf{(1.17)}$$

Where D_∞ is the hypothetical diffusion coefficient at infinite temperature, E_a is the activation energy of diffusing species (O), and R is the universal gas constant. This type of temperature sensitivity in voltammetry requires experiments to be performed under thermostatically controlled conditions.

1.3.2 Convection

Convection is the movement of species under the influence of a force, e.g. a density gradient (natural convection) or mechanical force/stirring (forced convection). Natural convection occurs due to density gradient (sometimes achieved due to thermal vibrations) caused by the flow of mass transfer from a denser region to a less dense region within the solution. It is rare in electroanalytical techniques, often difficult to predict and can be seen in electrolysis and coulometric experiments where high current is required to produce the density gradient.[25] In voltammetric experiments, natural convection can be minimised or by ensuring the time duration of measurement not exceed ca. 10-20 seconds.

Forced convection can be achieved by mechanical stirring or agitation of solution. It is often designed as a part of an experiment to dominate the effect of mass transfer. In hydrodynamic voltammetric experiments, if a fast rate of mass transfer is required, this can be achieved by applying forced convection. Therefore under such conditions, forced convection is achieved by stirring the solution with the help of a stirrer bar, by rotating the electrode (e.g. rotating disk electrode), by vibrating or sonicating the solution, or by flowing the solution over stationary electrodes.[23, 25] Mathematically, forced convection is the rate of change of concentration resulting the movement of solution with respect to velocity v_x and is given by the following equation.[6]

$$\frac{\partial C_o(x,t)}{\partial t} = -v_x \frac{\partial C_o(x,t)}{\partial x} \qquad \textbf{(1.18)}$$

1.3.3 Migration

Migration is the movement of charged species under the influence of an electric field (potential gradient).[7] When a potential is applied to a solution, a potential gradient is established across the electrode-electrolyte interface which results in the migration of charged species toward the electrode surface. This migration process contributes to the total rate of mass transfer in an electrochemical reaction. Thus the flux associated

with migration is called "*migratory flux*" $J_o(m)$ which is directly proportional to the concentration of electroactive species (O), C_o, an applied electric field and the ionic mobility and is given by the following equation.[6]

$$J_o(m) = -u_o C_o \frac{\partial \Phi}{\partial x} \qquad \textbf{(1.19)}$$

Where u_o is the ionic mobility, C_o is the concentration of species (O), and $\partial\Phi/\partial x$ is the potential gradient. The mobility of charged species (O) is given by the Einstein-Smoluchowski equation.[2, 4]

$$u_o = \frac{z_o F D_o}{RT} \qquad \textbf{(1.20)}$$

Where z_o is the charge on species (O), F is Faraday's constant, R is the universal gas constant, T is the absolute temperature, and D_o is the diffusion coefficient of species (O).

1.3.4 Effect of Convection and Migration on Voltammetry

In a voltammetric experiments, all three forms of mass transfer (diffusion, convection and migration) are considered during measurements, but it is very complicated and rigorous to predict all these effects simultaneously, especially migration.[2] Therefore in order to study an electrochemical reaction, the experimental setup is designed in such a way so that at least one or more of the contributions to the mass transfer can be minimized/neglected. For example, migration is very complicated and unfortunately unpredictable during electrochemical measurements. Thus in order to simplify this problem, voltammetry was done in such conditions where the migration effect can be neglected. This can be achieved by adding an excess amount of a chemically and electrochemically "*inert*" substance into the solution (electrolyte medium) called "*background/supporting electrolyte*" which is in high concentration, at least 30 times greater than the concentration of electroactive species, commonly 0.1 M is used.[6] The excess concentration of background electrolyte near the electrode-electrolyte interface cause the redistribution of cations and anions to ensure that the electric field ($\partial\Phi/\partial x$) do not build up beyond the electrical double layer, and essentially to maintain the electrical neutrality during electrolysis.[6]

The addition of background electrolyte has other advantages. Firstly, a high concentration of background electrolyte increases the conductivity of the solution, thus making it less resistive to the flow of current, which results in reduction of Ohmic drop. Secondly, excess background electrolyte results in the compression of electrical double layer to a very small region of approximate dimensions 10-20 Å. This small distance is short enough to facilitate electron transfer through mechanical tunnelling. Thirdly, the ionic strength of the solution effectively remains constant during electrolysis compared to the reactants and products. This means that the activity coefficient of an electroactive species remains constant which in turn keeps the electrode potential and rate of chemical reaction constant.[6]

The effect of convection during voltammetry experiment can be minimized by performing experiments under quiescent conditions; by preventing stirring, rotations, and vibrations of the solution and by using stagnant solutions with no density gradients.[23, 25]

1.4 Electrode Processes

The term electrode process can be described as all changes and processes that occur on the electrode surface and in the vicinity of the electrode-electrolyte interface when current is passed through an electrochemical cell as a result of applied potential. These processes involve two main phenomena (i) mass transfer (ii) electrode reaction. Mass transfer involves diffusion, convection and migration as discussed in section (1.3). The electrode reaction involves electron transfer between the electrode and an electroactive species present in the vicinity of electrode surface. The electrode reaction is usually called electrolysis and involves a couple of steps; (i) the electroactive species moves towards the electrode surface (mass transfer), (ii) when the species reaches close enough to the electrode surface (less than 2nm) electron transfer occurs as a result of quantum mechanical tunnelling,[24] (iii) the product moves away from the electrode surface and the concentration of electroactive species near the electrode is refreshed. Let's consider a simple redox reaction:

$$\mathrm{O} + ne^{-} \rightleftharpoons \mathrm{R} \qquad \textbf{(1.21)}$$

Where O is the oxidized species, R is the reduced species and *n* is the number of electrons transferred as a result of the redox reaction. If [O] is the concentration of

oxidized species and [R] is the concentration of reduced species, then the relationship between the concentrations of redox species and the Gibbs free energy (ΔG) is given by the following equation.[4]

$$\Delta G = \Delta G^{o} + RT \ln \frac{[R]}{[O]} \qquad \textbf{(1.22)}$$

Where ΔG^{o} (J mol^{-1}) is the standard Gibbs free energy, R is the universal gas constant (8.3145 Jmol^{-1} K^{-1}), and T is the absolute temperature. The ratio of [O]/[R] is related to Gibbs free energy and the relationship between the Gibbs free energy and potential is obtained by the amount of charge passed as a result of applied potential, given by the following equation.[2]

$$\Delta G = -nFE \qquad \textbf{(1.23)}$$

Where E is the maximum potential between two electrodes, called the equilibrium potential or open circuit potential (OPC), which is present when there is no current flowing through the electrochemical cell. The negative sign indicates a reduction process.

When a potential is applied across the electrode-electrolyte interface, electron transfer occurs and a current is produced as a result of a redox reaction. The transfer of charge (electrons) is called current and is given by the following equation:

$$i = \frac{dQ}{dt} \qquad \textbf{(1.24)}$$

Where i is the faradaic current (A), Q is the charge (C), and t is the time (s). The above equation helps us to determine the rate of the reaction and the current density.

1.5 Heterogeneous Electron Transfer

Heterogeneous electron transfer involves the transfer of electrons between the electrode and electrolyte interface and is called a faradaic process as discussed in section (1.2). The most acceptable model to describe the rate of heterogeneous electron transfer was proposed by Butler [26] and Volmer [27]. Let's consider a one electron transfer redox reaction where an oxidized species O accepts one electron and is reduced to species R as shown in equation (1.21). The current associated with

this faradaic process is called the faradaic current and is directly proportional to the flux according to the following equation:[2, 4]

$$i = -nFAJ \qquad \textbf{(1.25)}$$

Where *n* is the number of electrons transferred, *F* is Faraday's constant, *A* is the area of electrode and *J* is the flux. *J* is directly related to the rate at which an electroactive species transfers electrons at the solution/electrode interface. Let us consider that the flux associated with species O is J_o is given by the following equation.[6]

$$J_o = -k_{red}[\mathrm{O}] \qquad \textbf{(1.26)}$$

Where k_{red} is the rate constant for heterogeneous electron transfer of the forward reaction and the negative sign shows the reduction process. The flux associated with species R is J_R and is given by the following equation.[6]

$$J_R = k_{oxi}[\mathrm{R}] \qquad \textbf{(1.27)}$$

Where k_{oxi} is the rate constant for heterogeneous electron transfer of the backward (oxidation) reaction. Thus the current associated with both forward and backward redox processes is given by the following equations:

$$i_c = -FAk_{red}[\mathrm{O}] \qquad \textbf{(1.28)}$$

$$i_a = FAk_{oxi}[\mathrm{R}] \qquad \textbf{(1.29)}$$

Where i_c and i_a are the currents associated with the reduction of species O (cathodic current) and oxidation of species R (anodic current), respectively. The total current i_t is the sum of the forward current and backward current and is given by the following equation.[6]

$$i_t = i_a + i_c \qquad \textbf{(1.30)}$$

Therefore $$i_t = FAk_{oxi}[\mathrm{R}] - FAk_{red}[\mathrm{O}] \qquad \textbf{(1.31)}$$

By applying transition state theory, the rate constants for both forward (reduction process) and backward (oxidation process) reactions are given by the following equations.[4, 6]

$$k_{red} = k^o \exp\left(\frac{-\alpha F(E-E_f^o)}{RT}\right) \quad \textbf{(1.32)}$$

$$k_{oxi} = k^o \exp\left(\frac{(1-\alpha)F(E-E_f^o)}{RT}\right) \quad \textbf{(1.33)}$$

Where k^o is the standard heterogeneous rate constant, (E- E^o_f) is the overpotential (the difference between the applied potential and equilibrium potential, sometimes called formal potential, α is the transfer coefficient, a dimensionless parameter that gives information on the position of the transition state for reactants and products along the reaction coordinates. The value of α varies between 0 and 1 and usually estimated to be close to 0.5 which reflects that the transition state exist midway between species O and R.[4, 6]

By substituting equations (1.34) and (1.35) into equation (1.33), we can get a final relationship for Butler and Volmer equation which gives the total current i_t flowing through the working electrode as a result of a one electron transfer redox reaction:[4, 6]

$$i_t = FAk^o\left[[\mathrm{R}]\exp\left(\frac{(1-\alpha)F(E-E_f^o)}{RT}\right) - [\mathrm{O}]\exp\left(\frac{-\alpha F(E-E_f^o)}{RT}\right)\right] \quad \textbf{(1.34)}$$

This equation tells us how the observed current changes as a result of an applied overpotential (E- E^o_f).[6] This equation can be combined with the equations of mass transport to obtain a theoretical model for the relationship between the current response and the applied potential.[6]

When the solution under observation is well stirred and the concentration of electroactive species near the electrode surface is equal to the concentration of electroactive species in the bulk; ([O] = $[\mathrm{O}]_{bulk}$ and [R] = $[\mathrm{R}]_{bulk}$). Under these conditions, the electrochemical system is at equilibrium and there is no net current passed through the electrochemical cell as the cathodic current is balanced by an equal and opposite anodic current. In this situation, the Butler and Volmer equation can be simplified as follows:

$$i_t = i^o\left[\exp\left(\frac{(1-\alpha)F(E-E_f^o)}{RT}\right) - \exp\left(\frac{-\alpha F(E-E_f^o)}{RT}\right)\right] \quad \textbf{(1.35)}$$

Where i^o is the standard exchange current and can be given by the following equation.

$$i^o = FAk^o[\mathrm{R}]^{\alpha}_{bulk}[\mathrm{O}]^{1-\alpha}_{bulk} \qquad \textbf{(1.36)}$$

The standard exchange current i^o is an essential scaling factor to determine electron transfer kinetics and depends on the bulk concentrations of electroactive species and the standard rate constant. Let's consider two limiting cases corresponding to large or small value of the standard exchange current i^o. In both cases, the net current in the cell is zero when $E - E^o_f = 0$.[6]

In the first case, when the value of i^o is large this means the electron transfer has fast electrode kinetics. The electrochemical system is said to be "*reversible*" because under these conditions, no overpotential is required to drive the reaction in both directions and the rate of electron transfer is sufficiently fast enough to attain the equilibrium in a short time scale as the potential is varied.[6] The Butler-Volmer equation (1.35) simplifies to the exponential form of the Nernst equation (equation 1.1).

In the second case, when the value of i^o is small this means the electron transfer has relatively slow electrode kinetics. The electrochemical system is said to be "*irreversible*" because the rate of electron transfer is relatively slow enough on the timescale of the experiment. As a result, equilibrium is not attained at the applied potential close to the *formal potential* ($E°_f$). Under these conditions, a high overpotential is required to drive the reaction to induce the flow of electrons. Those electrochemical systems which have intermediate electrode kinetics are called "*quasi-reversible*" redox processes.[3, 6]

1.6 Coupled Homogeneous Reactions

In voltammetry, when an electrochemical reaction mechanism consists of a heterogeneous electron transfer coupled with homogeneous chemical step(s) with their individual rate constants then the chemical step can have a significant effect on the behaviour of the observed voltammetry. In this situation, an electrochemical method (cyclic voltammetry) is employed to study the kinetics and mechanisms of such reactions.[6, 23, 24] A simple notation has been used to describe the electrochemical and chemical steps, proposed by Testa and Reinmuth in 1961.[28] The letter "E" is used to describe the heterogeneous electron transfer step and the letter "C" is used to describe the homogeneous chemical step. These notations are combined together in

order to describe the different electrochemical reaction mechanisms such as EC, ECE and CE, some of which are discussed in this thesis. A brief discussion on these mechanisms is given below.

1.6.1 EC Mechanism

In an EC mechanism, the electrochemical step (E) produces an unstable product that undergoes a follow-up chemical step (C) through a first-order homogeneous decay and yield electrochemically inactive species (irreversible chemical step). For example

$$\text{E} \qquad A + e^- \overset{k^o}{\longrightarrow} B \qquad \textbf{(1.37)}$$

$$\text{C} \qquad B \overset{k_C}{\rightarrow} C \qquad \textbf{(1.38)}$$

Where k^o is the standard rate constant for electron transfer and k_C is the rate constant for the chemical step. An example of an EC mechanism is the oxidation of 1,4-aminophenol in acidic solution which is two electron oxidation process.[24]

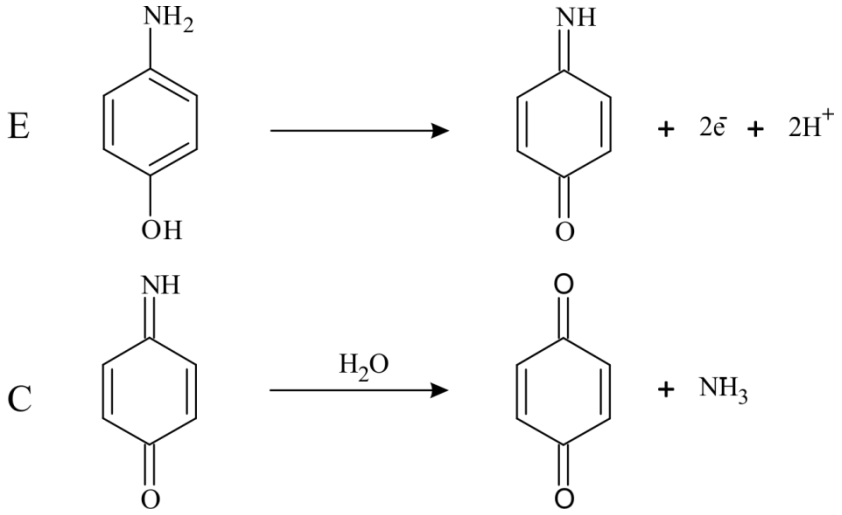

Figure 1.7: Reaction scheme for an EC mechanism

1.6.2 ECE Mechanism

In an ECE mechanism, the product of the chemical step is itself electrochemically active in the experimental potential window and further undergoes an electron transfer process. For example

$$\text{E} \qquad A + e^- \xrightarrow{k^o_1} B \qquad \textbf{(1.39)}$$

$$\text{C} \qquad B \xrightarrow{k_C} C \qquad \textbf{(1.40)}$$

$$\text{E} \qquad C + e^- \xrightarrow{k^o_2} D \qquad \textbf{(1.41)}$$

Where k^o_1 and k^o_2 are the standard rate constants for *A* to *B* and *C* to *D* electron transfer steps, respectively, and k_C is the rate constant for the chemical step. An example of an ECE mechanism is the reduction of 1,2-bromonitrobenzene in aprotic solvents, which begins with a one electron reduction process to the radical anion.[24]

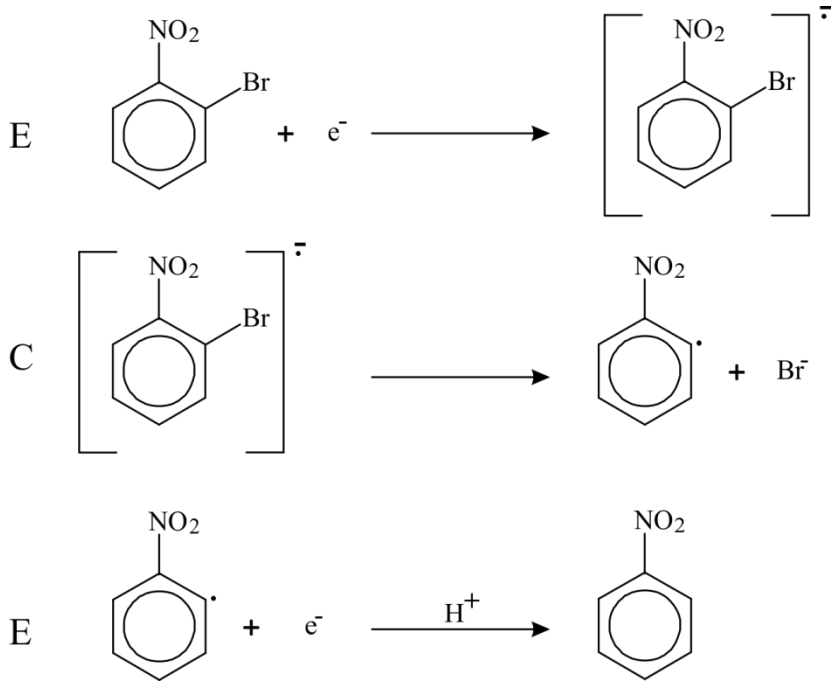

Figure 1.8: Reaction scheme for an ECE mechanism

1.6.3 CE Mechanism

In CE mechanism, the parent species first undergoes a homogeneous chemical step and a product of the chemical step is electrochemically active, which then undergoes an electron transfer process. For example

$$\text{C} \qquad A \xrightarrow{k_C} B \qquad \textbf{(1.42)}$$

$$\text{E} \qquad B + e^- \xrightarrow{k^o} C \qquad \textbf{(1.43)}$$

An example of a CE mechanism is the reduction of acetic acid in aqueous solution.[24]

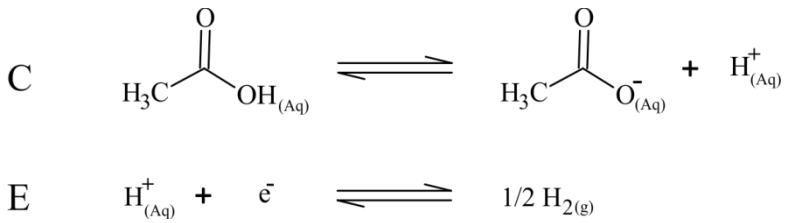

Figure 1.9: Reaction scheme for a CE mechanism

The work presented in this thesis is mostly based on E and ECE mechanisms such as the oxidation of hydrogen and the oxidation of ammonia, respectively, in room temperature ionic liquids (RTILs).

1.7 Practical Aspects of Voltammetry

A brief background on electrochemical processes and the various parameters related to electrochemical measurements has been discussed in the above sections. In this section we will describe the practical aspects of electrochemical experiments such as the design of the electrochemical cell, and the type of electrodes that are employed to study the work presented in this thesis.

1.7.1 Electrochemical Cells

An electrochemical cell is a device in which faradaic processes occur as a result of redox reactions. It can be either a *galvanic cell* where spontaneous redox reaction occurs or an *electrolytic cell* where non-spontaneous redox reaction occurs. Regardless of the type of cell, both contain two half-cells: one half-cell where the reaction of interest occurs and the second half-cell which has a fixed potential. In dynamic electrochemistry, a simple electrochemical cell consists of two electrodes, one is called working electrode (WE) where the reaction of interest occurs and second is called reference electrode (RE) which has constant and fixed potential, used to monitor the potential of working electrode. This setup is applied in those conditions when tiny current is passed through the WE, usually microelectrode.[4, 6]

However, in the case of a large electrode where a large current is passed through the cell, particularly if the cell has a relatively high resistance; a three electrode setup is used, which consists of a working electrode (WE), counter electrode (CE) and reference electrode. The function of the CE is to balance the reaction occurring at working electrode. The RE has a stable potential throughout the experiment and any

change in the external applied potential may lead to drive the reaction of interest on the WE. The distance between the WE and CE should be small enough to minimize the uncompensated solution resistance.[4] Consider a potential, E_{app}, applied between the working electrode and reference electrode given by the following equation:[6]

$$E_{app} = (\Phi_{WE} - \Phi_s) + iR_s + (\Phi_s - \Phi_{RE}) \qquad \textbf{(1.44)}$$

Where the term ($\Phi_{WE} - \Phi_s$) = E_{WE} is the potential difference across the working electrode/solution interface which drives the reaction of interest on the surface of WE. The second term, iR_s is called voltage drop or Ohmic drop in solution due to the passage of current (i) between the working and reference electrode and R_S is the compensated resistance of solution. The third term ($\Phi_s - \Phi_{WE}$) = E_{RE} is the potential difference across the reference electrode/solution interface which is considered to be fixed throughout the experiment.

For microelectrodes, only a tiny current is passed through the cell and therefore the term iR_s is considered very small or negligible. In this case the counter electrode and reference electrode can be combined together to give a two electrode setup in which the second electrode acts as a combined counter electrode and reference electrode. In this situation, the equation (1.44) can be simplified as:[6]

$$E_{app} = (\Phi_{WE} - \Phi_s) + constant \qquad \textbf{(1.45)}$$

1.7.2 Types of Electrodes

Electrodes are classified into different categories usually on the basis of their geometry. These include linear, spherical, hemispherical, conical, cylindrical, inlaid and arrays.[29] A linear geometry is the best representation of a disk electrode. Disk electrodes are classified into four categories commonly used in voltammetric experiments i.e. inlaid disk, recessed disk, including ring electrode and band electrode. In this thesis, we will present some of our work at inlaid disk electrodes e.g. conventional macrodisk and microdisk electrodes. Conventional macrodisk electrodes of various sizes are used. They have a conducting metal wire or disk (Pt, Au) sealed in an insulating material (e.g. PTFE) whose a cross section is exposed to form an inlaid disk electrode. In the case of microdisk electrodes, the conducting wire (Pt, Au) is sealed usually in glass and is polished on polishing pad using

alumina powder or diamond spray to form an inlaid microdisk electrode. Planar devices such as screen printed electrodes (SPEs) and thin-film electrodes (TFEs) are also used. These have a disk type working electrode along with integrated counter and reference electrodes, all fabricated on an insulating material (plastic or glass). Recessed microarray thin-film electrodes (MATFEs) are also used which have a gold or platinum working electrodes, covered with SU-8 layer on which an array of recessed micro-holes are drilled to form an array of recessed microdisk electrodes. Microband array electrodes have also been used. These are formed on an inlaid gold disk electrode by printing HDT (hexadecane thiol) micro-channels using PDMS (polydimethyl siloxane) stamps to form an array of microbands.

On the basis of electrode geometry, the diffusion of electroactive species can be divided into two main categories i.e. linear diffusion (planar) and radial diffusion (convergent). Both types of diffusion can be considered on an electrode, but on the basis of geometry alone, one could be dominant while the other could be suppressed. For a large size macrodisk electrode, linear diffusion occurs predominantly at the center of the disk with a small contribution of radial diffusion from the edges of the disk called the *edge effect* (illustrated in figure 1.10a).

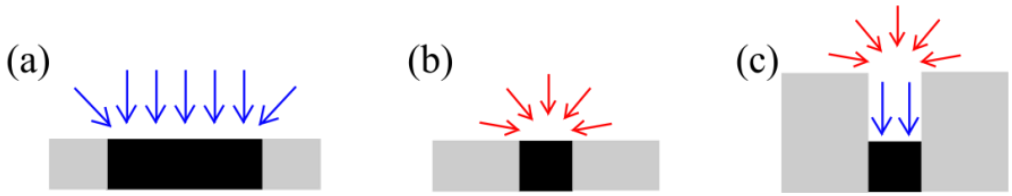

Figure 1.10: Comparison of diffusion regimes at (a) inlaid macrodisk, (b) inlaid microdisk, and (c) recessed microdisk electrodes.

While in the case of inlaid microdisk electrodes, where the size of the electrode is 25 μm or smaller called *ultramicroelectrodes*, radial diffusion occurs predominantly from the edges to the center with a negligible effect of linear diffusion. This leads to a steady state current response that is an ideal property of an inlaid disk ultramicroelectrode.[29] This type of mixed diffusion pattern is illustrated in figure 1.10b. In the case of a recessed microdisk electrode, radial diffusion occurs predominantly on the mouth of microhole along with a successive contribution of linear diffusion within the pore (illustrated in figure 1.10c). The current at an inlaid electrode of the same dimensions is dependent on the depth of the recession, according to the following equation:[30]

$$I_{\text{lim}} = \frac{4\pi n F_C D r^2}{4L + \pi r} \quad \textbf{(1.46)}$$

The mathematical expression to calculate the thickness of diffusion layer is given by:[4]

$$\delta = \sqrt{\pi D t} \quad \textbf{(1.47)}$$

Where δ (cm) is the thickness of diffusion layer which is in the range of 10^{-3}–10^{-1} cm,[4] D (cm^2 s^{-1}) is the diffusion coefficient of electroactive species, and t (s) is the time of experiment. This equation tells us about the diffusion regime on the electrode surface. On microelectrodes, at sufficiently short times (fast scan rates), the thickness of diffusion layer is much smaller than the radius of electrode (r_e), and the spherical electrode looks like a planar to the electroactive species at the edge of diffusion layer. Under these conditions, the electrode behaves like a macroelectrode and linear diffusion observed on the surface of microelectrode. In this case, the above equation can be written as:[6, 24]

$$\sqrt{\pi D t} \ll r_e \quad \textbf{(1.48)}$$

On the other hand, when the time of experiment is long (slow scan rates) at microelectrodes, the thickness of diffusion layer is much greater than the radius of electrode (r_e), and spherical behaviour of the electrode becomes dominant. Under these conditions, radial diffusion is observed on the surface of electrode, with a resultant steady state current response. In this case the above equation can be written as:[6, 24]

$$\sqrt{\pi D t} \gg r_e \quad \textbf{(1.49)}$$

On macroelectrodes, for shorter times (faster scan rates), linear diffusion is converted into radial diffusion due to the spherical expansion of diffusion layers on the surface of the electrode as time proceeds.[24]

Practically, both macro and micro electrodes have great advantages in voltammetry. Macroelectrodes are commercially available, easy to use and give high current with peak shaped responses due to one dimensional linear diffusion, and are mostly employed to study mechanisms of electrochemical reactions. On the other hand, on

microelectrodes the rate of mass transport is very fast compared to macroelectrodes, and these electrodes are preferred for fast electrochemical measurements. They give high current density with negligible ohmic drop and due to their small overall current response, provide an ease to simplify the experimental arrangement with a two electrode setup.

1.8 Voltammetric Techniques

A common feature of all voltammetric techniques is that they involve the application of a potential to the working electrode and monitor the current response over a period of time. Broadly voltammetry can be divided into two main classes; namely *potential sweep* and *potential step*. In *potential sweep*, the potential is swept linearly with time between two chosen values and the current is monitored as a function of applied potential. While in *potential step*, the potential is stepped to a fixed value and the current is monitored as a function of time. In this section, a brief discussion about voltammetric techniques that are used to perform experiments reported in this thesis will be given.

1.8.1. Linear Sweep and Cyclic Voltammetry

Linear sweep voltammetry (LSV) and cyclic voltammetry (CV) are a type of potential sweep voltammetry in which the potential is swept linearly from an initial potential, E_1, where there is no electron transfer occur (usually at that potential the current is zero), to the final potential, E_2, where the reaction is under mass transfer control. In LSV, the potential is stopped at E_2 and the sweep direction could be positive or negative, while in CV the potential is also swept in the reverse direction from E_2 to the initial potential E_1 at a constant sweep rate. In both voltammetric techniques (LSV and CV), the current is monitored across the potential ramp called *linear potential ramp* or *triangular potential ramp* respectively. The resulting plot of current, *i*, *vs* potential, *E*, is called a linear sweep voltammogram or a cyclic voltammogram. The linear and triangular potential ramp for these techniques is represented in figure (1.11). The shapes of the voltammograms depend on the concentration profile of redox species resulting from the potential sweep and diffusion pattern. According to Fick's second law, the current is directly proportional to the concentration gradient of an electroactive species near the electrode surface.[4] To demonstrate the relationship between the concentration profile and current-

voltage plot, a small increase in voltage across the voltammogram gives useful information about the corresponding concentration profile.[4]

1.8.1.1 Voltammetry at Macrodisk Electrodes

In the case of *macrodisk electrodes* with planar diffusion, both voltammograms (figure 1.11b & d) show that at an initial potential, E_1, the current is zero because the potential is not high enough to induce the redox reaction. As the potential is swept positively from E_1, the current starts to increase and reaches a maximum value corresponding to the oxidation of a redox species as a result of electron transfer. The current then starts to decrease due to the limiting mass transfer near the electrode surface. When the potential is swept back from E_2 to E_1 (in CV), the current starts to increase in the negative direction, corresponding to the reduction of the electrogenerated species near the electrode surface.

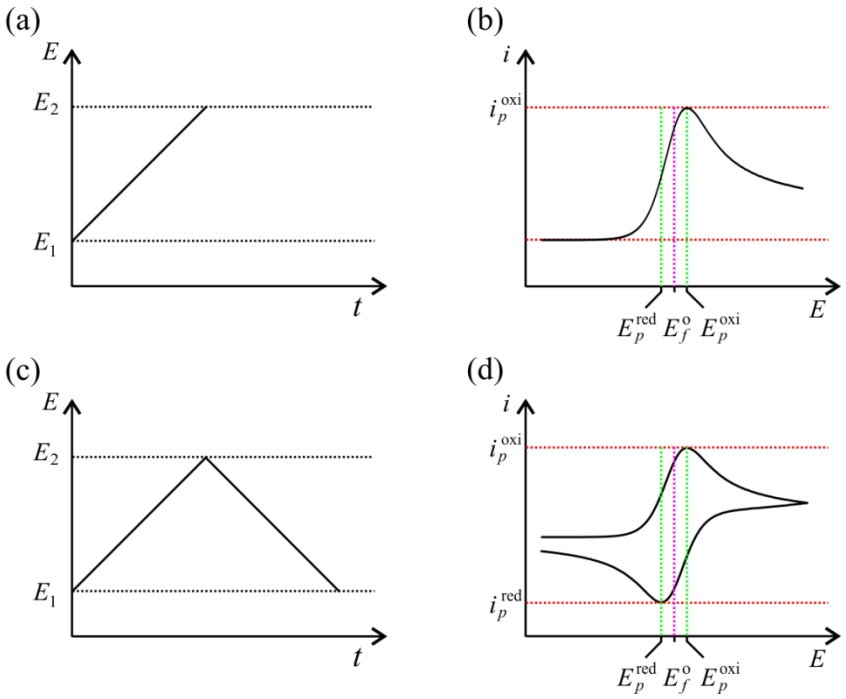

Figure 1.11: (a,c) Linear and triangular potential ramps showing the variation of potential, *E*, with time, *t*, (b,d) Linear sweep voltammetry and cyclic voltammetry showing the current response as a function of applied potential. The shape corresponds to an ideal 1-electron oxidation.

The shape and position of the voltammograms (peak potentials (E_p^{oxi} and E_p^{red}), peak currents (i_p^{oxi} and i_p^{red})) depend on many factors such as the initial and final potentials, formal potential ($E°_f$) sweep rate, analyte concentration, and size and geometry of electrode. All together, these provide characteristic information about

the reaction mechanism, rate of electron transfer, rate of mass transfer, any surface adsorption process, coupled homogeneous reactions, and electrochemical reversibility.[2, 4, 7]

The peak current for a reversible redox couple on planar electrode is given by the Randles-Sevcik equation.[4, 6, 24]

$$i_p = (2.69\times10^5)n^{3/2}AD^{1/2}v^{1/2}C_{bulk} \qquad \textbf{(1.50)}$$

Where i_p is the peak current, n is the number of electrons, A is the area of electrode, D is the diffusion coefficient, v is the scan rate and C is the concentration of analyte species. The peak current, i_p, for a reversible diffusional controlled process is directly proportional to the square root of scan rate, $v^{1/2}$, and a plot of i_p *vs* $v^{1/2}$ gives a straight line which passes through the origin. The gradient of the straight line gives the diffusion coefficient of the redox species.[4]

The position of peaks along the potential axis (E) is directly related to the formal potential ($E°_f$). For a reversible one electron transfer, the formal potential coincides with the mid potential (E_m) or half-wave potential ($E_{p/2}$), which is the potential at which the current reaches the half the peak current (i_p^{oxi} or i_p^{red}) and is given by the following equation:[4, 7, 23]

$$E_m = E_{p/2} = E_f^o = \frac{E_p^{oxi} + E_p^{red}}{2} \qquad \textbf{(1.51)}$$

If the rate of electron transfer is fast compared to the rate of mass transfer, then the redox process is called *electrochemically reversible* (see figure 1.12a) and the peak to peak separation (ΔE_p) for reversible redox couple is given by the following equation:[4, 7, 23]

$$\Delta E_p = E_p^{oxi} - E_p^{red} = 2.303\frac{RT}{nF} \qquad \textbf{(1.52)}$$

Where n is the number of electron transferred. For a one electron transfer process, the above equation can be written as:

$$\Delta E_p = E_p^{oxi} - E_p^{red} = \frac{0.059}{n} \qquad \textbf{(1.53)}$$

Thus the peak to peak separation helps us to determine the number of electron transferred. For a reversible redox couple involving a one electron transfer, the peak

to peak separation should be 59 mV at 298 K, and peak potentials are independent of the sweep rate. The ratio of peak currents (i_p^{oxi} and i_p^{red}) for a reversible redox couple should be equal to unity, given by the following equation:[4, 7, 23]

$$\left|\frac{i_p^{oxi}}{i_p^{red}}\right| = 1 \qquad \textbf{(1.54)}$$

When the rate of electron transfer is much slower than the rate of mass transfer, the shape of the voltammogram changes significantly. The individual peaks become broader and the peak current is reduced compared to a reversible redox process, also with an increased peak to peak separation. In this case, a greater overpotential is required for the same rate of electron transfer. As the rate of mass transfer overcomes the rate of electron transfer i.e. usually at very fast scan rate, the reverse peak becomes less pronounced and finally disappears. Under these conditions, the redox process is called *electrochemically irreversible* (see figure 1.12c). The peak current for an irreversible process is given by the following equation.[4, 7, 23]

$$i_p = (2.99\times10^5)n(\alpha n_{rd})^{1/2}AD^{1/2}v^{1/2}C_{bulk} \qquad \textbf{(1.55)}$$

Where i_p is the peak current for irreversible process, which increases linearly with the square root of scan rate for a diffusion controlled process, n_{rd} is the number of electrons transferred in the rate determining step and α is the electron transfer coefficient.

When the rate of electron transfer is in between the reversible and irreversible limits, the shape of the voltammogram becomes more drawn-out and the system is called *quasi-reversible* (see figure 1.12b). In this case, the rate of both forward and backward electron transfer is considered. The scan rate has a considerable effect on the shape of voltammogram and the peak current is not directly related to the square root of scan rate. At slow scan rates, the system looks similar to a reversible process but as the scan rate is increased, the rate of electron transfer is not fast enough to maintain Nernstian equilibrium. As a result the peak to peak separation is increased from 59/n mV at 298 K, and the peaks become broader with smaller peak currents than for a fully reversible redox process. For a quasi-reversible process, the ratio of peak currents is equal to unity when the value of electron transfer coefficient (α) is equal to 0.5.[4, 7, 23]

The shape of voltammograms for reversible, quasi-reversible and irreversible redox processes are given in figure (1.12).

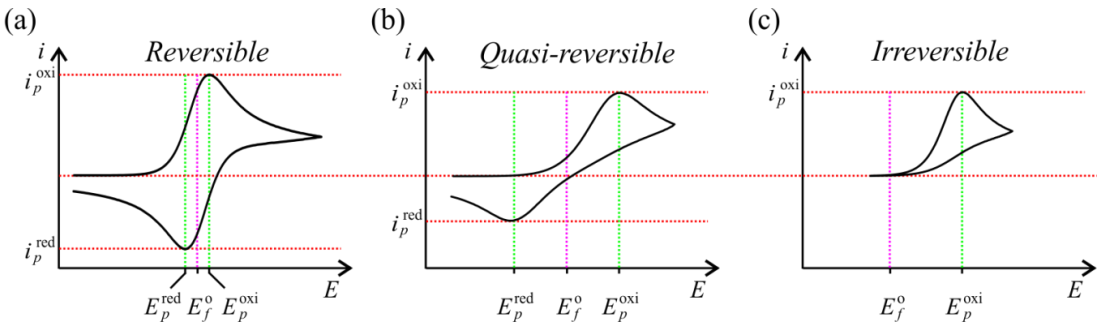

Figure 1.12: Comparison of typical cyclic voltammograms on planar macrodisk electrodes for (a) reversible, (b) quasi-reversible, and (c) irreversible redox processes. Figure adapted from Ref.[31]

1.8.1.2 Voltammetry at Microdisk Electrodes

Microdisk or microelectrodes can be defined as electrodes which possess at least one dimension small enough so that the mass transfer regime depends on the size of electrode. When the size of the electrode is reduced to sufficiently small enough (ca. ≥ 50 μm), the electrode behaves under steady-state conditions due to the predominant effect of radial diffusion. Under steady state conditions, the resulting current-voltage curve (voltammogram) is sigmoidal in shape (shown in figure 1.13) with a limiting current plateau called a steady-state current response. This steady-state behaviour is due to the fast rate of mass transfer to the surface of microelectrode as a result of the fast replenishment of redox species at the electrode. In this case, the concentration profile becomes independent of time at a given potential.

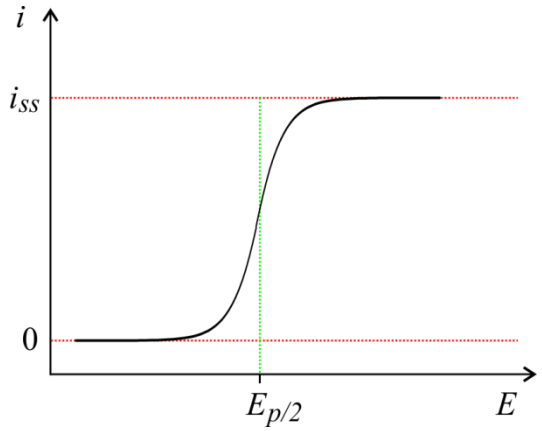

Figure 1.13: Typical steady state voltammetry (sigmoidal-shaped) at a microdisk electrode. Figure adapted from Ref.[31]

A steady-state voltammogram can be characterized with a half-wave potential ($E_{p/2}$) and a plateau of limiting current. For a reversible, fast electron transfer, the half-wave potential coincides with the formal potential ((E_f^o). At a limiting rate of electron transfer, it deviates from reversibility and the resulting current-voltage curve is said to be quasi-reversible or irreversible.[4]

The steady-state limiting current (i_{ss}) on a microdisk electrode is given by the following equation.[4, 23]

$$i_{ss} = 4nFDr_dC_{bulk} \qquad \textbf{(1.56)}$$

Where n is the number of electrons transferred, F is Faraday's constant, D is the diffusion coefficient of electroactive species, r_d is the radius of microdisk electrode, and C_{bulk} is the bulk concentration.

Voltammetry on microdisk electrode has many advantages over conventional macrodisk electrodes due to fast mass transport, large current density, decreased background current (charging current), and reduced ohmic drop, which allows the conduction of experiments in highly resistive media such as ionic liquids, or solutions in the absence of supporting electrolyte.[23]

1.8.2 Chronoamperometry

The study of the variation of current response as a function of time under potentiostatic control is called chronoamperometry.[10] It is a type of *potential step voltammetry*, in which the potential is stepped from an initial potential, E_1, where current is zero (no electron transfer) to a final potential, E_2, where electron transfer occurs and the reaction is usually under mass transfer control. The resulting plot of current, *i*, *vs* time, *t*, is called *chronoamperogram*. A potential-step waveform and resulting chronoamperogram is shown in figure (1.14).

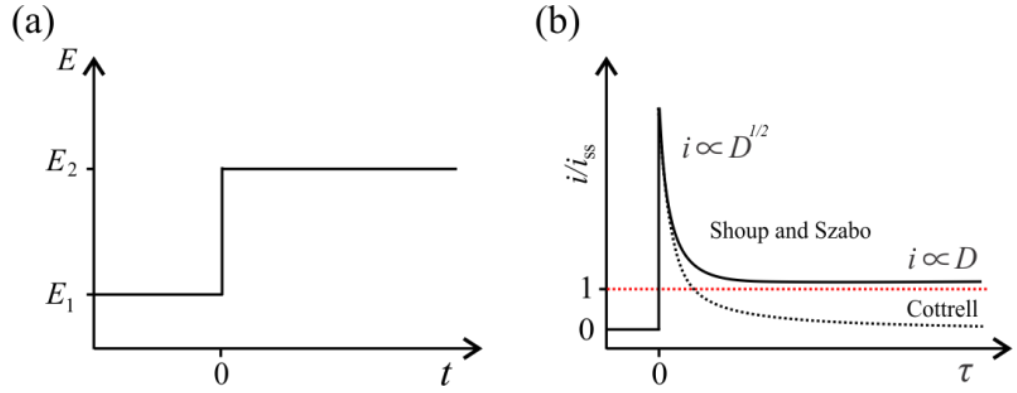

Figure 1.14: (a) Potential-step waveform as a function of time, and (b) the resulting current-time chronoamperogram on a microdisk electrode (following the Shoup and Szabo expression) compared to a macrodisk electrode (following the Cottrell expression). Figure adapted from Ref.[31]

On macrodisk electrodes, at an initial potential, E_1, the current is zero where no redox reaction occurs. As the potential is stepped to final step, E_2, initially a large current appears which falls steadily as a function of time. Due to the effect of planar diffusion, the potential step transient shows slow transition of diffusion limited current from Cottrellian to steady-state behaviour where the Cottrellian current is $i \propto D^{1/2}$.[32] The Cottrellian current (i_c) or diffusion limited current is given by the Cottrell equation:[4, 10]

$$i_c = \frac{nFAD^{1/2}C_{bulk}}{\pi^{1/2}t^{1/2}} \qquad \textbf{(1.57)}$$

Where n is the number of electrons transferred, F is Faraday's constant, D is the diffusion coefficient of electroactive species, A is the area of macrodisk electrode, C_{bulk} is the bulk concentration and t is the time. The plot of i *vs* $1/t^{1/2}$ gives a straight line which passes through the origin, and the slope of the best-fit line is given by the following equation.[4]

$$Slope = \frac{nFAD^{1/2}C_{bulk}}{\pi^{1/2}} \qquad \textbf{(1.58)}$$

For a macrodisk electrode with pure planar diffusion, the diffusion coefficient, D, can be calculated from the slope, as given below.

$$D = \frac{(slope)^2\pi}{(nFAC_{bulk})^2} \qquad \textbf{(1.59)}$$

Potential-step chronoamperometry is an excellent technique to measure diffusion coefficients for electroactive species very accurately using the Cottrell equation assuming that the diffusion is purely planar which can be achieved when the electrode is large enough and the concentration of species near the surface is equal to the bulk concentration.[4]

In the case of microdisk electrodes, where radial diffusion dominates, the current transient follows the Shoup and Szabo expression,[33] with two different time regimes. Firstly, a rapid decrease of chronoamperometric current at short times is directly related to the current ($i \propto D^{1/2}$) and secondly, a steady-state current response at longer times is a diffusion-controlled current with negligible impact of charging current [34, 35], ($i \propto D$).[32] In this case, the current can be given by Shoup and Szabo expression in terms of a dimensionless parameter τ.[33]

$$i = 4nFr_d DC_{bulk} f(\tau) \qquad \textbf{(1.60)}$$

Where (τ) is:

$$\tau = \frac{4Dt}{{r_d}^2} \qquad \textbf{(1.61)}$$

Where n is the number of electrons transferred, F is Faraday's constant, r_d is the radius of microdisk electrode, D is the diffusion coefficient, C_{bulk} is the bulk concentration and t is the time. In order to calculate the term $f(\tau)$, Aoki and Osteryoung [36] used two different expression for short-time and long-time expansion to describe the variation of i with the dimensionless parameter τ. Later on Shoup and Szabo give a single relationship which describes the variation of current, i, over the full range of τ and is given by the following equation:[33]

$$f(\tau) = 0.7854 + 0.8862\tau^{-1/2} + 0.21464e^{-0.7823\tau^{-1/2}} \qquad \textbf{(1.62)}$$

By fitting the experimental data obtained from the chronoamperometric transient to the Shoup and Szabo expression, the number of electrons transferred, diffusion coefficient and concentration of electroactive species, can be obtained simultaneously. However it is very important to mention here, the chronoamperometric transient does not provide any information about the electrode kinetics because the chosen potential to be stepped up always greater than the formal potential of the redox reaction.

1.8.3 Pulse Voltammetry

Potential step voltammetry is the basis of pulse voltammetry.[10] In the history of electrochemistry, Hevrovsky in 1922 invented a device called a *dropping mercury electrode* (DME) to measure surface tension. He discovered a technique called *polarography* which is the simplest form of voltammetry at a DME. A DME is a glass capillary tube through which mercury flows under gravity to form a successive drop of mercury on which redox reactions occur. Each new drop provides a fresh surface for a redox reaction and as the drop grows, the current starts to increase and then the current falls suddenly with the fall of a drop. The main objective of this technique is to increase the sensitivity with better limit of detection (LOD) which can be achieved by synchronizing the pulse with the growth of a mercury drop. Polarography with a DME was considered the best technique in early electrochemistry for analytical measurements but this technique has some limitations; firstly, mercury is toxic and dangerous to health over prolonged exposure. Secondly it is oxidized at very small positive potentials (+0.2 V), making the technique limited to analyse species which are oxidized in positive potentials. Thirdly, large residual current is observed due to large capacitance resulting from the growth of a mercury drop.[10] Later on this technique was developed and the DME was replaced with stationary electrodes along with more sophisticated potentiostats and computer controlled systems.[2]

Generally pulse voltammetry is divided into six subclasses; tast polarography, staircase voltammetry, normal pulse voltammetry, reverse pulse voltammetry, differential pulse voltammetry, and square wave voltammetry.[2] Tast polarography, staircase voltammetry, normal pulse voltammetry, and differential pulse voltammetry are the sequence bases for the historic development of polarography with a DME, while reverse pulse voltammetry, and square wave voltammetry are the later innovations in pulse voltammetry.[2] In this section two techniques are discussed: differential pulse voltammetry, and square wave voltammetry, as they are employed to study the work presented in the second half of this thesis.

1.8.3.1 Differential Pulse Voltammetry

Differential pulse voltammetry (DPV) is a type of pulse voltammetry in which a pulse of constant amplitude (10-100 mV) is superimposed at a regular intervals on a

slowly changing base potential which could be *linear potential ramp* or *potential staircase*. The current is sampled at two points for each pulse; just before the application of the pulse (S_1) and at the end of the pulse (S_2). The pulse width (t_p) is fixed at 50 ms while the total time for each pulse (T) is between 0.5 to 5 sec. The current is sampled at two points, S_1 and S_2 and the current associated with these point is i_1 and i_2. The current sampled at the start of the pulse (S_1/i_1) is the maximum contribution of non-faradic current, which decays exponentially, while the current sampled at the end of pulse (S_2/i_2) contains both faradaic and non-faradic current where the decay of faradic current is inversely proportional to the square root of time. Thus each pulse contains negligible capacitive current compared to faradaic current and this increased ratio of faradaic to non-faradaic current allows DPV to give a lower limit of detection and higher sensitivity.[37] The difference in current between these two points ($\Delta i = i_2 - i_1$) gives the total pulse current which is plotted against the applied potential (base potential). The resulting Δi *vs* E plot is called a differential pulse voltammogram where the peak current response and the height of peak current (Δi_p) is directly proportional to the concentration of redox species. The application of a pulse on the staircase along with the resulting current response (Δi *vs* E curve) is represented in figure (1.15).

For a reversible system, the peak potential (E_p) can be determined from the half-wave potential ($E_{p/2}$) and is given by the following equation:[2, 7, 10]

$$E_p = E_{p/2} \pm \frac{\Delta E_p}{2} \qquad \textbf{(1.63)}$$

Where ΔE_p is the amplitude of the pulse, with a positive sign (+ve) for a reduction process and a negative sign (-ve) for an oxidation process. For an irreversible system, the peak potential moves away from the half-wave potential and as the peak width increases (broader peak), and the height of the peak is reduced.[10]

The peak current (Δi_p) of a differential pulse voltammogram for a reversible system is given by the following equation:[2, 7, 10]

$$\Delta i_p = \frac{nFAD^{1/2}C_{bulk}}{\pi^{1/2}t_p^{1/2}}\left(\frac{1-\sigma}{1+\sigma}\right) \qquad \textbf{(1.64)}$$

Where σ is:

$$\sigma = exp\left(\frac{nF}{RT}\frac{\Delta E_p}{2}\right) \qquad \textbf{(1.65)}$$

Where n is the number of electrons transferred, F is Faraday's constant, A is the area of macrodisk electrode, D is the diffusion coefficient of electroactive species, C_{bulk} is the bulk concentration and t_p is the pulse duration, which should be at least 10 times smaller than the total time of the pulse (T).[24]

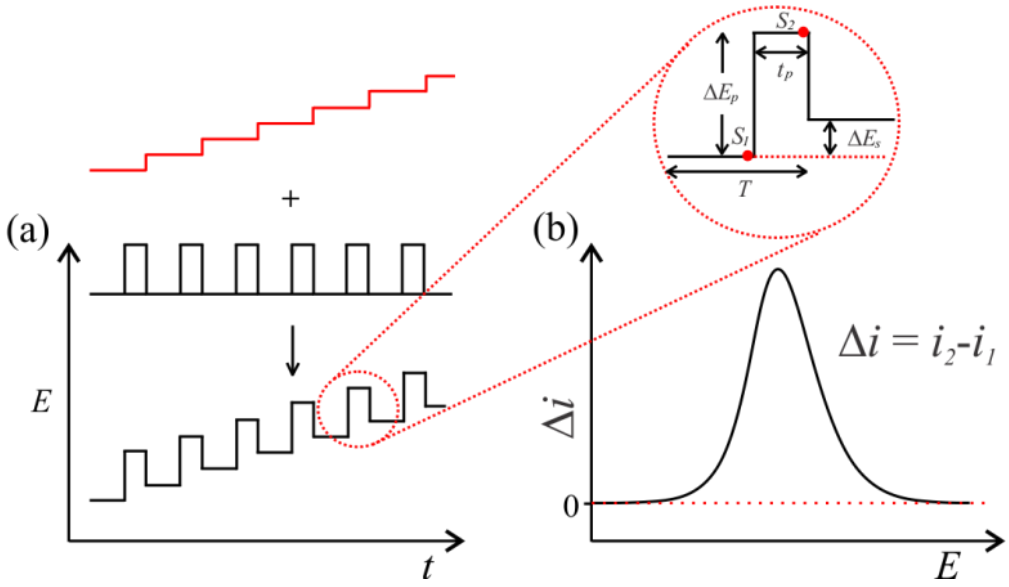

Figure 1.15: (a) Schematic representation of pulse on staircase and resulting pulse waveform (b) the resulting current response called a differential pulse voltammogram. The circular inset shows different parameters along the applied pulse; ΔE_p is the amplitude of pulse, ΔE_s is the step potential, t_p is pulse width (duration of pulse), and T is the total time of pulse. The red dots in the inset show sampling time at S_1 and S_2.

In equation (1.60), the term (1-σ)/(1+σ) describes the effect of pulse amplitude (ΔE_p) on peak current (Δi_p). For a large amplitude (ΔE_p), its value is unity and gives a maximum peak current which is equal to the faradaic current.[2, 10] When the pulse amplitude (ΔE_p) decreases (1-σ)/(1+σ) also decreases and finally reaches zero with $\Delta E_p = 0$.[2, 10]

In differential pulse voltammetry, the correction of charging background current (Δi_c) is very effective. The contribution of charging background current to the differential pulse current is negligible which makes the technique more sensitive and gives rise to low limits of detection (LODs) e.g. 10^{-8} M.[7]

1.8.3.2 Square Wave Voltammetry

Square wave voltammetry was originated from Kalousek commutator [38] and Barker's square-wave polarography [39] and later on developed by Osteryoung and coworkers

[40]. This is a advanced electrochemical technique, comprised of modern computer-controlled electroanalytical systems (e.g. potentiostats) which can be employed for both electrode kinetic and mechanistic measurements.[10, 41]

Square wave voltammetry is a high amplitude differential technique in which a symmetrical square wave pulse of amplitude, ΔE_p, is superimposed at a regular intervals on a staircase waveform of a step potential, ΔE_s, where the forward pulse of a square wave coincides with the staircase step, and both forward (positive) and backward (negative) pulses are on a single step.[41] The current is sampled at two points for each square wave cycle during the last few microseconds of each pulse; one at the end of the forward pulse (S_1) and the second at the end of the backward pulse (S_2).[41] The difference between the forward current (i_f) and backward current (i_b) gives the total square wave current ($\Delta i_p = i_f - i_b$) which is plotted against the applied staircase potential. The resulting Δi_p *vs* E plot is called a square wave voltammogram, which is a combination of all three plots in the form of peak current response; forward, backward and total current response *vs* the potential of the staircase. The forward current (i_f) is produced as a result of the oxidation of electroactive species and the backward current (i_b) as a result of the reduction of species produced in the forward pulse. The total current is larger than either the forward or backward components due to the difference of positive and negative currents (which is true for reversible and quasi-reversible system) and the height of the resulting peak current (Δi_p) is directly proportional to the concentration of redox species produced at the surface of electrode.[2] In square wave voltammetry, the contribution of charging background current (Δi_c) is very negligible because both forward and backward currents are sampled at the end of pulses, where the maximum contribution of faradaic processes occurs. The negligible charging current and fast speed of current sampling makes the technique very sensitive with low limits of detection (LODs) e.g. 10^{-8} M.[2, 25, 41]

Figure (1.16) shows a square wave cycle which is characterised by important parameters such as the square wave amplitude (ΔE_p) or pulse height, composed of two neighbouring pulses (positive and negative), the staircase height (ΔE_s), called step potential, pulse width or pulse time (t_p) and total time of one cycle called cycle period (T). The pulse time can be expressed in term of square wave frequency (f); the

number of square wave cycles per unit time which is reciprocal to the staircase period ($f = 1/T$) and each cycles contains two pulses ($T = 2t_p$).[2, 41]

$$f = \frac{1}{2t_p} \tag{1.66}$$

Where t_p is the duration of each pulse which is one-half of the staircase duration and given by the following equation.[41]

$$t_p = \frac{T}{2} \tag{1.67}$$

The square wave cycle with forward and backward pulses is repeated on each step of the staircase potential with an increment of fixed step potential (ΔE_s). Hence the step potential (ΔE_s) determines the effective scan rate for SWV and can be given by the following equation.[2]

$$v = \frac{\Delta E_s}{T} = \frac{\Delta E_s}{2t_p} = f\Delta E_s \tag{1.68}$$

Where ΔE_s is the step potential in mV and f is the frequency in Hz.

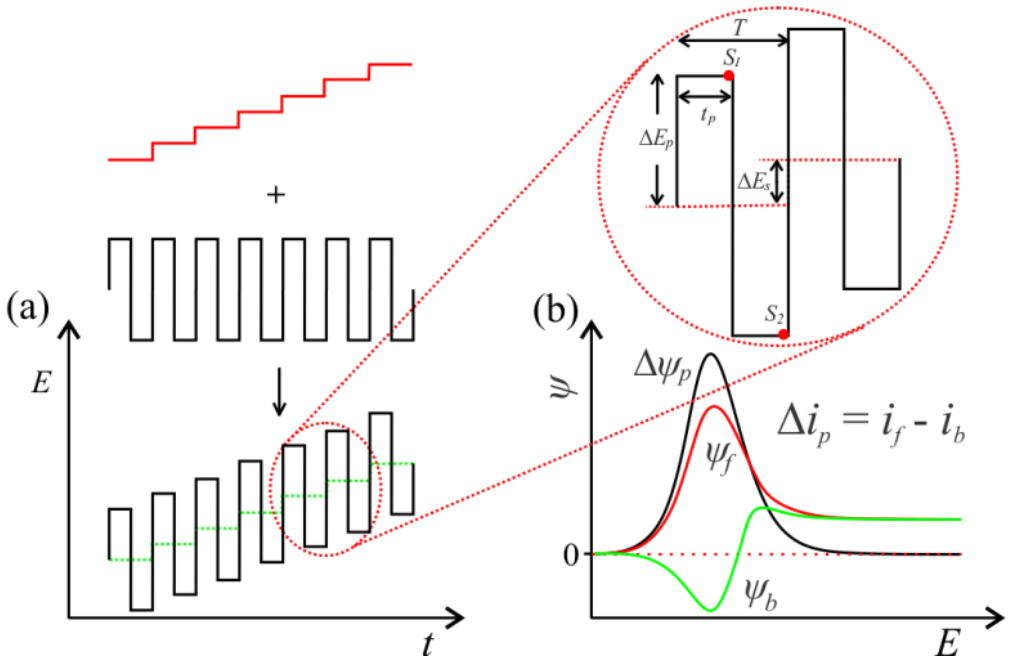

Figure 1.16: (a) Schematic representation of the application of a square wave on a staircase potential ramp and the resulting square waveform (b) a Δi *vs* E plot is called a square wave voltammogram. The circular inset shows different parameters along the applied square wave cycle; ΔE_p is the square wave amplitude, ΔE_s is the step potential, t_p is pulse width (duration of pulse), and T is the total time of a square wave cycle. The red dots in the inset show current sampling points at S_1 and S_2.

In experimental practice, the step potential is significantly less than the square wave amplitude which determines the total time of each cycle, and thus defines the resolution of voltammetric features.[2] The frequency is a critical time parameter in square wave voltammetry which determines the speed of measurements in voltammetric experiments. In modern instruments, its value ranges from 1-300 Hz, and thus makes the technique 100 times faster than other pulse techniques.[7] Therefore the analysis time for SWV measurements is drastically decreased; a complete voltammogram can be recorded within few seconds rather than 2-3 mins in differential pulse voltammetry.[7]

For a fast reversible redox couple ($O + e^- \rightleftharpoons R$), the net peak current (Δi_p) as a result of the forward and backward pulse can be calculated in terms of the dimensionless peak current ($\Delta\psi_p$) and is given by the following equation:[2, 41]

$$\Delta i_p = \frac{nFAD^{1/2}C_{bulk}}{\pi^{1/2}t_p^{1/2}}\Delta\psi_p \qquad \textbf{(1.69)}$$

Where n is the number of electrons transferred, F is Faraday's constant, A is the area of the macrodisk electrode, D is the diffusion coefficient of the electroactive species, C_{bulk} is the bulk concentration, t_p is the duration of the square wave pulse, and $\Delta\psi_p$ is the dimensionless peak current which is given by the following equation:[2, 41]

$$\Delta\psi_p = \frac{-\Delta i_p}{nFAC_{bulk}(Df)^{1/2}} \qquad \textbf{(1.70)}$$

Where the net peak current, $\Delta i_p = i_f - i_b$, can be expressed in terms of the dimensionless forward ($\Delta\psi_f$) and backward ($\Delta\psi_b$) currents as depicted in figure (1.16b). The dimensionless peak current, $\Delta\psi_p$, gauges the peak height in SWV, very similar to the ratio $(1-\sigma)/(1+\sigma)$ for DPV.[2] The voltammogram is characterized by a net peak current, Δi_p, and the corresponding staircase potential is called the net peak potential which is equal to the formal potential of the redox process. The net peak potential and the corresponding peak potential of both oxidative and reductive components are independent of the square wave frequency while the net peak current depends linearly on the square root of the square wave frequency (f).[41]

The dimensionless peak current, $\Delta\psi_p$, and half peak width, $\Delta E_{p/2}$, depends on the number of electrons multiplied by the square wave amplitude (ΔE_p)" i.e $n\Delta E_p$, and

"the number of electrons transferred multiplied by the step potential increment (ΔE_s) i.e. $n\Delta E_s$.[41] The larger the product $n\Delta E_s$, the greater the net peak current ($\Delta\psi_p$). This is because SWV experiments are usually performed on stationary solid electrodes and the effective scan rate is a linear function of the step potential increment. If the dimensionless peak current, $\Delta\psi_p$, and the ratio of dimensionless peak current and half peak width ($\Delta\psi_p/\Delta E_{p/2}$) is plotted against the product of the number of electrons multiplied by SW amplitude, $n\Delta E_p$, it will give the dependence of dimensionless peak current with respect to the applied amplitude and step potential, as depicted in figure (1.17). At a constant step potential product $n\Delta E_s$, with increasing SW amplitude $n\Delta E_p$, the slope value ($\partial\Delta\psi_p/\partial n\Delta E_p$) decreases continuously while the gradient value ($\partial\Delta E_{p/2}/\partial n\Delta E_p$) increases linearly to some extent and then starts to decrease (see figure 1.17). A maximum ratio ($\Delta\psi_p/\Delta E_{p/2}$) is obtained at 50 mV amplitude which is considered to be the optimum SW amplitude for SWV experiments.[41] In this thesis, a maximum SW amplitude of 50 mV and step potential of 5 mV is employed, which is 10 times smaller than the square wave pulse potential.

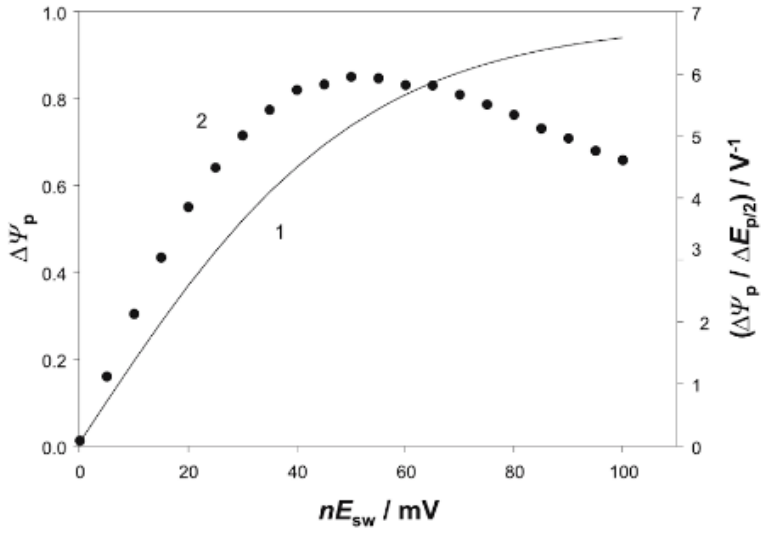

Figure 1.17: Plot of (1) the dependence of dimensionless peak current, $\Delta\psi_p$, and (2) the ratio of dimensionless peak current and half peak width ($\Delta\psi_p/\Delta E_{p/2}$) *vs* product of the number of electrons times SW amplitude ($n\Delta E_p$). Reproduced from Ref.[41]

For a reversible redox process, the net peak current (Δi_p) is proportional to the square root of SW frequency (f). Thus the SWV frequency (f) determines the reversibility of the redox process. This is true when there is no uncompensated Ohmic drop (iR drop) in the electrochemical cell. At a low frequency (f), the influence of uncompensated

(*iR* drop) is very small while at a large frequency (*f*), *iR* drop increased with the increase of SW frequency; the net peak current (Δi_p) is no longer a linear function of SW frequency.[41]

When the electrode process is not electrochemically reversible and the redox reaction is controlled by the electrode kinetics, the square wave response and reversibility of the reaction can be determined in terms of the dimensionless kinetic parameter (*K*) and the transfer coefficient (α). The dimensionless kinetic parameter is given by the following equation:[41]

$$K = k_s(D_o f)^{-1/2}(D_o/D_R)^{\alpha/2} \qquad \textbf{(1.71)}$$

Where k_s is the rate of electron transfer and D_o/D_R is the ratio of the diffusion coefficients of oxidized and reduced species.

If the value of the dimensionless kinetic parameter *K* is > 10, the reaction is reversible. If its value is < 0.01, then the reaction is irreversible and if it is in between $0.01 < K < 10$, the reaction is quasi-reversible.[25, 41]

For a quasi-reversible process, the dimensionless net peak current, $\Delta\psi_p$, decreases while the half peak width, $\Delta E_{p/2}$, and the net peak potential increases with the decrease of the kinetic parameter, *K*. In this case, the net peak current (Δi_p) is not a linear function of the SWV frequency.[41] Therefore the change in the net peak current (Δi_p) for a quasi-reversible process can be caused by the transformation of the backward component under the influence of increased frequency.[25]

For a totally irreversible process, the dimensionless net peak current, $\Delta\psi_p$, is a linear function of the transfer coefficient, α, given by the following equation:[25]

$$\Delta\psi_p = 0.235\alpha \qquad \textbf{(1.72)}$$

The real net peak current (Δi_p) is smaller than the forward current (i_f) because the backward current (i_b) is always positive for all potentials, regardless of the amplitude.[41] In this case the ratio $\Delta i_p/f^{1/2}$ and half peak width ($\Delta E_{p/2}$) both are independent of the square wave frequency (*f*) but the net peak potential (ΔE_p) is linear function of the logarithm of the SW frequency (*f*) with slope value ($-2.3RT/2\alpha nF$).[41] For a particular electrode reaction, the dependence of Δi_p on $f^{1/2}$ is a certain fraction of the general relationship and can be rationalized by two limiting

cases: (1) the redox process is reversible at small frequencies and quasi-reversible at large frequencies, (2) the reaction is quasi reversible at low frequencies and irreversible at large frequencies.[41]

1.9 Digital Simulation of Electrode Processes

Although voltammetric experiments provide sufficient information about the electrode processes taking place at the electrode-electrolyte interface, often the electrode reactions involve the complicated mechanisms such as coupled homogeneous reaction, adsorption process, etc. In this situation, the electrochemical process is complicated and it is difficult to solve the problem analytically.

Under these conditions; when the electrochemical process is unknown, digital simulation is an excellent tool to understand the behaviour of voltammetric problems. In this thesis, a software program called Digi-Elch containing integrated software based on the *Fast Implicit Finite Difference model* is used. This model provides a solution of partial differential equations associated with mass transport.[42, 43] These equations describe the relationship between the kinetics and diffusion processes of an electrochemical experiment with a set of differential equations that are solved numerically.[42, 44, 45] The theoretical solution of these differential equations involve approximations for different variables (time, distance, and concentration) and the simulation is based on the increments of these discrete variables, depending on the number of spatial dimensions involved. Let's consider a simple 1-dimensional case, in which the concentration of a redox species at a given time (t) over the range of distance (x) from the electrode surface needs to be determined. The space (x-coordinate) is divided into small intervals of length Δx, and the time, (t) into small time intervals Δt. Both x and t can be expressed as multiples of Δx and Δt given by the following equations.[43]

$$x = \Delta x \qquad \textbf{(1.73)}$$

$$t = \Delta t \qquad \textbf{(1.74)}$$

Figure (1.18) shows the resulting grid of points. At each drawn point on the grid, there is a concentration (C) of the species of interest which is considered an approximate value that varies linearly between the adjacent points. Now the digital simulation model involves developing rows of concentration values along the x-

coordinate with an increment of Δt. For a particular point on the grid, a concentration profile can be generated along x at a time t and using these linear equations, a time-dependent current plot can be calculated at the electrode/electrolyte interface adjacent to the electrode surface.

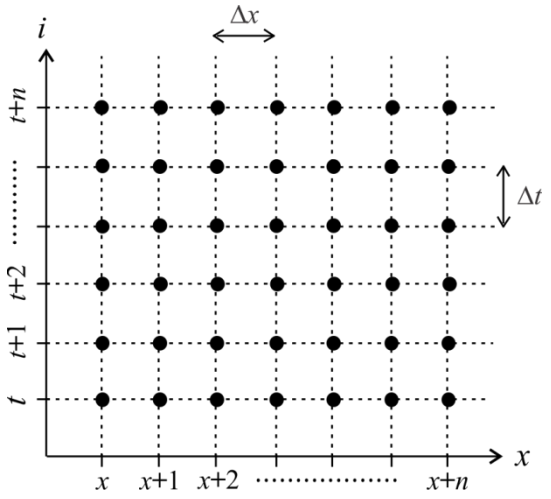

Figure 1.18: A point grid presenting the discrete variables x and t. Figure adapted from Ref.[31]

The software program Digi-Elch is an excellent tool for digital simulation of electrochemical processes involving complicated mechanisms using cyclic voltammetry and square wave voltammetry. This simulator provides a range of different parameters to be studied, such as the type of electrode geometry (planar and spherical), a range of mass transport (semi-infinite diffusion, finite diffusion and convection), single or multiple electron transfer reactions, proton coupled electron transfer reactions, first or second order coupled homogeneous chemical reactions, 2D simulations for band and disk microelectrodes, and the possibility to import experimental data for comparison and fitting with simulated data.[45] In this thesis we used Digi-Elch to simulate fast reversible, quasi-reversible and irreversible redox processes using cyclic voltammetry and square wave voltammetry and then used the optimised parameters for experimental analysis to study different analytes reported in this thesis.

References

1. Christine Lefrou, Pierre Fabry and J.-C. Poignet, *Electrochemistry, The Basics, With Examples*, Springer Heidelberg New York Dordrecht London, 2012.
2. A. J. Bard and L. R. Faulkner, *Electrochemical Methods: Fundamentals and Applications*, John Wiley New York, 2001.
3. R. G. Compton and G. H. W. Sanders, *Electrode Potentials*, Oxford University Press, Oxford, UK, 1998.
4. C. G. Zoski, *Handbook of electrochemistry*, Elsevier, 2006.
5. P. W. Atkin and J. De Paula, *Atkins' physical chemistry*, Oxford University Press, Oxford, UK, 8th Edition edn., 2006.
6. A. C. Fisher, *Electrode Dynamics*, Oxfort University Press, Oxford, UK, 1996.
7. J. Wang, *Analytical electrochemistry*, John Wiley & Sons, 2006.
8. D. J. Shaw, in *Introduction to Colloid and Surface Chemistry (Fourth Edition)*, Butterworth-Heinemann, Oxford, 1992, pp. 151-173.
9. H. Helmholtz, *Annalen der Physik*, 1879, **243**, 337-382.
10. C. M. A. Brett and A. M. O. Brett, *Electrochemistry: Principles, Methods, and Applications*, Oxford University Press, 1993.
11. G. Gouy, *Compt. Rend.*, 1910, **149**, 654.
12. D. L. Chapman, *Phil. Mag.*, 1913, **25**, 475.
13. O. Stern, *Elektrochem. Angew. Phys. Chem.* , 1924, **30**, 508-516.
14. D. C. Grahame, *Chem. Rev.*, 1947, **41**, 441.
15. M. V. Fedorov and A. A. Kornyshev, *Electrochimica Acta*, 2008, **53**, 6835-6840.
16. K. B. Oldham, *Journal of Electroanalytical Chemistry*, 2008, **613**, 131-138.
17. M. V. Fedorov, N. Georgi and A. A. Kornyshev, *Electrochemistry Communications*, 2010, **12**, 296-299.
18. M. V. Fedorov and A. A. Kornyshev, *Chem. Rev.*, 2014, **114**, 2978-3036.
19. S. Baldelli, *The Journal of Physical Chemistry B*, 2005, **109**, 13049-13051.
20. R. R. Dogonadze and Y. Chizmadjev, *Phys. Chem. Sec.*, 1964, **157**, 778.
21. D. M. Heyes and J. H. R. Clarke, *Journal of the Chemical Society, Faraday Transactions 2: Molecular and Chemical Physics*, 1981, **77**, 1089-1100.
22. W. Freyland, in *Ionic Liquids Uncoiled*, John Wiley & Sons, Inc., 2012, DOI: 10.1002/9781118434987.ch2, pp. 29-50.
23. A. M. Bond, *Broadening electrochemical horizons*, Oxford University Press, Oxford, 2002.
24. R. G. Compton and C. E. Banks, *Understanding voltammetry*, World Scientific, 2011.
25. F. Scholz, *Electroanalytical methods*, Springer, 2010.
26. J. A. V. Butler, *Transactions of the Faraday Society*, 1924, **19**, 729-733.
27. T. Erdey-Gruz and M. Volmer, *Z. Phys. Chem. A*, 1930, **150**, 203.
28. A. C. Testa and W. H. Reinmuth, *Anal. Chem.*, 1961, **33**, 1320-1324.
29. A. J. Bard, G. Inzelt and F. Scholz, *Electrochemical dictionary*, Springer Science & Business Media, 2008.
30. D. W. M. Arrigan, *Analyst*, 2004, **129**, 1157-1165.
31. D. S. Silvester, Doctoral dissertation, University of Oxford, 2008.
32. A. M. Bond, D. Luscombe, K. B. Oldham and C. G. Zoski, *J. Electroanal. Chem. Interfacial Electrochem.*, 1988, **249**, 1-14.
33. D. Shoup and A. Szabo, *Journal of Electroanalytical Chemistry and Interfacial Electrochemistry*, 1982, **140**, 237-245.
34. M. Sairi, J. Strutwolf, R. A. Mitchell, D. S. Silvester and D. W. M. Arrigan, *Electrochimica Acta*, 2013, **101**, 177-185.

35. L. Xiong, L. Aldous, M. C. Henstridge and R. G. Compton, *Analytical Methods*, 2012, **4**, 371-376.
36. K. Aoki and J. Osteryoung, *Journal of Electroanalytical Chemistry and Interfacial Electrochemistry*, 1981, **122**, 19-35.
37. A. Chen and B. Shah, *Analytical Methods*, 2013, **5**, 2158-2173.
38. M. Kalousek, *Collection of Czechoslovak Chemical Communications*, 1948, **13**, 105-115.
39. G. C. Barker and I. L. Jenkins, *Analyst*, 1952, **77**, 685-696.
40. J. G. Osteryoung and R. A. Osteryoung, *Analytical Chemistry*, 1985, **57**, 101A-110A.
41. V. Mirceski, S. Komorsky-Lovric and M. Lovric, *Square-wave voltammetry: theory and application*, Springer Science & Business Media, 2007.
42. M. Rudolph, *Journal of Electroanalytical Chemistry and Interfacial Electrochemistry*, 1991, **314**, 13-22.
43. D. Britz, *Digital simulation in electrochemistry*, Springer, 2005.
44. M. Rudolph, D. P. Reddy and S. W. Feldberg, *Analytical Chemistry*, 1994, **66**, 589A-600A.
45. M. Rudolph, *Journal of Electroanalytical Chemistry*, 2001, **503**, 15-27.

Chapter 2

2. Gas Sensors and Room Temperature Ionic Liquids

Sensors are technological devices that have the ability to convert physical or chemical transformations and properties into quantifiable electronic or electrical signals with the help of analytical devices and instrumentation.[1] Gas sensors are one type of chemical sensor which typically consist of two basic components connected in series; a chemical recognition system called a "*receptor*" which has the ability to interact with the analyte molecules to generate chemical signals, and a "*physicochemical transducer*" which can convert these chemical signals into electrical signals in the form of voltage, current or resistance that are detected by a detector.[1] In this chapter, fundamental aspects of gas sensors will be discussed including a brief description on different types of chemical sensors. Later, a discussion on different types of electrochemical gas sensors including amperometric (which is the one used in this thesis), and then discuss the fundamentals, construction, working and finally their modification with room temperature ionic liquids to make membrane-free, portable, cheap and miniaturized gas sensors.

2.1 Toxic Gases and Chemical Sensors

With the increase of urbanization and industrialization, man has started to release more and more wastes and pollutants into the atmosphere. These wastes and pollutants may include "criteria pollutants" (carbon monoxide, nitrogen dioxide, sulfur dioxide, ozone, lead and particulate matters), "air toxics" and "biological pollutants". Air toxics are sometimes also referred to as "Hazardous Air Pollutants" or toxic gases or aerosols that are very harmful to human, plant and animal life even at very low concentrations. These toxic gases include carbon monoxide, oxides of nitrogen, hydrogen sulfide, ammonia, methylamine, chlorine gas, ozone etc. The main sources of these gases are from mining, oil and gas, automotive, fertilizer, and refrigeration industries, in addition to the burning of gasoline, coal and fossil fuels and also military and security companies.[2, 3] These gases are a real concern for the environment and health, and can lead to other environmental hazards such as acid rain, global warming and the deterioration of the ozone layer. So it is essential that

these harmful gases be monitored for safety in industrial applications, medical applications, indoor air quality supervision and environmental monitoring.[4] Therefore on the basis of this great demand, there should be easily available devices that can monitor toxic gases to fulfil this demand. Chemical sensors are devices which can be designed to detect the presence of a given chemical species on the basis of their characteristic properties such as their chemical reactivity, optical or electrical properties, and their molecular mass which can distinguish them from their surrounding medium.[5] A chemical sensor would be considered an ideal device when it has these extensive properties; low cost, robust and portability and the ability to respond instantaneously, accurately, and selectively to any concentration of a particular species present in a specific surrounding medium.[5] Different strategies have been employed to monitor toxic gases with chemical sensors, such as metal oxide based gas sensors, calorimetric gas sensors, acoustic wave based gas sensors, optical gas sensors, and electrochemical gas sensors.[4, 6] Out of these strategies, the later one is our interest due to their inexpensive fabrication, low power consumption capacity, wide linear range, high sensitivity and selectivity, and their ability to be miniaturized.[2] Before moving to electrochemical sensors, a brief discussion of some other types of chemical sensors will be presented.

2.1.1Metal Oxide Gas Sensors

Metal oxide sensors, also called semiconductor/solid state gas sensors, are based on the change in conductivity of a heated substrate of a metal oxide (semiconductor) layer when exposed to combustible, reducing, or oxidizing gases. Semiconductor sensors are used to detect highly flammable, toxic gases such as propene, hydrogen sulfide, and carbon monoxide etc. and thus can operate at very high temperature, and usually employed in fuel applications in enclosed environments.[2] These sensors have advantages over other types of sensors; they are completely solid based sensors and thus have long shelf life. But these sensors cannot be employed to detect every toxic gas due to their limited selectivity and sensitivity along with high power consumption capacity.[2, 7]

2.1.2 Calorimetric Gas Sensors

Calorimetric gas sensors are conventional devices which can measure the calorific value (the amount of energy release as a result of complete combustion of fuel/gas)

when exposed to combustible fuel, natural gas, hydrogen gas, and coal etc.[8] They are used in steel mills, the petrochemical industry, and power houses to control the thermal input/ heat of combustion of fuels. Typically they are large in size, self-standing units.[8] These conventional sensors cannot be amenable for applications which require low cost, lower power consumption capacity, high sensitivity/selectivity, and trace detection of combustible toxic gases.[9] Over the last 40 years, a number of changes and improvements have been made to calorimetric sensors and a new type developed called a "pellistor".[4, 10] They consist of a detecting element which has small "pellets" of a catalyst (platinum or tungsten wire) loaded onto ceramic and work on the principle of detecting a variation in the temperature of a heated catalytic element when exposed to a mixture of combustible toxic gases and air.[8-10] Pellistors are further divided into two sub-classes on the basis of the detection method, called catalytic sensors and thermal conductivity sensors.[4] Catalytic sensors can detect the heat of combustion/reaction as a result of a catalytic oxidation of the combustible gas, while thermal conductivity sensors can detect thermal conductivity as a result of the change in resistance in the detecting element due to the combustion of analyte gas.[4] Calorimetric sensors have some limitations: limited selectivity due to a similar heat of combustion and thermal conductivity of many pure and mixtures of gases. Additionally their catalytic activity is inhibited due to poisoning of the catalyst when exposed to mixtures of analytes, thus have limited sensitivity which reduces the lifetime of these sensors.[4, 10]

2.1.3 Acoustic Wave Gas Sensors

Acoustic wave sensors are chemical sensors based on the measurement of the mechanical properties of species of interest such as mechanical waves/acoustic waves or sound waves.[5, 11, 12] They are used in many fields including industrial production,[13] environmental protection,[14] medical,[15] healthcare,[16] scientific research,[17] and defence applications.[18, 19] These devices are usually employed in a dual-sensor configuration in which one sensor acts as a reference sensor where a reference gas is passed through and the second acts as a working sensor that is exposed to the mixture of gas (analyte of interest). When a reference gas and a mixture of gas passes through or near the sensitive surface of particular material of both sensors it generates sound waves. These sound waves are influenced by some characteristic properties of the sensitive material (mass, density, modulus) that

results in a change in amplitude or velocity of the sound waves.[5] These changes can be monitored in the form of frequency or path difference travelled by the sound waves. The concentration of analyte gas can be calculated from the velocity of the sound waves, which is proportional to the change in frequency or path difference of sound propagation, to identify a particular gas where the sound velocity is different from others in a mixture of gas. By difference methods, the concentration of an analyte gas can be calculated from the change in frequency or path difference.[4] Conventional acoustic wave sensors have high precision but still have some limitations; firstly, it is very difficult to guarantee that the impact of the environment on both the reference and working sensors is identical. Secondly, because of high power consumption, it is very hard to build a wireless node to detect ultrasonic gas concentrations.[4]

2.1.4. Optical Gas Sensors

Optical sensors are a type of chemical sensor in which electromagnetic radiation is passed through a sensing medium that contains the analyte of interest. They are used in many applications including process plants, environmental and pollution monitoring, laboratory based analysis, military applications, clinical analysis, and medical applications.[20] They work on the principle that when light passes through the sensing medium, which could be a chemical reagent or sorbent phase, it interacts with the sensing medium causing quantifiable changes (absorption, reflection or transmission of light with gas molecules) that are related to the concentration of analyte.[5] A typical optical gas sensor consists of three basic parts; a *source of incident light* which could be a light emitting diode (LED), tungsten-halogen lamp or laser light, a sensing medium called an *optrode* that contains various types of chemical reagent, polymers or biologically active materials which are very selective to enhance the sensitivity and finally a *transducer* which detects the optical signals and converts them into electrical signals.[21] Optical gas sensors are mostly based on spectroscopic analysis, mainly involving emission and absorption spectroscopy which needs a sophisticated and complicated setup to obtain higher sensitivity and selectivity. As a result these sensors are very expensive and difficult to be miniaturized.[4]

2.2 Electrochemical Gas Sensors

Electrochemical sensors have great advantages over other types of chemical sensors due to their low cost, high sensitivity and selectivity, continuous monitoring capability, inexpensive fabrication steps, low power consumption capacity, wide linear range, and their better ability to be miniaturized.[2] They have a leading position among commercially available chemical sensors and have found applications in many fields including environmental monitoring, industrial manufacturing, clinical analysis, agricultural analyses, scientific research, and defence applications.[22] They are classified into three main types on the basis of their method of electrical signal quantification; if the measured response is voltage then the device is called potentiometric, if the response is resistance then the sensor is called conductometric, and if the measured response is current then the device is called amperometric.[5] Out of these three types of sensors, the later one is our area of interest and all of the work presented in this thesis is based on amperometric sensors. Before moving to amperometric sensors, we will discuss briefly about potentiometric and conductometric sensors.

2.2.1 Potentiometric Gas Sensors

Potentiometric sensors have found widespread practical applications since the early 1930s, due to their simplicity, rapidity, familiarity and low cost.[22] They are widely used in laboratory analysis, clinical analysis, medical applications, environmental monitoring and for scientific research.[22-24] Potentiometric sensors operate by measuring the potential difference between two-electrodes, the working (or indicator) electrode and a reference electrode.[1, 25] One commonly known class of potentiometric sensor is the ion-selective electrode (ISE). In an ISE, the indicator electrode usually comprises of a metal electrode and an ion selective membrane, and the reference electrode is usually silver/silver chloride (Ag/AgCl) immersed in a solution of potassium chloride (KCl) of known concentration (see figure 2.1). The concentration response of ISEs typically obeys the Nernst equation:[1, 25]

$$E_{ind} = E^{o} + \frac{RT}{nF} \ln a \qquad \textbf{(2.1)}$$

Where E_{ind} is the potential observed at the indicator electrode compared to the reference electrode, E^{o} is the standard electrode potential, R is the universal gas

constant, *T* is the absolute temperature, *n* is the number of electrons transferred, *F* is Faraday's constant, and *a* is the chemical activity of the analyte species, given by the following equation:[25]

$$a_o = \gamma_o[O] \qquad \textbf{(2.2)}$$

Where a_o is the activity of species O, which depends on its concentration, γ_o is the activity coefficient of species O which is dimensionless quantity and depends on the standard conditions of the electrochemical cell such as temperature, pressure, concentration, and the partial pressure of gas.[25] For very dilute solutions at [O] ≤ 0.001 mol/L, its value is considered unity; therefore the chemical activities of redox species are equal to their concentrations. A schematic representation of a potentiometric sensor with metal and ion-selective electrode as an indicator electrode is shown in figure 2.1.

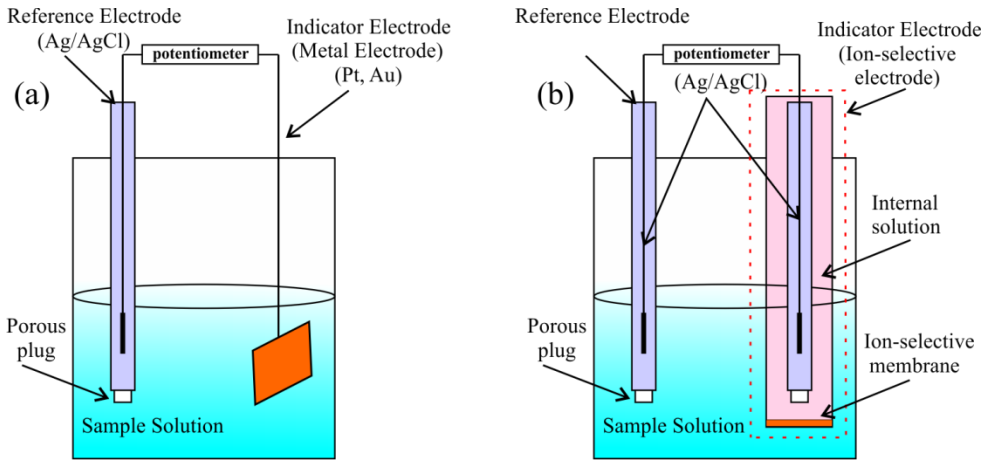

Figure 2.1: Schematic representation of a potentiometric sensor with (a) a metal electrode as an indicator electrode, and (b) an ion-selective electrode as an indicator electrode. Figure adapted from Ref.[1]

2.2.2 Conductometric Gas Sensors

Conductometric sensors are another type of electrochemical sensor that measures the conductivity (or resistivity) of the electrolyte in an electrochemical cell.[21]

Conductivity (σ) is a material property expressed as a ratio of current density (*J*) and strength of electric field (*E*), given by the following equation:[26]

$$\sigma = \frac{J}{E} \qquad \textbf{(2.3)}$$

Conductometric sensors can be classified into two main classes e.g. liquid based and solid based sensors as depicted in figure 2.2.[26] In liquid based conductometric sensors, the impedance is measured between the selective layer and the conducting ionic solution interface by applying an alternating current between the two electrodes. In solid based conductometric sensors, the change in conductivity (or resistivity) of the selective layer is measured by applying a constant current or DC voltage between the two electrodes. The most commonly used sensors of this type are *Taguchi* sensors which are ceramic material devices in which powdered solid material is pressed to form a selective layer.[1]

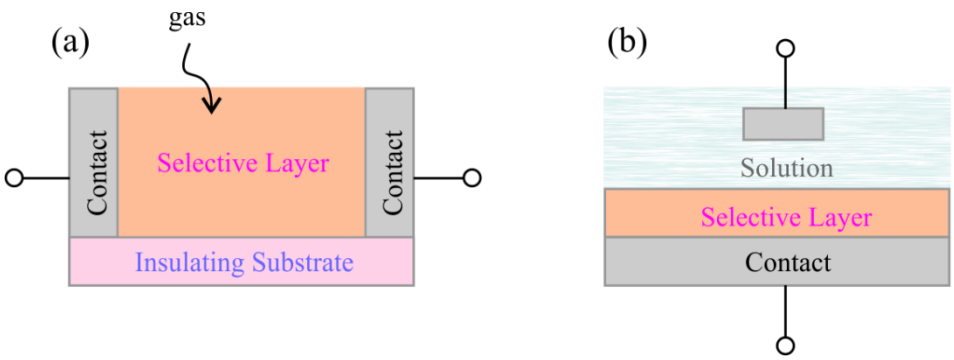

Figure 2.2: Schematic representation of conductometric sensors: (a) metal-oxide semiconductor based DC chemiresistor, and (b) impedimetric chemiresistor. Figure adapted from Ref.[26]

2.2.3 Amperometric Gas Sensors

Amperometric gas sensors (AGSs) are an important class of electrochemical sensors due to their unique properties such as their low-cost and portability, inexpensive fabrication steps, low-power consumption capacity, wide linear range, high sensitivity and selectivity, and their better ability to be miniaturized.[25, 27] They play an important role in many practical applications such as environmental monitoring, medical and health applications, laboratory analysis, industrial applications, defence and security surveillance, automotive industry and scientific research.[3] Amperometric gas sensors operate on the principal that the gas of interest reacts on the sensing surface as a result of an applied potential and produces electrical signals in the form of current that are a linear function of gas concentration.[3] The simplest amperometric gas sensor consists of a two electrode setup as illustrated in figure 2.3, where one electrode is called a *working electrode* where the redox reaction occurs and the second is a *counter electrode* where an opposite reaction occurs and both electrodes are immersed in an electrolyte solution.[25]

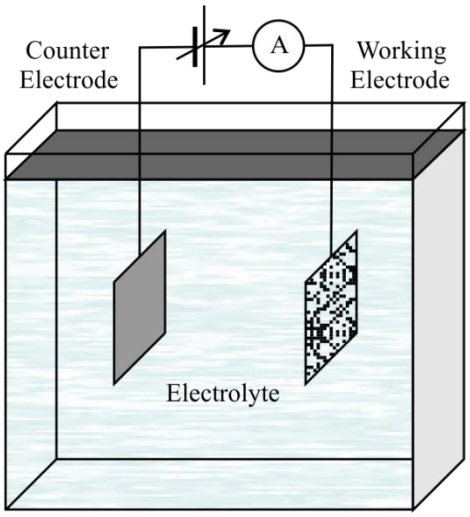

Figure 2.3: Schematic representation of an amperometric sensor with a two electrode setup. Figure adapted from Ref.[3]

When the sensor is exposed to the gaseous analyte, first gas partitions at the gas/liquid interface. When a potential is applied, the gas molecule diffuses through the liquid medium towards the working electrode and the electron transfer process occurs at the liquid/solid interface, governed by Faraday's law. An amperometric gas sensor operates on an external potential which could be constant or variable potential, applied by a potentiostat to drive the electron transfer process. When the reaction is under diffusion-limited conditions, the rate of reaction is determined by the thermodynamically applied potential. The current generated at diffusion-limited conditions is proportional to the concentration of analyte gas, derived from combining Fick's law of diffusion and Faraday's law.[3]

The observed current in an AGS depends on many factors including potential and concentration which can be expressed by complex mathematical expressions. There are two operating conditions called *limiting conditions* relating to the rate of the electrode reaction (r_r) and the rate of mass transfer (r_d) which can be used to simplify the resulting expression. These conditions include the situations when $r_r \ll r_d$, and $r_r \gg r_d$.[3] In order to fully understand the electrode process, these limiting conditions are very important for sensor applications and the resulting current related to both limiting conditions is called the *limiting current* (i_{lim}).[3]

In the first case, when the rate of mass transfer is greater than the rate of the electrode reaction ($r_r \ll r_d$), the gaseous analyte reaches the electrode surface much faster than the electron transfer process and the concentration of gas at the surface of

electrode is the same as in the bulk solution. In this case the electrode process is limited by the rate of the reaction (the rate limiting step) and the limiting current (i_{lim}) controlled by the rate of electron transfer process can be obtained in the kinetically controlled electrochemical region by the following equation.[3]

$$i_{\mathrm{lim}} = nFkAC_{bulk}\exp(\alpha nFE/RT) \qquad \textbf{(2.4)}$$

Where n is the number of electrons transferred, F is Faraday's constant, k is the standard rate constant, A is the area of the electrode, C_{bulk} is the bulk concentration, α is the transfer coefficient, E is the overpotential of electrode reaction, R is the universal gas constant, and T is the absolute temperature. When all parameters are kept constant, the limiting current is proportional to the concentration of gaseous analyte with an exponential temperature coefficient.[3] However, the limiting current obtained at the kinetically controlled region is not always constant due to the degradation of the electrode's catalytic activity, which can produce problems in the performance of AGSs.

To overcome this problem, AGSs are operated under diffusion controlled conditions rather than kinetic control and this condition can be obtained only when the rate of mass transfer (rate of diffusion) is much slower than the rate of electron transfer ($r_r \gg r_d$). Under this condition, the gaseous analyte reaches the electrode surface much slower than the electron transfer process and the limiting current is controlled by the diffusion of the gaseous analyte.[3] In this case the concentration of gas molecule at the surface of electrode is approximately equal to zero and every gas molecule reaching the electrode surface reacts immediately. Under these conditions, the rate of the electrode process may be limited by the rate of diffusion through the gas membrane which is present between the bulk analyte and sensing surface.[3] According to Fick's law of diffusion, the limiting current (i_{lim}) can be obtained from the rate at which the gaseous analyte reaches the surface of the electrode. This is directly proportional to the concentration of gas (C_{gas}) in units of parts per million per volume and the mass transfer limited current is given by the following equation.[28]

$$i_{\mathrm{lim}} = nFmAC_{gas} \qquad \textbf{(2.5)}$$

Where m is the mass transfer coefficient, and C_{gas} is the concentration of electrochemically active gas molecules that are undergo a redox reaction at the surface of the electrode.

A common characteristic of all AGSs is the monitoring of current as a result of redox reaction due to the applied potential between the working and counter electrode as a function of analyte concentration. If the sensing experiment is performed at constant potential then the technique is called *constant-potential amperometry* which is the basis of most commercially available amperometric gas sensors.[3] A major consideration in the design of AGSs is the composition of the electrolyte, electrode geometry/porosity, and material of the sensing surface, which can enable the gaseous analyte to transport at the interface of electrode/electrolyte more effectively and efficiently where fast electrode transfer processes could occur.[3] In AGSs, the sensitivity and selectivity is also an important consideration for a specific gaseous analyte which can be optimized by choosing a specific electrode material to facilitate or catalyse a particular reaction, or by controlling the electrode potential which is thermodynamically favourable either for the oxidation or reduction reaction of a particular analyte. Nobel metals such as gold and platinum are mostly used in AGSs as electrode surfaces due to their excellent chemical stability in the electrolyte medium and their high electrocatalytic stability toward many gaseous analytes (e.g. CO, H_2S, NH_3, O_2, Cl_2, and NO).[3] The incorporation of a selective membrane for a specific gas is also an important parameter in the design of AGSs. In the next section we will discuss the geometry and working of a Clark cell which is the basis of modern amperometric gas sensors, followed by a discussion on the replacement of aqueous electrolytes with room temperature ionic liquids to create membrane-free amperometric gas sensors which are used to detect toxic gases in this thesis.

2.2.3.1 Clark Sensor

One of the earliest successful and most important amperometric gas sensors was invented by Professor Leland Clark in the 1950s to measure the concentration of oxygen in blood. It was called a *Clark Cell* and is still used (with modifications) as a chemical sensor for toxic gases.[27, 29] In a two-electrode setup, a shiny platinum (Pt) WE cathode and potassium chloride calomel/Ag wire anode, are both placed in a glass tube and wrapped in a saline soaked cotton plug. Both electrodes are attached

to a power supply that is used to apply a controlled potential. Unlike the above simple design with a bare working electrode, the Clark cell has a cellophane covered platinum working electrode which shows enhanced selectivity for oxygen due to the presence of membrane that allows oxygen molecules to penetrate but prevents the red blood cells, and other ions and gases through. The oxygen molecules diffuse through the cellophane membrane, enter into the solution and get reduced at the Pt cathode when a potential of 0.6 V is applied. The current produced as a result of oxygen reduction is monitored with a galvanometer which is proportional to the concentration of oxygen present in the blood sample.[29] The success of the Clark cell with a cellophane covered working electrode has paved the way for the future design of AGSs and has many advantages over bare electrodes in terms of selectivity and sensitivity for several analytes over a wide range of concentration.

Modern AGSs operate on the same principle as a Clark cell; the gas of interest passes through a selective permeable membrane, diffuses into the solution and reaches the working electrode where electron transfer occurs. Typically they are employed in a three-electrode setup, with a working, counter and reference electrode all connected through a suitable electrolyte and covered with a gas permeable membrane. Commercially available AGSs prepared by many companies such as *Honeywell, Alphasense, Draeger* are based on the same original design. Figure 2.4(a) shows the basic design and components of a commercially available *Alphasense* AGS which hax three pins on the bottom that make connections to the working, counter and reference electrodes. These pins are inserted into a detector case to complete an electronic circuit to read the concentration of exposed gas.

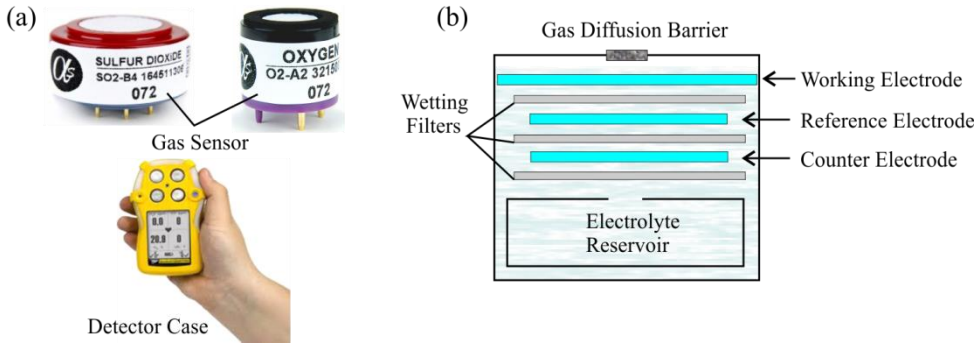

Figure 2.4: (a) Photo of a commercially available amperometric sensor along with their detector case (b) Schematic representation of the interior of an amperometric gas sensor with a three electrode setup and gas diffusion barrier. Reproduced from (http://www.alphasense.com) with permission (see certificate in Appendix A).

Figure 2.4(b) shows the interior of a commercially available *Alphasense* gas sensor with three electrodes: a working electrode on the top, a reference electrode in the middle, and a counter electrode in the bottom, all stacked parallel in an electrolyte (usually H_2SO_4/water mixture) and separated by a hydrophilic wetting filters which provide ionic electrical contact between the electrodes. All three electrodes are enclosed in a plastic case and the top of the working electrode is covered with a membrane called a gas diffusion barrier with various pore sizes to control the flux of toxic gas to the working electrode. The gas diffusion barrier also prevents the electrolyte from evaporating and enhances the selectivity for a specific gas. When the sensor is exposed to the gas of interest, the gas molecule passes through the gas diffusion barrier, diffuses through the electrolyte and reaches the working electrode where oxidation or reduction reaction occurs depending on the electrochemical nature of the gas. The gas concentration is determined from the current produced as a result of a redox reaction. The detector case gives a digital reading of the concentration of analyte gas.

The performance of an AGSs can be determined on the basis of four important properties: sensitivity, selectivity, response time, and lifespan of a sensor and all these properties are greatly depend on the presence of membrane, electrode material, and selection of electrolyte.[27] In the next section we will discuss briefly all three components of an AGS and their limitations in AGS and finally introduce a new class of electrolyte to incorporate in membrane-free AGSs.

2.2.3.2 Membranes in AGSs

Many different types of porous and permeable membranes used in AGSs are commercially available and include silicone membranes, solid Teflon films, and microporous Teflon films, made from inorganic or polymeric materials.[3] The selectivity and response times of an AGS depends on the thickness of the membrane and the membrane material. The selectivity can be enhanced by choosing a specific membrane material such as a silicon membrane which is permeable for oxygen sensing or a macroporous polytetrafluorethylene (PTFE) membrane which is strongly hydrophobic, selective for many gases (H_2, CO, CO_2, NO_2, CH_4,), allows the gas molecule to pass through and prevent the water molecule to penetrate thus inhibiting electrolyte evaporation.[30, 31] Solid polymer electrolytes such as Nafion membranes

can also be employed as sensing materials in electrochemical gas sensors. The sensitivity of solid polymer electrolyte-based AGSs can be improved with Au/Nafion based working electrode for NO_2 reduction at ambient temperature.[32] Sensitivity and selectivity both can be enhanced by using conducting polymer membranes such as a film of ultrathin polyaniline (PAN) which is sensitive for NO_2 and NH_3 sensors.[33] A composite film of polyaniline/Au/nafion as a working electrode, not only decreases the need for a separate working electrode but also increases the sensitivity of the sensor for NO_2 gas.[34] But the presence of a membrane in AGSs has some limitations on the performance of a sensor such as the response time, which is greatly affected by the thickness of membrane. The response time for a specific gas is limited by the time taken for diffusion of that gas through the membrane.[2, 27]

2.2.3.3 Electrodes in AGSs

The selection of electrode material is an important parameter which affects the performance of AGSs. Typically noble metals such as platinum (Pt) and gold (Au) are used as a working electrode in AGS due to their excellent stability at polarized potentials, which could be corrosive to other metals, and their better catalytic ability towards many analytes.[3] Carbon materials such as graphite and glassy carbon can also be used as a working electrodes, especially for biosensing applications.[3]

The selection of a counter electrode (CE) for a particular reaction is also an important component in AGSs. CEs should be stable in an electrolyte and must have a greater surface area for the complementary half reaction to the analyte reaction to not become limiting.[3] A Pt electrode/wire is often used as a counter electrode in AGSs. In addition to the WE and CE, the importance of the reference electrode (RE) cannot be ignored, which maintains a constant and stable potential relative to the WE. Usually a silver/silver chloride (Ag/AgCl) is used as a reference electrode in aqueous solutions, which has a fixed potential throughout the sensing experiments. A Ag or Pt electrode/wire can also be used as a reference electrode as a *pseudo*- or *quasi*-reference electrode and due to their unstable potential can be calibrated with an electrode of known potential.[3]

2.2.3.4 Electrolytes in AGSs

The selection of electrolyte is the most important component on the performance of AGSs as it provides ionic contact between the electrodes. It is a conducting medium composed of ions (organic/inorganic) and is responsible for carrying charges or species of interest to and from the electrodes, facilitating the electrode reaction. It should also have an ability to solubilize the redox species efficiently, and maintain a stable reference potential inside the electrochemical cell.[35] Commonly used electrolytes in AGSs are a combination of water with an inorganic salt e.g. water/sulphuric acid (H_2O/H_2SO_4), water/sodium hydroxide (H_2O/NaOH), water/potassium chloride (H_2O/KCl),[3] or conventional organic solvents with suitable supporting electrolyte e.g. propylene carbonate/lithium perchlorate,[36] acetonitrile/ tetra-N-butylammonium perchlorate (MeCN/TBAP).[37] The lifespan of an AGS greatly depends on the stability of the electrolyte. In most AGS applications such as in the oil and gas industry, the sensor has to operate at conditions where the temperature and pressure is very high.[27] Under these harsh conditions, aqueous or conventional organic electrolytes can dry-up very quickly, thus reducing the lifetime a sensor. This limitation of AGSs can be improved by introducing a new class of electrolyte called room temperature ionic liquids (RTILs) which have been attracting great attention[38] as replacement electrolytes in AGSs due to their unique physical properties such as low volatility and negligible vapour pressure.[27] Importantly, when exposed to a high gas flow, they do not evaporate, and can function in hot and dry environments, and due to their low volatility they can be used in "membrane-free" gas sensors. In addition to RTILs, polymer electrolytes or composite mixtures of polymers with RTILs can also be used as replacement electrolytes as they have low evaporation rate, high viscosity, and are resistant to leakage. They can thus be employed to make more robust amperometric gas sensors than those already available.[39, 40]

In the next section we will discuss room temperature ionic liquids as a replacement electrolyte to be incorporated in a membrane-free gas sensor design, which is the basis of all the work reported in this thesis.

2.3 Introduction to Room Temperature Ionic liquids

Ionic liquids are salts made entirely of ions and one subclass of these salts are called room temperature ionic liquids (RTILs) due to their existence in the liquid state at room temperature (25^{o}C). RTILs have attracted significant attention in the last few decades in many fields including electrochemistry,[41-43] catalysis,[42, 44] organic reactivity,[44, 45] and in the chemical industry[46] because of their outstanding physicochemical properties, such as low volatility, negligible vapor pressure, wide electrochemical windows, good chemical and thermal stability, good solvating ability, high ionic conductivity and a better ability to dissolve a wide range of compounds.[27, 44] They are typically comprised of a large organic cations (imidazolium, pyridinium, pyrrolidinium, or quaternary ammonium/phosphonium), paired with organic/inorganic anions that possess a highly delocalized charge (PF_6^-, BF_4^-, $TFPB^-$, $N(CF_3SO_2)_2^-$, $CF_3SO_3^-$), and are weakly associated to each other.[45] Because of the asymmetric configuration of bulky cations and highly delocalized anions, the electrostatic interaction between them is lowered, which prevents them from neatly packing together in a lattice and thus results in salts with lower melting temperatures.[47] Unlike conventional aqueous or organic electrolytes in AGSs, which are mixture of solvent and a dissociated charged species (e.g. KCl) as a solvent and electrolyte, therefore the behaviour of gases in RTILs may be different compared to conventional solvents. Figure 2.5 shows the chemical structures of some commonly used cations and anions of RTILs that are employed as electrolytes to study the toxic gases reported in this thesis.

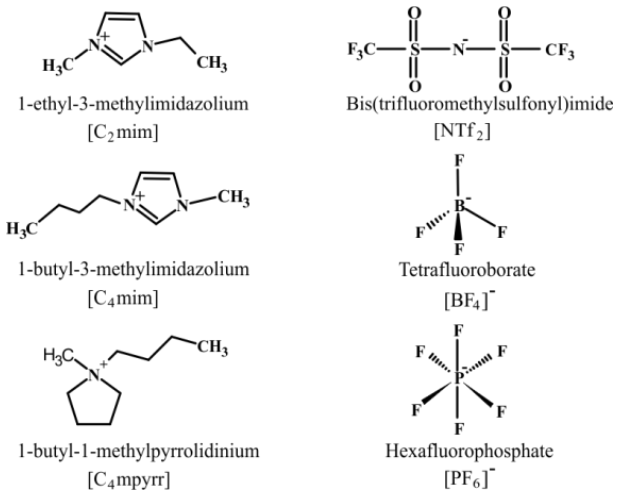

Figure 2.5: Molecular structures, full names, and abbreviations of commonly used cations and anions of RTILs reported in this thesis.

Recent studies of RTILs as an electrolyte show that they can be mixed with well-known polymers using various strategies, such as doping polymers with ionic liquids,[39] solution casting of ionic liquid/polymer mixtures,[40] and in situ polymerization of vinyl monomers in ionic liquids.[48] These room temperature ionic liquid/polymer mixtures, because of their unique properties have been used as electrolyte materials in lithium ion batteries,[49] fuel cells,[50] solar cells,[51] super-capacitors,[52] and electrochemical gas sensors.[38, 53, 54] It is the latter application that is our focus for the sensing of toxic gases using room temperature ionic liquids (RTILs) as an electrolyte, and then will be used this as the basis for the suggested design of more robust, membrane-free improved gas sensors.

2.3.1 Properties of Room Temperature Ionic Liquids

Room temperature ionic liquids have unique properties that make them useful for a wide range of applications in many fields.[41] In this section we will describe the important physical properties of RTILs when used as an electrolyte in amperometric gas sensors.

2.3.1.1 Electrochemical Windows

The electrochemical window of an electrolyte is the potential range or potential difference of the oxidation and reduction potential of background electrolyte and solvent where the decomposition of cations and anions comprising an electrolyte starts.[27] It can be determined by subtracting the reduction potential limit from the oxidation potential limit. A wide electrochemical window is an advantageous property of an electrolyte and helps us to detect a greater range of electroactive species without masking from the background current. Some electroactive species and gases are oxidized or reduced at very positive or negative potentials where conventional electrolytes may degrade but some RTILs are stable at these potentials which makes them ideal electrolytes for many electrochemical applications.[38, 55] For example, the aqueous electrolyte (H_2O/NaOH) possesses very narrow electrochemical window (2.4 V) due to the oxidation and reduction of water, while in conventional organic solvents with supporting electrolytes, it can be much wider (e.g. 5.0 V for acetonitrile with what supporting electrolyte?).[27] However the electrochemical window of RTILs typically ranges from 3–7 V, which is considered a wide range due to the robustness of the cations and anions to oxidation and

reduction, respectively.[27] Thus wider electrochemical windows pave the way to study those gases and species that cannot be oxidized or reduced in aqueous electrolytes due to their smaller potential window.

There are certain factors that influence the width of the electrochemical window in RTILs: the material of the working electrode, the presence of impurities and changes in temperature.[27, 56] The dependence of electrode material on the electrochemical window was studied by Zhang and Bond at gold, platinum, boron-doped diamond, and glassy carbon in eight RTILs and found that glassy carbon has the largest electrochemical window.[56] The effect of water as an impurity was studied by O'Mahony et al. in a range of RTILs and it was found that increased water contents significantly decreased the electrochemical window of all RTILs, but was less dominant in RTILs containing more hydrophobic anions due to the their lower water uptake ability.[56] They also studied the effect of temperature for vacuum dried, atmospheric, and wet samples at different temperatures and found that the electrochemical windows of RTILs decrease in the following order; vacuum-dried > atmospheric > wet and 298 K > 318 K > 338 K.[57]

2.3.1.2 Volatility and Vapour Pressure

Low volatility and negligible vapour pressure are the most advantageous properties of RTILs which make them ideal to be used as electrolytes in AGSs. They are able to operate under extreme conditions (e.g. high temperatures and pressures) where commercially available AGSs fail due to the evaporation of electrolyte. The volatility of a solvent is determined by its vapour pressure, defined as the pressure exerted by vapours on the surface of liquid when in equilibrium with the liquid phase.[27] A high vapour pressure solvent has a high tendency to evaporate due to weak intermolecular forces and this property is more facilitated at extreme environmental conditions. Room temperature ionic liquids have low volatility and negligible vapour pressure (few milli-pascal (mPa)) compared to conventional organic or aqueous electrolytes (e.g. 3167.73 Pa at 298 K for pure water) which can be evident by X-ray photo-electron spectroscopy (XPS).[27] XPS is usually employed under ultra-high vacuum where aqueous or organic solvents evaporate easily, while RTILs are stable under this extreme environment, which is evidence that they can be employed in AGSs to make more robust, long-life, and stable sensing devices.

2.3.1.3 Thermal Stability

The high thermal stability of RTILs as an electrolyte in AGS devices enables them to operate under harsh conditions.[45] Many RTILs exhibit high thermal stability compared to conventional organic solvents because they remain in a liquid state over a wide range of temperatures. For example, $[C_4mim][NTf_2]$ can remain in a liquid state between 184-723 K, compared to water which is in liquid state only between 273-373 K at 1 atmosphere of pressure.[27] Studies in the literature show that RTILs can evaporate at >400 ^oC below their decomposition temperature.[45] The thermal stability of RTILs depends on the ionic structure of the organic and inorganic components, the hydrophobicity of the anion, and the size of the cation and anion.[27, 45] It has been suggested that the thermal stability of RTILs increased with increasing hydrophobicity and anion size in the order $[PF_6]^-$ > $[NTf_2]^-$ > $[BF_4]^-$ > halides, but is independent for different cations.[45] For imidazolium based RTILs, thermal stability also increased as the carbon chain length of imidazolium cation increase from $[C_2mim]^+$ to $[C_8mim]^+$.[45, 58] It has been also found that RTILs containing imidazolium based cations are more stable compared to those containing tetralkylammonium based cations.[58] The high thermal stability of RTILs over a wide range of temperature has advantages over conventional solvents when used as sensing media in many industrial applications where high temperatures are involved.

2.3.1.4 Conductivity

The conductivity of RTILs is also an important property that depends on the number of charges species and their mobility. The conductivity of RTILs typically lies in the range of 0.12 - 8 $m\Omega^{-1}$ cm^{-1} which is comparable to the conductivity of conventional organic solvents with supporting electrolytes (0.1M TBAP, tetrabutylammonium perchlorate) in the range of 0.5 - 8 $m\Omega^{-1}$ cm^{-1}.[27] The conductivity of RTILs strongly depends on the viscosity and the structure of constituent ions of the RTILs. Usually RTILs are comprised of large bulky ions and have high viscosities, thus reducing the specific conductivities. For example, $[C_2mim][NTf_2]$ has a relatively low viscosity (34 cP) and results in a larger conductivity (9.2 $m\Omega^{-1}$ cm^{-1}) compared to $[C_6mim][NTf_2]$ (0.22 $m\Omega^{-1}$ cm^{-1}).[27, 59] Another factor which reduces the mobility and conductivity is the formation of intramolecular hydrogen bonding between O and F in those ionic liquids which are comprised from fluoro- (F) and oxy- (O) substituted

ions and thus due to hydrogen bonding, their conductivity lies in the range of 0.14 – 1.3 $m\Omega^{-1}$ cm^{-1}.[60] The conductivity also depends on external factors such as temperature; as temperature increases, the viscosity of liquid is decreases, so the conductivity of RTILs also increases due to an increase in mobility of ions.[27]

2.3.1.5 Solubility of Gases in RTILs

The solubility of gases in RTILs has a great influence in many fields including gas sensing applications. Most commercially available gas sensors are based on water/H_2SO_4 mixture as an electrolyte. Gas molecules partition into the liquid solvent and the partition constant depend on the solubility of gas in the solvent. Literature studies show that a lot of work has been done on measuring the solubility of gases in aqueous and conventional organic solvents, in addition to RTILs.[61-67] It has been found that many gases such as H_2S, CO_2 are highly soluble in RTILs as compared to aqueous or convention organic solvents.[63, 68] The solubility of gases is believed to depend on their polarity, as polar gases (e.g. H_2S, NH_3, SO_2) are typically more soluble compared non-polar gases (e.g. O_2, H_2).[68-70] For example H_2S (polar gas) is seven times more soluble in [C_2mim][NTf_2] compared to water suggesting that RTILs may be more favourable sensing media in AGS devices. Table 2.1 shows the solubilities of polar and non-polar gases in the RTIL [C_2mim][NTf_2], water, and acetonitrile, calculated by electrochemical methods.

Table 2.1: Solubilities of gases in [C_2mim][NTf_2], water, and acetonitrile at 298 K and 1 atm. pressure.

Solvents	Polar gases		Non-polar gases	
	H_2S/mM	SO_2/mM	H_2/mM	O_2/mM
[C_2mim][NTf_2]	530[68]	230[69]	4.2[70]	10.8[38]
Water	74[71]	1470[72]	0.8[73]	16[73]
Acetonitrile	-	-	-	8.1[38]

The solubility of gases also depends on other factors such as the chemical structure of the ions, in addition to external factors such as temperature and pressure.[74-76] As RTILs are comprised of organic cations and inorganic anions, and have excellent tunability, the desired composition of RTILs can be obtained by altering either component.[74] Thousands of combinations of RTILs can be obtained and every combination has different solubilities and other physical and chemical properties for

a particular gas. Temperature is also an important parameter that determines the solubility of gases in RTILs;[75] as the solubility of gases increases with temperature, so this can have advantages for AGSs operating under extreme (e.g. high temperature) conditions.

Despite the many advantages of RTILs over aqueous and organic solvents, their use as an electrolyte in commercial AGS devices is still in the development process. One factor is their large viscosities, which slows the diffusion of gases through the RTIL, and their sensitivity to moisture which reduces the electrochemical response. However, highly hydrophobic and less viscous RTILs may prove good sensing media for future AGS devices.

2.4 Sensing of Gases on Miniaturized AGS in RTILs

Room temperature ionic liquids (RTILs) are an excellent option as replacement electrolytes in AGSs to produce devices that can survive under hot and dry conditions.[77] A literature study shows that a variety of gases (H_2S, CO_2, O_2, NH_3, H_2, SO_2 and NO_2) have been studied in RTILs focusing on fundamentals and mechanistic understanding.[55] For example the electrochemical sensing of CO_2 in RTILs where wide electrochemical windows are required,[63, 67] and the reduction of H_2S in RTILs where a wide range of temperature is required.[68] This information is highly encouraging, suggesting that RTILs may be employed as sensing media in AGSs.

The unique properties of RTILs such as wide electrochemical window, intrinsic conductivity, high thermal stability and better ability to dissolve a wide range of gases makes them many advantage over aqueous or conventional solvents as a replacement electrolyte to develop a more robust, and stable gas sensor. The low volatility and negligible vapour pressure prevents the RTILs from evaporating and allows them to withstand drastic environments such as high temperatures and pressures. In addition, this property of RTILs prevents the solvent from evaporation. As discussed in section (2.2.3.2), the presence of a membrane in AGSs reduces the response time as it limits the diffusion rate of gas molecules through the pores of the membrane. In the case of RTILs, no membrane is required due to their zero volatility, which thus enables the development of membrane-free AGSs where fast

response times are possible. Figure 2.6 shows a schematic representation of RTIL based membrane-free AGS.[27]

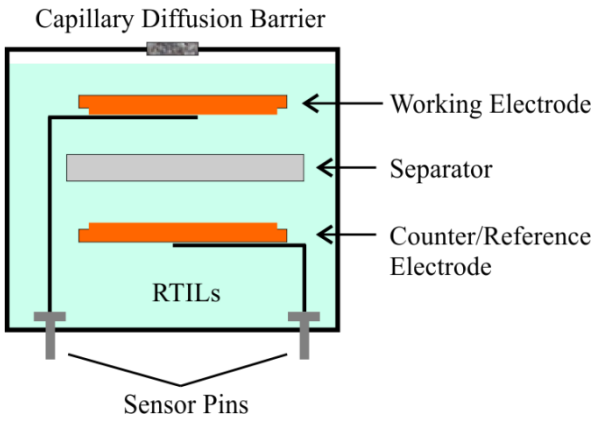

Figure 2.6: Schematic representation of s membrane-free RTIL AGS. Figure adapted from Ref.[27]

Recent studies show that there is continuous struggle for the advancement of amperometric gas sensors (AGSs) towards their miniaturization as portable sensing devices. For this purpose "lab-on a chip" type AGSs devices were introduced because of their many advantages such as low manufacturing costs, ease of manufacturing and their usefulness in many applications where portability is essential (e.g. gas sensors on clothing of personnel exposed to toxic gases).[78] It has been revealed that screen printed electrodes (SPEs) are being explored as increasingly favourable sensing surfaces due to their low cost and commercial availability.[79] SPEs comprise of three electrodes (working, counter and reference) that are deposited onto an inert ceramic substrate using screen-printing techniques.[79] A previous study has shown that SPEs with microliter quantities of RTIL solvents have proved to be good gas sensing devices due to the unique low-volatility of RTILs as compared to aqueous solvents.[79-81]

In this thesis we also explore new commercially available sensing devices called thin-film electrodes (TFEs) and microarray thin-film electrode (MATFEs) that typically consist of a three electrode system (working, counter and reference) incorporated onto a small area on a Pyrex substrate using thin-film technology. Both TFEs and MATFEs are 100% purely metal-based, with dimensions of the electrode devices of 2 mm in size, 150 nm thickness of Pt thin-film and enabling a very small sample volume (1-5µL). Both TFEs and MATFEs have some inherent properties,

such as low cost, disposable, reusable, high fabrication resolution, high sensitivity, low reagent consumption, as well as non-tedious pre-cleaning procedure, which provide an excellent pathway for the design of robust and miniaturized AGSs. Figure 2.7 shows photos of a SPE, TFE and MATFE. Most of the work presented in this thesis is based on TFE and MATFE sensors.

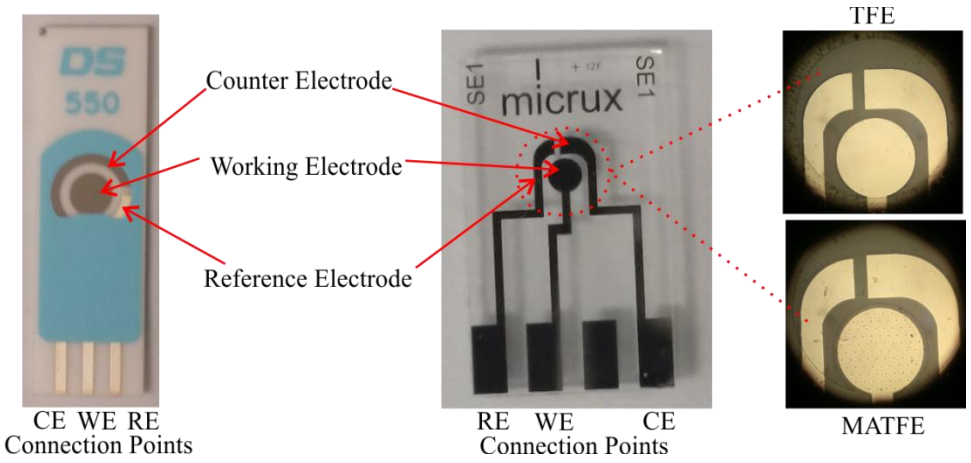

Figure 2.7: Photograph of SPE, TFE and MATFE from commercial suppliers (DropSens and Micrux).

2.5 AGSs with Modified Sensing Surfaces

The sensitivity of the sensing surfaces in AGSs is an important factor when detecting a particular gaseous analyte, especially in more viscous systems such as RTILs, where the diffusion rate of the electrogenerated product away from the electrode surface is relatively slow compared to aqueous or conventional solvents.[82] As a result, the sensitivity of a sensor can be reduced due to deterioration or fouling of the sensing surface.[2, 83] In this case, the highly sensitive surfaces have great advantages due to their extra active sites which can be achieved by modifying the sensing surface with different sensitive materials. Different strategies can be employed to improve the sensitivity of sensing surfaces in AGS devices; by chemical or electrochemical modification with metal nanoparticles (e.g. noble metals such as gold, platinum, silver),[84-86] semiconductor nanoparticles,[84, 87] with carbon materials such as carbon nanotubes (single-walled carbon nanotubes, multi-walled carbon nanotubes, graphene),[88, 89] or by modifying the sensing surfaces with polyelectrolytes,[90] conducting polymers or polymer/ionic liquid mixture which not only improve the sensitivity but also increase the robustness of a sensor.[34, 91] Hutton

et al. introduce an amperometric sensor for oxygen reduction in aqueous media which was based on a polycrystalline boron doped diamond electrode modified with platinum nanoparticles (PtNPs).[92] These PtNP modified electrodes have advantages over bare Pt surfaces such as wider electrochemical windows in aqueous media, smaller background signals, better sensitivity for oxygen reduction and also have good resistance to fouling of the sensing surface.[92, 93]

Langer et al. employed a supported platinum catalyst onto a graphite electrode for the electro-oxidation of sulfur dioxide (SO_2) gas in aqueous electrolyte.[94] Chiou at al. introduced a dispersed catalyst gas diffusion electrode in an AGS device for the electrochemical oxidation of SO_2 gas.[85] For this purpose, they employed a composite material of gold as a catalyst with carbon black. The gold nanoparticles on a porous electrode provided active sites and catalysed the electro-oxidation of SO_2 gas with an enhanced response time.[85] Recently Chiou et al. introduced a facile method of hydrogen bubble-assisted electrodeposition to deposit metal nanoparticles (silver, palladium, nickel nanoparticles) from protic ionic liquid (ethylammonium nitrate, EAN) on glassy carbon and platinum electrodes.[95] Mild evolution of hydrogen bubbles on the working electrode acts as a barrier to aggregate the metal nanoparticles and produce a uniform thin-layer of electrocatalyst which is sensitive to the oxygen reduction reaction (ORR) in aqueous media.[95]

Recent studies show that polymer-based AGS (e.g. polydimethylsiloxane, PDMS) have attracted a significant attention due to their permselectivity, excellent hydrophobicity, and enhanced sensitivity for a particular gaseous analytes where no inner electrolyte is required, thus making more robust and miniaturized gas sensors.[91, 96] Mizutani et al. introduced a PDMS-based AGS device which can be prepared by dip-coating the sensing probe into a PDMS emulsion that is sensitive to the rapid and selective determination of oxygen and nitric oxide.[91] This porous, hydrophobic polymer layer on the working electrode replaced the need for an inner electrolyte, was only permeable for gaseous analytes (O_2, NO), and strongly restricted the transport of hydrophilic species such as water and hydrogen peroxide.[91]

Despite all this information, there are very limited studies on RTIL-based amperometric gas sensors with modified sensing surfaces. In this thesis we will explore new approaches to improve the performance of RTIL-based amperometric

gas sensors by modifying their sensing surfaces with different metal nanoparticles such as platinum nanoparticles (PtNPs), gold nanoparticles (AuNPs), various RTIL/polymer mixtures, and polymerised ionic liquids as a polyelectrolyte thin-film, in order to make highly robust, membrane-free, and low-cost miniaturized amperometric gas sensors and finally employed these modified sensing devices for ammonia, oxygen, and hydrogen gas sensors.

2.6 Aims of This Thesis

The main aim of this thesis is to work towards improving the sensitivity of amperometric sensors to detect toxic/flammable gases (ammonia, hydrogen chloride, hydrogen) at low concentrations in RTIL systems. The current (USA) Occupational Safety and Health Administration Permissible Exposure Limit (OSHA PEL) for NH_3 and HCl is 25 ppm and 5 ppm respectively, therefore low concentrations can be lethal. Hydrogen is highly flammable and its lower explosive limit is 4 %. Thus in order to detect low concentrations of these gases in RTILs, we have adopted two approaches: (1) modification of electrode surfaces with different nanomaterials (metal nanoparticles, 2D and 3D nanostructures, nanoparticle modified microchannels) to improve their sensitivity, (2) use of different voltammetric techniques to investigate which is the most sensitive for a particular gas. Finally, from all this information, we should be able to recommend what surface and which electrochemical technique can be employed together with RTILs in amperometric devices to produce low cost, miniaturized, and fast responding gas sensors that are able to detect toxic gases at trace concentrations with adequately high sensitivities and low limits of detection.

References

1. P. Gründler, *Chemical Sensors: An Introduction for Scientists and Engineers*, Springer Science & Business Media, 2007.
2. R. Knake, P. Jacquinot, A. W. E. Hodgson and P. C. Hauser, *Analytica Chimica Acta*, 2005, **549**, 1-9.
3. J. R. Stetter and J. Li, *Chem. Rev.*, 2008, **108**, 352-366.
4. X. Liu, S. Cheng, H. Liu, S. Hu, D. Zhang and H. Ning, *Sensors*, 2012, **12**.
5. S. Zhuiykov, in *Encyclopedia of Analytical Chemistry*, John Wiley & Sons, Ltd, 2006, DOI: 10.1002/9780470027318.a1320.pub2.
6. E. Bakker, *Analytical Chemistry*, 2004, **76**, 3285-3298.
7. C. Wang, L. Yin, L. Zhang, D. Xiang and R. Gao, *Sensors (Basel, Switzerland)*, 2010, **10**, 2088-2106.

8. N.-H. Park, T. Akamatsu, T. Itoh, N. Izu and W. Shin, *Sensors (Basel, Switzerland)*, 2014, **14**, 8350-8362.
9. V. Casey, J. Cleary, G. D'Arcy and J. B. McMonagle, *Sensors and Actuators B: Chemical*, 2003, **96**, 114-123.
10. P. N. Bartlett and S. Guerin, *Analytical Chemistry*, 2003, **75**, 126-132.
11. G. Fischerauer, A. Mauder and R. Müller, in *Sensors*, Wiley-VCH Verlag GmbH, 1995, DOI: 10.1002/9783527620180.ch5, pp. 135-180.
12. J. W. Grate and G. C. Frye, *Sensors Update*, 1996, **2**, 37-83.
13. S. Y. Liang, R. L. Hecker and R. G. Landers.
14. D. T. Blumstein, D. J. Mennill, P. Clemins, L. Girod, K. Yao, G. Patricelli, J. L. Deppe, A. H. Krakauer, C. Clark and K. A. Cortopassi, *Journal of Applied Ecology*, 2011, **48**, 758-767.
15. G. H. Barnett, D. W. Kormos, C. P. Steiner and J. Weisenberger, *Journal of neurosurgery*, 1993, **78**, 510-514.
16. S. Stansfeld, B. Brown and M. Haines, *Reviews on environmental health*, 2000, **15**, 43-82.
17. K. S. Suslick, *science*, 1990, **247**, 1439-1446.
18. C. Lang, J. Fang, H. Shao, X. Ding and T. Lin, *Nature Communications*, 2016, **7**, 11108.
19. M. V. Ghiurcau, C. Rusu, R. C. Bilcu and J. Astola, *Signal Processing*, 2012, **92**, 829-840.
20. K. T. V. Grattan and B. T. Meggitt, *Optical fiber sensor technology*, Springer, 1995.
21. J. Fraden, *Handbook of modern sensors*, Springer, 2010.
22. N. R. Stradiotto, H. Yamanaka and M. V. B. Zanoni, *Journal of the Brazilian Chemical Society*, 2003, **14**, 159-173.
23. E. Bakker and K. Chumbimuni-Torres, *Journal of the Brazilian Chemical Society*, 2008, **19**, 621-629.
24. A. Bratov, N. Abramova and A. Ipatov, *Analytica chimica acta*, 2010, **678**, 149-159.
25. G. Korotcenkov, S. D. Han and J. R. Stetter, *Chem. Rev.*, 2009, **109**, 1402-1433.
26. J. Janata, *Principles of chemical sensors*, Springer Science & Business Media, 2010.
27. L. Xiong and R. G. Compton, *Int. J. Electrochem. Sci*, 2014, **9**, 7152-7181.
28. C. G. Zoski, *Handbook of electrochemistry*, Elsevier, 2006.
29. L. C. Clark, Wolf R, Granger D and Taylor Z, *J Appl Physiol*, 1953, **6**, 189-193.
30. T. Graunke, K. Schmitt, S. Raible and J. Wöllenstein, *Sensors*, 2016, **16**.
31. B. Adhikari and S. Majumdar, *Progress in Polymer Science*, 2004, **29**, 699-766.
32. J.-S. Do and R.-Y. Shieh, *Sensors and Actuators B: Chemical*, 1996, **37**, 19-26.
33. D. Li, Y. Jiang, Z. Wu, X. Chen and Y. Li, *Sensors and Actuators B: Chemical*, 2000, **66**, 125-127.
34. J.-S. Do and W.-B. Chang, *Sensors and Actuators B: Chemical*, 2001, **72**, 101-107.
35. G. Inzelt, A. Lewenstam and F. Scholz, *Handbook of reference electrodes*, Springer, 2013.
36. H. P. Chen, J. W. Fergus and B. Z. Jang, *Journal of The Electrochemical Society*, 2000, **147**, 399-406.
37. Q. Li, C. Batchelor-McAuley, N. S. Lawrence, R. S. Hartshorne and R. G. Compton, *Journal of Electroanalytical Chemistry*, 2013, **688**, 328-335.
38. M. C. Buzzeo, C. Hardacre and R. G. Compton, *Analytical Chemistry*, 2004, **76**, 4583-4588.
39. M. Doyle, S. K. Choi and G. Proulx, *Journal of the Electrochemical Society*, 2000, **147**, 34-37.
40. Y. He, P. G. Boswell, P. Bühlmann and T. P. Lodge, *The Journal of Physical Chemistry B*, 2007, **111**, 4645-4652.
41. R. D. Rogers and K. R. Seddon, *Science*, 2003, **302**, 792-793.

42. M. C. Buzzeo, R. G. Evans and R. G. Compton, *ChemPhysChem*, 2004, **5**, 1106-1120.
43. D. S. Silvester and R. G. Compton, *Zeitschrift für Physikalische Chemie*, 2006, **220**, 1247-1274.
44. T. Welton, *Chemical reviews*, 1999, **99**, 2071-2084.
45. C. Chiappe and D. Pieraccini, *Journal of Physical Organic Chemistry*, 2005, **18**, 275-297.
46. S. Chowdhury, R. S. Mohan and J. L. Scott, *Tetrahedron*, 2007, **63**, 2363-2389.
47. K. R. Seddon, *Journal of Chemical Technology and Biotechnology*, 1997, **68**, 351-356.
48. M. A. B. H. Susan, T. Kaneko, A. Noda and M. Watanabe, *Journal of the American Chemical Society*, 2005, **127**, 4976-4983.
49. H. Shobukawa, H. Tokuda, S.-I. Tabata and M. Watanabe, *Electrochimica acta*, 2004, **50**, 305-309.
50. A. Noda, M. A. B. H. Susan, K. Kudo, S. Mitsushima, K. Hayamizu and M. Watanabe, *The Journal of Physical Chemistry B*, 2003, **107**, 4024-4033.
51. R. Kawano, H. Matsui, C. Matsuyama, A. Sato, M. A. B. H. Susan, N. Tanabe and M. Watanabe, *Journal of photochemistry and photobiology A: Chemistry*, 2004, **164**, 87-92.
52. A. S. Shaplov, R. Marcilla and D. Mecerreyes, *Electrochimica Acta*, 2015, **175**, 18-34.
53. J. Lee, G. Du Plessis, D. W. M. Arrigan and D. S. Silvester, *Analytical Methods*, 2015, **7**, 7327-7335.
54. J. Lee and D. S. Silvester, *Analyst*, 2016, **141**, 3705-3713.
55. E. I. Rogers, A. M. O'Mahony, L. Aldous and R. G. Compton, *ECS Transactions*, 2010, **33**, 473-502.
56. C. Zhao, G. Burrell, A. A. J. Torriero, F. Separovic, N. F. Dunlop, D. R. MacFarlane and A. M. Bond, *The Journal of Physical Chemistry B*, 2008, **112**, 6923-6936.
57. A. M. O'Mahony, D. S. Silvester, L. Aldous, C. Hardacre and R. G. Compton, *Journal of Chemical & Engineering Data*, 2008, **53**, 2884-2891.
58. H. L. Ngo, K. LeCompte, L. Hargens and A. B. McEwen, *Thermochimica Acta*, 2000, **357**, 97-102.
59. J. A. Widegren and J. W. Magee, *Journal of Chemical & Engineering Data*, 2007, **52**, 2331-2338.
60. M. S. Miran, H. Kinoshita, T. Yasuda, M. A. B. H. Susan and M. Watanabe, *Chemical Communications*, 2011, **47**, 12676-12678.
61. A. A. Oliferenko, P. V. Oliferenko, K. R. Seddon and J. S. Torrecilla, *Physical Chemistry Chemical Physics*, 2011, **13**, 17262-17272.
62. L. F. Vega, O. Vilaseca, F. Llovell and J. S. Andreu, *Fluid Phase Equilibria*, 2010, **294**, 15-30.
63. M. B. Shiflett and A. Yokozeki, *The Journal of Physical Chemistry B*, 2007, **111**, 2070-2074.
64. A. Yokozeki and M. B. Shiflett, *Industrial & Engineering Chemistry Research*, 2007, **46**, 1605-1610.
65. D. Tuma and G. Maurer, in *Ionic Liquids: Science and Applications*, American Chemical Society, 2012, vol. 1117, ch. 10, pp. 217-238.
66. D. Camper, P. Scovazzo, C. Koval and R. Noble, *Industrial & Engineering Chemistry Research*, 2004, **43**, 3049-3054.
67. Z. Lei, C. Dai and B. Chen, *Chemical reviews*, 2013, **114**, 1289-1326.
68. A. M. O'Mahony, D. S. Silvester, L. Aldous, C. Hardacre and R. G. Compton, *The Journal of Physical Chemistry C*, 2008, **112**, 7725-7730.
69. L. E. Barrosse-Antle, D. S. Silvester, L. Aldous, C. Hardacre and R. G. Compton, *The Journal of Physical Chemistry C*, 2008, **112**, 3398-3404.

70. D. S. Silvester, K. R. Ward, L. Aldous, C. Hardacre and R. G. Compton, *J. Electroanal. Chem.*, 2008, **618**, 53-60.
71. G. Kuranov, B. Rumpf, N. A. Smirnova and G. Maurer, *Industrial & engineering chemistry research*, 1996, **35**, 1959-1966.
72. A. Douabul and J. Riley, *Journal of Chemical and Engineering Data*, 1979, **24**, 274-276.
73. W. C. Barrette Jr and D. T. Sawyer, *Analytical chemistry*, 1984, **56**, 653-657.
74. L. Xiong, A. M. Fletcher, S. G. Davies, S. E. Norman, C. Hardacre and R. G. Compton, *Chemical Communications*, 2012, **48**, 5784-5786.
75. A. Finotello, J. E. Bara, D. Camper and R. D. Noble, *Industrial & Engineering Chemistry Research*, 2008, **47**, 3453-3459.
76. P. Scovazzo, D. Camper, J. Kieft, J. Poshusta, C. Koval and R. Noble, *Industrial & Engineering Chemistry Research*, 2004, **43**, 6855-6860.
77. L. E. Barrosse-Antle, A. M. Bond, R. G. Compton, A. M. O'Mahony, E. I. Rogers and D. S. Silvester, *Chemistry–An Asian Journal*, 2010, **5**, 202-230.
78. K. Malzahn, J. R. Windmiller, G. Valdes-Ramirez, M. J. Schoning and J. Wang, *Analyst*, 2011, **136**, 2912-2917.
79. J. P. Metters, R. O. Kadara and C. E. Banks, *Analyst*, 2011, **136**, 1067-1076.
80. J.-L. Chang, G.-T. Wei and J.-M. Zen, *Electrochemistry Communications*, 2011, **13**, 174-177.
81. D. V. Chernyshov, N. V. Shvedene, E. R. Antipova and I. V. Pletnev, *Analytica Chimica Acta*, 2008, **621**, 178-184.
82. D. Morgan, L. Ferguson and P. Scovazzo, *Industrial & Engineering Chemistry Research*, 2005, **44**, 4815-4823.
83. K. Murugappan, J. Lee and D. S. Silvester, *Electrochem. Commun.*, 2011, **13**, 1435-1438.
84. F. Wang and S. Hu, *Microchim. Acta*, 2009, **165**, 1-22.
85. C.-Y. Chiou and T.-C. Chou, *Electroanal.*, 1996, **8**, 1179-1182.
86. L. Rassaei, F. Marken, M. Sillanpää, M. Amiri, C. M. Cirtiu and M. Sillanpää, *Trends Anal. Chem.*, 2011, **30**, 1704-1715.
87. N. Barsan and U. Weimar, *J. Phys.: Condens. Matter*, 2003, **15**, R813.
88. P. Santhosh, K. M. Manesh, A. Gopalan and K.-P. Lee, *Sens. Actuators, B*, 2007, **125**, 92-99.
89. T. Gan and S. Hu, *Microchim. Acta*, 2011, **175**, 1.
90. K. S. Alber, J. A. Cox and P. J. Kulesza, *Electroanalysis*, 1997, **9**, 97-101.
91. F. Mizutani, S. Yabuki, T. Sawaguchi, Y. Hirata, Y. Sato and S. Iijima, *Sensors and Actuators B: Chemical*, 2001, **76**, 489-493.
92. L. Hutton, M. E. Newton, P. R. Unwin and J. V. Macpherson, *Analytical Chemistry*, 2009, **81**, 1023-1032.
93. R. G. Compton, J. S. Foord and F. Marken, *Electroanalysis*, 2003, **15**, 1349-1363.
94. S. E. Lyke and S. H. Langer, *Journal of The Electrochemical Society*, 1991, **138**, 1682-1687.
95. M. Asnavandi and C. Zhao, *ACS Sustainable Chemistry & Engineering*, 2017, **5**, 85-89.
96. G. S. Korotchenkov, *Handbook of Gas Sensor Materials: Properties, Advantages and Shortcomings for Applications Volume 1: Conventional Approaches*, Springer New York, USA, 2013.

Chapter 3

3. General Experimental Procedures

This chapter will list the general chemicals and describe the general experimental procedures including the gas mixing setup, glass cells, and different types of electrodes. The details of any experimental setup or apparatus that is specific for a particular investigation will be described in the relevant chapter.

3.1 Chemical reagents

All chemicals used in this thesis were commercially available and used as received and are listed in Table 3.1.

Table 3.1: All purchased chemicals, reagents, and solvents used to perform experiments reported in this thesis, along with their abbreviations, commercial supplier and purity.

Name	Formula/Abbreviation	Supplier	Purity
Ethanol	C_2H_5OH /EtOH	Aldrich	99 %
Acetone	$(CH_3)_2CO$	Aldrich	99 %
Sulfuric acid	H_2SO_4	Aldrich	98 % w/w
Zinc chloride	$ZnCl_2$	Aldrich	40 % w/v
Acetonitrile	CH_3CN /MeCN	Fischer	>99.8 %
Ferrocene	$Fe(C_5H_5)_2$ /Fc	Aldrich	98 %
Potassium chloride	KCl	Fluka	>99.5 %
Potassium hexacyanoferrate (III) (potassium ferricyanide)	$K_3Fe(CN)_6$	Aldrich	99 %
Tetrabutylammonium perchlorate	$(C_4H_9)_4N(ClO_4)$/TBAP	Aldrich	98 %
Gold (III) chloride trihydrate	$HAuCl_4.3H_2O$	Aldrich	≥99.9 %
Chloroplatinic acid hydrate	$H_2PtCl_6.xH_2O$	Aldrich	≥99.9 %
Poly(methyl methacrylate)	$(C_5O_2H_8)_n$ /PMMA	Aldrich	M_w~15000
Hydroquinone	$C_6H_6O_2$ /HQ	Aldrich	≥99 %

A list of the toxic and non-toxic gases employed throughout this thesis is shown in Table 3.2.

Table 3.2: List of gases used in this thesis, with their supplier, and purity/concentration.

Name	Formula	Supplier	Purity
Nitrogen	N_2	BOC gases	≥99.99 %
Oxygen	O_2	BOC gases	>99.5 %
Hydrogen	H_2	BOC gases	>99.5 %
Hydrogen chloride	HCl	CAC gases	0.2 % in N_2
Ammonia	NH_3	CAC gases	0.2 % in N_2
Ammonia	NH_3	CAC gases	0.05% in N_2
Ammonia	NH_3	CAC gases	0.005% in N_2

All room temperature ionic liquids (RTILs) used as the solvent/electrolyte in electrochemical experiments reported in this thesis are listed in Table 3.3.

Table 3.2: List of RTILs used in this thesis with their full names, abbreviation, and supplier. All RTILs were ultra-high purity (electrochemical grade) and no additional purification/cleaning steps were employed before use.

Name	Formula/Abbreviation	Supplier
1-ethyl-3-methylimidazolium bis(trifluoromethylsulfonyl)imide	$[C_2mim][NTf_2]$	Merck
1-butyl-3-methylimidazolium bis(trifluoromethylsulfonyl)imide	$[C_4mim][NTf_2]$	Merck
1-butyl-3-methylimidazolium trifluorotris(pentafluoroethyl)phosphate	$[C_4mim][FAP]$	Merck
1-butyl-3-methylimidazolium hexafluorophosphate	$[C_4mim][PF_6]$	Merck
1-butyl-3-methylimidazolium tetrafluroborate	$[C_4mim][BF_4]$	Merck
1-hexyl-3-methylimidazolium trifluorotris(pentafluoroethyl)phosphate	$[C_6mim][FAP]$	Merck
N-butyl-N-methylpyrrolidinium bis(trifluoromethylsulfonyl)imide	$[C_4mpyrr][NTf_2]$	Merck

3.2 General Electrochemical Procedures

All electrochemical experiments were performed using a PGSTAT101 Autolab potentiostat (Eco, Chemie, Netherlands) interfaced to a PC with Nova 1.9-1.11 software. All experiments were carried out on different types of gold, platinum,

graphite, and glassy carbon electrodes (see section 3.4) at standard laboratory temperature (294 ± 1K) in the fume cupboard, inside an aluminium Faraday cage (see Figure 3.1) to reduce electrical interference. Prior to the introduction of analyte gases (ammonia, hydrogen chloride, oxygen, hydrogen), purging of the solvent was carried out using nitrogen gas for about 10 to 60 minutes, depending on the type of electrode and electrochemical setup. This step was necessary to remove impurities (i.e. water, air) naturally present in the RTIL and obtain a blank scan. When a stable baseline was obtained (after ~ 10-60 minutes, depending on the setup), the analyte gas then was introduced into one arm of the glass T-cell in which the electrode with the RTIL is present. The gas was allowed to pass over the RTIL to allow partitioning of the gas via the gas/liquid interface. The gas was then allowed to diffuse into the RTIL until equilibrium was obtained. Excess gas was expelled from the other arm of the cell into a fume cupboard via PTFE tubing.

3.3 Gas Mixing System

The general gas mixing system employed for gas sensing experiments is illustrated in Figure 3.1. It consists of two gas cylinders, one for the analyte gas (details of supplier and concentration is described in Table 3.2) and the other for nitrogen gas for further dilution of the analyte gas. Both gas cylinders were attached with two digital flow controllers through ¼ inch (outer diameter) PTFE tubing and Swagelok joints (Swagelok, Kardinya, WA, Australia). In order to obtain different concentrations of analyte gases (ammonia, hydrogen chloride, oxygen, hydrogen), the desired gas was diluted with nitrogen through the use of two digital flow controllers (0-1.0 L/min, John Morris Scientific, NSW, Australia, and 0-10 L/min, Aalborg, New York USA), one connected to the analyte gas cylinder (NH_3, HCl, H_2, O_2) and the other to nitrogen. Both gases passed through an additional gas mixing segment[1] and into one arm of the specially designed glass T-cell. The gas mixing segment (see enlargement at the bottom left in Figure 3.1) consists of two opposing tapered glass-needles inserted into a small piece of PTFE tube for support, to generate gas turbulence and to ensure adequate mixing of both gases. The other arm of the glass cell was attached with further PTFE tubing and exhausted into the fume cupboard. The relative flow rates were used to calculate the different concentrations of gas introduced into the T-cell.

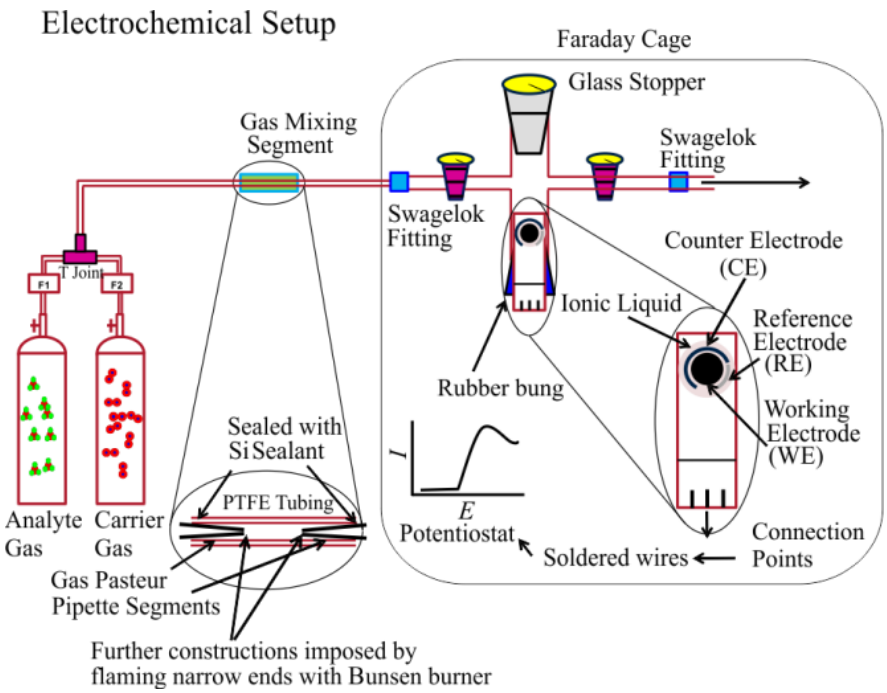

Figure 3.1: Schematic representation of the gas mixing system and glass T-cell used for voltammetric experiments on chip-based electrodes (e.g. thin-film electrodes, screen printed electrodes) where F1 and F2 are the digital flow-controllers attached to the gas cylinders. The glass electrochemical T-cell cell is placed inside an aluminium Faraday cage. The whole setup was situated in a fume cupboard.

3.4 Electrodes and Electrochemical Cells

Different types of gold, platinum, and glassy carbon electrodes of various sizes were employed as sensing surfaces throughout this thesis. These electrodes are macroelectrodes and microelectrodes including thin-film electrodes (TFEs), microarray thin-film electrodes (MATFEs), screen printed electrodes (SPEs), home-made microdisk electrode (μ-disk), and conventional macrodisk electrode. In this section these electrodes will be discussed in detail, describing their geometry and proposed electrochemical cell setup.

3.4.1 Thin-Film and Microarray Thin-Film Electrodes

The first type of electrode used for gas sensing experiments are platinum (Pt) thin-film electrodes (TFEs) from Micrux Technologies, Oviedo, Spain (see Figure 3.2a). These are relatively new commercially available electrodes, comprising of three electrodes, with the working electrode (1 mm diameter), counter and reference electrode, all made from pure platinum. The Pt thin-film (150 nm thickness) was fabricated by thin-film technology on a Pyrex substrate. A protective layer of SU-8

resin is used to cover the connection traces and enable the use of a very small sample volume (1-5 µL).

The second type of electrode is platinum microarray thin-film electrodes (MATFE) from Micrux Technologies, Oviedo, Spain (see Figure 3.2b). These are similar to the TFEs except the working electrode is covered with a layer of SU-8 resin into which 90 µ-holes of 10 µm diameter are made to create 90 recessed microelectrodes. Prior to employed both electrodes for gas experiments, the TFEs and MATFEs were electrochemically activated in 0.5 M $H_2SO_{4\,(aq)}$ by a potential scanning between -0.21 and +1.3 V (TFE), or -0.27 and + 1.4 V (MATFE) *vs* an external Ag/AgCl (0.1 M KCl) reference electrode (BASi, Indiana, USA) and Pt coil counter electrode (Goodfellow, Cambridge Ltd., UK) at a scan rate of 500 mVs^{-1} for ca. 200 cycles. For gas sensing experiments, in both the TFE and MATFE, the RTIL (2-3 µL) was drop-cast and spread over the three electrodes in the form of thin film.

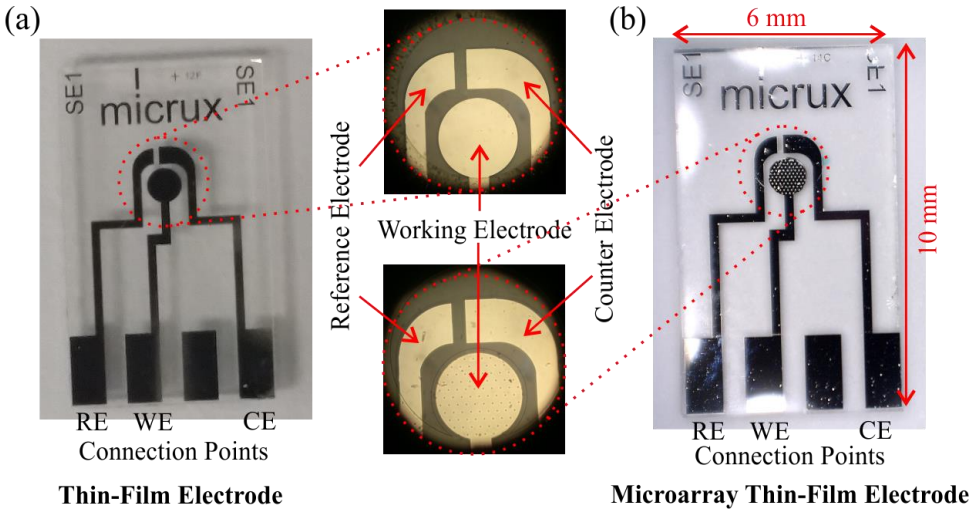

Figure 3.2: Photographs of (a) TFE and (b) MATFE used for voltammetric experiments. RE, WE and CE correspond to the working, reference and counter electrodes, respectively.

3.4.2 Screen Printed Electrodes

The third type of electrodes employed for electrochemical measurements are Pt screen printed electrodes (SPEs) from DropSens (Asturias, Spain) which consist of a Pt working electrode (4 mm diameter) with an integrated Pt counter electrode and Ag quasi-reference electrode (see Figure 3.3). 8 µL of RTIL is drop cast on the (larger)

surface of the electrode, which is enough to cover all three electrodes. The working electrode is not cleaned or activated, as recommended by the manufacturer.

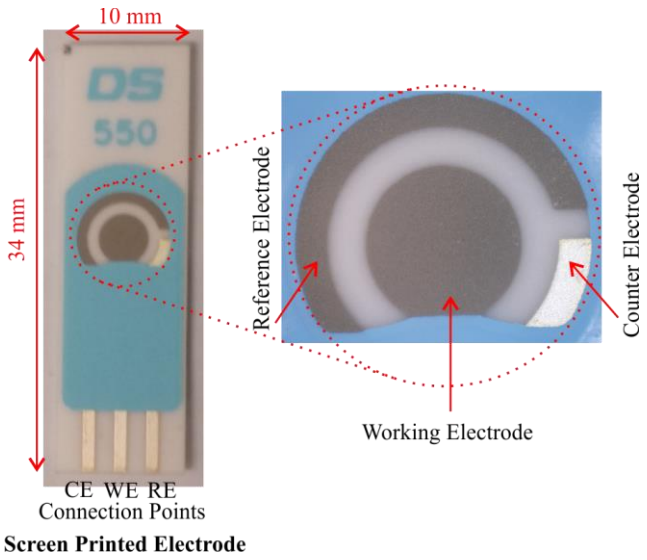

Figure 3.3: Photographs of a Pt screen printed electrode from DropSens (Spain) and a close-up of the working, reference and counter electrode surfaces.

For gas sensing experiments, the TFEs, MATFEs and SPEs were soldered with aluminium wires (using 40 % w/v $ZnCl_2$ solution as soldering flux) and placed into a modified rubber bung. The connecting wires were on the outside of the cell and the electrodes were on the inside of the cell. The RTIL (2-3 µL for TFEs and MATFEs, and 8 µL for SPEs) was drop-cast onto the electrodes. Then the electrodes were then placed inside the rubber bung and inserted very gently into one arm of a specially designed glass cell (a modified form of a previously reported T-cell).[1, 2] The second tapered joint was closed with a glass stopper. The cell also has two openings, an inlet where the analyte gas (ammonia, hydrogen chloride, oxygen, hydrogen, or its mixture with nitrogen) entered and passed over the electrochemical cell to diffuse through the RTIL, and the outlet that led into the fume cupboard.

Figure 3.4 shows a photograph of the specially designed glass 'T-cell' with one side containing planar electrodes (TFE, MATFE, SPE) inside a rubber bung, and the second side closed with glass stopper.

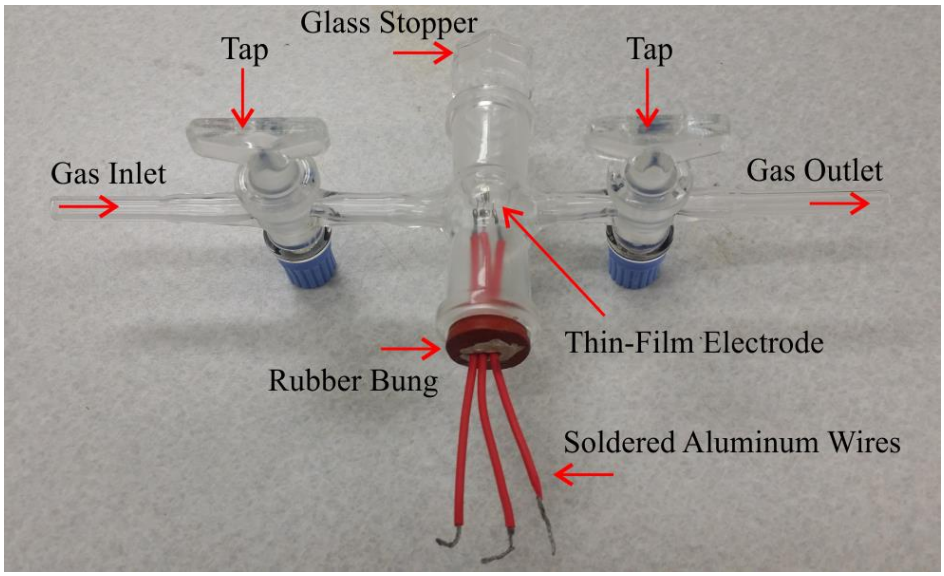

Figure 3.4: Photograph of the glass 'T-cell' with a rubber bung containing a thin-film electrode (TFE). The TFE was connected to the potentiostat via soldered aluminium wires.

3.4.3 Home-Made Microdisk Electrode

The fourth type of electrode that was employed for gas sensing experiments is a home-made microdisk electrode (see Figure 3.5) which was kindly donated by Prof. Neil Rees (formerly at Oxford University, UK). A micron sized metal wire (Pt) was sealed in a glass tube. A cross section of that wire was polished on a polishing pad using alumina to form an inlaid microdisk electrode. The Pt wire is attached with a conducting wire (copper or aluminium) to a connection at the bottom, which is sealed with epoxy resin. A tapered joint is added to the glass body to enable insertion into the 'T-cell'. Electrochemical studies of various toxic gases such as hydrogen sulfide, ammonia, hydrogen, and sulfur dioxide have been reported previously on similar types of electrodes.[3-6]

For gas sensing experiments, the electrochemical cell comprised of two electrode arrangement: a conventional home-made microdisk electrode as the working electrode (8.3 µm radius) and a silver wire (0.5 mm diameter, Sigma Aldrich) as a combined counter and quasi-reference electrode. A disposable micropipette tip was cut so that it could be fixed at the top of microdisk electrode and secured with parafilm to provide a cavity in which 25 µL ionic liquid was placed. Then the electrode was housed very gently into the bottom of a specially designed glass T-cell,[4, 5, 7] whose top was closed with a stopper containing a Ag wire quasi-reference

electrode, which was suspended into the ionic liquid. Figure 3.5 shows a cartoon and photograph of a home-made microdisk electrode used for gas sensing experiments. Figure 3.6 shows a photograph of the modified glass T-cell with a microdisk working electrode.

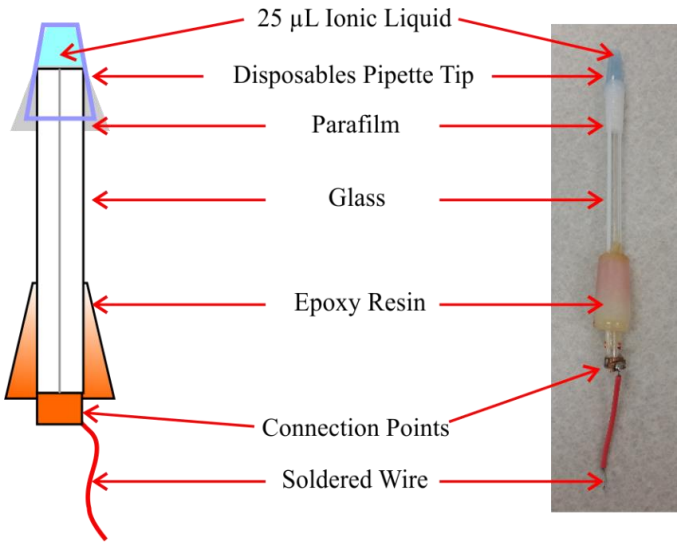

Figure 3.5: Cartoon and photograph of a home-made microdisk electrode used for gas sensing experiments.

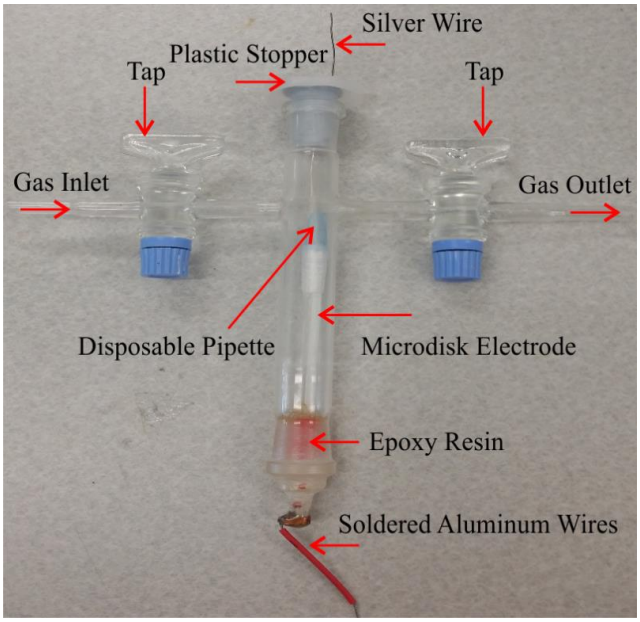

Figure 3.6: Photograph of a glass 'T-cell' whose bottom contains a microdisk working electrode and from the top is a silver wire suspended through a plastic stopper into the RTIL.

3.4.4 Macrodisk PINE Electrode

The fifth type of electrode used for gas sensing experiments were macrodisk electrodes (gold, platinum and glassy carbon from *PINE* Research Instrumentation (North Carolina, USA). The PINE research electrodes are specified for a rotating disk electrode setup, but we employed these electrodes for gas sensing experiments by modification of the electrochemical cell. The metal disk electrodes were all 5 mm in diameter and 4 mm thick. The electrochemical cell comprised different components; *disk core assembly* in which gold, platinum or glassy carbon disk is inserted, *PTFE holder* to hold disk, the core assembly and RTIL, and a *PTFE stopper* with a Pt coil counter electrode and a Ag wire quasi-reference electrode. The disk core assembly is composed of a *stainless disk core* which connects the different components together, such as a *U-cup* to hold the macrodisk electrode, a *U-cup nut* which attaches the U-cup containing the disk core (metal electrode) firmly, a *disk core washer* which prevents the disk core nut from being locked with the threads of disk core, and a *disk core nut* to lock the disk core assembly thus making an electrical connection with the electrode through a stainless steel shaft. Figure 3.7 shows photographs of the different components of the disk core assembly and the three macrodisk electrode stubs employed (gold, platinum, and glass carbon).

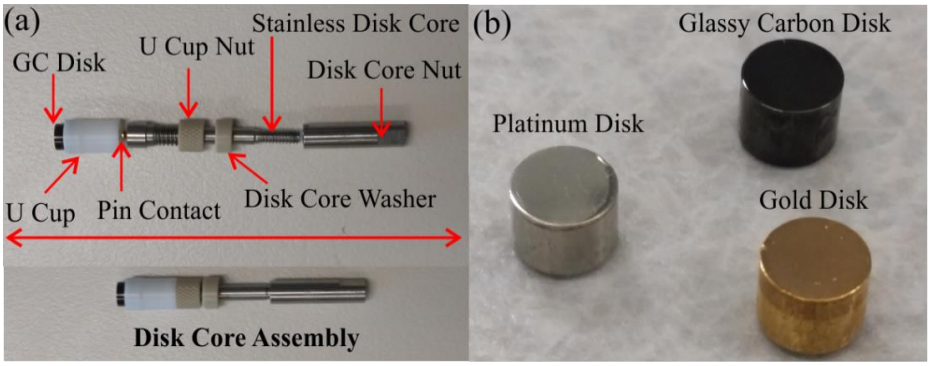

Figure 3.7: Photographs of (a) different components of the disk core assembly, and (b) gold, platinum, and glassy carbon macrodisk electrode stubs from *PINE* Research Instruments.

For gas sensing experiments, the disk core assembly with either a gold, platinum, or glassy carbon electrode is inserted into the PTFE holder and tightened with a disk core nut at the bottom to lock it. Then, 300 µL of ionic liquid was added into the cavity of the PTFE holder to ensure that all three electrodes were immersed into the RTIL. After that the PTFE holder with the disk working electrode was housed very

gently into the bottom of a modified glass T-cell.[4, 5, 7] The top of the cell was closed with a PTFE stopper containing holes for a Ag wire quasi-reference electrode and Pt coil counter electrode, to be suspended into the ionic liquid. Figure 3.5 shows a photograph of the modified glass T-cell with a PTFE holder containing a glassy carbon macrodisk working electrode, and a PTFE stopper containing a silver wire quasi-reference electrode and Pt coil counter electrode suspended into RTIL.

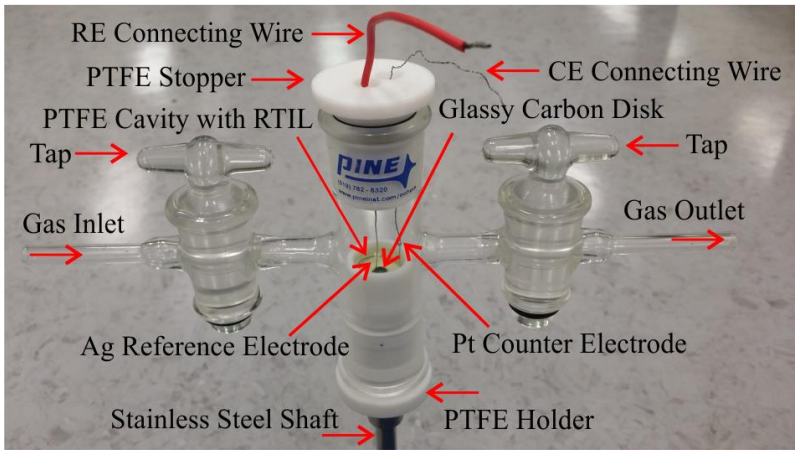

Figure 3.8: Photograph of the glass T-cell employed for the 'change disk' electrode experiments.

3.4.5 Conventional Macrodisk Electrode

The final type of electrode employed for gas sensing experiments are conventional macrodisk electrodes (gold and platinum) from BASi (Indiana, USA). These electrodes have either a gold or platinum disk (1.6 mm diameter), enclosed in a PCTFE (Polychlorotrifluoroethylene) plastic body mounted with a brass rod to connect the working electrode with the potentiostat. Figure 3.9 shows a photograph of gold and platinum macrodisk electrodes.

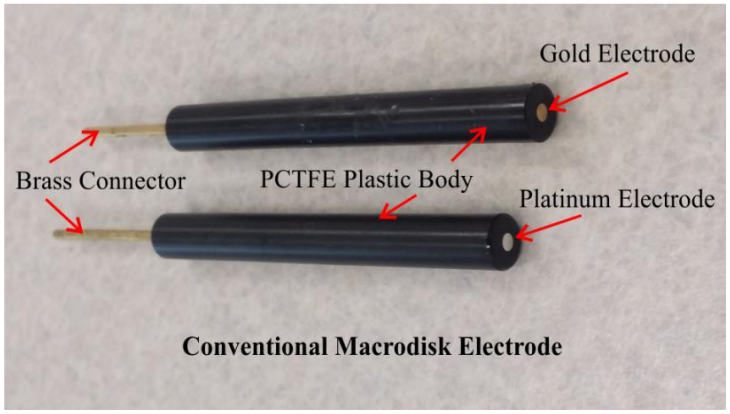

Figure 3.9: Photograph of gold and platinum conventional macrodisk electrodes

For gas sensing experiments, gold macrodisk electrode as *microband electrodes*. Microband electrodes are employed to enhance the response time. For this we modified a gold disk with hexadecanethiol (HDT) using polydimethyl siloxane (PDMS) stamps to create HDT micro-channels or micro-bands and then employed these microband working electrodes with a Pt wire counter electrode and a Ag wire reference electrode (see figure 3.10). A tiny droplet of RTIL is drop cast on the working electrode and is used to fill the microchannels with the help of a micropipette. To connect the RTIL filled microchannels with the counter electrode and reference electrodes, another tiny droplet of RTIL is placed close to one side of the microchannels. The Ag wire (RE) and Pt wire (CE) were placed at an angle of 120 to ensure that all electrodes are in contact. For gas sensing experiments, using a rubber bung, the electrode was inserted gently into the same glass cell as used for the planar electrodes. The analyte gases (ammonia, hydrogen chloride) entered and passed over the electrochemical cell and excess gas was released through the outlet. Figure 3.10 shows a photograph of electrochemical cell that is used with HDT microchannel modified electrodes.

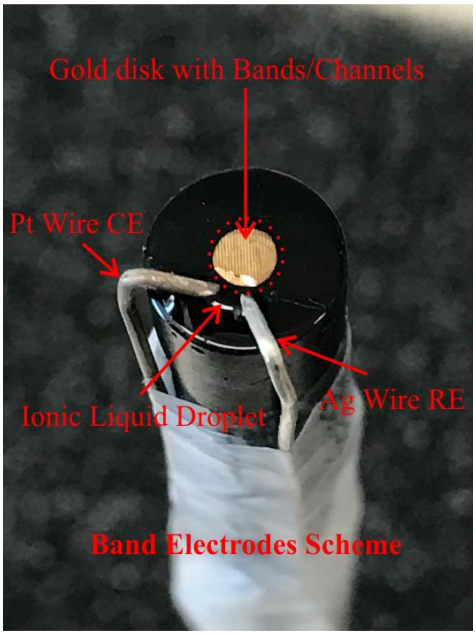

Figure 3.10: Photograph of the electrochemical cell with a conventional gold macrodisk electrode modified with HDT microchannels, along with a Pt wire counter electrode and a Ag wire quasi-reference electrode.

All of the above discussed electrodes have been employed throughout this thesis for the sensing of toxic gases in room temperature ionic liquids. Detailed experimental procedures will be described in the relevant chapter.

3.5 Surface Characterization Experiments

The electrode surfaces employed for gas sensing experiments were characterized using scanning electron microscopy (SEM) and atomic force microscopy (AFM).

3.5.1 Scanning Electron Microscopy (SEM)

Scanning electron microscopy (SEM) experiments were performed on the modified and unmodified working electrodes of all planar devices (TFE, SPE and MATFE), and the conventional macrodisk electrodes with HDT microchannels. SEM Images were obtained using Zeiss Evo (40XVP model), with a voltage of 2.0 kV and MIRA3 (MIRA VP-FESEM), with a voltage of 5.0 kV.

3.5.2 Atomic Force Microscopy (AFM)

Atomic force microscopy (AFM) experiments were performed using Bruker FastScan and WITech alpha 300SAR instruments on the modified and unmodified planar and conventional macrodisk electrodes to image the geometry and morphology of the electrode surfaces.

3.5.3 Confocal Optical Imaging (COI)

The confocal optical imaging was performed on RTILs filled modified microchannels using WITec (alpha300 series) confocal Raman microscope.

References

1. J. Lee, K. Murugappan, D. W. M. Arrigan and D. S. Silvester, *Electrochim. Acta*, 2013, **101**, 158-168.
2. K. Murugappan, J. Lee and D. S. Silvester, *Electrochem. Commun.*, 2011, **13**, 1435-1438.
3. A. M. O'Mahony, D. S. Silvester, L. Aldous, C. Hardacre and R. G. Compton, *The Journal of Physical Chemistry C*, 2008, **112**, 7725-7730.
4. X. Ji, D. S. Silvester, L. Aldous, C. Hardacre and R. G. Compton, *J. Phys. Chem. C*, 2007, **111** 9562–9572.
5. D. S. Silvester, L. Aldous, C. Hardacre and R. G. Compton, *The Journal of Physical Chemistry B*, 2007, **111**, 5000-5007.
6. L. E. Barrosse-Antle, D. S. Silvester, L. Aldous, C. Hardacre and R. G. Compton, *The Journal of Physical Chemistry C*, 2008, **112**, 3398-3404.
7. U. Schroder, J. D. Wadhawan, R. G. Compton, F. Marken, P. A. Z. Suarez, C. S. Consorti, R. F. de Souza and J. Dupont, *New J. Chem.*, 2000, **24**, 1009-1015.

Chapter 4

4. Detection of sub-ppm Concentrations of Ammonia on "Filled" Recessed Microarrays

In this chapter, cyclic voltammetry (CV) was performed on different electrode surfaces to study the mechanism of ammonia oxidation in the RTILs. In order to study the analytical utility and limit of detection (LOD) for ammonia oxidation in [C_2mim][NTf_2], we will use linear sweep voltammetry along with potential-step chronoamperometry (due to lower background currents). For this study, three commercially-available planar devices are used, all with platinum (Pt) working electrodes: thin-film electrode (TFE), screen-printed electrode (SPE) and micro-array thin film electrode (MATFE), along with an "ideal" conventional Pt microdisk electrode for comparison. The microholes on the recessed MATFE are then further 'filled' with electrodeposited platinum, in order to improve the radial diffusion characteristics and give higher current densities, closer to the ideal values on the conventional microdisk electrode. Finally we will employ the 'filled' recessed microarrays and standard microarrays as a comparison for low concentration (0.1-2 ppm) detection of ammonia in RTILs. The work that forms the basis of this chapter has been published in Analytical Chemistry.[1]

4.1 Introduction

The detection of ammonia (NH_3) gas at low concentrations is of great importance due to its high toxicity and use in a wide range of industries e.g. oil and gas industry, fertilizer industry, refrigeration industry etc.[2] Concentrations as low as 500 ppm can be lethal, and the current (USA) Occupational Safety and Health Administration Permissible Exposure Limit (OSHA PEL) for NH_3 is 25 ppm in the gas phase. Although a range of different strategies have been employed to monitor toxic gases,[2, 3] but electrochemical gas sensors are most commonly used devices due to their low cost and portability, low power consumption capacity, high sensitivity and selectivity and their better ability to be miniaturised.[4, 5] Commercially available amperometric gas sensors (AGSs) for ammonia are sold by a range of companies,[6] but a major drawback with these sensors is their solvent/electrolyte combination (typically water/sulphuric acid) which can dry-up very quickly in harsh conditions (particularly

in hot and dry environments) and thus decrease the lifetime of a sensor. As a result, non-volatile room temperature ionic liquids (RTILs) have been attracting great attention[7-13] as replacement electrolytes in "membrane-free" AGSs. An advantage of using RTILs for gas sensing, is that polar gases such as ammonia are highly soluble,[14] which may be beneficial for detection at very low concentrations.

The reaction mechanism for ammonia oxidation in ionic liquids has been well studied at higher (percent) concentrations of ammonia in ionic liquids on Pt microdisk electrodes,[15, 16] and also on screen-printed electrodes.[17] However, studies focussed on the sensing of ammonia in ionic liquids at low concentrations (less than 100 ppm) are rather limited. Carter et al.[18] employed a home-made prototype printed gas sensor using a constant biasing technique (long-term chronoamperometry) for ammonia sensing at 10-1000 ppm. Linear responses (current vs concentration) were observed best in the lower concentration range up to 200 ppm. A limit of detection (LOD) of 2 ppm was calculated based on the calibration curve in the 10-50 ppm concentration range. The same group[19] reported another printed AGS for detecting ammonia in three different ionic liquids. LODs of 0.12-0.47 ppm were reported from calibration graphs in the 10-40 ppm concentration range, again using a constant biasing technique. Oudenhoven et al.[20] later reported the sensing of ammonia on a planar interdigitated Pt electrode using a thin layer (5 μm thick) of RTIL. Concentrations down to 1 ppm could be distinguished from the blank response, and it was suggested that cyclic voltammetry/linear sweep voltammetry was the preferred technique over long-term chronoamperometry, due to evidence of electrode fouling for amperometry during exposure to ammonia.

The above-mentioned work, in addition to various other studies,[21-24] has shown that there is continuous trend towards the miniaturisation of sensing devices. The ease and low-cost of manufacturing, and their usefulness in applications where portability is essential (e.g. wearable sensors)[25] is driving research in this area. As a result, we are investigating new low-cost, miniaturised, commercially available thin-film electrode surfaces. Their small size means that only a few microliters (or less) of RTIL solvent is needed. Three different types of commercially available planar electrodes have been employed in this work and one of the devices has also been modified with electrodeposited platinum, to enhance the analytical performance and compared results on all these surfaces with an "ideal" conventional Pt microdisk

electrode. The results from this work will help us to determine whether the low-cost miniaturised electrodes with RTILs can be employed in the design of cheap, portable and robust gas sensors for ammonia, and in particular, which electrode geometry and electrochemical technique is the most favourable for low-concentration detection of ammonia in RTILs.

4.2 Experimental

4.2.1 Chemical Reagents

All chemicals were commercially available and used as received. Ethanol (EtOH, 99 %, Sigma-Aldrich), acetone (99%, Sigma-Aldrich), sulfuric acid (98% w/w [18.4 M], Sigma-Aldrich) and zinc chloride ($ZnCl_2$, 40 % w/v, Sigma-Aldrich, used as a soldering flux for connecting wires with electrodes), chloroplatinic acid hydrate ($H_2PtCl_6.xH_2O$, anhydrous, trace metal basis, ≥ 99.9 %, Sigma-Aldrich), ferrocene ($Fe(C_5H_5)_2$, 98 % purity, Fluka) and tetra-*N*-butylammonium perchlorate (TBAP, 98 % purity, Sigma-Aldrich) were used as received. The room temperature ionic liquid (RTIL) 1-ethyl-3-methylimidazolium bis(trifluoromethylsulfonyl)imide ($[C_2mim][NTf_2]$, high purity grade), was purchased from Merck, Kilsyth, Victoria, Australia. Ultrapure water with a resistance of 18.2 MΩcm was prepared by an ultrapure water purification system (Millipore Pty Ltd., North Ryde, NSW, Australia). Acetone (>99.9 %, Sigma-Aldrich) was used for washing the electrodes before and after use. Ammonia gas cylinders (500 ppm and 50 ppm, in nitrogen) were purchased from CAC gases (Auburn, NSW, Australia). Nitrogen gas (for further dilution of NH_3) was obtained from a ≥ 99.99 % high purity compressed nitrogen cylinder (BOC gases, Welshpool, WA, Australia).

4.2.2 Electrochemical Experiments

All experiments were performed at laboratory room temperature (294±1 K) in a fume cupboard, inside an aluminium Faraday cage to reduce electrical interference. A PGSTAT101 Autolab potentiostat (Eco, Chemie, Netherlands) interfaced to a PC with Nova 1.11.2 software was employed. Platinum (Pt) thin-film electrodes (TFEs) and Pt microarray thin-film electrodes (MATFEs) were obtained from Micrux Technologies, Oviedo, Spain (ED-SE1-Pt and ED-mSE-10-Pt, respectively). The TFE and MATFE from Micrux have the same design (1mm diameter Pt working

electrode, Pt reference and Pt counter electrodes), except the working electrode of the MATFE is covered with a layer of SU-8 resin into which 90 μ-holes of 10 μm diameter are drilled to create 90 recessed microelectrodes. In both the TFE and MATFE, the Pt thin-film (150 nm thickness) was fabricated by thin-film technology on a Pyrex substrate. Pt screen-printed electrodes (SPEs) were obtained from DropSens, Spain (DRP-550), and consisted of a Pt-based WE (4 mm diameter), a Pt CE and a Ag quasi-RE. The screen-printed paste consists of conductive Pt particles, binding materials and solvents, but the manufacturer does not disclose the exact chemical composition.

The TFEs and MATFEs were electrochemically activated in 0.5 M $H_2SO_{4\ (aq)}$ by scanning the potential between -0.21 and +1.3 V (TFE), or -0.27 and + 1.4 V (MATFE) vs an external Ag/AgCl (0.1 M KCl) reference electrode (BASi, Indiana, USA) and Pt coil counter electrode (Goodfellow, Cambridge Ltd., UK) at a sweep rate of 500 mVs^{-1} for ca. 200 cycles. The electrodes were washed with ultrapure water and dried under a stream of nitrogen. The Pt SPE was used "as is" (without electrochemical activation or pre-treatment), as recommended by the manufacturer. The microholes of the MATFE were filled with Pt by depositing from a 5 mM solution of H_2PtCl_6 in 0.5 M H_2SO_4, starting from the open circuit potential, then holding the potential at -0.05 V (vs an external Ag/AgCl reference electrode and Pt wire counter electrode) for 300 seconds, under fast magnetic stirring to ensure a fast rate of mass transfer. For gas sensing experiments, the planar electrodes were placed into a modified rubber bung and inserted into the glass cell (a modified version of a T-cell).[26] 2 μL of RTIL was drop-cast on the TFE and MATFE, and 8 μL on the SPE. Prior to the introduction of ammonia gas, the cell was purged with nitrogen to remove dissolved gases and impurities. When the baseline was stable (after ca. 20 minutes), ammonia gas was introduced into the cell and continuously flowed over the electrode.

For experiments on the microdisk electrode, a conventional home-made Pt microelectrode (16.6 μm diameter) was employed. The electrode was polished on soft polishing pads (Buehler Illinois) with decreasing size of alumina powder (3 μm, 1 μm and 0.5 μm, Kemet, NSW, Australia). The diameter was calibrated electrochemically using 1mM ferrocene (deaerated) in acetonitrile with 0.1 M TBAP vs a silver wire reference electrode and a Pt coil counter electrode. A disposable

micropipette tip was fixed at the top of Pt microelectrode to provide a cavity into which 25 µL of [C_2mim][NTf_2] was placed. The electrode was housed in a specially designed glass T-cell[27, 28] with a Ag wire (combined counter and quasi-reference electrode) inserted in from the top. The cell was purged under vacuum (Edwards high vacuum pump, Model ES 50) for ca. 90 minutes to remove dissolved impurities (e.g. oxygen or water) present in the ionic liquid. When a clean blank voltammogram was obtained, ammonia gas was introduced into the cell.

4.2.3 Gas Mixing System

In order to obtain different concentrations of ammonia, cylinders of ammonia standards (500 ppm and 50 ppm, nitrogen fill), were diluted with nitrogen using a gas mixing system as reported previously by our group.[17, 26] This consists of two digital flow meters one for ammonia (0-1.0 L/min, John Morris Scientific, NSW, Australia), and one for nitrogen (0-10 L/min, Aalborg, New York USA), with a gas-mixing segment to increase turbulence and ensure adequate mixing of the gases. The relative flow rates were used to calculate the different concentrations of ammonia introduced into the T-cell. A sufficiently long time (ca. 25 minutes initially, and 10 mins between concentration changes) was left in order to ensure complete saturation of the gas in the ionic liquid and obtain a stable current. It is noted that the time for saturation may be less than this, but measuring response times will be the focus of future publications.

4.2.4 Electrode Imaging

Scanning electron microscopy (SEM) experiments were performed on the working electrodes of the three planar devices (TFE, SPE and MATFE), and on the filled MATFE. SEM Images were obtained using Zeiss Evo 40XVP model, with a voltage of 2.0 kV (see Figure 4.1). Atomic force microscopy (AFM) was performed using a Bruker FastScan instrument on the MATFE to image the geometry and depth of the μ-holes, and the filling of the μ-holes, and analysed using NanoScope analysis 1.5 software. The resolution of the instrument is up to 10 μm in height (Z-range, Icon AFM Scanner).

4.3 Results and Discussion

4.3.1 Characterisation of Electrode Surfaces Using SEM and AFM

In this study, three types of commercially available planar electrode devices (all with Pt working electrodes) have been employed - thin-film electrode (TFE), screen-printed electrode (SPE) and microarray thin-film electrode (MATFE), along with a modified MATFE (where Pt has been electrodeposited into the microholes to create almost inlaid electrodes), and a conventional microdisk electrode. Figure 4.1 shows scanning electron microscopy (SEM) images for the different electrode surfaces employed. It was not possible to obtain an image for the microdisk electrode due to its large size and inability to fit into the SEM machine.

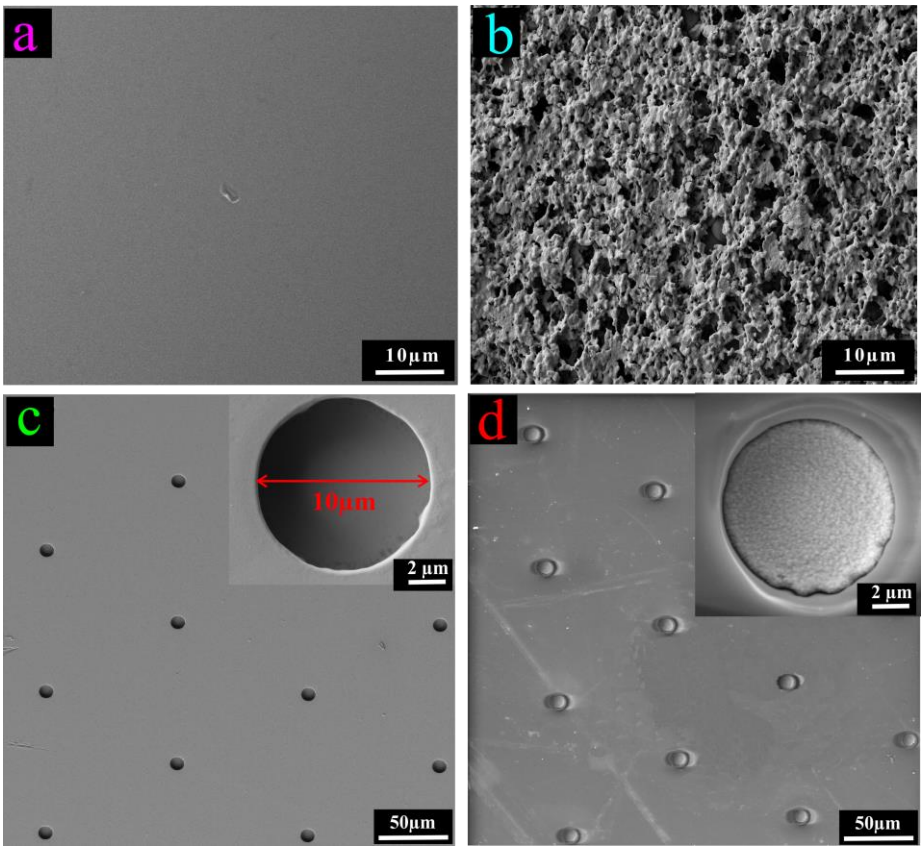

Figure 4.1: Scanning electron microscopy (SEM) images of a Pt (a) TFE, (b) SPE and (c) MATFE. The MATFE consists of a Pt TFE covered by an inert layer of SU-8 polymer with holes to create 90 recessed Pt microdisks (depth = 3±0.5 μm, diameter = 10 μm). Figure (d) shows close-up SEM images of a recessed microhole, and a filled microhole (holes were filled by electrodeposition from a solution of 5 mM H_2PtCl_6 in 0.5 M H_2SO_4).

The image on the TFE (Figure 4.1a) shows a very flat and smooth surface, which is highly beneficial for reproducible electrochemical experiments, and shows the high

quality of the manufacturing process. Atomic Force Microscopy (AFM) of these surfaces revealed some very small features on the surface, with heights of ca. 10 nm, and may be small defects from the Pt sputtering process or during packaging and transportation. In contrast, the SPE surface (Figure 4.1b) is very rough and porous, due to the electrode material being made of a mixture ("paste") of conductive Pt particles, polymeric binding materials and solvents, as reported previously.[26, 29] The height of the paste was out of the range of the AFM machine, indicating that it is > 10 μm thick. The MATFE (Figure 4.1c) has the same underlying Pt surface as the TFE, but it is covered with a layer of SU-8 polymer, into which 90 microholes of 10 μm in diameter are created, leaving 90 recessed electrodes; Figure 4.1c shows a section of the whole array. Depth profiling with AFM revealed that the thickness of the SU-8 layer was consistent across a single device, but varied between 2.6 and 3.4 μm on different electrodes (sample size of 5), which is within the manufacturer's statement of 3±0.5 μm. Figure 4.1d (top) shows a close-up image of one microhole of the MATFE, and Figure 4.1d (bottom) shows an image of one microhole that has been filled with electrodeposited Pt to create an almost inlaid electrode array. It is expected that the filled arrays will provide enhanced radial diffusion characteristics of analyte species towards the electrode, and will give improved analytical responses compared to the recessed MATFE. Details of the deposition process are shown in the experimental section and a small discussion is given below.

4.3.2 Deposition of Pt into the Microholes

In order to fill the microholes of the MATFE, the electrode was placed into a solution of 5 mM chloroplatanic acid (H_2PtCl_6) in 0.5 M H_2SO_4, and various deposition parameters were explored. Both pulse and constant potential deposition techniques were carried out, in line with literature reports for Pt nanoparticle deposition.[30-33] Constant potential deposition was chosen since it gave the most stable and reproducible deposits (noting that the overall size of the deposits was on the micrometer (not nanometer) scale, due to the size of the microholes). It was found that if the overpotential was too high, or the deposition time was too long, cauliflower-shaped deposits were obtained. During this process, the holes were observed to fill preferentially around (and then over) the edges of the pores, with less deposit in the centre of the pore. This will be explored in the next chapter. The final deposition parameters (given in the Experimental Section) involved holding at the

open circuit potential (OCP = 0.75 V), followed by deposition in the kinetically controlled region (-0.05 V vs Ag/AgCl) holding for 5 minutes, under fast magnetic stirring to ensure a fast rate of mass transfer and to produce controlled growth of the nucleation sites. AFM revealed that the hole was uniformly filled from the centre to the edges, up to a depth of ca. 0.9 μm below the surface (noting that the diameter of the pores is 10 μm). This amount of filling was enough to produce the desired radial diffusion characteristics (see Figure 4.3).

4.3.3 Electrochemical Oxidation Mechanism for Ammonia on the Planar Electrode Devices

The RTIL [C_2mim][NTf_2] was chosen as the solvent/electrolyte in this work due to its wide electrochemical window (> 4.5 V), good chemical and thermal stability, high intrinsic conductivity and lowest viscosity of the RTILs available in our laboratory. The electrochemical response for ammonia oxidation in this RTIL (at higher concentrations) has also been well studied.[15-17] Before undertaking analytical studies on the new planar electrode devices employed in this work, the electrochemical reaction mechanism for ammonia should first be understood. It is noted here that there was a different mechanism for oxygen reduction in [C_2mim][NTf_2] on DropSens Pt screen-printed electrodes (compared to conventional Pt macrodisk electrodes).[26] This was suggested to be a reaction of the electrogenerated superoxide with the imidazolium cation, catalysed by compounds present in the paste of the SPE. However, no unusual reaction was observed to take place for oxygen on Pt TFEs[34] and MATFEs.[21] For ammonia, the mechanism on SPEs was found to be the same as on conventional Pt electrodes in previous work,[17] but the behaviour on TFEs and MATFEs has not yet been reported.

Figure 4.2 shows cyclic voltammograms (CVs) at 100 mVs^{-1} for the oxidation of 500 ppm ammonia on the five Pt electrodes employed in this study: (a) TFE, (b) SPE, (c) µ-disk electrode, (d) recessed MATFE and (e) filled MATFE. In all figures, the dashed red line is the blank CV in the absence of ammonia. According to the number of peaks present in the CVs in Figure 4.2, the mechanism for ammonia oxidation on all surfaces appears to be the same as that reported previously.[15, 16] Firstly, there is a single broad oxidation peak/process between 0.9 to 2.0 V labelled as peak I, followed by two reduction processes, peak II (ca. 0.0 to -0.5 V) and peak III (ca. -0.5 V to -1.0

V), followed by an oxidation peak IV (ca. -0.5 to 0.0 V). It is noted that the variation in ammonia oxidation peak potential is likely to be due to the different (integrated) quasi-reference electrodes employed. The identities of the peaks are described by the following equations:[15, 16]

Peak (I) $$NH_3(g) + 3A^- \rightarrow \frac{1}{2}N_2(g) + 3HA + 3e^- \quad \textbf{(4.1)}$$

Where A^- = the RTIL anion ($[NTf_2]^-$). The mechanistic study of ammonia oxidation in RTILs shows that, the proton produced as a result of oxidation of ammonia is solvated by anion of RTIL to form HA which is in equilibrium reaction with another molecule of ammonia.[35]

$$HA + NH_3(g) \rightleftharpoons NH_4^+ + A^- \quad \textbf{(4.2)}$$

Two reduction processes can then occur: the reduction of HA (eq 4.3) or the reduction of NH_4^+ (eq 4.4).

Peak (II) $$HA + e^- \rightarrow A^- + H_{(ads)} \quad \textbf{(4.3)}$$

Peak (III) $$NH_4^+ + e^- \rightarrow NH_3(g) + H_{(ads)} \quad \textbf{(4.4)}$$

Peak IV on the reverse oxidative sweep is believed to be the oxidation of the electrogenerated adsorbed proton.[15, 16]

Peak (IV) $$H_{(ads)} \rightarrow H^+ + e^- \quad \textbf{(4.5)}$$

The shape of all the voltammograms in Figure 4.2 is similar to that reported previously at higher concentrations of ammonia on microdisk and screen-printed electrodes.[15-17] Peak-shaped oxidation waves were observed on the macro-sized TFE and SPE electrodes, consistent with predominantly linear diffusion occurring at these surfaces. In contrast, a steady-state oxidation wave was obtained on the micron-sized electrodes (recessed and filled MATFEs and Pt μ-disk electrode) due to the increased contribution from radial diffusion. While the response reaches an ideal steady-state plateau on the μ-disk electrode, the response on the recessed MATFE shows a steady-state current response that continues to rise after the plateau. The behaviour of the filled MATFE is somewhere in between, indicating that the holes are almost filled to create inlaid electrodes, but there may be some non-uniformity to the platinum deposit (e.g. holes/pores). A slanted plateau is also observed on nanoarray electrodes in liquid/liquid electrochemistry experiments,[36, 37] and although the exact

reason is unclear, it could be due to the nature of the electrode array (as opposed to a single electrode), and overlapping diffusion profiles. However, we note that this behaviour was not observed for a more "ideal" redox couple (1mM ferrocene in acetonitrile with 0.1 M TBAP, (results are not shown)) on the MATFE, where true steady-state behaviour was obtained.

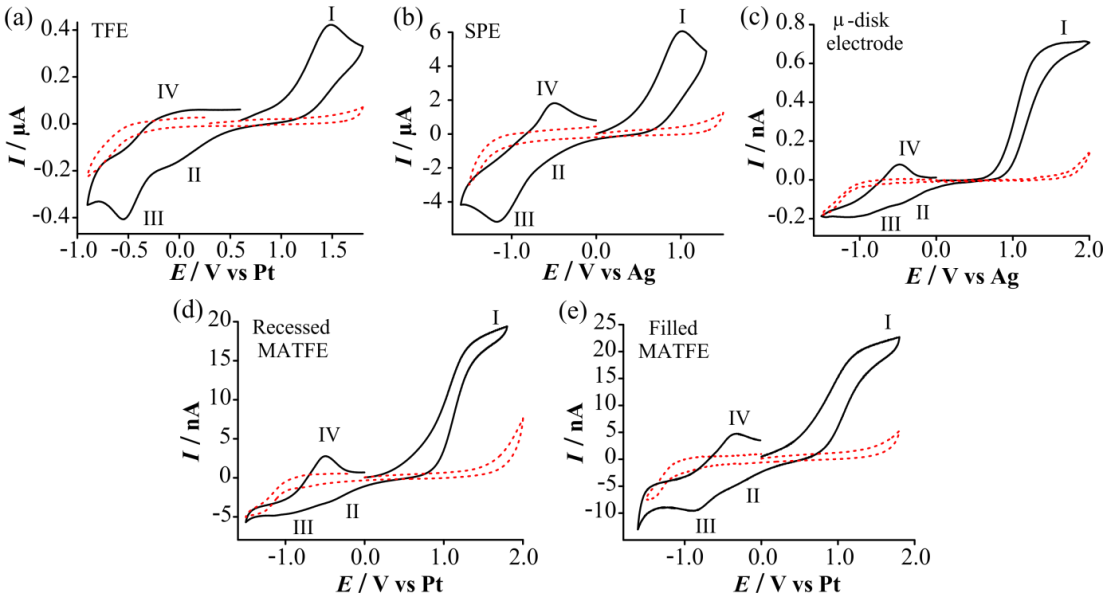

Figure 4.2: Cyclic voltammetry for 500 ppm ammonia oxidation in $[C_2mim][NTf_2]$ on a Pt (a) TFE (diameter 1mm), (b) SPE (diameter 4 mm), (c) μ-disk electrode (diameter 16.6 μm), (d) MATFE (90 recessed electrodes, diameter 10 μm), (e) MATFE with the recessions filled with electrodeposited Pt. Dashed red line is the response in the absence of ammonia. Scan rate 100 mVs^{-1}.

4.3.4 Current Density Comparison

In order to compare the oxidation of ammonia at Pt electrodes of varying size, the current density (*J*) was calculated from the oxidation peak current divided by the electrode area. Figure 4.3 shows a plot of *J* for 500 ppm ammonia on the five different electrodes. *J* is the smallest for the larger electrodes (1 mm diameter TFE and 4 mm diameter SPE) due to the predominantly linear diffusion occurring at these surfaces. *J* for the μ-disk electrode is significantly higher, as expected due to the faster rate of mass transport (radial diffusion) to micron-sized electrodes.[38]

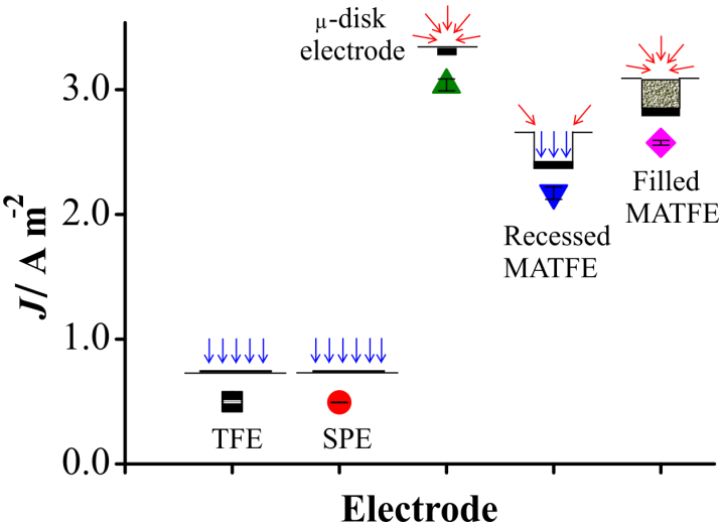

Figure 4.3: Current density (*J*) plot for the oxidation of 500 ppm ammonia in [C_2mim][NTf_2] on a Pt: TFE (■), SPE (●), *μ*-disk electrode (▲), recessed MATFE (▼) and filled MATFE (◆). Sketches of the expected diffusion processes (linear, radial and linear and radial combined) based on the electrode geometry are also shown. Error bars are small, and represent 1 standard deviation (n=4).

However, *J* for the recessed MATFE is lower than the *μ*-disk electrode, even though the diameter of each recessed electrode is smaller than the *μ*-disk electrode diameter. One explanation for this could be the contribution from linear diffusion within the pores, which lowers the current response, as expected for recessed electrodes.[39, 40] However, even when the pores are filled to create almost inlaid electrodes (filled MATFE in Figure 4.3), *J* is still not as high as expected. This points to the possibility that the geometry of the array is not fully optimised, giving rise to the overlapping of diffusion layers and reducing the expected current. This is consistent with our observations for oxygen reduction on the same MATFE devices.[21] Based on the plot in Figure 4.2, it is expected that the micron-sized electrodes will provide a better resolution of peak currents at very low concentrations of analyte, so therefore the analytical response of these electrodes was further studied.

4.3.5 Analytical Response for Ammonia on the Planar Electrode Devices

To study the ability for these electrodes to detect ammonia, the analytical utility and sensitivity for ammonia in [C_2mim][NTf_2] was investigated. Two electrochemical techniques (linear sweep voltammetry (LSV) and potential-step chronoamperometry (PSCA)) were carried out on the five different Pt surfaces, to identify what technique and which electrode is the most sensitive towards low (ppm) concentrations of ammonia gas.

4.3.5.1 Linear Sweep Voltammetry

Figure 4.4 shows linear sweep voltammetry (LSV) for the oxidation of 10-100 ppm of ammonia in $[C_2mim][NTf_2]$ on a Pt (a) TFE, (b) SPE, (c) μ-disk electrode (d) recessed MATFE and (e) filled MATFE at a scan rate of 100 mVs^{-1}. The response in the absence of ammonia is shown as a dashed red line. The insets show the corresponding calibration plots of oxidation current (baseline corrected) *vs* gas-phase concentration of ammonia. In this lower concentration range, peak-shaped behaviour was still observed on the larger TFE and SPE devices. Steady-state behaviour was observed on the μ-disk electrode (Figure 4.4c), a slanted steady-state response on the recessed MATFE (Figure 4.4d), and a more ideal steady-state response on the filled MATFE (Figure 4.4e). On all of the electrodes, the response at 10 ppm ammonia was clearly distinct from the blank response, which is highly encouraging from an analytical perspective. The calibration graphs showed excellent linearity (R^2 > 0.998), with a slightly more curved response on the SPE.

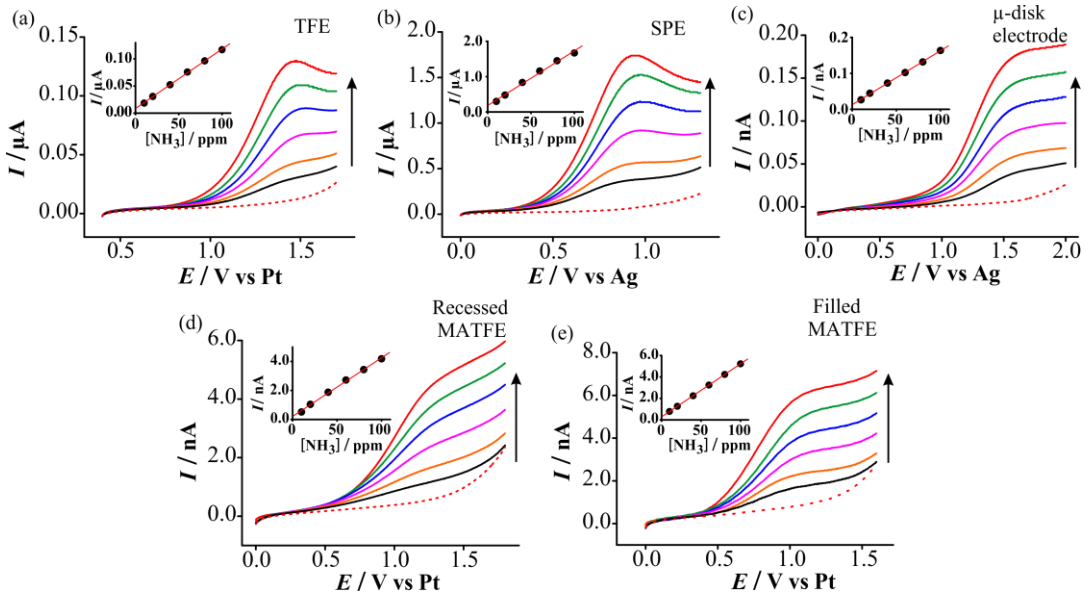

Figure 4.4: Linear sweep voltammetry (LSV) for the oxidation of ammonia (10-100 ppm) in $[C_2mim][NTf_2]$ on a Pt (a) TFE, (b) SPE, (c) μ-disk electrode (diameter 16.6 µm), (d) recessed MATFE (90 electrodes, diameter 10 μm, depth 3±0.5 μm), (e) MATFE with the recessions filled with electrodeposited Pt at a scan rate of 100 mVs^{-1}. Dotted line is the response in the absence of ammonia. Currents on the recessed MATFE were measured from a fixed potential of 1.4 V, due to the absence of a limiting current plateau. The insets show calibration plots of peak current (baseline corrected) vs concentration, along with the line of best fit.

Table 4.1 shows the analytical parameters resulting from the calibration graphs in Figure 4.4. The data was highly reproducible on several days (n=4) with error bars (1

standard deviation) that were <4 % on all surfaces. Sensitivities were calculated from the gradient of the line of best fit and limits of detection (LODs) were calculated using three times the standard deviation of the slope of the line of best fit, over the concentration range studied. The sensitivities were higher on the larger surfaces, as expected. Importantly, the sensitivity of the filled MATFE was > 20 % greater than for the recessed MATFE, indicating that filling the holes is beneficial from an analytical perspective. The LODs on all surfaces (0.3 to 9.2 ppm) were well below the OSHA PEL for ammonia (25 ppm), and this could further be lowered by studying a lower concentration range, as discussed later. The most important observation from Table 4.1 is that the recessed and filled MATFEs give the lowest LODs, and therefore these electrodes have been chosen to detect ammonia at even lower concentrations (see section 4.3.6).

4.3.5.2 Potential-Step Chronoamperometry

Under the same experimental conditions as for LSV, potential-step chronoamperometry (PSCA) was also carried out. Figure 4.5 shows PSCA transients for 10-100 ppm ammonia oxidation in $[C_2mim][NTf_2]$ on a Pt (a) TFE, (b) SPE, (c) μ-disk electrode, (d) recessed MATFE and (e) filled MATFE. The red dotted line is the response in the absence of ammonia. The potential was stepped from 0 V to an appropriate value after the peak (or on the current plateau), and measured for 10 seconds. For simplicity, the current response was measured as an average of the last 100 milliseconds of the transient. The corresponding calibration graphs (baseline corrected current vs concentration) are shown in the insets of the figures, and excellent linearity was observed, with $R^2 > 0.999$.

The transients for the larger TFE and SPE surfaces (Figure 4.5a and 4.5b) show typical Cottrellian behaviour,[41] where I is $\propto D^{1/2}$. In comparison, the current transients for the Pt μ-disk electrode (Figure 4.5c) have two different time regimes, where I is $\propto D^{1/2}$ at short times and I is $\propto D$ at longer times, described by the Shoup and Szabo expression.[40] We note that the experimental data on the μ-disk electrode was attempted to be fitted to the Shoup and Szabo expression,[40] but was unsuccessful due to the complicated mechanism, consistent with a previous report.[16] The shape of the transients on the recessed MATFE (figure 4.5d) are similar to that on the μ-disk electrode, but there is a much more abrupt change in current between the two time

regimes. This behaviour has been reported to be due to the recessed nature of the working electrode.[37, 39] The transient on the filled MATFE is somewhere in between the μ-disk electrode and the recessed MATFE, consistent with the shapes of the LSV in Figure 4.4.

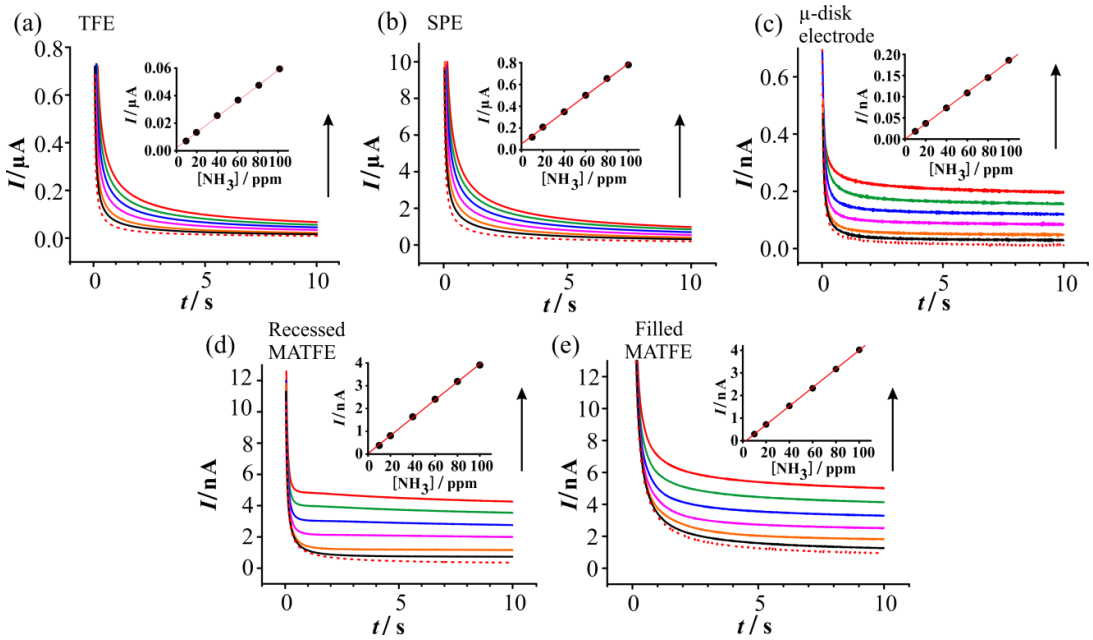

Figure 4.5: Potential-step chronoamperometry (PSCA) for the oxidation of ammonia (10-100 ppm) in [C_2mim][NTf_2] on a Pt (a) TFE, (b) SPE, (c) μ-disk electrode, (d) recessed MATFE and (e) filled MATFE. The potential was stepped from 0 to (a) + 1.6 V, (b) + 1.1 V, (c) + 1.9 V, (d) + 1.5 V and (e) 1.4 V. Dotted line is the response in the absence of ammonia. The insets are the corresponding calibration plots of current (averaged over the last 10 data points) vs concentration, along with the line of best fit.

Table 4.1: Analytical parameters (sensitivity and limit of detection, LOD) calculated for ammonia oxidation (10-100 ppm) on different Pt electrodes using linear sweep voltammetry (LSV) and potential-step chronoamperometry (PSCA). Data obtained from the 0.1-2 ppm range is also included for the MATFEs.

Electrode	LSV		PSCA	
	Sensitivity / $Appm^{-1}$	LOD / ppm	Sensitivity / $Appm^{-1}$	LOD / ppm
TFE	1.1×10^{-9}	2.7	5.6×10^{-10}	2.5
SPE	1.6×10^{-8}	9.2	7.4×10^{-9}	4.5
μ-disk electrode	1.5×10^{-12}	2.7	1.8×10^{-12}	2.5
Recessed MATFE	4.0×10^{-11}	2.0 (0.11)*	4.0×10^{-11}	2.1
Filled MATFE	4.9×10^{-11}	0.3 (0.02)*	4.1×10^{-11}	1.5

* calculated from the calibration graph at the 0.1-2 ppm range.

The analytical parameters obtained from the PSCA experiments are shown in Table 4.1. The sensitivities were highest on the larger electrodes, and lowest on the (single) μ-disk electrode. There was some improvement in the LODs using PSCA compared to LSV, except on the MATFEs, where LSV was slightly superior. For PSCA, the LODs on all surfaces (1.5 to 4.5 ppm) were significantly lower than the permissible exposure limit of 25 ppm for ammonia.

4.3.6 Low concentration study on recessed and filled MATFEs using LSV

Since LSV on the recessed and filled MATFEs gave the lowest LODs, this technique and these electrodes were used for further studies at lower concentrations to examine the true limit of detection. Figure 4.6 shows linear sweep voltammetry for the oxidation of ammonia from 0.1 to 2 ppm, with the response in the absence of ammonia shown as the red dotted line. Plots of current vs concentration are shown as insets to the figure. Even at concentrations of less than 1 ppm, the response for ammonia oxidation is clearly distinct from the blank response. In contrast, on the larger electrodes (TFE and SPE), current responses at this concentration were much more difficult to observe above the noise. Additionally, the current on the (single) microdisk electrode was extremely small and too low to measure accurately with the standard potentiostat.

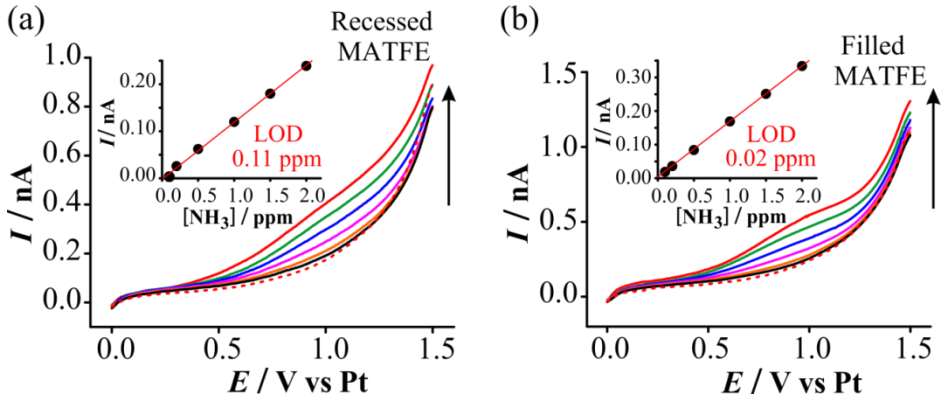

Figure 4.6: LSV for the oxidation of ammonia in [C_2mim][NTf_2] at low concentrations (0.1 to 2 ppm) on a Pt (a) recessed MATFE and (b) filled MATFE. The red dotted line is the response in the absence of ammonia. The insets show calibration plots of peak current (baseline corrected) vs concentration, along with the line of best fit.

The shape of the voltammetry is clearly more steady-state like on the filled MATFE (Figure 4.6b) compared to the recessed MATFE (Figure 4.6a) at these low concentrations, and the current is also larger (higher sensitivity), supporting the

suggestion of the larger contribution from radial diffusion on the filled MATFE. This increased sensitivity has resulted in an improvement in the LOD for ammonia from 0.11 ppm (recessed MATFE) to 0.02 ppm (filled MATFE). This is a very significant result, since these LODs are one order of magnitude lower than that reported previously for ammonia in ionic liquids,[18-20] and opens up the possibility to use these cheap planar electrode devices for trace detection of ammonia gas at concentrations much less than 1 ppm. It is noted that ppb detection limits have been reported previously for ammonia using a low-cost chemoresistive sensor based on single-walled carbon nanotubes,[42] but this is believed to be the first time that ammonia has been detected at such low concentrations using an amperometric technique.

4.4 Conclusions

The electrochemical oxidation ammonia has been studied in $[C_2mim][NTf_2]$ on four different types of Pt planar electrode devices (three commercially-available and one modified surface), with the reaction mechanism appearing to be the same as on conventional μ-disk electrodes. Current density was the smallest on the large TFE and SPE surfaces, but much higher on the μ-disk and MATFE surfaces. Calibration graphs obtained from 10-100 ppm ammonia were linear on all surfaces, with the lowest LODs found on the filled and recessed MATFEs using linear sweep voltammetry. These electrodes were subsequently used to investigate even lower concentrations from 0.1 to 2 ppm, giving the lowest limits of detection for ammonia in ionic liquids to date (20 ppb on the filled MATFE). Not only were all of the electrodes able to easily detect concentrations lower than the permissible exposure limit (25 ppm), but the filled MATFE was capable of detecting sub ppm concentrations, opening up the possibility of using ionic liquids and planar electrode devices for accurate monitoring of ammonia at trace concentrations.

References

1. G. Hussain and D. S. Silvester, *Anal. Chem.*, 2016, **88**, 12453-12460.
2. B. Timmer, W. Olyhuis and A. van den Berg, *Sens. Act. B*, 2005, **107**, 666-677.
3. X. Liu, S. Cheng, H. Liu, S. Hu, D. Zhang and H. Ning, *Sensors*, 2012, **12**, 9635-9665.
4. E. Bakker, *Anal. Chem.*, 2004, **76**, 3285-3298.
5. F. Opekar and K. Stulik, *Journal*, 2009, 1-24.
6. L. Xiong and R. G. Compton, *Int. J. Electrochem. Sci.*, 2014, **9**, 7152-7181.
7. M. C. Buzzeo, C. Hardacre and R. G. Compton, *Anal. Chem.*, 2004, **76**, 4583-4588.

8. X.-J. Huang, L. Aldous, A. M. O 'Mahony, F. J. del Campo and R. G. Compton, *Anal. Chem.*, 2010, **82**, 5238-5245.
9. S.-Q. Xiong, Y. Wei, Z. Guo, X. Chen, J. Wang, J.-H. Liu and X.-J. Huang, *J. Phys. Chem. C*, 2011, **115**, 17471-17478.
10. J. Gębicki, A. Kloskowski, W. Chrzanowski, P. Stepnowski and J. Namiesnik, *Crit. Rev. Anal. Chem.*, 2016, **46**, 122-138.
11. A. Rehman and X. Zeng, *RSC Adv.*, 2015, **5**, 58371-58392.
12. D. S. Silvester, *Analyst*, 2011, **136**, 4871-4882.
13. D. S. Silvester and L. Aldous, in *Electrochemical Strategies in Detection Science*, ed. D. W. M. Arrigan, RSC, Cambridge, UK, 2016.
14. L. E. Barrosse-Antle, A. M. Bond, R. G. Compton, A. M. O 'Mahony, E. I. Rogers and D. S. Silvester, *Chem. Asian J.*, 2010, **5**, 202-230.
15. M. C. Buzzeo, D. Giovanelli, N. S. Lawrence, C. Hardacre, K. R. Seddon and R. G. Compton, *Electroanal.*, 2004, **16**, 888-896.
16. X. Ji, D. S. Silvester, L. Aldous, C. Hardacre and R. G. Compton, *J. Phys. Chem. C*, 2007, **111** 9562–9572.
17. K. Murugappan, J. Lee and D. S. Silvester, *Electrochem. Commun.*, 2011, **13**, 1435-1438.
18. M. T. Carter, J. R. Stetter, M. W. Findlay and V. Patel, *ECS Trans.*, 2012, **50**, 211-220.
19. M. T. Carter, J. R. Stetter, M. W. Findlay and V. Patel, *ECS Trans.*, 2014, **64**, 95-103.
20. J. F. M. Oudenhoven, W. Knoben and R. van Schaijk, *Procedia Eng.*, 2015, **120**, 983-986.
21. J. Lee and D. Silvester, S., *Analyst*, 2016, **141**, 3705–3713.
22. J. Wang, *Electroanal.*, 2007, **19**, 415-423.
23. A. Heller and B. Feldman, *Chem. Rev.*, 2008, **108**, 2482–2505.
24. X. Pang, M. D. Shaw, A. C. Lewis, L. J. Carpenter and T. Batchellier, *Sens. Act. B*, 2017, **240**, 829-837.
25. K. Malzahn, J. R. Windmiller, G. Valdes-Ramirez, M. l. J. Schoning and J. Wang, *Analyst*, 2011, **136**, 2912-2917.
26. J. Lee, K. Murugappan, D. W. M. Arrigan and D. S. Silvester, *Electrochim. Acta*, 2013, **101**, 158-168.
27. D. S. Silvester, L. Aldous, C. Hardacre and R. G. Compton, *J. Phys. Chem. B*, 2007, **111**, 5000-5007.
28. D. S. Silvester, A. J. Wain, L. Aldous, C. Hardacre and R. G. Compton, *J. Electroanal. Chem.*, 2006, **596**, 131-140.
29. J. Lee, D. W. M. Arrigan and D. S. Silvester, *Anal. chem.*, 2016, **88**, 5104-5111.
30. J. J. Burk and S. K. Buratto, *J. Phys. Chem. C*, 2013, **117**, 18957−18966.
31. S. Domínguez-Domínguez, J. Arias-Pardilla, A. Berenguer-Murcia, E. Morallón and D. Cazorla-Amorós, *J. Appl. Electrochem.*, 2008, **38**, 259-268.
32. S. Kim, Y. Kwon, Y. Jung and S.-J. Park, *Solid State Phenomena*, 2007, **124-124**, 1039-1042.
33. H. M. Yasin, G. Denuault and D. Pletcher, *J. Electroanal. Chem.*, 2009, **633**, 327-332.
34. J. Lee, G. Du Plessis, D. Arrigan, W. M. and D. Silvester, S., *Anal. Methods*, 2015, **7**, 7327-7335.
35. X. Ji, C. E. Banks, D. S. Silvester, L. Aldous, C. Hardacre and R. G. Compton, *Electroanal.*, 2007, **19**, 2194 – 2201.
36. Y. Liu, M. Sairi, G. Neusser, C. Kranz and D. Arrigan, W. M., *Anal. Chem.*, 2015, **87**, 5486−5490.
37. M. Sairi, J. Strutwolf, R. A. Mitchell, D. S. Silvester and D. W. M. Arrigan, *Electrochim. Acta*, 2013, **101**, 177-185.
38. R. G. Compton and C. E. Banks, *Understanding Voltammetry*, World Scientific: Singapore, 2007.

39. A. M. Bond, D. Luscombe, K. B. Oldham and C. G. Zoski, *J. Electroanal. Chem. Interfacial Electrochem.*, 1988, **249**, 1-14.
40. D. Shoup and A. Szabo, *J. Electroanal. Chem. Interfacial Electrochem.*, 1982, **140**, 237-245.
41. R. G. Compton and C. E. Banks, *Understanding Voltammetry*, World Scientific, Singapore, 2007.
42. X. Wang, G. Li, R. Liu, H. Ding and T. Zhang, *J. Mater. Chem.*, 2012, **22**, 21824-21827.

Chapter 5

5. Pt 2D Nanostructured and 3D Cauliflower Decorated Microarrays for Ammonia Sensing in RTILs

In the previous chapter, it was found that 'filled' recessed MATFEs gave a higher current response and larger current density compared to recessed MATFEs. In this chapter we will further decorate the μ-holes of MATFEs with Pt-deposits of various sizes and shapes to go from 2D nanostructured deposits to 3D cauliflower deposits. These modified electrodes will be employed for ammonia sensing in RTILs.

5.1 Introduction

The nature of the sensing surfaces is of great attention in many practical applications including sensors,[1-4] dye-sensitized solar cells,[5, 6] fuel cells,[7-9] batteries,[9-11] and supercapacitors.[9, 12] Different materials with large surface area have been employed to enhance the sensitivity of the surface, including noble metal nanoparticles (platinum, gold, silver), [13-15] semiconductor nanoparticles (zinc oxide, tin oxide), [13, 16] and carbon materials such as carbon nanotubes.[17-19] Over the last decade, nanostructures with different shapes and geometries such as nanowires,[20, 21] nanorods,[22, 23] mesoporous,[24, 25] and dendritic structures [26, 27] are reported to have great importance in many fields. Recently nanostructures with two-dimensional (2D) and three-dimensional (3D) architectures have received significant attention due to their large electroactive surface area, excellent conductivity, and efficient electrocatalytic ability.[28-30] To date, significant progress has been made to produce 2D and 3D nanostructures with different shapes, geometries and morphologies such as nanoflowers, nanopetals, nanourchins, cauliflowers, raspberries etc.[31-35]

Different strategies have been employed to grow these 2D and 3D shaped nanostructures with various sizes, shapes, and densities.[31] The most commonly used methods are chemical vapor deposition (CVD), physical vapor deposition (PVD), galvanic displacement, and electrodeposition.[33] Kong *et al*. produced nanocube-aggregated cauliflower-like copper hierarchical 3D nanostructures by electroless deposition and used the deposits to study the electrocatalytic reduction of oxygen.[30]

Zhang *et al*. developed a thin film of 3D hierarchical ZnO nanostructures with different shapes such as nanourchins and nanoflowers using a simple hydrothermal approach, and employed these for photocatalytic studies of organic dyes.[36] Chen *et al*. synthesized 3D shaped nanoflowers of tin oxide semiconductor by using thermal pyrolysis of a tin organometallic precursor.[37] Nizhad *et al*. produced gold nanostructures of various shapes and geometries on semiconductor wafer such as indium phosphide and gallium arsenide via galvanic displacement reactions.[38] Tiwari *et al*. electrodeposited Pt-nanopetals onto highly ordered silicon nanocones using anodized aluminium as a template, and used this for the electrocatalytic oxidation of methanol in fuel cell applications.[39] All these nanostructures with 2D or 3D architectures either involve semiconductor materials or expensive fabrication techniques (CVD or PVD), or complicated methodologies to produce modified surfaces.

Electrodeposition is a highly competitive alternative technique compared to those described above, due to its simplicity, relatively low cost, low power consumption capacity, and a wide range of controllable parameters to produce the desired size of nanostructures (e.g. pure metals) with large electroactive surface areas. Noble metals typically produce deposits including dendritic nanostructures or sphere-like nanoparticles. There are very limited studies on the direct electrodeposition of pure noble metals (e.g. platinum or gold) into 3D nanostructures in a single step. Jayashree *et al*. prepared silicon-based membrane electrodes by the electrodeposition of pure Pt and Pd into dendritic and spherical shapes for the electrocatalytic oxidation of formic acid in micro fuel cells.[40] The concentration of metal precursor is also thought to affect the morphology of the deposits. In general, a low concentration of noble metal precursor produces nanoparticles, while a higher concentration produces dendritic shaped nanostructures.[31] In the previous chapter, we showed that 'filled' recessed microarrays with Pt-deposits give a higher current response than unmodified microarrays.[41] During the filling of the μ-holes, we found that we can fill the μ-holes with Pt-deposits of different shapes and geometries due to competing diffusion regimes (linear and radial) of precursor into the μ-holes,. In this chapter, we will expand the electrodeposition process to produce Pt-deposits of various shapes and thickness. This will produce 2D nanostructures and 3D cauliflowers in a single step to fill the μ-holes of microarray thin film electrodes (MATFEs). Finally, we will

incorporate these decorated microarrays for the sensing of ammonia gas in room temperature ionic liquids (RTILs).

5.2 Experimental

5.2.1 Chemical Reagents

All chemicals were commercially available and used as received. Ethanol (EtOH, 99%, Sigma-Aldrich), acetone (99% purity, Sigma-Aldrich), sulfuric acid (98% w/w [18.4 M], Sigma-Aldrich) and zinc chloride ($ZnCl_2$, 40% w/v, Sigma-Aldrich, used as a soldering flux for connecting wires with electrodes), chloroplatinic acid hydrate ($H_2PtCl_6.xH_2O$, anhydrous, trace metal basis, ≥ 99.9 %, Sigma Aldrich), were used as received. The room temperature ionic liquids (RTILs) 1-ethyl-3-methylimidazolium bis(trifluoromethylsulfonyl)imide ($[C_2mim][NTf_2]$), was purchased from Merck, Kilsyth, Victoria, Australia, at ultra-high purity electrochemical grade. The RTIL was used as received. Ultrapure water with a resistance of 18.2 MΩcm was prepared by an ultrapure water purification system (Millipore Pty Ltd., North Ryde, NSW, Australia). Acetonitrile (MeCN, >99.8%, Fischer Scientific) was used for washing the electrodes before and after use. Ammonia gas cylinders (500 ppm, in nitrogen) were purchased from CAC gases (Auburn, NSW, Australia). Nitrogen gas (for further dilution of NH_3) was obtained from a ≥ 99.99 % high purity, compressed nitrogen cylinder (BOC gases, Welshpool, WA, Australia).

5.2.2 Electrochemical Experiments

All experiments were performed using a PGSTAT101 Autolab potentiostat (Eco, Chemie, Netherlands) interfaced to a PC with Nova 1.10 software, at laboratory room temperature (294±1 K) inside an aluminium Faraday cage present in the fume cupboard to reduce electrical interference. Platinum (Pt) microarray thin-film electrodes (MATFEs) were obtained from Micrux Technologies, Oviedo, Spain (ED-mSE1-Pt). The MATFE from Micrux is a three electrodes setup, having 1 mm diameter of Pt working electrode, Pt counter and Pt reference electrodes on a Pyrex glass substrate. The working electrode of the MATFE is covered with a layer of SU-8 resin into which 90 μ-holes of 10 μm diameter are drilled to create 90 recessed microelectrodes. The center-to-center distance of the μ-holes is 100±1 μm (10× the

diameter). In MATFE, the Pt thin-film (150 nm thickness) was fabricated by thin-film technology on a Pyrex substrate which is also covered with a layer of SU-8 resin except the connection points, to delimit the electrochemical cell and thus to enable the use of very small volumes of RTILs.

Before gas sensing experiments, the recessed μ-holes are filled with Pt-deposits of various thickness and shapes from 2D Pt-nanostructures to 3D Pt-cauliflowers. During the deposition process, different parameters were considered such as the concentration of Pt complex, deposition potential, rate of mass transfer, and deposition time. Prior to filling of μ-holes, the MATFEs were electrochemically activated in 0.5 M $H_2SO_{4\,(aq)}$ by scanning the potential between -0.27 and + 1.4 V vs an external Ag/AgCl (0.1 M KCl) reference electrode (BASi, Indiana, USA) and Pt coil counter electrode (Goodfellow, Cambridge Ltd., UK) at a sweep rate of 500 mVs^{-1} for ca. 300 cycles. The electrodes were washed with ultrapure water and dried under nitrogen stream. The μ-holes of the MATFE were filled with Pt-deposits using 5 mM or 20 mM solution of N_2-saturated H_2PtCl_6 in 0.5 M H_2SO_4. The electrochemical deposition of Pt involved holding at the open circuit potential (OCP, ~0.75 V), then applying a potential at two different regions (vs stable Ag/AgCl reference electrode): (i) underpotential (-0.025, -0.05 V) to kinetically control the nucleation and growth of Pt,[42-44] and (ii) overpotential (-0.2 V) to produce instant nucleation and growth of Pt-deposits of various thickness and shapes.[31, 44-47] Deposition times of 300 or 600 seconds were employed, under either no stirring or a fast rate of magnetic stirring to control the desired rate of mass transfer. Thus in order to study the effect of the different electrochemical parameters, four different electrochemical procedures were adopted and the resulting modified electrodes were named: (a) 'partially filled' MATFE, (b) 'half-filled' MATFE, (c) 'cauliflower A' MATFE, and (d) 'cauliflower B' MATFE. The detailed procedures are given below.

Procedure 1: For 'partially filled' MATFEs where Pt-deposits only partially fill the μ-holes, a stirred N_2-saturated solution of 5 mM H_2PtCl_6 in 0.5 M H_2SO_4 was used. Constant-potential deposition (CPD) was employed, stepping the potential from the OCP (0.75 V) to the underpotential region at -0.05 V,[43, 48] at the start of the second reduction peak, for 300s. The nucleation and growth of Pt-deposits is under kinetic control at this potential, and strong magnetic stirring was employed to ensure a fast rate of mass transfer.

Procedure 2: The same solution as used in procedure 1 was employed. A two-step deposition was employed to achieve 'half-filled' MATFEs with 2D Pt-nanostructures that approximately half-fill the μ-holes. The first step was the same as procedure 1. In the second step, the potential was stepped to a less negative potential (-0.025 V) compared to the first step, and was held for an additional 300 seconds grow the Pt-deposits in a controlled manner, under fast magnetic stirring.

Procedure 3: For 'cauliflower A' MATFEs, a N_2 saturated solution of 20 mM H_2PtCl_6 in 0.5 M H_2SO_4 was used. A single step was employed by using constant-potential deposition (CPD) from the OCP (0.75 V) to an overpotential (-0.2 V) for 300 seconds. Instantaneous nucleation and growth of the Pt-deposits occurred,[46] forming cauliflower type structures. The solution was unstirred to ensure only a moderate flux rate.

Procedure 4: For 'cauliflower B' MATFEs, the protocol was the same as procedure 3, except the deposition was carried out under strong magnetic stirring to ensure a fast flux rate and a larger size of deposit.

Prior to starting gas sensing experiments, the 2D or 3D Pt-deposited MATFEs were electrochemically activated in 0.5 M H_2SO_4 (aq) by scanning the potential between -0.27 and +1.4 V vs. an external Ag/AgCl (0.1 M KCl) reference electrode (BASi, Indiana, USA) and Pt coil counter electrode (Goodfellow, Cambridge Ltd., UK) at a sweep rate of 500 mVs^{-1} for ca. 5 cycles to ensure there was no oxide layer or chloride ions (Cl^-) adsorbed on the active sites.[43] The electrochemical surface area (ESA) of the Pt-deposited MATFEs was calculated from the area under hydrogen adsorption/desorption peaks using standard methods.[43, 49]

For gas sensing experiments, the Pt-deposited MATFEs were placed into a modified rubber bung and inserted into the glass cell (a modified version of a T-cell).[50-52] 2 μL of RTIL was drop-cast on the Pt-deposited MATFEs. Prior to the introduction of ammonia, the cell was purged with nitrogen to remove dissolved gases and impurities. When the baseline was stable (after ca. 20 minutes), ammonia gas was introduced into the cell and continuously flowed over the electrode.

5.2.3 Gas Mixing System

In order to obtain different concentrations of ammonia, 500 ppm ammonia gas was diluted with nitrogen gas through gas mixing system as reported by Lee et al.[52] which consisted of two digital flow meters (0-1.0 L/min, John Morris Scientific, NSW, Australia), one connected with analyte gas cylinder (NH_3) and other with nitrogen cylinder through PTFE tubing via a Swagelok T-joint (Swagelok, Kardinya, WA, Australia). The mixture of both desired gases (NH_3/N_2) was then passed through an additional gas-mixing segment[52] to increase turbulence and to ensure adequate mixing of both gases. The relative flow rates were used to calculate the different concentrations of ammonia introduced into the T-cell.

5.2.4 Electrode Imaging

Scanning electron microscopy (SEM) was performed on the working electrodes of bare and all four Pt-deposited MATFEs. SEM Images were obtained using MIRA3 (MIRA VP-FESEM), with a voltage of 5.0 kV. Atomic force microscopy (AFM) was performed using WITech alpha 300SAR instrument on the bare and Pt-deposited MATFEs to image the geometry, depth, and filling of the µ-holes, and the size of the 3D cauliflowers was measured using WITech Project Four data analysis software.

5.3 Results and Discussion

5.3.1 Electrodeposition of Pt 2D Nanostructures and 3D Cauliflowers

In order to ensure the correct potential for electrodeposition, first cyclic voltammetry (CV) was performed in a deaerated solution of 20 mM H_2PtCl_6 in 0.5 M H_2SO_4 at 100 mVs^{-1} *vs* an external Ag/AgCl reference electrode and Pt wire counter electrode. Initially the potential was scanned cathodically from +0.8 V (black CV) and two reduction features were observed at ~ +0.02 V (peak I) and ~ -0.17 V (peak II) which correspond to the reduction of Pt (IV) to Pt (II) and Pt (II) to Pt (0) respectively.[43, 48, 53-55] As the cathodic range is increased, process (III) was observed at -0.25 V that corresponds to the evolution of bulk hydrogen.[43] On the reverse scan, the oxidation peaks at ca. -0.04 V correspond to the hydrogen desorption peaks. Hydrogen adsorption peaks may also be present at a similar potential to peak (II), but they are reportedly hard to differentiate on a Pt surface in acidic media.[43, 55] When the potential was scanned from +0.4 V in the anodic direction (red CV), peak (V) was

observed, which corresponds to the oxidation of PtNPs/Pt surface to form Pt-oxide. This peak has a corresponding reduction peak (VI), which is attributed to the reduction of Pt-oxide and this cannot be seen during the first scan.[49, 56, 57] The identities of peaks (I) and (II) in Figure 5.1 can be described by the following equations:

Peak (I) $$Pt^{IV}Cl_6^{2-} + 2e^- \rightarrow Pt^{II}Cl_4^{2-} + 2Cl^- \quad \textbf{(5.1)}$$

Peak (II) $$Pt^{II}Cl_4^{2-} + 2e^- \rightarrow Pt^0 + 4Cl^- \quad \textbf{(5.2)}$$

For the electrodeposition of Pt into the μ-holes of the MATFE, the deposition was performed at two different potential regions; underpotential (-0.05 < E < -0.17 V) and overpotential (-0.17 < E < -0.25 V) using constant potential deposition (CPD). Figure 5.2 shows the current transients and corresponding electrochemical parameters, along with cartoons to show the expected 2D and 3D Pt-deposits in the μ-holes. For the formation of 'partially filled' MATFEs, 5 mM H_2PtCl_6 was used and the potential was stepped from the OCP at +0.75 V to a potential of -0.05 V (underpotential region) for 300 seconds under fast magnetic stirring to ensure a fast rate of mass transfer. The current transient in Figure 5.2a shows an initial large current followed by a slow decrease in current after 5 seconds, with a smooth shaped transient. This suggests that the formation of new nucleation sites in the kinetically controlled region is quite slow.

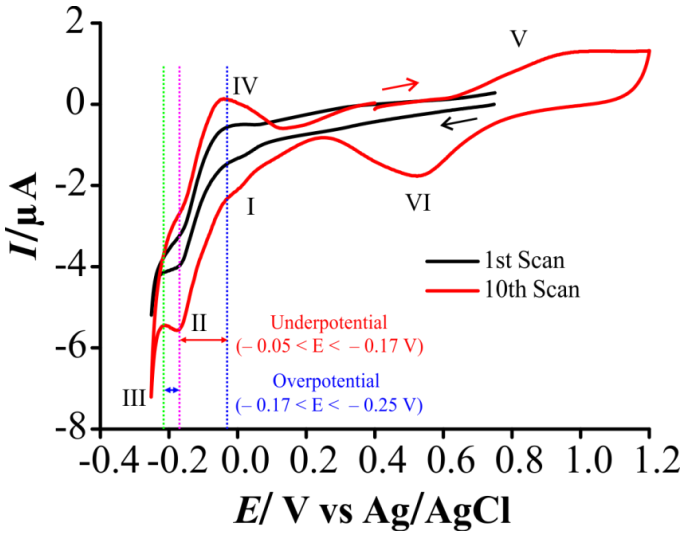

Figure 5.1: Cyclic voltammograms recorded on a Pt recessed MATFE in a solution of N_2-saturated 20 mM H_2PtCl_6 in 0.5 M H_2SO_4 at 100 mVs^{-1}.

In the case of 'half-filled' MATFEs, the deposition was achieved in two steps (Figure 5.2b); during the first step, the formation of new nucleation sites was observed at a kinetically controlled potential (-0.05 V) where large nanoparticles partially fill the μ-holes. During the second step, new nucleation sites were produced at a slower rate compared to the first step. This is due to the less negative potential (-0.025) that results in filling the spaces between the bigger nanoparticles to obtain smoother, more uniform 2D Pt-nanostructures. Figure 5.2b shows the current transients, along with a schematic reporting the deposition parameters. The current transient for the second step has a larger initial current during the first few seconds of the measurement due to the increased surface area as a result of the nanoparticle deposits. However, for the deposition from 5 to 300 seconds, a similar current profile can be seen as the first step, which indicates the formation of new nucleation sites on top of the nanoparticles produced in the first step.

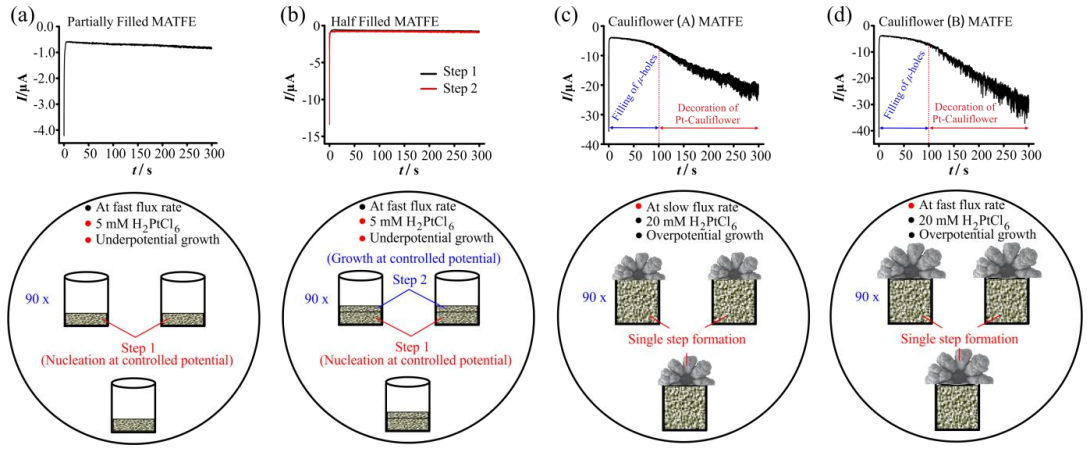

Figure 5.2: Chronoamperometric transients for Pt-deposition on Pt recessed MATFEs using a 5 mM or 20 mM N_2-saturated H_2PtCl_6 in 0.5 M H_2SO_4. The potential was stepped from 0.0 V (OCP) to (a) -0.05V for 'partially filled' MATFE, (b) -0.05 V for the first pulse and -0.025 V for the second pulse for 'half-filled' MATFE, (c) -0.2 V for 'cauliflower A' MATFE, and (d) -0.2 for 'cauliflower B' MATFE. The cartoons below circular show the expected filling of the recessed pores and the electrochemical parameters employed for Pt deposition.

For 'cauliflower A' MATFEs, the deposition of Pt into the μ-holes was achieved in a single step using a high concentration of Pt precursor (20 mM H_2PtCl_6). The formation of 3D Pt-cauliflowers was achieved by applying an overpotential (-0.2 V) for 300 s in an unstirred solution. Figure 5.2c shows the current transient for the formation of 3D Pt-cauliflowers. After an initial high current, there is a slow decrease in current from 5 to 100 seconds corresponding to filling of the μ-holes.

However, after *ca.* 100 seconds, oscillation/spikes in the current signals can be seen, which indicates the beginning of cauliflower formation over the edges of the μ-holes. This is due to the instantaneous nucleation and growth of nanoparticles as a result of the high overpotential.[43, 45, 47] As the deposition time proceeds from 100 seconds to 300 seconds, the intensity of the current spikes increase, showing the growth of Pt-cauliflowers into bigger sizes.

Figure 5.2d shows the current transient plot and cartoon with deposition parameters for 'cauliflower B' MATFE. All electrochemical parameters were similar to procedure 3 except the flux rate, where vigorous stirring was applied to increase the rate of mass transfer to the electrode. The current transient in Figure 5.2d shows a similar initial large current, followed by a gradual decrease in current over time from 5 to 100 seconds, corresponding to filling of the μ-holes. However, after ca. 100 seconds, the intensity in the current spikes are much larger compared to 'cauliflower A' MATFE (see Figure 5.2c) due to the faster rate of mass transfer which results in the formation of larger 3D Pt-cauliflowers.

5.3.2 Characterisation of Pt 2D Nanostructures and 3D Cauliflowers Using SEM and AFM

In this study, all four 2D and 3D Pt-deposit modified MATFEs and an unmodified recessed MAFTE were analysed using scanning electron microscopy (SEM) and atomic force microscopy (AFM). Figure 5.3 shows SEM images for all five surfaces employed. The AFM 3D image of μ-holes for the unmodified recessed MATFE along with its depth profile is also shown. The SEM image of the recessed MATFE (Figure 5.3a) shows an image of an array of μ-holes (90 in total when zoomed out) which are fabricated using a thin layer of SU-8 polymer covering the Pt surface, and holes made in the SU-8 layer to form recessed microarrays. The inset figure shows a zoomed in image of one μ-hole with a diameter of 10 μm. The depth of the μ-hole is 2.8 µm, confirmed from the depth profile of an AFM 3D image (see Figure 5.3f,g) which is within the manufacturers statement of 3±0.5 µm. Figure 5.3b shows an SEM image of a 'partially filled' MATFE, achieved by depositing 2D Pt-nanostructures at an underpotential region (-0.05 V). The inset shows a close-up image of a partially filled μ-hole with 2D Pt-nanostructures. AFM characterization revealed that the μ-holes were filled partially from the center to the edges with a

thickness of ca. 2.6±0.03 µm from the surface (see Figure 5.4a). This amount of filling is enough to produce enhanced radial diffusion at the edges of the μ-holes, rather than linear diffusion within the recession, enhancing the voltammetric response (see later).

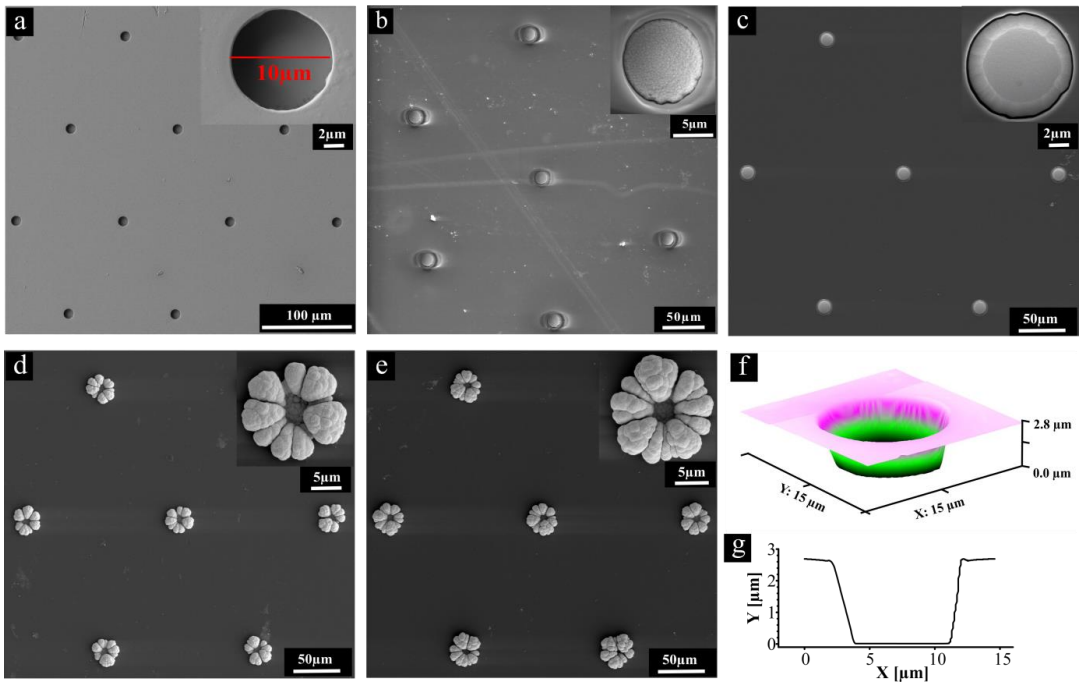

Figure 5.3: Scanning electron microscopy (SEM) images of recessed, 2D and 3D Pt-modified MATFEs (a) recessed MATFE (90 recessed electrodes, diameter 10 µm, depth 3±0.5 µm), (b) 'partially filled' MATFE (filling 2.6±0.03 µm), (c) 'half-filled' MATFE (filling 1.5±0.1 µm), (d) 'cauliflower A' MATFE (diameter of cauliflower 18±0.5 µm), and (e) 'cauliflower B' MATFE, (diameter of cauliflower 22±1 µm). (f) Atomic force microscopy (AFM) 3D image of a microhole on the recessed MATFE, and (g) depth profile of the same microhole.

Figure 5.3c shows a SEM image of a half-filled MATFE with 2D Pt nanostructures obtained in two steps (see details in the previous section). The inset shows a close-up image of the half-filled μ-hole, where AFM confirmed that the filling of the μ-holes was 1.5±0.1 µm (see Figure 5.4b). The SEM image of 'cauliflower A' MATFE (Figure 5.3d) shows an array of 3D cauliflower shaped Pt nanostructures which were obtained in single step, with each cauliflower having an average diameter of 18±0.5 µm. The formation of this unique shape occurred due to the higher concentration of Pt precursor[31] and the use of overpotential deposition (-0.2 V) to produce instantaneous growth of small size nanoparticles that fill the μ-holes and then grow over the edges into 3D cauliflower shaped Pt nanostructures.[43, 45, 47] As the amount of deposit increased within the μ-holes, the effect of radial diffusion become dominant

at the edges as compared to the linear diffusion within the recession. The resultant deposit shows more Pt nanoparticles at the edges rather than at the centre of the μ-holes, growing into 3D cauliflowers over an extended period of time (300 seconds). Figure 5.3e shows the image of 'cauliflower B' MATFE with an inset of a close-up of one 3D cauliflower. The average diameter of 'cauliflower B' deposits were found to be slightly higher (22±1 µm) than the 'cauliflower A' due to a faster rate of mass transfer. Figure 5.4 shows the AFM 3D images of Pt-deposited MATFEs, along with depth profile for 2D nanostructures and height profile for 3D cauliflower shaped nanostructures.

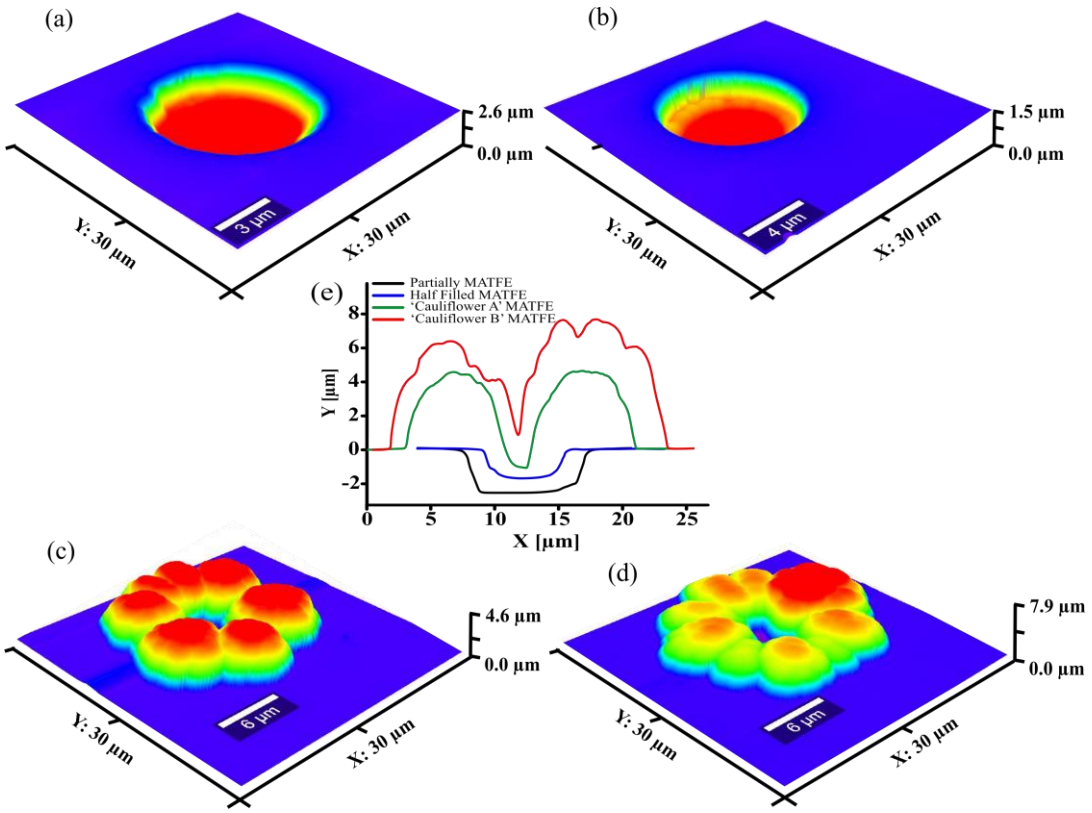

Figure 5.4: Atomic force microscopy (AFM) 3D images of MATFEs (a) partially filled MATFE (depth = 2.6±0.03 µm), (b) half-filled MATFE (depth = 1.5±0.1 µm), (c) cauliflower (A) MATFE (diameter of cauliflower 18±0.2 µm, height = 4.6±0.03 µm, depth = 1.1±0.02 µm), (d) cauliflower (B) MATFE, (diameter of cauliflower 22±0.3 µm, height = 7.9±0.2 µm, depth = 0.6±0.02 µm), and (e) depth profiles of 2D and 3D Pt-deposits.

Figure 5.5 shows SEM images of Pt-deposits in and around the microholes of the whole working electrode of Pt MATFEs, where all 90 electrodes are visible. On the partially filled MATFE (Figure 5.5a), a uniform deposition of 2D Pt nanostructures is seen in most μ-holes throughout the array, but with slightly less deposits within the

μ-holes situated in the corner positions. This pattern is repeated for the 'half filled' and 'cauliflower A' and 'cauliflower B' MATFEs, where the deposits on the corner μ-holes are not as regular in shape compared to those near the centre. This could be due to the different amounts of mass transfer affecting the μ-holes at the edges, compared to those near the centre where the diffusion layers are partially overlapping.[58, 59]

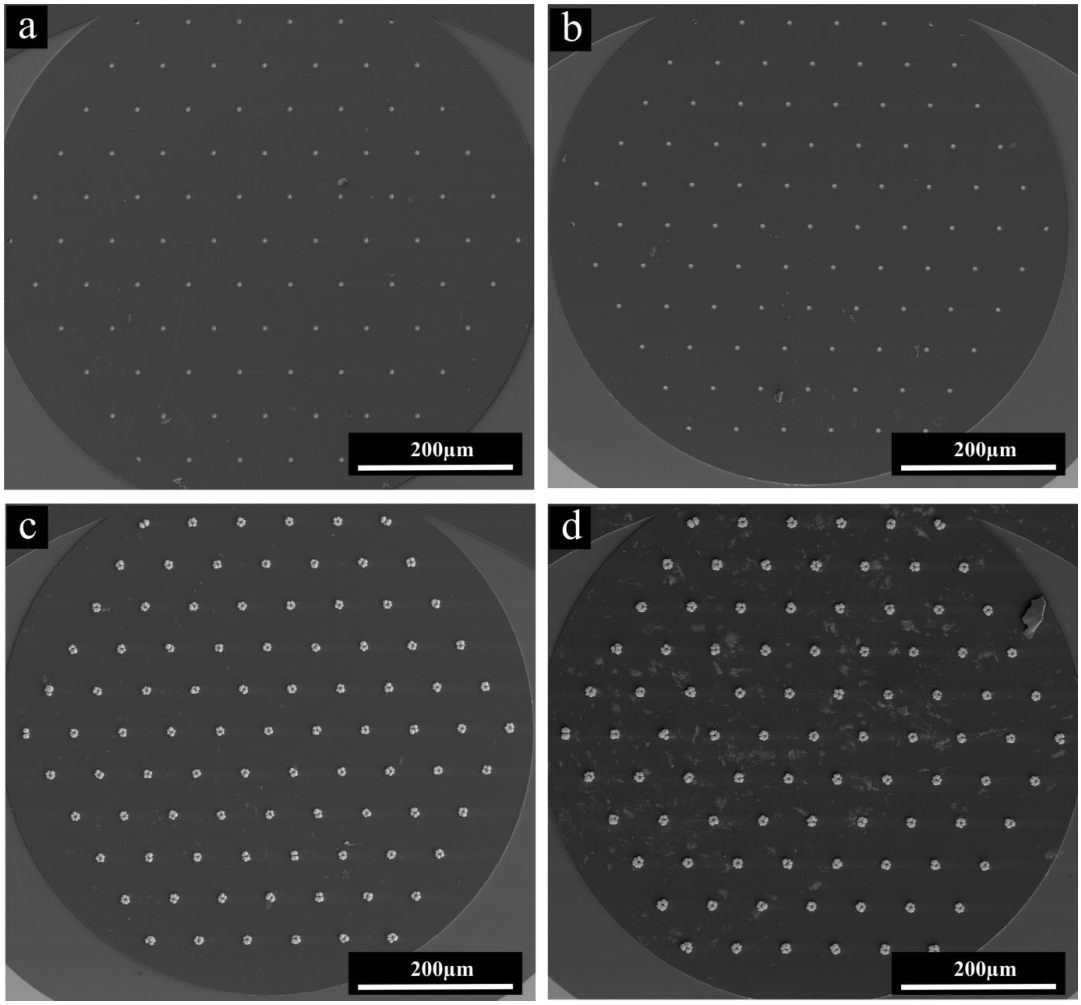

Figure 5.5: Scanning electron microscopy (SEM) images of Pt-deposits on the microholes of the working electrode of Pt MATFEs: (a) 'partially filled' MATFE, (b) 'half-filled' MATFE, (c) 'cauliflower A' MATFE, and (d) 'cauliflower 'B' MATFE.

Figure 5.6 shows magnified SEM images for a single μ-hole on the same four modified surfaces. For the 'partially filled' hole (Figure 5.6a), the deposit appears quite regular over the electrode surface. For the 'half filled' hole (Figure 5.6b) there is some deposit in the centre of the array and a greater density of nanoparticles near the edges. The distribution of nanoparticles in the μ-hole also shows an uneven/coarse surface due to the larger size of nanoparticles produced as a result of

underpotential deposition for longer time (300 seconds). The zoomed image of one half-filled MATFE (Figure 5.6b) reveals the fine distribution of 2D Pt nanostructures at the center of μ-hole, which is achieved in the first step due to kinetically controlled growth of new nucleation sites,[43, 44] followed by growth of these nanoparticles into bigger sized nanoparticles over time (300 seconds). In the second step, new nucleation sites are grown at less negative potential (-0.025 V) between the previous deposited nanoparticles to achieve fine and uniform filling of μ-holes.

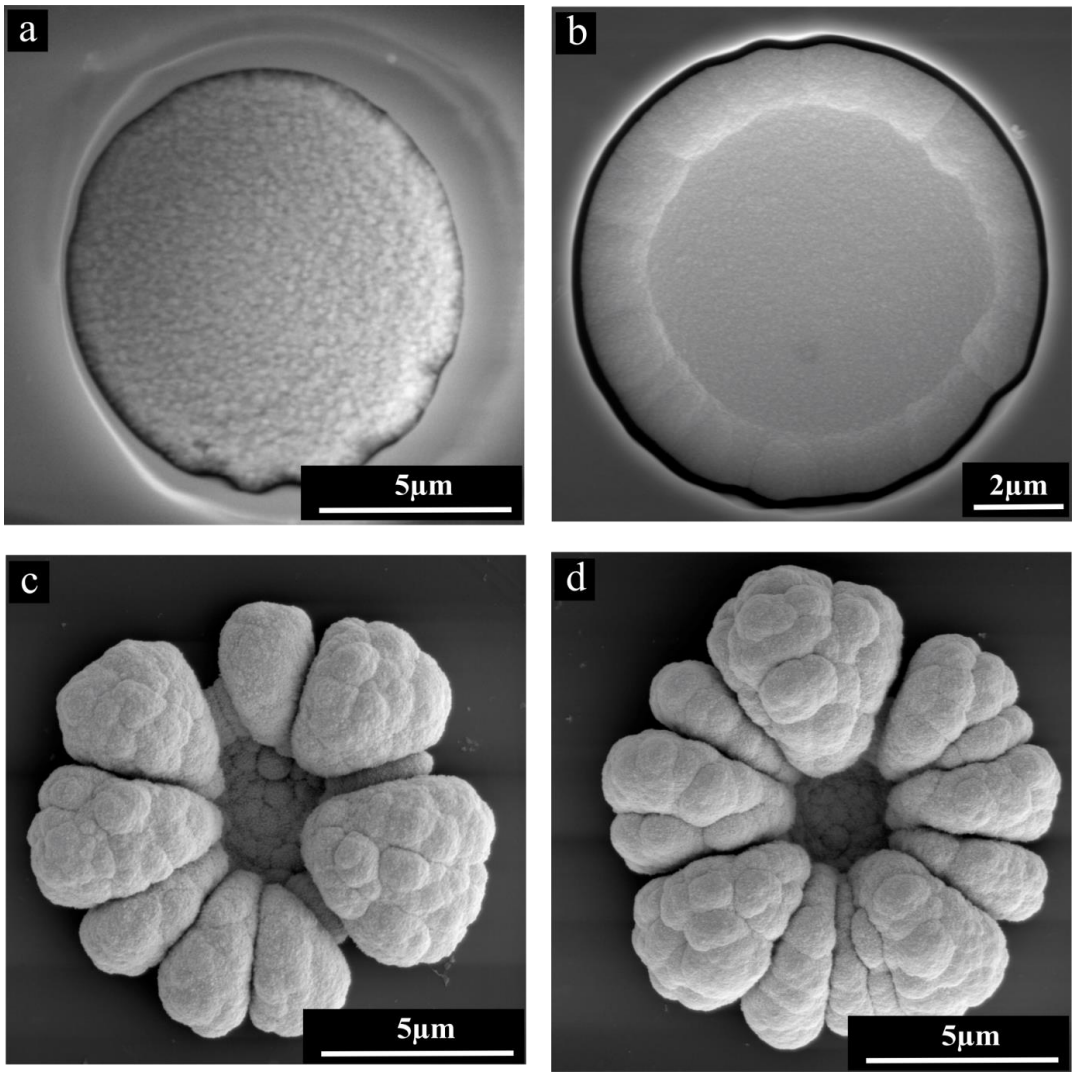

Figure 5.6: Scanning electron microscopy (SEM) images of a single microhole showing Pt deposits on MATFEs: (a) 'partially filled' MATFE, (b) 'half-filled' MATFE, (c) 'cauliflower A' MATFE, and (d) 'cauliflower B' MATFE.

In the case of 'cauliflower A' and 'cauliflower B' MATFEs (Figure 5.6 c,d), the filled μ-holes can be seen very clearly with aggregated nanoparticles at the centre of the cauliflowers. On the edges of μ-holes, the Pt-deposits grow separately in a flower petal-type pattern due to the dominant radial diffusion at the edges of the μ-holes.

However, cauliflower bud-type patterns can also be observed on each individual petal, produced due to the instantaneous nucleation and growth of smaller size nanoparticles as a result of overpotential.[31, 43, 45, 47] The number of cauliflower petals and the appearance of the buds are more uniform and pronounced on 'cauliflower B' MATFE than 'cauliflower A' due to the faster rate of mass transfer, resulting in larger sized 3D cauliflower shaped Pt nanostructures.[31]

5.3.3 Electrochemical Oxidation of Ammonia on Pt 2D Nanostructured and 3D Cauliflower Microarrays

Five electrode surfaces were employed for this study; the four Pt-deposited 2D and 3D decorated MATFEs, as described above, and one recessed MATFE for comparison. The RTIL [C_2mim][NTf_2] was employed as the electrolyte for ammonia oxidation due to its wide electrochemical window (>4.5 V), good chemical and thermal stability, high ionic conductivity and its relatively low viscosity compared to other available RTILs. In previous work, it was also reported to have the best electrochemical response for ammonia oxidation.[60, 61] Prior to studying the analytical response on these modified microarrays, cyclic voltammetry (CV) was first performed to study the electrochemical mechanism for ammonia oxidation in [C_2mim][NTf_2]. Figure 5.7 shows the cyclic voltammograms for the oxidation of 500 ppm ammonia on all five electrodes at a scan rate of 100 mV/s. The red dashed lines are the response in the absence of ammonia. The mechanism of ammonia oxidation on all four 2D and 3D Pt-deposited MATFEs in [C_2mim][NTf_2] was very similar to the recessed MATFE, with four peaks present[41] and was consistent with that reported previously on microdisk electrodes (see chapter 4).[61-63] It can be seen in all five voltammograms that the steady state responses were obtained between 0.0 V and +2.0 V for ammonia oxidation process I, followed by two reduction peaks, peak II (ca. 0.0 V to -0.5 V) the reduction of the solvated proton and peak III (ca. -0.5 V to -1.5 V) the reduction of the ammonium ion.[61, 62] Peak IV belongs to the oxidation of electrogenerated adsorbed proton, produced in the two reduction processes.[61, 62] The identities of all these peaks process on microarrays are well described in a previous study.[41]

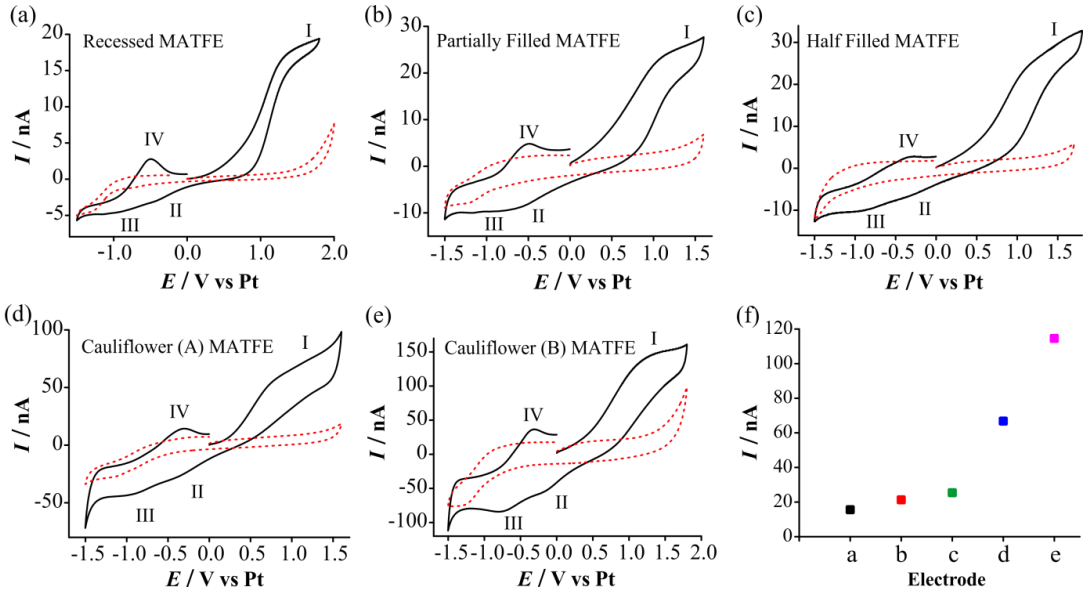

Figure 5.7: Cyclic voltammetry for 500 ppm ammonia oxidation in $[C_2mim][NTf_2]$ on a Pt: (a) recessed MATFE (diameter 10 µm, depth 2.8±0.5 µm), (b) 'partially filled' MATFE (filling 2.6±0.03 µm), (c) 'half-filled' MATFE (filling 1.5±0.1 µm), (d) 'cauliflower A' MATFE (diameter 18±0.5 µm), (e) 'cauliflower B' MATFE (diameter 22±1 µm). Dashed red line is the response in the absence of ammonia. Scan rate 100 mVs^{-1}. (f) Absolute current for process I for 500 ppm NH_3 on all five surfaces.

A slight increase in current response for ammonia oxidation (peak I) can be seen from partially filled MATFE to half-filled MATFE. This is due to the improved radial diffusion as a result of partially or half-filled μ-holes. However a dominant increase in current response can be seen when the μ-holes are filled completely and decorated with 3D cauliflower like nanostructures. The response shows a slanted steady-state shape, consistent with that observed previously in chapter 4. On 'cauliflower A' MATFE, the current for peak I is *ca.* four times higher than for the recessed MATFE. This is due to the 3D cauliflower like nanostructures with a large active surface area, which enhances the current response. In the case of 'cauliflower B' MATFE, a more steady-state shape current response for peak I can be seen, and it is likely that the diffusion profiles will overlap as a result of the larger 3D cauliflower deposits. The current response for ammonia oxidation peak I on 'cauliflower B' MATFE is *ca.* seven times higher than for the recessed MATFE. Figure 5.7f shows the current response (background subtracted) for ammonia oxidation peak I on all five surfaces. A roughly linear increase in current response can be seen from the recessed to the half-filled MATFE containing 2D nanostructure,s and then a steeper rise in current for the 3D cauliflower decorated

MATFEs. Table 5.1 shows a comparison of the oxidation current for peak I for 500 ppm ammonia on all these surfaces.

5.3.4 Comparison of Current Density

In order to compare the oxidation of ammonia on the Pt-deposited 2D and 3D cauliflower microarrays *vs* recessed microarrays, the current density (*J*) was calculated from the steady-state oxidation current divided by the electroactive surface area (ESA). The ESA of all electrodes was determined from the hydrogen adsorption/desorption peaks using deaerated 0.5 M H_2SO_4. For this, an external Ag/AgCl reference electrode and Pt wire counter electrode was employed. Then, cyclic voltammetry (CV) was performed between -0.27 and +1.4 V at a scan rate of 500 mVs^{-1}. The area ($I \times t$) under the hydrogen adsorption/desorption peaks give the electroactive surface area (ESA) which can be calculated using standard methods.[43, 49] The ESA is defined by the following equation.[43]

$$ESA = \frac{Q_H}{210\ \mu C} \qquad \textbf{(5.3)}$$

Where Q_H is the charge calculated by integrating the hydrogen adsorption/desorption peaks from -0.2V to 0.4 V, and is given by the following equation.[43]

$$Q_H = I \times t \qquad \textbf{(5.4)}$$

where I = current and t = time. The ESA can also be calculated from the charge associated with Pt-oxide reduction peak which is a less common method. This method gave a charge slightly higher compared to charge calculated from the hydrogen adsorption/desorption peaks. This could be due to more positive scanning at 1.4 V to produce more oxide layers on the Pt-surface. It is important to mention here that the surface roughness of the modified surfaces is believed to not be affected by fast scanning at 500 mV/s in 0.5 M H_2SO_4, since only a few CV cycles (5 to 10) were performed. Figure 5.8a shows the current density (*J*) plot for 500 ppm ammonia oxidation the five MATFEs in $[C_2mim][NTf_2]$, along with the corresponding CVs of the electrodes in 0.5 M H_2SO_4 (Figure 5.8b). The inset in Figure 5.8b shows the H_2 desorption peaks (background subtracted) whose integrated charge ($Q = I \times t$) is used to calculate the electroactive surface area (ESA). The current density plot shows two linear regimes; a slight increase in *J* from recessed to half-filled MATFEs which is

due to the improved characteristics of radial diffusion due to filling of μ-holes as compared to linear diffusion in the recession. The same increase in the integrated charge and electroactive surface area can be seen for H_2 desorption peaks except the half-filled MATFE where the average charge and calculated ESA has a slightly smaller value than the expected. This may be due to the more uniform filling of μ-holes in the second step where the deposition was performed under kinetic control (-0.025 V). This uniform filling of μ-holes could decrease the roughness of the surface, which in turn decreases the ESA. Similar observations can be seen very clearly from the SEM images of 'partially filled' and 'half-filled' MATFE where the 'half-filled' MATFE have a more flat and smooth surface.

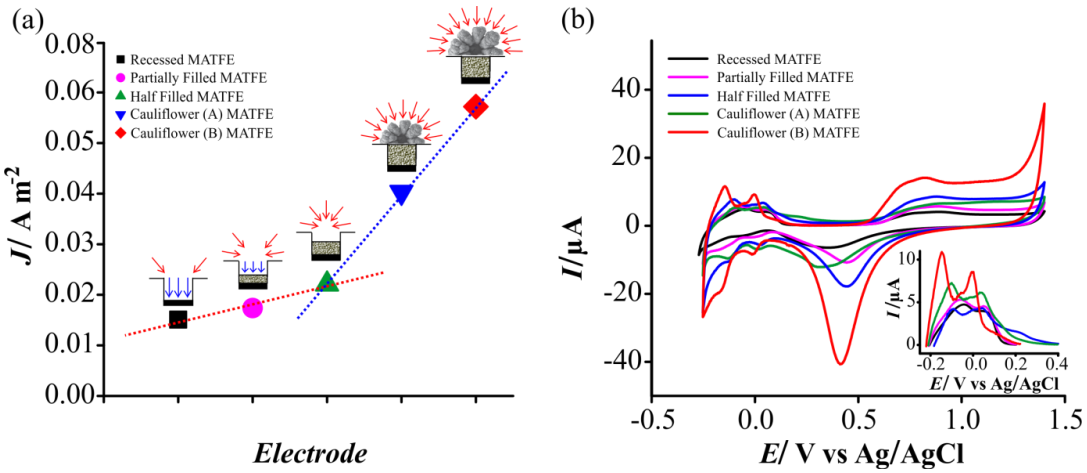

Figure 5.8: (a) Current density (J) plot for the oxidation of 500 ppm ammonia in $[C_2mim][NTf_2]$ on a Pt: recessed MATFE (■), partially filled MATFE (●), half-filled MATFE (▲), cauliflower (A) MATFE (▼) and cauliflower (B) MATFE (◆). Sketches of the expected diffusion processes (radial and linear combined, and radial) based on the electrode geometry are also shown. (b) Cyclic voltammograms recorded on the five MATFEs between +1.4 V and -0.25 V in a N_2-saturated solution of 0.5 M H_2SO_4 at 500 mVs^{-1}. The inset shows the H_2 desorption peaks (background subtracted) whose integrated area ($Q = I \times t$) is used to calculate the electrochemical surface area (ESA).

A dominant increase in J can be seen from 'half-filled' MATFE to 'cauliflower B' MATFE. This is due to the 3D cauliflower shaped nanostructures where the multidimensional radial diffusion enhanced the current density. Based on these observations, the Pt-deposited MATFEs with 2D nanostructures and 3D cauliflowers were employed for further analytical experiments, to investigate whether these modified MATFEs can be used for low concentration detection of ammonia in RTILs.

5.3.5 Analytical Response for Ammonia Oxidation on Pt 2D and 3D Decorated Microarrays

In order to investigate the ability of the Pt-deposited MATFEs to detect ammonia, the analytical utility and sensitivity for ammonia in $[C_2mim][NTf_2]$ was studied and compared to the recessed MATFE. For this, linear sweep voltammetry was employed to study ammonia oxidation in RTILs. Potential step chronoamperometry (PSCA) was also employed on the recessed and Pt-deposited 3D cauliflower decorated MATFEs to test the ability of the modified microarrays for "real-time" analyte detection, also allowing the calculation of response times.

5.3.5.1 Linear Sweep Voltammetry

Figure 5.9 shows linear sweep voltammetry (LSV) for the oxidation of 10-100 ppm ammonia in $[C_2mim][NTf_2]$ on all five surfaces at a scan rate of 100 mV/s. The red dashed line is the response in the absence of ammonia. The insets show the corresponding calibration plots for steady-state oxidation currents (baseline corrected) *vs* ammonia concentration in gas phase.

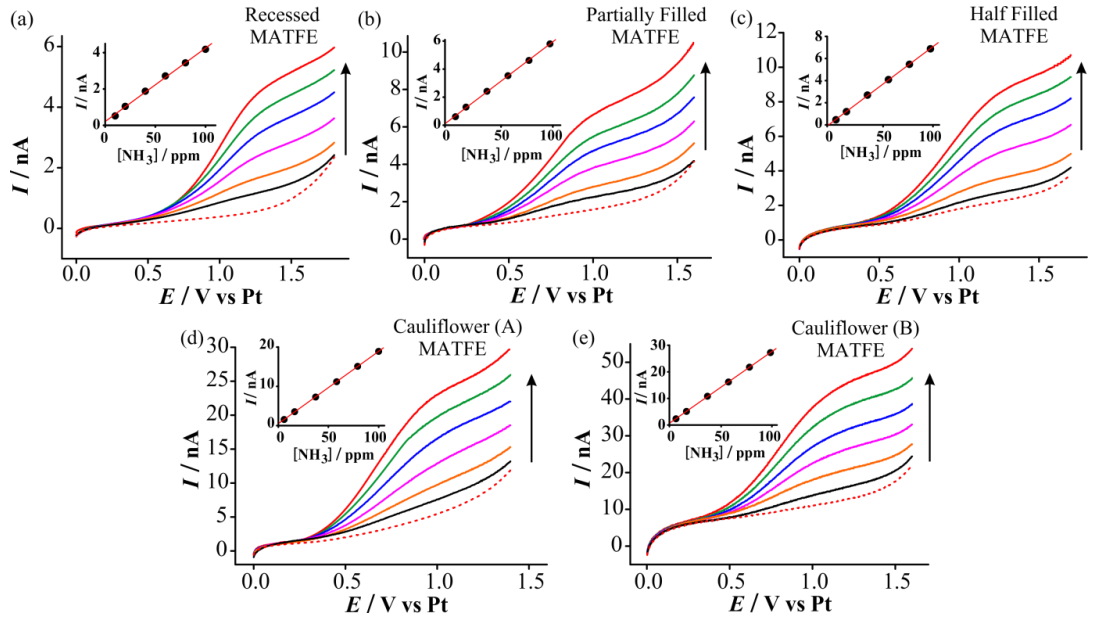

Figure 5.9: Linear sweep voltammetry (LSV) for the oxidation of ammonia (10-100 ppm) in $[C_2mim][NTf_2]$ on a Pt (a) recessed MATFE, (b) 'partially filled' MATFE, (c) 'half-filled' MATFE, (d) 'cauliflower A' MATFE, (e) 'cauliflower B' MATFE at a scan rate of 100 mVs^{-1}. Dotted line is the response in the absence of ammonia. Currents on all MATFE were measured from a fixed potential of 1.3 V. The insets show the calibration plots of peak current (baseline corrected) vs concentration, along with the line of best fit.

A slanted steady-state response is observed for all electrodes, but with current increasing linearly with concentration. An increase in the background current is also noted for the higher surface area cauliflower structures due to the increased surface area. Oxidation peak currents were measured from a fixed potential of +1.3 V and plotted against the respective concentration. Excellent linearity (R^2 > 0.999) was obtained on all Pt-deposited MATFEs for the concentration range studied. Figure 5.10 shows the absolute currents *vs* different concentrations of ammonia (10-100 ppm) plotted together for recessed and Pt-deposited MATFEs. The gradient for recessed MATFE has the smallest current (background subtracted) while the gradients for partially filled and half-filled MATFEs have slightly higher currents due to the filling in the centre of the μ-holes. However, the currents on the 'cauliflower A' and 'cauliflower B' MATFEs are greatly increased due to the higher amount of radial diffusion towards the 3D nanostructures compared to partially/half-filled or recessed MATFEs.

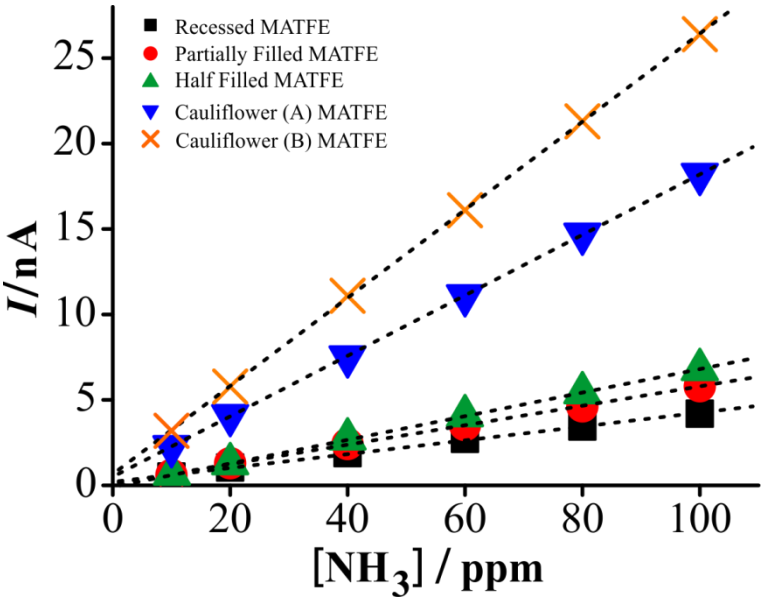

Figure 5.10: Plot of absolute current vs ammonia concentration for the oxidation of 10-100 ppm ammonia in [C_2mim][NTf_2] on a Pt: recessed MATFE (■), 'partially filled' MATFE (●), 'half-filled' MATFE (▲), 'cauliflower A' MATFE (▼) and 'cauliflower B' MATFE (×).

Table 5.1 shows the analytical parameters obtained from the calibration plots in Figure 5.10, along with the integrated charge (Q_H), calculated electroactive surface areas, current density (J), and oxidation peak current (I_p) for 500 ppm ammonia observed on recessed and all Pt-deposited MATFEs. The sensitivity values were calculated from the gradient of the best-fit straight line and limits of detection

(LODs) were obtained using three times the standard deviation of the slope of the line of best fit, over the concentration range studied. The sensitivities of partially filled and half-filled MATFEs are higher than the recessed MATFE; the 2D nanostructures enhanced their sensitivities by 42% and 72 %, respectively, compared to the recessed μ-holes. However when the μ-holes were completely filled and decorated with 3D cauliflower shaped nanostructures, the sensitivities values were 4.5 times higher for 'cauliflower A' and 6.5 times higher for 'cauliflower B' compared to the recessed MATFEs. The LOD values calculated for the 10-100 ppm ammonia concentration range on recessed and all Pt-deposited MATFEs were much lower (0.8 to 2 ppm) than the OSHA PEL of 25 ppm in the gas phase. Importantly, they are the lowest for the two cauliflower deposits, showing enhanced sensitivity due to a higher electroactive surface area and 3D shape. The LODs could be further improved when a lower concentration range is studied, as discussed in chapter 4. These observations are highly encouraging that the filled μ-holes with 3D cauliflower shaped nanostructures can be employed to detect ammonia at very low concentrations in RTILs.

Table 5.1. Analytical parameters (charge (Q_H), electrochemical surface area (ESA) calculated from the integration of H_2 desorption peak obtained in N_2-saturated 0.5 M H_2SO_4 at 500 mVs^{-1} vs Ag/AgCl reference electrode and Pt counter electrode, oxidation peak current (I_p) for 500 ppm ammonia, measured at fixed potential +1.3 V, current density (J) for 500 ppm NH_3, sensitivity and limit of detection (LOD) calculated for ammonia oxidation (10-100 ppm) on recessed MATFE and all Pt-deposited MATFEs using linear sweep voltammetry (LSV).

Electrode	$Q_H = I \times t$ (μC)	ESA (μm^2)	I_p (μA)	J (Am^{-2})	Sensitivity ($Appm^{-1}$)	LOD (ppm)
Recessed MATFE	2.16	1.03	1.6×10^{-02}	1.5×10^{-02}	4.0×10^{-11}	2.0
Partially Filled MATFE	2.58	1.23	2.1×10^{-02}	1.7×10^{-02}	5.7×10^{-11}	1.7
Half Filled MATFE	2.42	1.15	2.5×10^{-02}	2.2×10^{-02}	6.9×10^{-11}	1.4
'Cauliflower A' MATFE	3.48	1.66	6.7×10^{-02}	4.0×10^{-02}	1.8×10^{-10}	0.8
'Cauliflower B' MATFE	4.20	2.00	1.1×10^{-01}	5.7×10^{-02}	2.6×10^{-10}	0.8

5.3.5.2 Potential Step Chronoamperometry

In order to test the ability of 3D cauliflower decorated MATFEs *vs* recessed MATFEs for "real-time" detection of ammonia in RTILs and to calculate response time, potential step chronoamperometry (PSCA) was performed. Figure 5.11 shows the current response for 10 ppm ammonia on both recessed and 'cauliflower B' MATFE in $[C_2mim][NTf_2]$. The maximum current obtained on 'cauliflower B'

MATFE was twelve times higher than for the recessed MATFE. The response time was calculated from 90% of the maximum current.[64] For the recessed MATFE, the response time was *ca.* 315 ± 20 seconds while on 'cauliflower B' MATFE, it was *ca.* 200 ± 15 seconds. The thickness of the RTIL layer was estimated to be 0.14 ± 0.03 mm thickness for [C_2mim][NTf_2] (volume of 2 µL). A small decrease after the maximum current response was observed on both the recessed and 'cauliflower B' MATFE. This could be due to some fouling of the surface due to a build-up of electrogenerated products, as reported in the literature.[64-66]

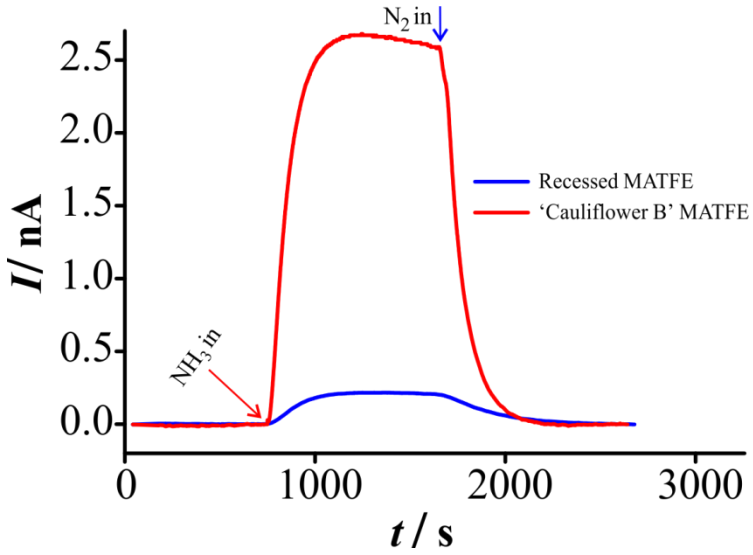

Figure 5.11: Potential step chronoamperometry for 10 ppm ammonia oxidation on the recessed and 'cauliflower B' MATFEs in the RTIL [C_2mim][NTf_2]. The potential was stepped from 0 to + 1.3 V vs. Pt. The arrows correspond to the introduction of 10 ppm ammonia gas, then pure nitrogen gas.

5.4 Conclusions

The electrochemistry of ammonia oxidation has been investigated in the RTIL [C_2mim][NTf_2] on four Pt-deposited MATFEs with 2D nanostructures and 3D cauliflower decorated microarrays and compared with recessed MATFE. The reaction mechanism was the same on all modified surfaces. Current density for 500 ppm ammonia was ca. 4 times higher on microarrays decorated with cauliflower structures compared to recessed microarrays. The calibration plots obtained from 10-100 ppm ammonia were linear on all Pt-modified MATFEs, with the highest sensitivities found on cauliflower decorated MATFEs. The lowest LODs (0.8 ppm) were found on 'cauliflower A' and 'cauliflower B' MATFEs. To test the ability of 3D cauliflower decorated microarrays based sensors for "real time" analyte

detection, potential step chronoamperometry was performed on both recessed and 'cauliflower B' MATFEs where the cauliflower decorated microarrays gave a much higher (12 times) response compared to recessed microarrays. All these results are highly encouraging and suggest that low-cost miniaturised electrodes can be decorated with 3D Pt-cauliflower shaped nanostructures to detect ammonia gas with higher sensitivities at low concentrations.

References

1. A. Kaniyoor, R. I. Jafri, T. Arockiadoss and S. Ramaprabhu, *Nanoscale*, 2009, **1**, 382-386.
2. A. Walcarius, *Anal. bioanal. chem.*, 2010, **396**, 261-272.
3. A. Walcarius, *Electroanal.*, 2008, **20**, 711-738.
4. B. J. Melde, B. J. Johnson and P. T. Charles, *Sensors*, 2008, **8**, 5202-5228.
5. L. M. Peter, *Phys. Chem. Chem. Phys.*, 2007, **9**, 2630-2642.
6. L.-L. Li, C.-W. Chang, H.-H. Wu, J.-W. Shiu, P.-T. Wu and E. W.-G. Diau, *J. Mater. Chem.*, 2012, **22**, 6267-6273.
7. H. Chang, S. H. Joo and C. Pak, *J. Mater. Chem.*, 2007, **17**, 3078-3088.
8. S. Sun, F. Jaouen and J. P. Dodelet, *Adv. Mater.*, 2008, **20**, 3900-3904.
9. A. S. Aricò, P. Bruce, B. Scrosati, J.-M. Tarascon and W. Van Schalkwijk, *Nat. mater.*, 2005, **4**, 366-377.
10. Y. G. Guo, J. S. Hu and L. J. Wan, *Adv. Mater.*, 2008, **20**, 2878-2887.
11. S. W. Lee, B. M. Gallant, H. R. Byon, P. T. Hammond and Y. Shao-Horn, *Energy Environ. Sci.*, 2011, **4**, 1972-1985.
12. H. Jiang, J. Ma and C. Li, *Adv. mater.*, 2012, **24**, 4197-4202.
13. F. Wang and S. Hu, *Microchim. Acta*, 2009, **165**, 1-22.
14. C.-Y. Chiou and T.-C. Chou, *Electroanal.*, 1996, **8**, 1179-1182.
15. L. Rassaei, F. Marken, M. Sillanpää, M. Amiri, C. M. Cirtiu and M. Sillanpää, *Trends Anal. Chem.*, 2011, **30**, 1704-1715.
16. N. Barsan and U. Weimar, *J. Phys.: Condens. Matter*, 2003, **15**, R813.
17. P. Santhosh, K. M. Manesh, A. Gopalan and K.-P. Lee, *Sens. Actuators, B*, 2007, **125**, 92-99.
18. T. Gan and S. Hu, *Microchim. Acta*, 2011, **175**, 1.
19. M. Trojanowicz, *Trends anal. chem.*, 2006, **25**, 480-489.
20. Y. Cui, Q. Wei, H. Park and C. M. Lieber, *Science*, 2001, **293**, 1289-1292.
21. U. Yogeswaran and S.-M. Chen, *Sensors*, 2008, **8**, 290-313.
22. D. Luo, L. Wu and J. Zhi, *ACS nano*, 2009, **3**, 2121-2128.
23. L. C. Tien, P. W. Sadik, D. P. Norton, L. F. Voss, S. J. Pearton, H. T. Wang, B. S. Kang, F. Ren, J. Jun and J. Lin, *Appl. Phys. Lett.*, 2005, **87**, 222106.
24. Z.-j. Wang, Y. Xie and C.-j. Liu, *J. Phys. Chem. C*, 2008, **112**, 19818-19824.
25. Y. Yamauchi, A. Tonegawa, M. Komatsu, H. Wang, L. Wang, Y. Nemoto, N. Suzuki and K. Kuroda, *J. Am. Chem. Soc.*, 2012, **134**, 5100-5109.
26. N. Zhang, K. Yu, Q. Li, Z. Q. Zhu and Q. Wan, *J. Appl. Phys.*, 2008, **103**, 104305.
27. J. Fu, C. Zhao, J. Zhang, Y. Peng and E. Xie, *ACS appl. mater. interfaces*, 2013, **5**, 7410-7416.
28. C. Wang, L. Yin, L. Zhang, Y. Qi, N. Lun and N. Liu, *Langmuir*, 2010, **26**, 12841-12848.
29. X. Niu, M. Lan, H. Zhao and C. Chen, *Anal. chem.*, 2013, **85**, 3561-3569.

30. C. Kong, S. Sun, J. Zhang, H. Zhao, X. Song and Z. Yang, *CrystEngComm*, 2012, **14**, 5737-5740.
31. F. Ren and S. J. Pearton, *Semiconductor-Based Sensors*, World Scientific, 2016.
32. B. Zhang, L. Lu, Q. Hu, F. Huang and Z. Lin, *Biosens. Bioelectron.*, 2014, **56**, 243-249.
33. R. K. Sonker, S. R. Sabhajeet, S. Singh and B. C. Yadav, *Mater. Lett.*, 2015, **152**, 189-191.
34. H. Zhang, R. Wu, Z. Chen, G. Liu, Z. Zhang and Z. Jiao, *CrystEngComm*, 2012, **14**, 1775-1782.
35. S. Sun, X. Zhang, Y. Sun, J. Zhang, S. Yang, X. Song and Z. Yang, *RSC Adv.*, 2013, **3**, 13712-13719.
36. X. Zhang, J. Jiang and W. Shi, *Micro Nano Lett.*, 2014, **9**, 509-513.
37. A. Chen, X. Peng, K. Koczkur and B. Miller, *Chem. Commun.*, 2004, 1964-1965.
38. M. R. Hormozi Nezhad, M. Aizawa, L. A. Porter, A. E. Ribbe and J. M. Buriak, *Small*, 2005, **1**, 1076-1081.
39. J. N. Tiwari, R. N. Tiwari and K.-L. Lin, *ACS Appl. Mater. Interfaces*, 2010, **2**, 2231-2237.
40. R. S. Jayashree, J. S. Spendelow, J. Yeom, C. Rastogi, M. A. Shannon and P. J. A. Kenis, *Electrochim. Acta*, 2005, **50**, 4674-4682.
41. G. Hussain and D. S. Silvester, *Anal. Chem.*, 2016, **88**, 12453-12460.
42. E. Herrero, L. J. Buller and H. D. Abruña, *Chem. Rev.*, 2001, **101**, 1897-1930.
43. J. J. Burk and S. K. Buratto, *J. Phys. Chem. C*, 2013, **117**, 18957-18966.
44. G. Gotti, K. Fajerwerg, D. Evrard and P. Gros, *Electrochim. Acta*, 2014, **128**, 412-419.
45. H. F. Waibel, M. Kleinert, L. A. Kibler and D. M. Kolb, *Electrochim. Acta*, 2002, **47**, 1461-1467.
46. F. Nasirpouri, *Journal*, 2017, **62**, 123-185.
47. E. Sheridan, J. Hjelm and R. J. Forster, *J. Electroanal. Chem.*, 2007, **608**, 1-7.
48. A. M. Feltham and M. Spiro, *Chem. Rev.*, 1971, **71**, 177-193.
49. A. J. Bard and L. R. Faulkner, *Electrochemical Methods: Fundamentals and Applications*, John Wiley New York, 2001.
50. U. Schroder, J. D. Wadhawan, R. G. Compton, F. Marken, P. A. Z. Suarez, C. S. Consorti, R. F. de Souza and J. Dupont, *New J. Chem.*, 2000, **24**, 1009-1015.
51. D. S. Silvester, A. J. Wain, L. Aldous, C. Hardacre and R. G. Compton, *J. Electroanal. Chem.*, 2006, **596**, 131-140.
52. J. Lee, K. Murugappan, D. W. M. Arrigan and D. S. Silvester, *Electrochim. Acta*, 2013, **101**, 158-168.
53. M. Miyake, T. Ueda and T. Hirato, *J. Electrochem. Soc.*, 2011, **158**, D590-D593.
54. S. Domínguez-Domínguez, J. Arias-Pardilla, Á. Berenguer-Murcia, E. Morallón and D. Cazorla-Amorós, *J. Appl. Electrochem.*, 2008, **38**, 259-268.
55. M. N. Dešić, M. M. Popović, M. D. Obradović, L. M. Vračar and B. N. Grgur, *J. Serb. Chem. Soc.*, 2005, **70**, 231-242.
56. H. Angerstein-Kozlowska, B. E. Conway and W. B. A. Sharp, *J. Electroanal. Chem. Interfacial Electrochem.*, 1973, **43**, 9-36.
57. D. Pletcher and S. Sotiropoulos, *J. Chem. Soc. Faraday Trans.*, 1994, **90**, 3663-3668.
58. J. Lee and D. S. Silvester, *Analyst*, 2016, **141**, 3705-3713.
59. T. J. Davies and R. G. Compton, *Journal of Electroanalytical Chemistry*, 2005, **585**, 63-82.
60. J. G. Huddleston, A. E. Visser, M. W. Reichert, H. D. Willauer, G. A. Broker and R. D. Rogers, *Green Chem.*, 2001, **3**, 156-164.
61. X. Ji, D. S. Silvester, L. Aldous, C. Hardacre and R. G. Compton, *J. Phys. Chem. C*, 2007, **111** 9562–9572.
62. X. Ji, C. E. Banks, D. S. Silvester, L. Aldous, C. Hardacre and R. G. Compton, *Electroanal.*, 2007, **19**, 2194 – 2201.

63. K. Murugappan, J. Lee and D. S. Silvester, *Electrochem. Commun.*, 2011, **13**, 1435-1438.
64. M. T. Carter, J. R. Stetter, M. W. Findlay and V. Patel, *ECS Trans.*, 2012, **50**, 211-220.
65. M. T. Carter, J. R. Stetter, M. W. Findlay and V. Patel, *ECS Trans.*, 2014, **64**, 95-103.
66. J. F. M. Oudenhoven, W. Knoben and R. van Schaijk, *Procedia Eng.*, 2015, **120**, 983-986.

Chapter 6

6. Fast Responding Hydrogen Gas Sensors Using Platinum Nanoparticle Modified Microchannels Filled With Room Temperature Ionic Liquids

In this chapter, conventional gold electrodes are modified with highly hydrophobic hexadecanethiol (HDT), using polydimethyl siloxane (PDMS) stamps, to create exposed Au microchannels. Platinum nanoparticles (PtNPs) are electrodeposited in the Au microchannels to obtain PtNP modified microband electrodes. Finally, these PtNPs modified electrodes are employed to sense hydrogen gas in RTILs, and are compared to conventional Au electrodes with PtNPs (with no microchannels) and also to bare Pt electrodes. To investigate the sensitivity for hydrogen gas on these electrodes, two electrochemical techniques; cyclic voltammetry (CV) and long term chronoamperometry (LTCA) are employed. The microchannel-modified electrodes show stable responses, dramatically enhanced current signals and very fast response times compared to conventional electrodes.

6.1 Introduction

The monitoring of hydrogen gas is of great importance due to its flammable and explosive nature. It is widely used in aeronautic, aerospace, automobile, medical and industrial applications.[1-4] Hydrogen is explosive when mixed with oxygen/air in the concentration range of 4-75 % by volume.[5] The lower end of this limit (4 %) is called the lower explosive limit (LEL) and the upper limit (75 %) is called the upper explosive limit (UEL). The accidental release of hydrogen has contributed to many disasters; including the Hindenburg disaster in 1937, Three Mile Island accident in 1979, Chernobyl accident in 1986, and more recently, the Fukushima nuclear power plant explosion in 2011 that resulted in several deaths and released a large amount of radioactivity which will have long-term effects on the environment, human, animal and marine life.[6-10]

Despite its flammable/explosive nature, the use of hydrogen as a fuel in power generation applications is of great interest currently, due to the formation of less less polluting emission products (i.e. water).[11] Recently hydrogen fuel cell vehicles have

found great importance in developed countries and including hydrogen-powered cars, buses, trucks, submarines, and ships where hydrogen combines with oxygen to produce electricity, water and heat as a byproduct.[12-15] Hydrogen also used as a cryogenic fuel in rockets during aerospace operations, and lifting gas in weather balloons.[16, 17] Hydrogen fuel cells and batteries are used in space stations and satellites.[18, 19] In power generation systems, hydrogen is used as a coolant, and has wide applications in the chemical industry e.g. in the synthesis of ammonia in the Haber process and for the production of fertilizers, methanol, cyclohexane and acetic acid.[3]

There is continuous need for selective, more accurate and faster detection methods for hydrogen at concentrations below the LEL due to its wide-spread, yet potentially hazardous use. This could alert the formation of potentially explosive gas/air mixture and thus to prevent against possible explosion/accidents,[20] especially in transportation applications, power plants, the petroleum industry, and the nuclear industry, Different chemical methods have been employed to monitor hydrogen gas such as gas chromatography or mass spectrometry, where the gas molecules are separated using a column or identified on the basis of their deflection from a magnetic field, respectively. These instruments are very costly, large in size, need high maintenance and have a relatively slow in sampling time.

However, there has been continuous struggle on the miniaturization of hydrogen sensing devices over the last few decades.[20, 21] These include solid state hydrogen sensors based on noble metal hybrid thin films coupled with micro-electro-mechanical systems (MEMS) where a change in resistance is used to detect hydrogen.[22] Sadek *et al*. reported a conducting polymer based conductometric hydrogen gas sensor where doped and dedoped polyaniline nanofibers were deposited onto a sapphire transducer to measure the resistance of the sensitive layer upon exposure to hydrogen at room temperature.[23] Recently, Gu *et al*. reviewed hydrogen gas sensors based on semiconductor metal oxide (SMO) thin layer nanostructures that measure the resistance, work function, optical properties, and acoustic waves of the SMO layer when the sensors are exposed to hydrogen gas.[24] However all these sensors are still in the development phase and a lot of research is required to improve their sensitivity, selectivity, response time, along with their cost, portability, robustness, miniaturization, and their power consumption capacity.

There have been different types of commercially available hydrogen sensors which are mostly based on solid-state sensing materials and are relatively expensive and large in size.[25, 26] Recently, Stetter *et al*. reviewed amperometric hydrogen gas sensors which can be chip based devices, having a high sensitivity and selectively, with fast response time, small in size, cheap, portable, and can operate at both low and high temperature using liquids, polymers and solid electrolytes.[21, 27] Recently, Gunawan *et al*. reported a robust and versatile method to fabricate ionic liquid microarrays on gold surfaces for sensing devices using microcontact printing techniques. Thiol-functionalized ionic liquid micropatterns were printed onto a gold substrate and used for a range of applications.[28] In this chapter, we follow a similar strategy where we microfabricate the highly hydrophobic thio-functionalized organic molecules, hexadecanethiol (HDT) onto gold surfaces using polydimethyl siloxane (PDMS) stamps to create Au microchannels with HDT micropattern to form the arrays of microband electrodes. Then we modify the Au microchannels with PtNPs electrochemically and finally employed these PtNPs modified Au microchannels (PtNPs Au microchannels) for hydrogen gas sensing with room temperature ionic liquids. The results on PtNPs Au microchannels were also compared with PtNPs modified gold and bare Pt macrodisk electrodes, to investigate whether the PtNP modified Au microchannels can be employed together with RTILs in amperometric devices to form low-cost, spill-less, robust, miniaturized, fast responding, and membrane free microarrays hydrogen gas sensors which can give fast responses (few seconds) for hydrogen at even low concentrations.

6.2 Experimental

6.2.1 Chemical Reagents

All chemicals were commercially available and used as received. Ethanol (EtOH, 99 %, Sigma-Aldrich), acetone (99%, Sigma-Aldrich), sulfuric acid (98% w/w [18.4 M], Sigma-Aldrich), chloroplatinic acid hydrate ($H_2PtCl_6.xH_2O$, anhydrous, trace metal basis, ≥ 99.9 %, Sigma-Aldrich), and hexadecanethiol (HDT, 99.9 %, Sigma-Aldrich) were used as received. The room temperature ionic liquids (RTILs) 1-ethyl-3-methylimidazolium bis(trifluoromethylsulfonyl)imide, ($[C_2mim][NTf_2]$), N-butyl-N-methylpyrrolidinium bis(trifluoromethylsulfonyl)imide ($[C_4mpyrr][NTf_2]$), were purchased from Merck (Kilsyth, Victoria, Australia) at ultra-high purity

electrochemical grade. Ultrapure water with a resistance of 18.2 MΩcm was prepared by an ultrapure water purification system (Millipore Pty Ltd., North Ryde, NSW, Australia). Acetone (>99.9 %, Sigma-Aldrich) was used for washing the electrodes before and after use. Ethanol (99%, Sigma-Aldrich) was used to wash the HDT printed gold electrode prior to starting gas experiments. Hydrogen gas (100%, high purity) and nitrogen gas (≥ 99.99 %, high purity compressed gas used for further dilution of H_2) cylinders were purchased from BOC gases, Welshpool, WA, Australia.

6.2.2 Fabrication of HDT Microchannels and Electrodeposition of PtNPs on Au Microchannels

The gold macrodisk electrode was employed as an array of microband electrodes using the microcontact printing technique, developed by A/Prof Chuan Zhao's group (UNSW, Australia). Microbands or microarrays electrodes are usually employed when enhanced current density and fast response time is required.[28-30] For this, the gold surface was printed with hexadecanethiol (HDT) using a polydimethyl siloxane (PDMS) stamp to create an array of Au microchannels or microbands. For this, a polished and cleaned gold macrodisk electrode was employed for modification with HDT microchannels. If the surface is not clean enough, a poor HDT micropattern was obtained with broken HDT microchannels, so a clean electrode was essential. Figure 6.1 shows a schematic illustration for the printing process of the HDT microchannels on a gold substrate.

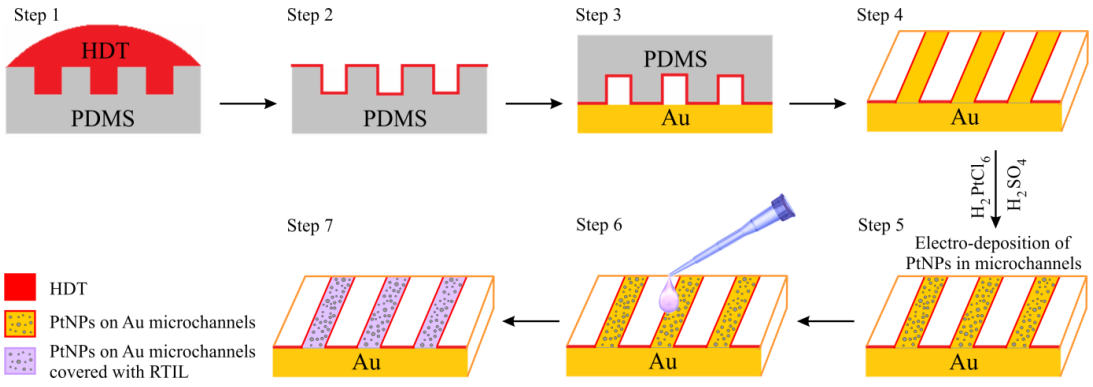

Figure 6.1: Schematic illustration of the protocol for the creation of Au microchannels with HDT and electrochemical deposition of PtNPs into these Au microchannels.

A microcontact printing technique was used to create uniform size and shape of Au microchannels along with the electrochemical modification of these Au microchannels with PtNPs. Prior to modification, the PDMS stamp was sonicated in ethanol for 2 minutes to ensure no previous ink or impurities were present on the stamp. To print HDT microchannels, the PDMS stamp was inked with one drop of 5 mM ethanolic HDT solution for 1 minute (step 1). The excess HDT droplet was removed and the stamp was dried gently under nitrogen stream for 30 seconds (step 2) and printed onto the gold electrode for ca. 50 seconds (step 3). After printing the HDT microchannels, the gold electrode with the micropattern was rinsed twice in ethanol and then dried gently under a nitrogen stream (step 4).

In step 5, the Au microchannels were electrochemically modified with PtNPs. For this, the HDT modified gold working electrode was employed in a conventional three electrode arrangement, with a stable Ag/AgCl reference electrode (0.1 M KCl, BASi, Indiana, USA) and Pt wire counter electrode (diameter 0.5 mm, Goodfellow, Cambridge Ltd., UK), suspended into a home-made glass cell which contained 2-3 mL deaerated solution of 5 mM H_2PtCl_6 in 0.5 M H_2SO_4. The electrochemical deposition of PtNPs was started from the open circuit potential (0.68 V), then the potential was held at -0.2 V for 10 seconds. After deposition, the electrode was washed with ultrapure water and dried gently under nitrogen stream. A tiny droplet of RTIL was drop cast on the PtNPs modified Au microchannels (step 6) and then spread with the help of micropipette to fill the PtNPs Au microchannels (step 7). Excess RTIL was removed by using lint-free tissue or by back suction with a micropipette. To connect the RTIL filled Au microchannels to the counter and reference electrodes, another tiny droplet of RTIL was drop cast close to one end of the microchannels on the insulating plastic body of the working electrode. The Ag and Pt wires were dipped into this tiny droplet of RTIL at an angle of 120^o to connect the working, counter and reference electrodes.

Figure 6.2 shows the cartoon of microcontact printed amperometric gas sensor with PtNPs modified Au microchannel working electrode, along with Pt wire counter electrode and Ag wire reference electrodes. It can be seen (Figure 6.2a) that both counter and reference electrodes were in contact with PtNP modified Au microchannels through the RTIL. This is the hardest part during the fabrication of the microelectrochemical cell. Figure 6.2b shows the 3D view of microarray gas sensor. It can be assumed that when the microelectrochemical cell was exposed to the

analyte gas, a fast response time can be obtained due to a very small thickness of RTIL as a result of the small diffusion path of the gaseous analyte.

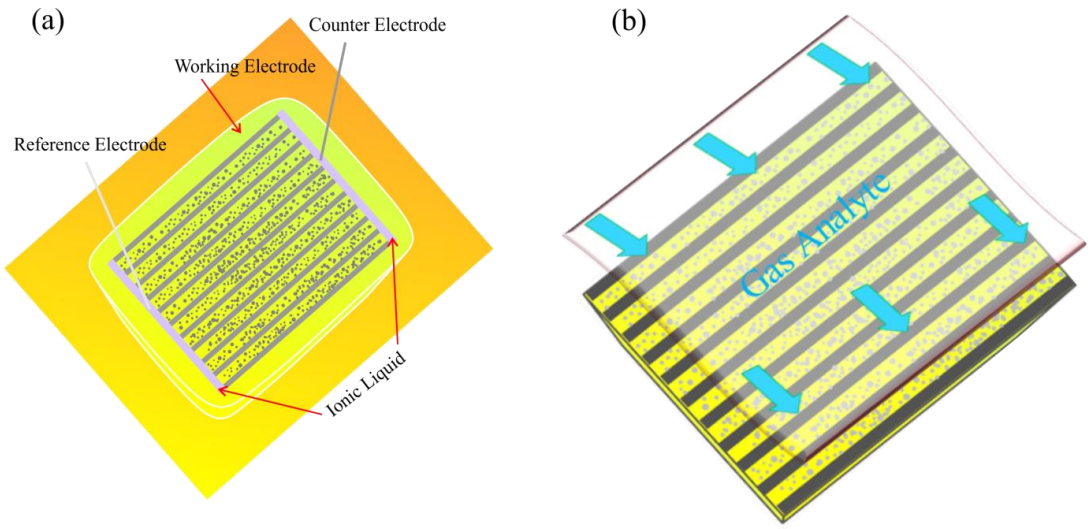

Figure 6.2: (a) Schematic illustration of microcontact printed amperometric gas sensor with working, counter and reference electrodes, (b) 3D view of microarray gas sensor with PtNPs modified gold microchannels. [adapted from][31] Note: the working electrode is a gold macrodisk electrode (not rectangular as shown in the image).

6.2.3 Electrochemical Experiments

All experiments were performed using a PGSTAT101 Autolab potentiostat (Eco, Chemie, Netherlands) interfaced to a PC with Nova 1.11 software, at laboratory room temperature (294±1 K) inside an aluminium Faraday cage present in the fume cupboard to reduce electrical interference. Gold (Au) and platinum (Pt) conventional macrodisk electrodes (diameter 1.6 μm) from BASi (Indiana, USA) were employed as gas sensing surfaces. Prior to starting gas experiments, the surface of both electrodes was mechanically polished on soft polishing pads (Buehler Illinois) with decreasing size of alumina powder (3 µm, 1 µm and 0.05 µm, Kemet, NSW, Australia). After polishing, the electrodes were cleaned by ultrasonication first in ethanol, then in milli-Q water for 5 minutes each, and finally washed with ultrapure water and dried under a nitrogen stream.

For gas sensing experiments, PtNPs modified Au microchannels was employed as an array of microband electrode along with the gold and bare Pt macrodisk electrodes for comparison. Prior to start gas sensing experiment on gold macrodisk electrode, the surface was electrodeposited with PtNPs for 10 seconds using 5 mM H_2PtCl_6

with the same method as discussed above, since hydrogen is not electrochemically active on gold surfaces.[32, 33]

For gas sensing experiments, all three electrodes employed a Pt wire counter electrode and a silver (Ag) wire quasi-reference electrode. 4 μL of RTIL was drop-cast on the PtNP modified gold electrode and bare Pt macrodisk electrode. For gas experiments, the electrochemical cell was placed into a modified rubber bung and then housed very gently into the bottom of a specially designed glass T-cell,[34] whose top was closed with a glass stopper. The cell had two openings: an inlet from where the analyte gases (hydrogen, nitrogen) entered and passed over the electrodes, and an outlet to allow the gas to be expelled into the fume cupboard. Prior to the introduction of hydrogen gas, the cell was purged with nitrogen to remove any dissolved gases and impurities present in the RTIL. When the baseline was stable (after ca. 20 minutes), hydrogen gas was introduced into the cell and continuously flowed over the electrode.

Prior to recording cyclic voltammetry, the potential was hold at + 2.0 V for 60 seconds for pretreatment of the electrode surface, before scanning between – 0.6 V and + 0.6 V. The potential was stepped from where the current is zero and then held at a suitable overpotential for a given time until a stable baseline was obtained. Then the hydrogen gas was introduced into the cell at different concentrations (10-100 %, 1-10 %) over time until a stable, maximum steady state response was obtained, with a N_2 flushing step in between each concentration range.

6.2.4 Gas Mixing System

A high purity hydrogen gas cylinder (100 %) was used as a standard. In order to obtain different concentrations of hydrogen gas, highly compressed nitrogen gas was used for further dilution using a gas mixing system as reported previously by our group.[34, 35] This consists of two digital flow meters (0-1.0 L/min, John Morris Scientific, NSW, Australia), one connected with hydrogen gas cylinder and other with nitrogen cylinder through PTFE tubing via a Swagelok T-joint (Swagelok, Kardinya, WA, Australia). The mixture of both gases (H_2/N_2) was then passed through an additional gas-mixing segment[36] to increase turbulence and to ensure adequate mixing of both gases. The relative flow rates were used to calculate the different concentrations of hydrogen gas introduced into the cell.

6.2.5 Electrode Imaging

A light microscope (Nikon Optiphot-2) was used to take reflection micrographs of bare and RTIL filled Au microchannels. Scanning electron microscopy (SEM) experiments were performed on the bare Au microchannels and PtNP modified Au microchannel electrodes. SEM Images were obtained using MIRA3 (MIRA VP-FESEM), with a voltage of 5.0 kV (see Figure 6.3). Atomic force microscopy (AFM) was performed using WITech alpha 300SAR on the PtNP modified Au microchannels to investigate the morphology of the PtNPs, the depth of the Au microchannels, and the thickness of the blocking HDT microchannels.

6.3 Results and Discussion

6.3.1 Characterisation of Bare and PtNP Modified Au Microchannels Using SEM and AFM

In this study, two HDT modified gold electrodes have been employed – bare Au microchannels and PtNPs modified Au microchannels. Reflection micrographs for bare Au microchannels and Au microchannels filled with RTIL are shown in Figure 6.3a,b. Figure 6.3a shows the uniform size and shape of the HDT micropattern (HDT layer width 52 μm) which creates bare Au microchannels (width 48 μm). Figure 6.3b shows the RTIL present in the Au microchannels and not on the HDT micropattern. This can be attributed due to the different strengths of intermolecular forces between the gold substrate and HDT modified microchannels. The strength of intermolecular forces between the two different surfaces usually follow a trend of hydrophilic/hydrophilic > hydrophilic/hydrophobic > hydrophobic/hydrophobic.[37] Thus a hydrophobic RTIL will preferentially bond to the hydrophilic gold substrate rather than the hydrophobic HDT. After printing of HDT microchannels, the area covered by RTIL micropattern was approximately half (48 μm exposed gold *vs* 52 μm HDT micropattern) of the total area of the bare gold macrodisk electrode. A detailed investigation of the RTIL micropattern shows that a very thin film of RTIL is formed on the Au microchannels with clear straight edges (Figure 6.3b). The thickness of the RTIL film in the filled Au microchannels was measured to be 10 ± 0.5 μm by confocal microscopy and the volume of RTILs used to fill the microchannels was 20 nL plus additional tiny droplet at the side to connect the microchannels with CE and RE together. This thin film of RTIL with nanolitter

volume is favourable to enhance the response time for an analyte gas, compared to a conventional macrodisk electrode where a droplet of RTIL (ca. 1.0 ± 0.05 mm) is required to connect the electrodes.

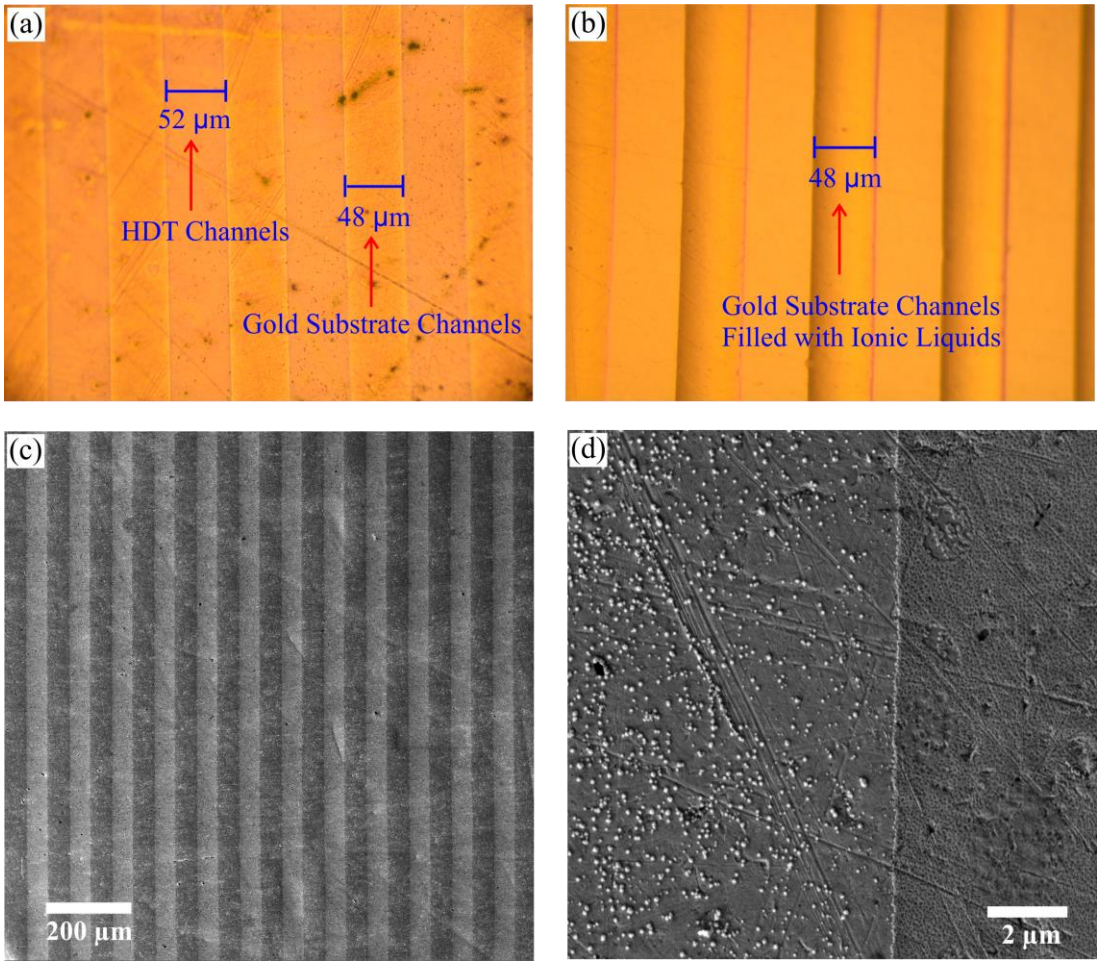

Figure 6.3: Reflection micrographs of (a) Au microchannels made by a HDT stamp on a gold macrodisk electrode, and (b) the same Au microchannels filled with ionic liquid (width of Au micochannels = 48 µm, width of HDT microchannels = 52 µm). Scanning electron microscopy (SEM) images of (c) bare Au microchannels, (d) electrodeposited PtNP modified Au microchannels.

Figure 6.3c shows an SEM image of bare Au microchannels (light grey) with printed HDT channels (dark grey). Uniform bare gold microchannels are present, each with a width of 48 μm. The HDT layer width was 52 μm, with a uniform thickness of ca. 50 ± 4 nm, measured using atomic force microscopy. Figure 6.3d shows one Au microchannel modified with PtNPs, next to a HDT covered channel. It can be seen very clearly that there is no deposition of PtNPs in the HDT channels. This is due to the long chain of carbon atoms attached to the thiol group that renders the gold surface as an insulator. The size and density of PtNPs were found to be 54 ± 20 μm

and 254 ± 0.2 NPs/μm^2, respectively, measured using image *J*. The spacing between the nanoparticles to be ca. 300 nm, which is small compared to the thickness of the electrolyte (10 ± 0.5 μm). The electroactive surface area (ESA) of PtNP Au microchannels was calculated from the hydrogen desorption peaks [38, 39] which is (6.83 ± 0.2 μm^2), 1.7 times higher than the PtNP modified gold (4.11 ± 0.1 μm^2) and 2.3 times higher than the bare Pt (2.97 ± 0.01 μm^2) macrodisk electrodes.

6.3.2 Electrochemical Mechanism for Hydrogen Oxidation on Macrodisk and Microchannel Electrodes

Four different surfaces were employed for a mechanistic study of hydrogen oxidation; (i) bare platinum and (ii) bare gold macrodisk electrodes, (iii) PtNP modified gold and (iv) PtNP modified Au microchannels. The RTIL [C_2mim][NTf_2] was used as an electrolyte due to its relatively low viscosity, clear peak shaped response for 100% hydrogen and chemically reversible voltammetry as reported previously.[40, 41] Figure 6.4 shows overlaid voltammograms for the oxidation of 100% hydrogen at a scan rate of 100 mVs^{-1}. The mechanism for hydrogen oxidation was found to be the same on all surfaces except on the bare gold electrode (red CV), where no oxidation peaks were observed. This is because hydrogen is electrochemically inactive on gold surfaces.[32, 33] On the PtNP modified gold electrode (black CV), a transient peak shaped voltammeteric response was obtained, corresponding to the oxidation of hydrogen gas. The reverse scan corresponds to the reduction of the solvated proton ($H[NTf_2]_x$) in the reverse scan, as reported previously.[32, 33] Larger peak currents were obtained on the PtNP modified Au electrode compared to the bare Pt electrode. This is due to the presence of PtNPs on the gold surface which not only makes the gold surface electrochemically active for hydrogen oxidation but also provides a large electroactive surface area, sharper peaks and enhanced current response compared to the bare Pt electrode. The peak to peak separation (ΔE_p) was calculated from the corresponding peak potentials. A value of 114 mV was measured, suggesting that the oxidation of hydrogen in [C_2mim][NTf_2] on PtNPs modified gold electrode is an electrochemically quasi-reversible process, consistent with previous reports.[33] In the case of a bare Pt macrodisk electrode (blue CV), a slightly smaller curent is observed compared to the the PtNP modified gold electrode, with a lower current fall-off after the oxidation peak. The decrease in peak current is possibly due to a lower electroactive surface area than the PtNP modified

gold electrode. It is also noted that when the potential is scanned more positive on the bare Pt electrode, a small shoulder appeared in the limiting current region (results not shown) that could be due to the oxidation of an oxide layer or impurities present on the surface of the Pt electrode.

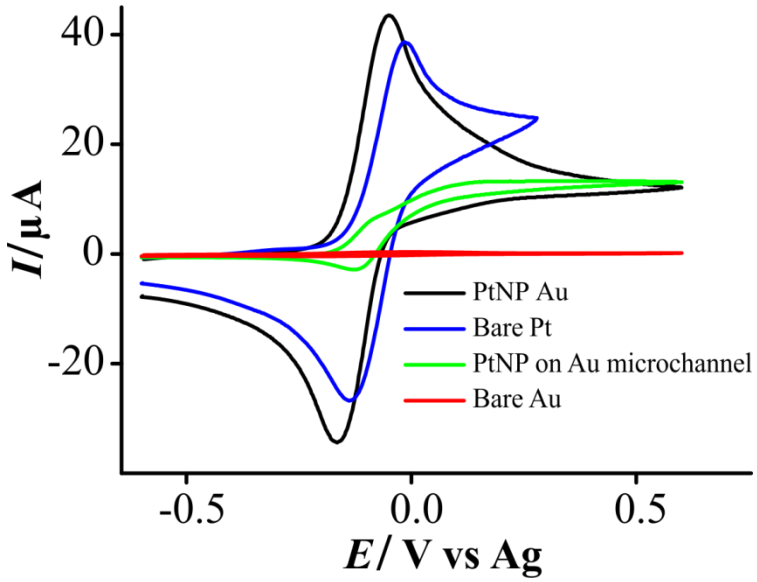

Figure 6.4: Electrochemical oxidation of 100 % H_2 on (black) PtNP modified gold electrode, (blue) bare Pt electrode, (green) PtNP modified Au microchannels, (red) bare gold electrode in $[C_2mim][NTf_2]$ at a scan rate of 100 mVs^{-1}.

The voltammetric response for hydrogen oxidation on the PtNP modifed gold microchannel electrode (green CV) has a steady-state shaped oxidation response. This is probably due to the geometry of the Au microchannels, where a mixture of radial diffusion and linear diffusion patterns are present in the microchannels.[42, 43] However, on the reverse sweep, the reduction was peak shaped and transient in nature, likely to be due to the different diffusion coefficient of the electrogenerated proton compared to hydrogen[32, 33, 44-46] (also observed previously for the oxygen/superoxide redox couple in RTILs).[44] The peak to peak separation (ΔE_p), could not be calculated due to a pseudo-steady state current response. Comparatively, the current response obtained on the PtNP Au microchannels was three times smaller than for the PtNP modified gold macrodisk electrode since the active area on the microchannel electrodes is the area that is covered by the Pt-nanoparticles. This is about one half of the total electrode area (the rest of electrode is covered by HDT micropattern) and explains why the current response obtained on the microband electrodes was three times smaller. The identity of the oxidation peak on all surfaces can be described by the following equation:[33]

Oxidation Peak $$H_2(g) + 2A^- \rightarrow 2HA + 2e^-$$ **(6.1)**

Where A^- is the RTIL anion ($[NTf_2]^-$).

6.3.3 Analytical Response for Hydrogen Oxidation on Macrodisk and PtNP Modified Microchannel Electrodes

In order to investigate the ability of PtNP modified microchannels *vs* PtNP modified Au and bare Pt electrodes to detect hydrogen gas, the analytical utility and sensitivity for hydrogen oxidation was studied in $[C_2mim][NTf_2]$. On PtNP modified Au microchannel electrodes, the results were compared in two RTILs: $[C_2mim][NTf_2]$ and $[C_4mpyrr][NTf_2]$. Two electrochemical techniques were employed: cyclic voltammetry (CV) and long-term chronoamperometry (LTCA) to study the limits of detection (LODs) and response times for hydrogen oxidation.

6.3.3.1 Cyclic Voltammetry on PtNP Modified Au vs Bare Pt Electrodes

Figure 6.5 shows cyclic voltammetry (CV) for the oxidation of 10-100 % of hydrogen in $[C_2mim][NTf_2]$ on (a) PtNPs modified gold electrode, and (b) bare Pt electrode at a scan rate of 100 mVs^{-1}. The red dashed line shows the response in the absence of hydrogen. The insets show the corresponding calibration plots of oxidation peak currents (baseline corrected) *vs* hydrogen concentration in the gas phase.

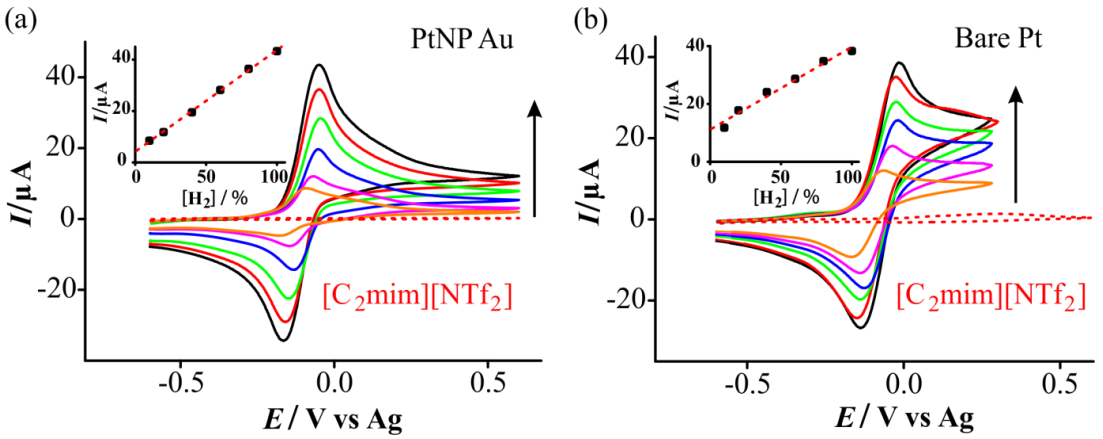

Figure 6.5: Electrochemical oxidation of 10-100 % H_2 on a (a) PtNP modified gold electrode, and (b) bare Pt electrode in $[C_2mim][NTf_2]$ at a scan rate of 100 mVs^{-1}. Inset shows the calibration plots of peak current (baseline corrected) vs concentration, along with the line of best fit. Dotted line is blank voltamogram in the absence of H_2.

On both electrodes, peak shaped behaviour was obtained with stable peak potentials *vs* a Ag wire quasi-reference electrode. Sharp peaks with slightly higher currents were observed on the PtNP modified gold electrodes as compared to the bare Pt electrode. On both surfaces, as the concentration of hydrogen increased from 10 % to 100 %, the current response increased linearly. The oxidation peak currents were plotted against the respective concentrations range with excellent linearity (R^2 > 0.999) observed on the PtNP modified gold electrode. Whereas on bare Pt electrode, a slightly curved response was obtained (R^2 = 0.979) where the straight line deviated at lower concentrations (10 %) and did not pass close to the origin. Since the H_2 oxidation process is reported to be more complicated that a simple diffusion controlled process (due to the presence of surface oxides),[33] this behaviour is not surprising. The better response on the PtNP modified electrode may be due to the fresher Pt deposits and less surface oxide formation than the bare Pt electrode.

6.3.3.2 Cyclic Voltammetry on PtNP Modified Au Microchannel Electrodes

Figure 6.6 shows cyclic voltammetry (CV) for the oxidation of 10-100 % of hydrogen on PtNP modified Au microchannels in the RTILs (a) [C_2mim][NTf_2], and (b) [C_4mpyrr][NTf_2] at a scan rate of 100 mVs^{-1}. The response in the absence of hydrogen is shown by the dashed red line. The insets show the corresponding calibration plots of oxidation currents (baseline corrected) *vs* gas phase concentration of hydrogen.

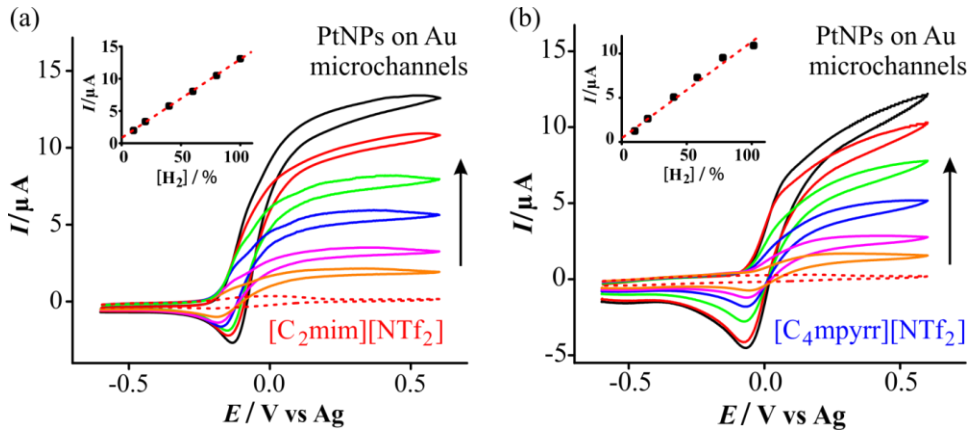

Figure 6.6: Electrochemical oxidation of 10-100 % H_2 on PtNP modified Au microchannels on gold electrode in (a) [C_2mim][NTf_2], and (b) [C_4mpyrr][NTf_2] at a scan rate of 100 mVs^{-1}. Insets show the calibration plots of peak current (baseline corrected) *vs* concentration, along with the line of best fit. Dotted line is blank voltamogram in the absence of H_2.

During the forward scan in both RTILs, a steady state response was obtained for the oxidation process, while the reverse process was peak shaped. In $[C_2mim][NTf_2]$, relatively higher currents were obtained with steady state current plateaus, whereas in $[C_4mpyrr][NTf_2]$, slightly smaller currents were observed with a sloping steady state response, particularly at higher concentrations. The difference in current response is due to the higher viscosity of $[C_4mpyrr][NTf_2]$ compared to $[C_2mim][NTf_2]$, which results in a smaller diffusion coefficient of H_2 and consequently a decrease in the current response.[46] The sloping steady state response in $[C_4mpyrr][NTf_2]$ may also be due to the effect of the thickness of the electrolyte; the *i*R resistance effect due to a thin layer cell which results in depletion of analyte in the electrolyte space.[47] To investigate the analytical utility and LODs on PtNP modified Au microchannels, the steady state oxidation currents were measured from a fixed potential of +0.4 V and plotted against the respective concentration. Excellent linearity ($R^2 = 0.999$) was obtained in $[C_2mim][NTf_2]$, while in $[C_4mpyrr][NTf_2]$, the gradient deviated slightly from linearity ($R^2 = 0.996$) at higher concentrations (100 %).

Table 6.1 shows the analytical parameters resulting from the calibration plots for 10-100 % hydrogen oxidation. The sensitivity values were calculated from the gradient of the line of best fit and limits of detection (LODs) were calculated using three times the standard deviation of the slope of the line of best fit, over the concentration range studied. The sensitivities were higher on the PtNPs modified gold electrode, as expected due to its larger electroactive surface area compared to the bare Pt electrode. Importantly, the sensitivity of the PtNP modified Au microchannel electrode was comparatively higher (given that more than one half of its total active area is blocked by HDT) than the other modified or unmodified electrodes, indicating that the AuNPs gold microchannels are beneficial from an analytical perspective. The LODs on the PtNP modified Au microchannel electrodes were ca. 7 times smaller (2.5 %) than the bare Pt electrodes (17 %) for the higher concentration range (10-100%) studied, but is still below the lower explosive limit (LEL) for hydrogen (4 %). This could be further lowered by studying a lower concentration range, as discussed in the next section. The most important observation from Table 6.1 is that the lowest LODs were obtained on PtNP modified Au microchannel electrodes, and

thus these micropattern electrodes have been chosen to detect hydrogen at even lower concentrations (1-10%) in two different RTILs.

Table 6.1: Analytical parameters (sensitivity and limit of detection, LOD) calculated for hydrogen oxidation (10-100 %) in [C_2mim][NTf_2] and [C_4mpyrr][NTf_2] on PtNP modified Au microchannels, along with bare Pt and PtNP modified Au macrodisk electrodes in [C_2mim][NTf_2] using cyclic voltammetry (CV) and long-term chronoamperometry (LTCA). Data obtained from the 1-10 % range is also included for PtNPs Au microchannels in both RTILs.

Electrode	Concentration / %	CV		LTCA		
		Sensitivity / $A\%^{-1}$	LOD / %	Sensitivity/$A\%^{-1}$	LOD / %	t_{90}/ s
PtNP Au	10-100	4.0×10^{-7}	3.9	8.2×10^{-8}	3.6	39
Bare Pt	10-100	2.9×10^{-7}	17	5.2×10^{-8}	24	46
PtNP Au Microchannels	10-100 1-10	1.2×10^{-7} 2.1×10^{-7}	2.5 0.4	9.6×10^{-8} 1.5×10^{-7}	3.4 0.1	2 4
PtNP Au Microchannels*	10-100 1-10	1.0×10^{-7} 1.6×10^{-7}	7.2 0.7	3.7×10^{-8} 3.4×10^{-8}	23 0.5	2 5

* The RTIL used is [C_4mpyrr][NTf_2]

6.3.3.3 Low Concentration Voltammetry on PtNP Modified Au Microchannel Electrodes

Figure 6.7 shows the voltammetric response for the oxidation of hydrogen at the low concentration range from 1-10 % on the PtNP modified Au microchannel electrode in the RTILs (a) [C_2mim][NTf_2], and (b) [C_4mpyrr][NTf_2] at a scan rate of 100 mVs^{-1}. The red dashed line shows the response in the absence of hydrogen. The calibration plots for current *vs* concentration are shown in the corresponding insets. The shape of the voltammograms in both RTILs are steady state in this low concentration range. The most important observation from Figure 6.7 is that, even at low concentrations of 1 % hydrogen, the steady state response for hydrogen oxidation is clearly distinct from the blank response (noting the presence of some impurity peaks in the RTIL, particularly in [C_2mim][NTf_2]). Like for the higher concentration range, comparatively larger currents were observed in [C_2mim][NTf_2] compared to [C_4mpyrr][NTf_2]. To measure the sensitivity and LODs, the steady state peak currents were plotted *vs* concentration range. Excellent linearity (R^2 = 0.999) was obtained in [C_2mim][NTf_2], with a very low LOD (0.4 %), while in

[C4mpyrr][NTf2], a slight deviation in gradient (R^2 = 0.997) can be seen at lower concentrations (1 %) which results in a slightly higher LOD (0.7 %).

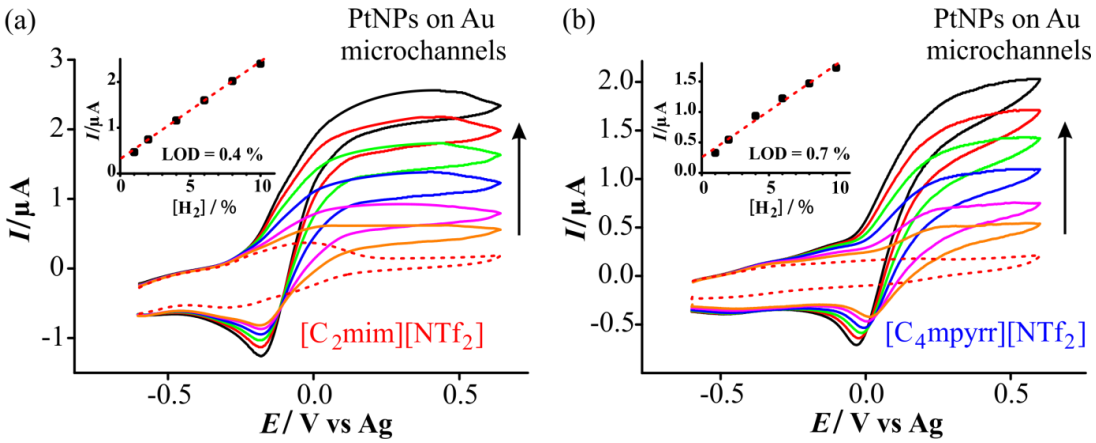

Figure 6.7: Electrochemical oxidation of 1-10 % H_2 on PtNP modified Au microchannels in (a) [C2mim][NTf2], and (b) [C4mpyrr][NTf2] at a scan rate of 100 mVs^{-1}. Insets show the calibration plots of peak current (baseline corrected) *vs* concentration, along with the line of best fit. Dotted line is blank voltamogram in the absence of H_2.

6.3.3.4 Scan Rate Study on PtNP Modified Au Microchannel Electrodes

In order to understand the voltammetric response on PtNP modified Au microchannels, cyclic voltammetry was performed at varyious scan rates in two RTILs: [C2mim][NTf2] and [C4mpyrr][NTf2]. Figure 6.8 shows CVs for 10 % hydrogen oxidation on PtNP Au microchannel electrodes in (a) [C2mim][NTf2] and (c) [C4mpyrr][NTf2] over a range of scan rates (10, 50, 100, 200, 300, 400, 500, 700, 1000 mV/s), with corresponding plots for peak current *vs* square root of scan rates and *vs* scan rate on the same plot. In both RTILs, the mechanism for hydrogen oxidation is believed to be the same as reported previously according to equation 6.1.[32, 33] It can be seen on both plots (Figure 6.8a,c) that the oxidation peak shape changes from steady-state at low scan rates to peak shaped at high scan rates. This type of voltammetry is usually observed on microelectrodes due to the intermediate behaviour between macro/micro diffusion regimes. It is important to note that when gases are studied in RTILs on microelectrodes, such transient behaviour is often observed at higher sweep rates, whereas a steady state response is seen at slower scan rates and can be described by the inequality in the following equation.[33, 48]

$$v \ll \frac{RTD}{nFr_e^2} \qquad \textbf{(6.2)}$$

where v is the scan rate, R is the universal gas constant, T is the absolute temperature, D is the diffusion coefficient, n is the number of electrons transferred, F is the Faraday constant, and r_e is the width of microchannel. This behaviour (transient to steady state) can be demonstrated when the radius of the electrode is known. However in the microchannel electrodes employed in this work, it is difficult to calculate the exact electroactive area. But from both plots (Figure 6.8a,c), it can be seen that transient behaviour starts at a sweep rate of 200 mV/s, while steady state is observed at 100 mV/s and below.

This behaviour can also be demonstrated in terms of thickness of the diffusion layer of an analyte species *vs* width of the microchannels. On microelectrodes, using CV at fast scan rates (sufficiently short times), the thickness of the diffusion layer (calculated to be 25 μm), is smaller than the width of the microchannels (r_e = 48 μm), and the microchannels appear more like a planar electrode to the electroactive species at the edge of the diffusion layer. Under these conditions, the microchannels could behave like a macroelectrode and linear diffusion may be observed on the surface of the microchannels, which results in a peak shaped response for fast scan rates. This behaviour can be expressed by the following equation:[49, 50]

$$\sqrt{Dt} \ll r_e \qquad \textbf{(6.3)}$$

Where D is the diffusion coefficient and t is the time of the experiment. As the time of the experiment increases, steady state behaviour starts to appear below ca. 200 mV/s. This indicates that at a longer experimental time, the diffusion layer thickness (57 μm for 200 mV/s) is equal to or greater than the width of the microchannels, so radial diffusion becomes dominant resulting in a steady state response.

Interestingly, in both plots, a peak shaped response was observed for reduction of the electrogenerated proton at all scan rates studied. This is due to the slower diffusion coefficient of the solvated proton ($\sim 10^{-7}$ cm^2 s^{-1}) compared to hydrogen ($\sim 10^{-5}$ cm^2 s^{-1}).[46] The peak current for H_2 oxidation in both RTILs was plotted *vs* both scan rate and square root of scan rate. A curved response with a second order polynomial was obtained for the plot of peak current *vs* square root of scan rate, suggesting that hydrogen oxidation on this surface is not a fully diffusion-controlled process. The plot of peak current *vs* scan rate is more linear (R^2 = 0.996 in [C_2mim][NTf_2] and R^2

= 0.992 in [C4mpyrr][NTf2]), which suggests that hydrogen adsorbs on the surface of the deposited PtNPs inside the Au microchannels before being oxidised.

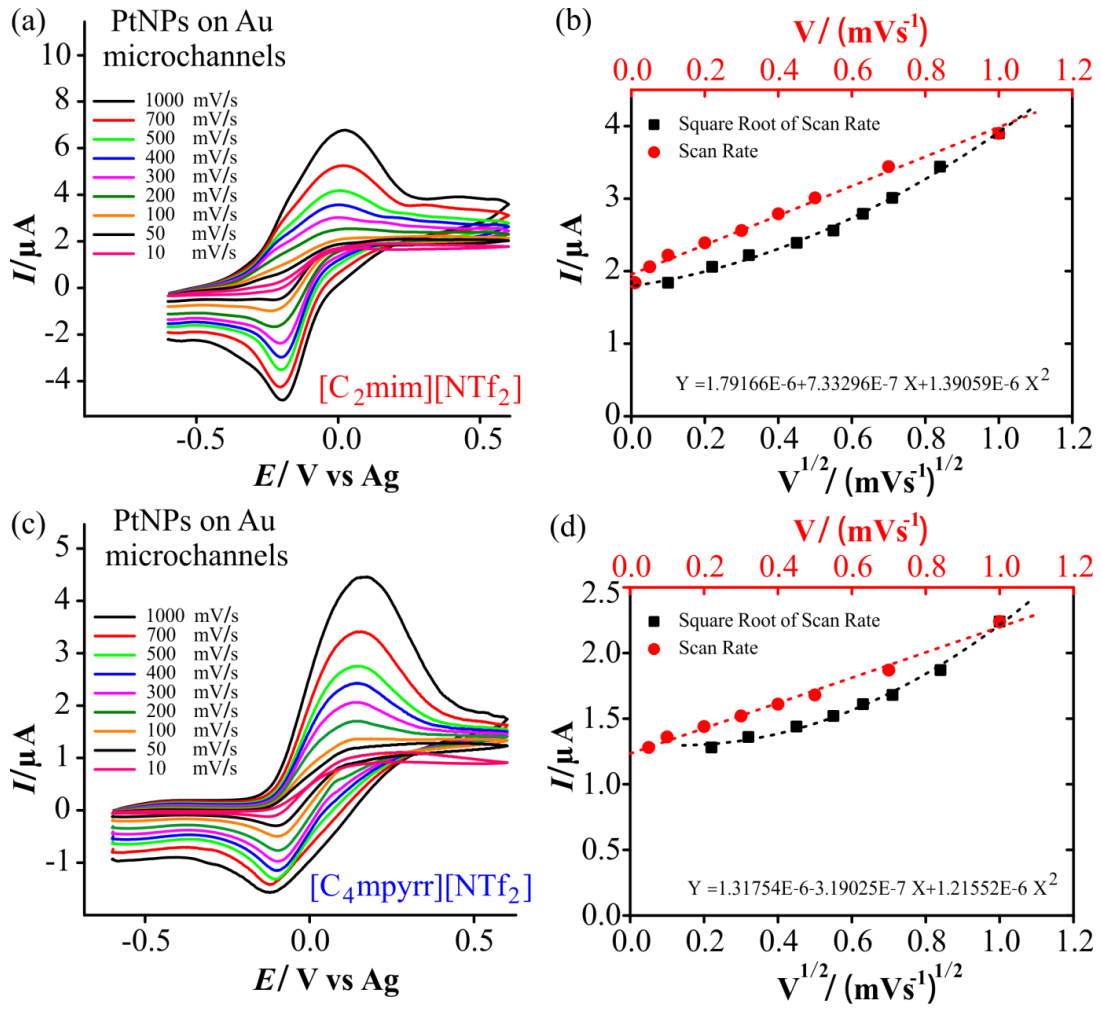

Figure 6.8: Cyclic voltammetry for the oxidation of 10 % hydrogen gas on PtNP modified Au microchannels in (a) [C2mim][NTf2], and (c) [C4mpyrr][NTf2] at a range of scan rates. Figures (b) and (d) show the corresponding plots for oxidation peak current *vs* scan rate and *vs* square root of scan rate.

6.3.3.5 Long-Term Chronoamperometry

In order to test the ability of the modified surfaces for "real-time" hydrogen gas sensors and to measure the response time (t_{90}), long-term chronoamperometry (LTCA) was performed for 10-100 % hydrogen on all three surfaces. On PtNPs Au microchannels, two concentrations ranges (10-100 % and 1-10 %) were studied in two different RTILs, [C2mim][NTf2] and [C4mpyrr][NTf2] for comparison. For this, initially the electrochemical cell was purged with 99.99% nitrogen for ca. 20 minutes and then the potential was stepped from – 0.45 V to a suitable overpotential (a) + 0.6 V (PtNP Au), (b) + 0.2 V (bare Pt), (c) + 0.6 (PtNP Au microchannels), and (d) + 0.6

(PtNP Au microchannels) and held for an extended period of time until a stable baseline was obtained. Hydrogen gas was introduced into the cell at different concentrations (100-10 %) for a sufficient time (ca. 100-150 seconds) until a maximum current was obtained. During each different concentration addition, nitrogen "flushing" was performed for ca. 200 seconds until a stable baseline was obtained. On each surface, initially the current was zero in the absence of hydrogen. When hydrogen gas was introduced into the cell at different concentrations, the current started to increase and reached a maximum current. Figure 6.9 shows the amperometric current-time (*I-t*) response for 10-100 % hydrogen in $[C_2mim][NTf_2]$ on (a) PtNP modified Au, (b) bare Pt, (c) PtNP modified Au microchannels, along with the corresponding calibration plots of maximum current *vs* concentration.

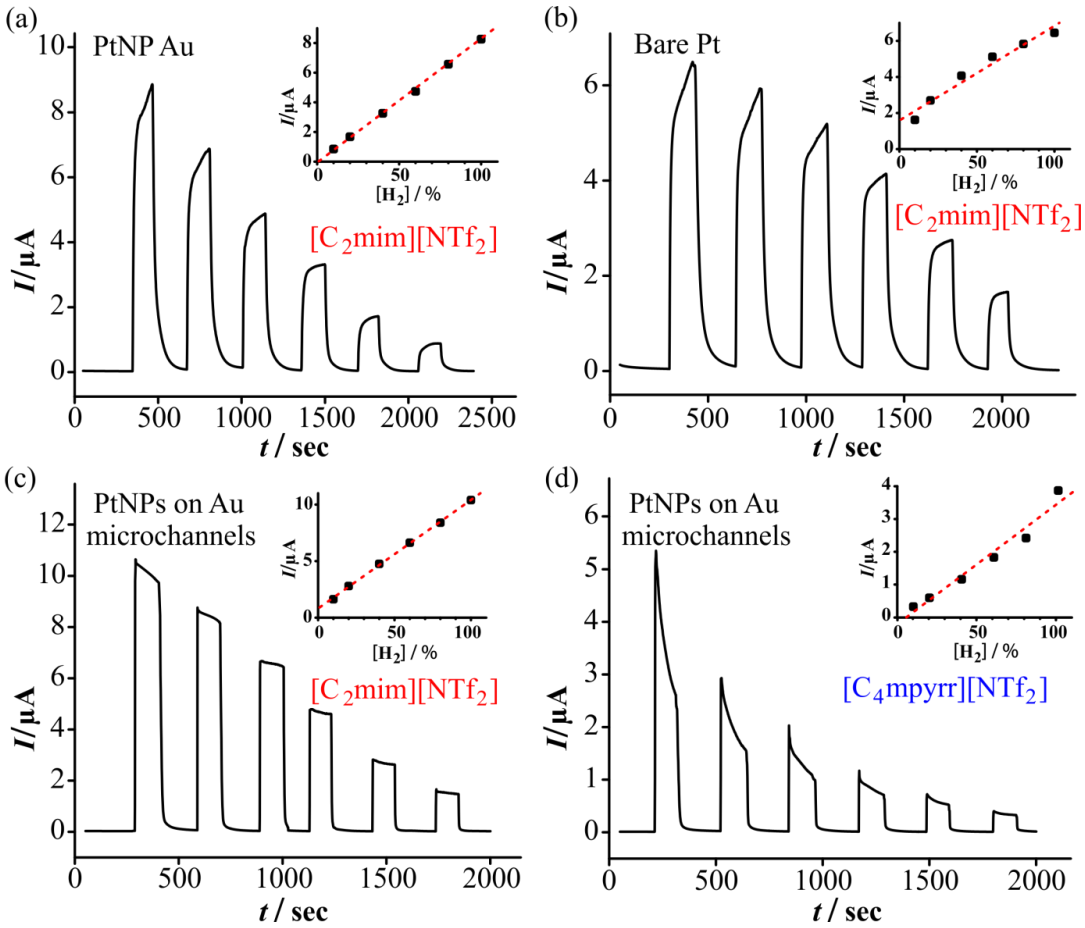

Figure 6.9: Long-term chronoamperometry (LTCA) for 10-100 % H_2 on (a) PtNP modified gold electrode, (b) bare Pt electrode, (c) PtNP modified Au microchannels in $[C_2mim][NTf_2]$, and (d) PtNP modified Au microchannels in $[C_4mpyrr][NTf_2]$. The potential was stepped from -0.45 V to (a) +0.6 V, (b) +0.2 V, (c) +0.6 V, (d) +0.6 V. Insets show the calibration plots of current (baseline corrected) *vs* concentration, along with the line of best fit.

Figure 6.9d shows the *I-t* response in $[C_4mpyrr][NTf_2]$ on PtNPs Au microchannels for comparison. On the PtNP modified Au and bare Pt electrodes (Figure 6.9a,b), the current continues to increase over time without reaching a stable plateau. However, on the PtNP modified Au microchannels (Figure 6.9c,d), initially the current reaches to maximum plateau within a few seconds, then starts to fall slightly in $[C_2mim][NTf_2]$ at higher concentrations, but is more stable at lower concentrations. Whereas in $[C_4mpyrr][NTf_2]$, a relatively smaller current was obtained due to the higher viscosity of the RTIL. It can be seen very clearly, in $[C_4mpyrr][NTf_2]$, the drop in current after the peak is very steep initially and then becomes relatively stable at lower concentrations. This could be due to resistance effect in thin layer cell where the more viscous RTIL has higher resistance.[47] On all surfaces, the maximum currents were plotted *vs* concentration (see insets to Figure). The sensitivities and LODs were calculated from the line of best fit and are reported in Table 6.1. The highest sensitivity (9.6×10^{-8} $A\%^{-1}$) was obtained on the PtNP modified Au microchannels (Figure 6.9c) even though more than half of the electrode surface is not active for hydrogen sensing. A slightly smaller sensitivity (8.2×10^{-8} $A\%^{-1}$) was obtained on the PtNP modified Au macrodisk electrode despite having more than half of the geometric area of the microchannel electrodes. Comparatively, the smallest sensitivity (5.2×10^{-8} $A\%^{-1}$) was obtained on the bare Pt macrodisk electrodes (Figure 6.9b). When the sensitivity of the PtNP modified Au microchannels was compared in $[C_2mim][NTf_2]$ and $[C_4mpyrr][NTf_2]$, the lowest sensitivity was obtained in $[C_4mpyrr][NTf_2]$, with a large LOD (23 %), suggesting that $[C_4mpyrr][NTf_2]$ is not very suitable for hydrogen gas sensing. The smallest LOD (3.4 %) was obtained on PtNP Au microchannels in the 'higher concentration' range (10-100%), which can be further improved by studying a lower concentration range (discussed later in later section 6.3.3.6).

Figure 6.10 shows the comparison of *I-t* response in two consecutive experiments on the same electrode for 100-1 % hydrogen in $[C_4mpyrr][NTf_2]$ on PtNP modified Au microchannels. In Figure 6.10 a, the solid line shows the first performed experiment and the red dashed line shows the second experiment. In both experiments, It is clearly observed that the decrease in maximum current is very sharp at higher concentrations from 100-40 % hydrogen, whereas at 40 % and below, the current is more stable and reproducible. Figure 6.10b shows the comparison of corresponding

calibration plots for maximum currents *vs* different concentrations. An approximate 36 % decrease in maximum current was observed at 100 % H_2 but the current becomes stable between 20-1 % hydrogen. The rapid decrease in current with time can be explained in terms of electrolyte resistance in a thin layer cell, as discussed by Bard et al. in 1972.[47] In the microchannel electrodes, the electrolyte thickness is very small (ca. 10 μm), and as a result, *i*R drop is observed at high analyte concentrations (e.g. 100 % H_2). This effect is more pronounced in the more viscous ionic liquid. During and following the applied pulse, redistribution and accumulation of electrogenerated products occurs inside the microchannels.[47, 51] As a result, fouling of the microchannels occurs rapidly at higher concentrations of H_2, which results in a rapid drop of the plateau current. The rapid decrease in current with time at higher concentrations of analyte can also be explained in terms of electrolyte thickness vs diffusion layer thickness in a thin layer cell. Here, the plateau current drops rapidly when the thickness of the ionic liquid film (10 μm) in the microchannels is much smaller than the thickness of the diffusion layer (242 μm), as discussed by Oglesby et al. in 1965.[52] These observations suggest that for long-term sensing of hydrogen, [C_4mpyrr][NTf_2] is not a good choice, but that [C_2mim][NTf_2] is a good candidate.

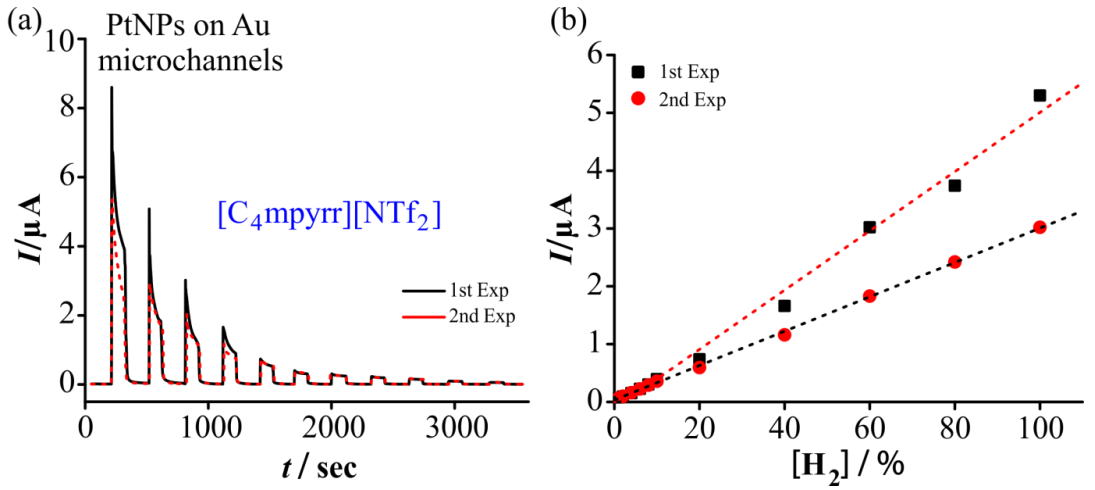

Figure 6.10: (a) Comparison of long-term chronoamperometric current response obtained during the first (black) and the second (dotted red) experiment for 10-1 % and 100-10 % H_2 on PtNP modified Au microchannels in [C_4mpyrr][NTf_2]. (b) Corresponding calibration plots of current (baseline corrected) *vs* concentration, along with the line of best fit.

6.3.3.6 Low Concentration Amperometric Response on PtNP Modified Au Microchannels

Figure 6.11 shows the long-term chronoamperometry for 10-1 % hydrogen on PtNP modified Au microchannels in (a) $[C_2mim][NTf_2]$ and (b) $[C_4mpyrr][NTf_2]$ with a N_2 flushing step between each concentration range. The insets show the corresponding calibration plots for maximum current *vs* concentration.

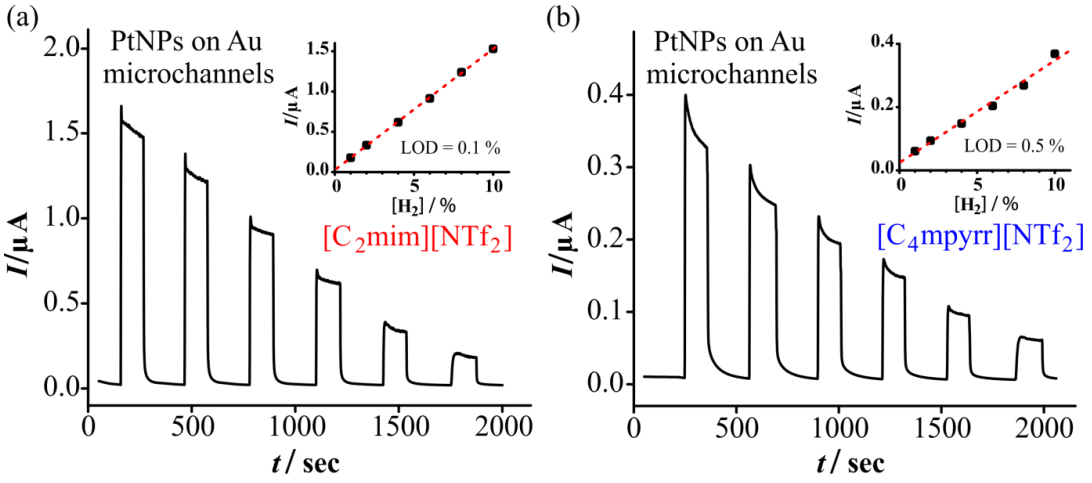

Figure 6.11: Long-term chronoamperometry (LTCA) for 1-10 % H_2 on PtNP modified Au microchannels in (a) $[C_2mim][NTf_2]$, and (b) $[C_4mpyrr][NTf_2]$. The potential was stepped from -0.45 V to +0.6 V. Insets show the calibration plots of currents (baseline corrected) *vs* concentration, along with the line of best fit.

Relatively, stable plateaus were obtained in $[C_2mim][NTf_2]$ with a very stable baseline, while a larger decrease in current after the maximum was observed in $[C_4mpyrr][NTf_2]$ with a longer time required to return to the baseline. Excellent linearity (R^2 = 0.999) for current *vs* concentration was obtained in $[C_2mim][NTf_2]$, while in $[C_4mpyrr][NTf_2]$, the straight line (R^2 = 0.998) deviated slightly from the origin. The sensitivities and LODs were calculated from the gradient and are shown in Table 6.1 for this lower concentration range. In $[C_2mim][NTf_2]$, ca. 4 times higher sensitivity was obtained compared to $[C_4mpyrr][NTf_2]$. The smallest calculated LOD (0.1%) was obtained for hydrogen on PtNP modified Au microchannels in the RTIL $[C_2mim][NTf_2]$ for the low concentration range, which is 40 times smaller than the lower explosive limit (LEL) of 4%.

6.3.4 Reproducibility for Hydrogen Sensing on PtNP Au Microchannels

In order to test the ability of the micropatterned electrochemical sensor for long-term monitoring of hydrogen gas at low concentration and to test the reproducibility of

PtNP modified Au microchannels, long-term chronoamperometry (LTCA) was performed at a constant concentration in two RTILs. For this hydrogen gas was introduced into the cell at a concentration of 4 % until a stable, maximum plateau current was obtained. Nitrogen "flushing" was performed between each addition of 4 % H_2 to ensure that the baseline is stable. Figure 6.12 shows the response for multiple additions of 4 % hydrogen on PtNP modified Au microchannels in (a) [C_2mim][NTf_2], (c) [C_4mpyrr][NTf_2]. The corresponding plots for maximum current and the response times for different additions (n=5) of hydrogen are shown in Figures 6.12b, & d. In [C_2mim][NTf_2], a stable reproducible response was obtained for 4 % hydrogen, with a steady baseline. However, in [C_4mpyrr][NTf_2], a slight decrease in plateatu current can be seen for every successive addition, possibly due to passivation with time due to the adsorption of hydrogen in this particular RTIL.[33]

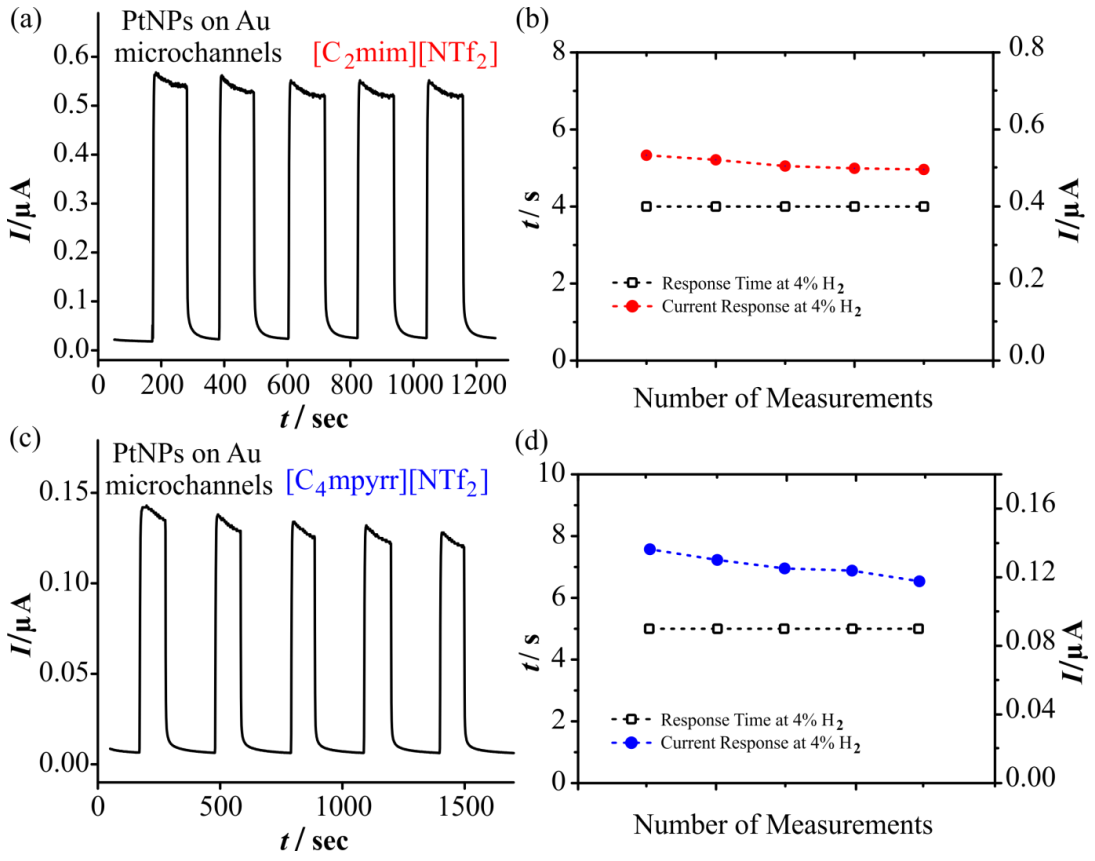

Figure 6.12: Reproduciblity experiment for 4 % H_2 on PtNP modified Au microchannels in (a) [C_2mim][NTf_2], and (c) [C_4mpyrr][NTf_2] *vs* Pt wire CE and Ag wire RE. The potential was stepped from -0.45 V to +0.6 V. Figures (b) and (d) show the corresponding plots for current response and response time at 4 % H_2 *vs* number of measurements.

A similar behavior was observed at higher concentrations in $[C_4mpyrr][NTf_2]$ where the fall off in current after the maximum was observed. It is noted that perfect behaviour is not expected for this system since the analyte gas is not under pure diffusion control.

The response time was also calculated for each addition of hydrogen, and was found very constant in both RTILs, which is 4 seconds in $[C_2mim][NTf_2]$, and 5 seconds in $[C_4mpyrr][NTf_2]$. More discussion on response times will be presented in the next section.

6.3.5 Response Time on PtNP Au Microchannels vs Macrodisk Electrodes

The response time (t_{90}) is an important parameter to test the ability of a sensor to respond for a particular gaseous analyte. In this work, it is defined as the time taken to reach 90% of the maximum current from the baseline.[53, 54] Typically, this corresponds to a plateau current, but in this work it is noted that a plateau isn't always observed, so the maximum current is taken. Figure 6.13 shows a comparison of response times for 60 % hydrogen in $[C_2mim][NTf_2]$ on PtNP modified Au microchannels *vs* PtNP modified gold, and bare Pt macrodisk electrodes. Table 6.1 shows the analytical parameters along with response times for hydrogen on different surfaces. On the PtNP modified Au microchannel electrode, a very fast response time (2 seconds) was obtained which is ca. 20 times faster than macrodisk electrode (39 ± 7) where a larger droplet of RTIL is employed. Importantly, this fast response time was very consistent for different concentrations between 10-100 % hydrogen in $[C_2mim][NTf_2]$. However at the low concentration range (1-10 %), t_{90} was slightly increased (4 seconds), possibly due to small numbers of analyte molecules compared to the carrier gas (N_2 gas), which can hinder the movement of H_2 molecules towards the electrode surface. This excellent performance (fast response time, high sensitivity and good reproducibility) of the PtNP Au microchannel electrode compared to the macrodisk electrodes (PtNPs Au, bare Pt) was attributed to the presence of the microchannels which requires the use of only a very thin layer of ionic liquid. This small thickness (10 ± 0.5 μm) in the microchannels, compared to macrodisk electrodes (1.0 ± 0.05 mm), allows faster partitioning and movement of hydrogen to the electrode surface. It is important to note here, the fast response time for hydrogen

relative to other gases in RTILs is probably due to the smaller size of the hydrogen molecules also and their non-polar nature, which can facilitate the diffusion faster compared to polar and larger molecules (e.g. ammonia, hydrogen chloride).

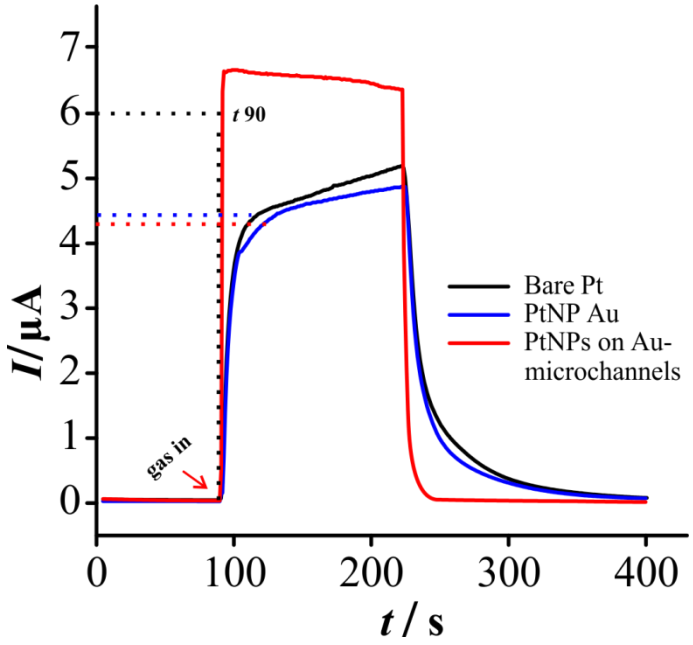

Figure 6.13: Chronoamperometric response for 60 % H_2 on a bare Pt electrode (black), PtNP modified Au electrode (blue), and PtNP modified Au microchannels (red) in [C_2mim][NTf_2]. The dotted lines show the 90 % current responses.

6.4 Conclusions

The electrochemical oxidation of hydrogen has been investigated in the RTIL [C_2mim][NTf_2] on PtNP modified Au microchannel electrodes, PtNP modified gold electrodes and bare Pt macrodisk electrodes. On micropatterned electrodes (PtNP Au microchannels), the results were compared in [C_2mim][NTf_2] and [C_4mpyrr][NTf_2] to investigate which RTIL is better for H_2 sensing. The gradients obtained between 10-100 % and 1-10 % hydrogen in [C_2mim][NTf_2] showed excellent linearity on PtNP modified Au microchannels whereas on PtNP modified Au electrodes or bare Pt macrodisk electrodes, the straight line deviated at low concentrations and did not pass directly through the origin. The highest sensitivity and lowest LOD (2.5 %) was obtained on PtNP modified Au microchannels in [C_2mim][NTf_2] when cyclic voltammetry was performed in the higher concentration range. To measure the response time (t_{90}) and to test the ability of modified microchannels based microarrays sensor for “real time” hydrogen detection, LTCA was performed on the PtNP modified microchannel electrode at two concentration ranges (10-10 % and 1-

10 %) and the results were compared with PtNPs the other surfaces. The highest current was obtained on the PtNP modified microchannels whereas the smallest current-time response was obtained on the bare Pt macrodisk electrode. A very fast response time of 2 seconds was obtained on the modified microchannels, which is ca. 20 times faster than on macrodisk electrodes. The lowest reported LOD (0.1 %, low concentration range) was obtained on the PtNP modified Au microchannels which is 40 times smaller than the lower explosive limit (4 %). The RTIL $[C_4mpyrr][NTf_2]$ is not the best choice for long-term hydrogen detection due to the large fall off in current, especially at higher concentrations. All these investigations are highly encouraging and suggest that gold surfaces modified with PtNP microchannels can be employed together with RTILs in amperometric devices to produce fast responding, microarray-based hydrogen gas sensors which can detect hydrogen at low concentrations (40 times lower than the LEL).

References

1. B. J. Dixon, J. Tang and J. H. Zhang, *Med. Gas Res.*, 2013, **3**, 10.
2. M. Momirlan and T. N. Veziroglu, *Int. J. Hydrogen Energy*, 2005, **30**, 795-802.
3. R. Ramachandran and R. K. Menon, *Int. J. Hydrogen Energy*, 1998, **23**, 593-598.
4. C.-S. Huang, T. Kawamura, Y. Toyoda and A. Nakao, *Free Radic. Res.*, 2010, **44**, 971-982.
5. K. L. Cashdollar, I. A. Zlochower, G. M. Green, R. A. Thomas and M. Hertzberg, *J. Loss Prev. Process Ind.*, 2000, **13**, 327-340.
6. W. W. Lace, *The Hindenburg Disaster of 1937*, Infobase Publishing, 2008.
7. R. Saxén, T. K. Taipale and H. Aaltonen, *Radioactivity of wet and dry deposition and soil in Finland after the Chernobyl accident in 1986*, Finnish Centre for Radiation and Nuclear Safety, 1987.
8. E. J. Bromet, *J. Prev. Psychiatry*, 1982.
9. M. Rogovin, *Three Mile Island: A report to the commissioners and to the public*, Nuclear Regulatory Commission, Washington, DC (USA), 1979.
10. K. Buesseler, M. Aoyama and M. Fukasawa, *Environ. Sci. Technol.*, 2011, **45**, 9931-9935.
11. B. Árnason and T. I. Sigfússon, *Int. J. Hydrogen Energy*, 2000, **25**, 389-394.
12. M. Z. Jacobson, W. G. Colella and D. M. Golden, *Science*, 2005, **308**, 1901-1905.
13. M. Delucchi, *Hydrogen fuel cell vehicles*, Institute of Transportation Studies, UC Davis, 1992.
14. S. Koca, *Transition to Hydrogen Fuel Cell Vehicles*, Nova Science Publishers, 2010.
15. I. P. Jain, *Int. J. Hydrogen Energy*, 2009, **34**, 7368-7378.
16. W. Peschka, *Liquid hydrogen: fuel of the future*, Springer Science & Business Media, 2012.
17. J. E. Philpott, *Platin. Met. Rev.*, 1976, **20**, 110-113.
18. B. Cook, *Eng. Sci. Educ. J.*, 2002, **11**, 205-216.
19. M. Warshay and P. R. Prokopius, *J. power sources*, 1990, **29**, 193-200.

20. T. Hübert, L. Boon-Brett, G. Black and U. Banach, *Sens. Actuators B Chem.*, 2011, **157**, 329-352.
21. J. R. Stetter and J. Li, *Chem. Rev.*, 2008, **108**, 352-366.
22. F. DiMeo, S. Chen, P. Chen, J. Neuner, A. Roerhl and J. Welch, *Sens. Actuators B Chem.*, 2006, **117**, 10-16.
23. A. Z. Sadek, W. Wlodarski, K. Kalantar-Zadeh, C. Baker and R. B. Kaner, *Sens. Actuators A Phys.*, 2007, **139**, 53-57.
24. H. Gu, Z. Wang and Y. Hu, *Sensors*, 2012, **12**, 5517-5550.
25. M. J. Madou and S. R. Morrison, *Chemical sensing with solid state devices*, Elsevier, 2012.
26. G. F. Fine, L. M. Cavanagh, A. Afonja and R. Binions, *Sensors*, 2010, **10**.
27. G. Korotcenkov, S. D. Han and J. R. Stetter, *Chem. Rev.*, 2009, **109**, 1402-1433.
28. C. A. Gunawan, M. Ge and C. Zhao, *Nat. Commun.*, 2014, **5**, 3744.
29. D. H. Craston, C. P. Jones, D. E. Williams and N. El Murr, *Talanta*, 1991, **38**, 17-26.
30. G. Hussain and D. S. Silvester, *Anal. Chem.*, 2016, **88**, 12453-12460.
31. A. Khan, C. A. Gunawan and C. Zhao, *ACS Sustainable Chem. Eng.*, 2017, **5**, 3698-3715.
32. D. Silvester and R. Compton, 2009.
33. D. S. Silvester, L. Aldous, C. Hardacre and R. G. Compton, *J. Phys. Chem. B*, 2007, **111**, 5000-5007.
34. J. Lee, K. Murugappan, D. Arrigan, W. M. and D. Silvester, S., *Electrochim. Acta*, 2013, **101**, 158-168.
35. K. Murugappan, J. Lee and D. S. Silvester, *Electrochem. Commun.*, 2011, **13**, 1435-1438.
36. J. Lee, K. Murugappan, D. W. M. Arrigan and D. S. Silvester, *Electrochim. Acta*, 2013, **101**, 158-168.
37. H. Awada, G. Castelein and M. Brogly, *Surf. Interface Anal.*, 2005, **37**, 755-764.
38. A. J. Bard and L. R. Faulkner, *Electrochemical Methods: Fundamentals and Applications*, John Wiley New York, 2001.
39. J. J. Burk and S. K. Buratto, *J. Phys. Chem. C*, 2013, **117**, 18957-18966.
40. D. S. Silvester, K. R. Ward, L. Aldous, C. Hardacre and R. G. Compton, *J. Electroanal. Chem.*, 2008, **618**, 53-60.
41. X. Ji, D. S. Silvester, L. Aldous, C. Hardacre and R. G. Compton, *J. Phys. Chem. C*, 2007, **111** 9562–9572.
42. J. A. Alden, J. Booth, R. G. Compton, R. A. W. Dryfe and G. H. W. Sanders, *J. Electroanal. Chem.*, 1995, **389**, 45-54.
43. I. Streeter, N. Fietkau, J. del Campo, R. Mas, F. X. Mũnoz and R. G. Compton, *J. Phys. Chem. C*, 2007, **111**, 12058-12066.
44. M. C. Buzzeo, O. V. Klymenko, J. D. Wadhawan, C. Hardacre, K. R. Seddon and R. G. Compton, *J. Phys. Chem. A*, 2003, **107**, 8872-8878.
45. R. G. Evans, O. V. Klymenko, S. A. Saddoughi, C. Hardacre and R. G. Compton, *J. Phys. Chem. B*, 2004, **108**, 7878-7886.
46. C. L. Bentley, A. M. Bond, A. F. Hollenkamp, P. J. Mahon and J. Zhang, *J. Phys. Chem. C*, 2014, **118**, 29663-29673.
47. I. B. Goldberg, A. J. Bard and S. W. Feldberg, *The Journal of Physical Chemistry*, 1972, **76**, 2550-2559.
48. M. C. Buzzeo, R. G. Evans and R. G. Compton, *ChemPhysChem*, 2004, **5**, 1106-1120.
49. A. C. Fisher, *Electrode Dynamics*, Oxfort University Press, Oxford, UK, 1996.
50. R. G. Compton and C. E. Banks, *Understanding voltammetry*, World Scientific, 2011.
51. C. Gabrielli, M. Keddam, N. Portail, P. Rousseau, H. Takenouti and V. Vivier, *The Journal of Physical Chemistry B*, 2006, **110**, 20478-20485.

52. D. M. Oglesby, S. H. Omang and C. N. Reilley, *Analytical Chemistry*, 1965, **37**, 1312-1316.
53. M. T. Carter, J. R. Stetter, M. W. Findlay and V. Patel, *ECS Trans.*, 2012, **50**, 211-220.
54. J. Lee, D. W. M. Arrigan and D. S. Silvester, *Anal. chem.*, 2016, **88**, 5104-5111.

Chapter 7

7. Comparison of Voltammetric Techniques for Ammonia Sensing in Room Temperature Ionic Liquids

The work presented in this thesis up until now has employed potential sweep voltammetry i.e. cyclic voltammetry (CV) or linear sweep voltammetry (LSV), in addition to potential step voltammetry i.e. chronoamperometry. It would be interesting to see if pulse voltammetric techniques give higher current responses and better LODs, since this is well known to occur for many analytes in protic solvents. Thus, in this chapter, a comparison of three different voltammetric techniques has been employed for ammonia sensing: linear sweep voltammetry (LSV), differential pulse voltammetry (DPV) and square wave voltammetry (SWV), over a concentration range of 10-100 ppm ammonia (a chemically and electrochemically irreversible redox process). As in the previous chapters, a room temperature ionic liquid (RTIL) was used as the electrolyte. For this study, three different commercially available planar electrode devices were used: Pt screen-printed electrodes (SPEs), thin-film electrodes (TFEs), and microarray thin-film electrodes (MATFEs), along with an "ideal" Pt microdisk electrode (μ-disk) for comparison. Calibration plots (current vs. concentration) for all three different electrochemical techniques on all four surfaces are presented, to investigate which electrochemical technique and what surface is the best for the electrochemical detection of ammonia at low concentrations.

7.1 Introduction

Over the last 50 years, different voltammetric techniques have been developed and employed for electroanalytical applications such as cyclic voltammetry (CV), linear sweep voltammetry (LSV), differential pulse voltammetry (DPV), and square wave voltammetry.[1-3] These voltammetric techniques have found great importance in electroanalytical applications in many fields including environmental monitoring (heavy metals and other contaminant analysis),[4, 5] medical applications,[6] clinical analysis,[7] in the pharmaceutical[8] and food industries,[9, 10] in chemical/biosensors,[11]

and in the characterization of energy storage devices.[3, 12, 13] Selection of these electrochemical techniques for the detection of a particular analyte/electrolyte system is an important task to achieve the optimum sensitivity and lowest limits of detection (LODs). A survey on electroanalysis for last decade shows that pulse techniques have been most commonly employed in the development of electrochemical sensors and biosensors.[3] Cyclic voltammetry (CV) is most often used as a tool for the determination of redox mechanisms, electron transfer kinetics and formal potentials.[14] Square wave voltammetry (SWV) and differential pulse voltammetry (DPV) are commonly used in electroanalysis applications, typically in aqueous solvents, as they are usually an order of magnitude more sensitive than linear sweep voltammetry (LSV)/cyclic voltammetry (CV), e.g. detection limits are typically in the nanomolar range for SWV, which is far superior than for LSV). Over the last ten years, these techniques are often applied in the development of sensitive electrochemical sensors and biosensors due to their negligible capacitive current compared to faradaic current in protic organic solvents.[3, 15]

The main principle behind pulse techniques that makes them more sensitive than CV/LSV is the difference in the decay rates of the faradaic and non-faradaic current. The increased ratio of faradaic to non-faradaic current allows pulse techniques to have higher sensitivity and measure lower limits of detection when employed in conventional organic solvents.[3, 15] This generally only applies when electrolysis of the analyte is reversible in the chemical sense.[16-19] To the best of our knowledge, there are very limited studies concerning the sensitivity of SWV, DPV and LSV for the sensing of gaseous analytes in RTIL solvents.[20] For other non-gas analytes, Villagran *et al.* investigated the electroanalytical quantification of dissolved trace chloride ions in RTILs and found that SWV is more sensitive than LSV in RTILs.[21] Recent studies on low concentration detection of ammonia gas in RTILs using long-term chronoamperometry reveal that this technique is not useful for long term sensing and hampered the sensitivity due to fouling of surfaces as a result of the build-up of electrogenerated products.[22-24] In this chapter, three different electrochemical techniques will be employed for ammonia gas detection in the RTIL $[C_2mim][NTf_2]$: linear sweep voltammetry (LSV), differential pulse voltammetry (DPV), and square wave voltammetry (SWV), over the concentration range of 10-100 ppm NH_3. Commercially available Pt thin-film electrodes (TFEs), screen-printed

electrodes (SPEs), and microarray thin-film electrodes (MATFEs) will be employed, and the results compared to an "ideal" Pt microdisk electrode (μ-disk). The aim is to investigate which electrochemical technique is the most sensitive for low-concentration detection of ammonia gas in the more viscous RTIL systems.

7.2 Experimental

7.2.1 Chemical Reagents

All chemicals were commercially available and used as received. Ethanol (EtOH, 99%), acetone (99% purity), sulfuric acid (98% w/w [18.4 M]) and zinc chloride ($ZnCl_2$, 40% w/v, used as a soldering flux for connecting wires with electrodes), ferrocene ($Fe(C_5H_5)_2$, 98 % purity), potassium hexacyanoferrate (III) ($K_3Fe(CN)_6$, ACS reagent, ≥99% purity), and tetra-N-butylammonium perchlorate (TBAP, 98 % purity) were all purchased from Sigma Aldrich. The room temperature ionic liquid (RTIL) 1-ethyl-3-methylimidazolium bis(trifluoromethylsulfonyl)imide ($[C_2mim][NTf_2]$) was purchased from Merck KGaA (Kilsyth, Victoria, Australia) at ultra-high purity electrochemical grade and were used as received. Ultrapure water with a resistance of 18.2 MΩcm was prepared by an ultrapure water purification system (Millipore Pty Ltd., North Ryde, NSW, Australia). Acetonitrile (MeCN, >99.8%, Fischer Scientific) was used for washing the electrodes before and after use. Ammonia gas (500 ppm, in nitrogen) was purchased from CAC gases (Auburn, NSW, Australia). Nitrogen gas (for further dilution of NH_3) was obtained from a ≥ 99.99 % high purity, compressed nitrogen cylinder (BOC gases, Welshpool, WA, Australia).

7.2.2 Electrochemical Experiments

All experiments were performed using a PGSTAT101 Autolab potentiostat (Eco, Chemie, Netherlands) interfaced to a PC with Nova 1.10 software, at laboratory room temperature (294±1 K). The electrochemical cell was placed inside an aluminium Faraday cage in the fume cupboard to reduce electrical interference. Platinum (Pt) thin-film electrodes (TFEs) and Pt microarray thin-film electrodes (MATFEs) were obtained from Micrux Technologies, Oviedo, Spain (ED-SE1-Pt and ED-mSE-10-Pt, respectively). The TFE and MATFE have a similar design (1mm diameter Pt working electrode, Pt reference and Pt counter electrodes), except the

working electrode of the MATFE is covered with a layer of SU-8 resin into which 90 µ-holes of 10 µm diameter are drilled to create 90 recessed microelectrodes. In both the TFE and MATFE, the Pt thin-film (150 nm thickness) was fabricated by thin-film technology on a Pyrex substrate. The commercially available Pt screen-printed electrodes (SPEs) were obtained from DropSens, Spain (DRP-550), and consisted of a Pt-based WE (4 mm diameter), a Pt CE and a Ag quasi-RE. The screen-printed paste contains conductive Pt particles, binding materials and solvents, but the manufacturer has not disclosed the exact chemical composition.

TFEs and MATFEs were electrochemically activated in 0.5 M H_2SO_4 (aq) by scanning the potential between -0.21 and +1.3 V (TFE), or -0.27 and + 1.4 V (MATFE) *vs* an external Ag/AgCl (0.1 M KCl) reference electrode (BASi, Indiana, USA) and Pt coil counter electrode (Goodfellow, Cambridge Ltd., UK) at a sweep rate of 50 mVs^{-1} for ca. 200 cycles. The electrodes were washed with ultrapure water and dried under a stream of nitrogen. The Pt SPE was used "as is" (without electrochemical activation, polishing or acid pre-treatment), as recommended by the manufacturer. For gas sensing experiments, the planar electrodes were placed into a modified rubber bung and inserted into the glass cell (a modified version of a T-cell).[25-27] 2 µL of RTIL was drop-cast on the TFE and MATFE, and 8 µL on the SPE. Prior to the introduction of ammonia, the cell was purged with nitrogen to remove dissolved gases and impurities. When the baseline was stable (after ca. 20 minutes), ammonia gas was introduced into the cell and continuously flowed over the electrode.

For experiments on the microdisk electrode, a conventional home-made Pt microelectrode (µ-disk electrode, 16.6 µm diameter) was employed. The electrode was polished and electrochemically calibrated using the methods described in Chapter 3. For gas experiments, a disposable micropipette tip was fixed at the top of Pt microelectrode to provide a cavity into which 25 µL of $[C_2mim][NTf_2]$ was placed. The electrode was housed into the bottom of a glass T-cell[25, 28, 29] with a Ag wire (combined counter and quasi-reference electrode) inserted into the ionic liquid. The cell was purged under vacuum (Edwards high vacuum pump, Model ES 50) for ca. 90 minutes to remove dissolved impurities (e.g. oxygen or water) present in the

ionic liquid. When a clean blank voltammogram was obtained, ammonia gas was introduced into the cell.

LSV, DPV and SWV were performed between 10 to 100 ppm ammonia to investigate which technique and what surface is the most sensitive for ammonia oxidation in RTIL. For all three techniques, the potential was scanned between 0.0 V and + 2.0 depending on the oxidation. The voltametric parameters for DPV and SWV were optimized to obtain a prominent peak-shaped voltammogram. Optimised parameters correspond to a step potential of 5 mV, amplitude of 50 mV, a modulation time of 25 ms, and a frequency of 20 Hz. This was done to ensure the same sweep rate (100 mV/s) for all three voltammetric techniques. To confirm the sensing behaviour of ammonia, 1mM of a standard redox probe, ferrocene was also studied in acetonitrile with 0.1 M TBAP vs. a silver wire reference electrode and a Pt coil counter electrode.

7.2.3 Gas Mixing System

In order to obtain the different concentrations of gas, the desired gas was diluted with nitrogen gas through a gas mixing system as reported by Lee et al.[27] which consisted of two digital flow controllers (0-1.2 L/min, John Morris Scientific, NSW, Australia), one connected with the analyte gas cylinder (NH_3) and other with a nitrogen cylinder through PTFE tubing via a Swagelok T-joint (Swagelok, Kardinya, WA, Australia). The mixture was then passed through an additional gas-mixing segment[27] to increase turbulence and to ensure adequate mixing of both gases. The relative flow rates were used to calculate the different concentrations of ammonia introduced into the cell.

7.3. Results and Discussion

7.3.1 Analytical Response for Ammonia Using Different Electrochemical Techniques

In an aim to improve the sensitivity and LOD for ammonia sensing, three different electrochemical techniques, namely linear sweep voltammetry (LSV), differential pulse voltammetry (DPV), and square wave voltammetry (SWV) were employed on four different Pt surfaces. A concentration range of 10-100 ppm was chosen for these experiments due to it being easier to distinguish the currents from the blank scans. It

is noted that a lower concentration range will likely result in a lower limit of detection (as discussed in chapter 4).

7.3.1.1 Linear Sweep Voltammetry

Figure 7.1 shows linear sweep voltammetry (LSV) for the oxidation of 10, 20, 40, 60, 80 and 100 ppm ammonia in [C_2mim][NTf_2] on Pt (a) TFE, (b) SPE, (c) MATFE, and (d) µ-disk electrode at a scan rate of 100 mVs^{-1}. The ammonia oxidation peak corresponding to the following electrochemical equation:[12]

(Oxidation peak) $$NH_3(g) + 3A^- \rightarrow \frac{1}{2}N_2(g) + 3HA + 3e^- \quad \textbf{(7.1)}$$

Where A^- = the RTIL anion ($[NTf_2]^-$) and HA is the solvated proton. The mechanism has been discussed previously in chapter 4.

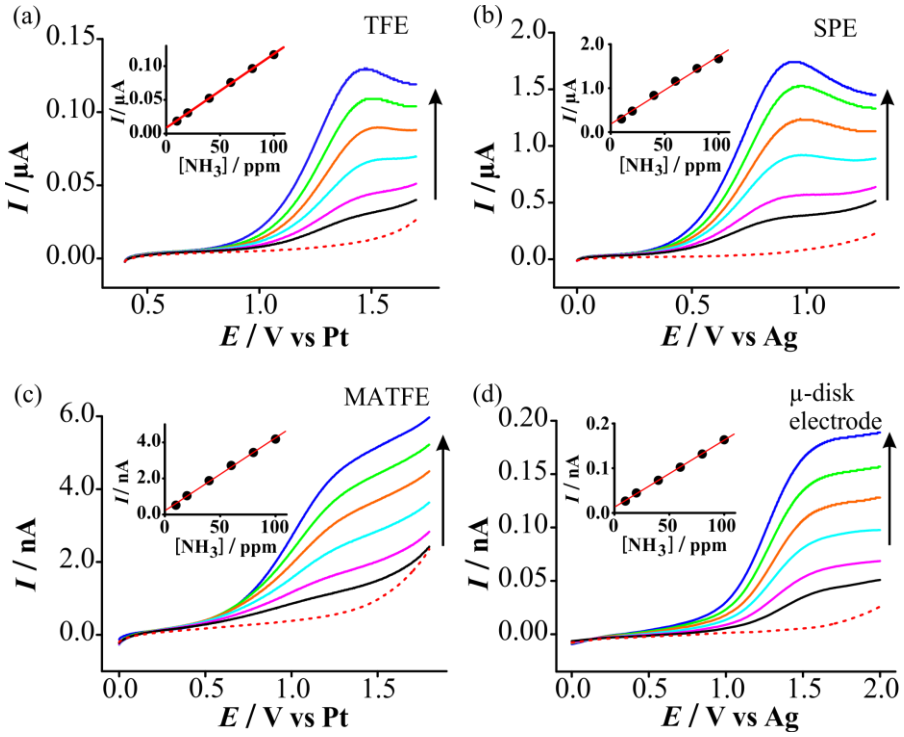

Figure 7.1. Linear sweep voltammetry (LSV) for the oxidation of ammonia (10-100 ppm) in [C_2mim][NTf_2] on a Pt (a) TFE, (b) SPE, (c) recessed MATFE (90 electrodes, diameter 10 µm, depth 3±0.5 µm), and (d) µ-disk electrode (diameter 16.6 µm) at a scan rate of 100 mVs^{-1}. Dotted line is the response in the absence of ammonia. Currents on the recessed MATFE were measured from a fixed potential of 1.4 V, due to the absence of a limiting current plateau. The insets show calibration plots of peak current (baseline corrected) vs concentration, along with the line of best fit.

In RTILs, the oxidation reaction is believed to be diffusion controlled,[12, 28, 30] as evidenced by linear plots of peak current vs square root of scan rate. In addition to

being chemically irreversible, the oxidation is suggested to have very slow (irreversible) electrode kinetics in RTILs [30], although a heterogeneous electrochemical rate constant for this reaction is not yet reported, probably due to the complex follow-up chemistry. The response in the absence of ammonia is shown as a dashed line. The insets show the corresponding calibration plots between oxidation current (baseline corrected) and ppm (gas phase concentrations. A peak shaped response was observed on the larger TFE and SPE surfaces. In contrast, a steady state response was obtained on the micron sized electrodes (MATFE and µ-disk) (Figure 7.1, c & d), noting a sloping plateau current in the case of the MATFE. The possible explanation for the steepness in the steady state response for the MATFE can be explained in terms of the thickness of the electrolyte layer *vs* the size of the electrode. The thickness of the RTIL layer on the MATFE was estimated to be 0.14 ± 0.03 mm for [C_2mim][NTf_2] (volume of 2 µL). Thus, due to a very thin-film of IL on the recessed microarray, every microhole may behave like a thin layer cell which can give resistive signals.[31-33] Interestingly this steepness in steady state response on the MATFE was not observed in a conventional redox system e.g. for 1mM ferrocene in acetonitrile with 0.1 M TBAP supporting electrolyte (see Figure 7.2c).

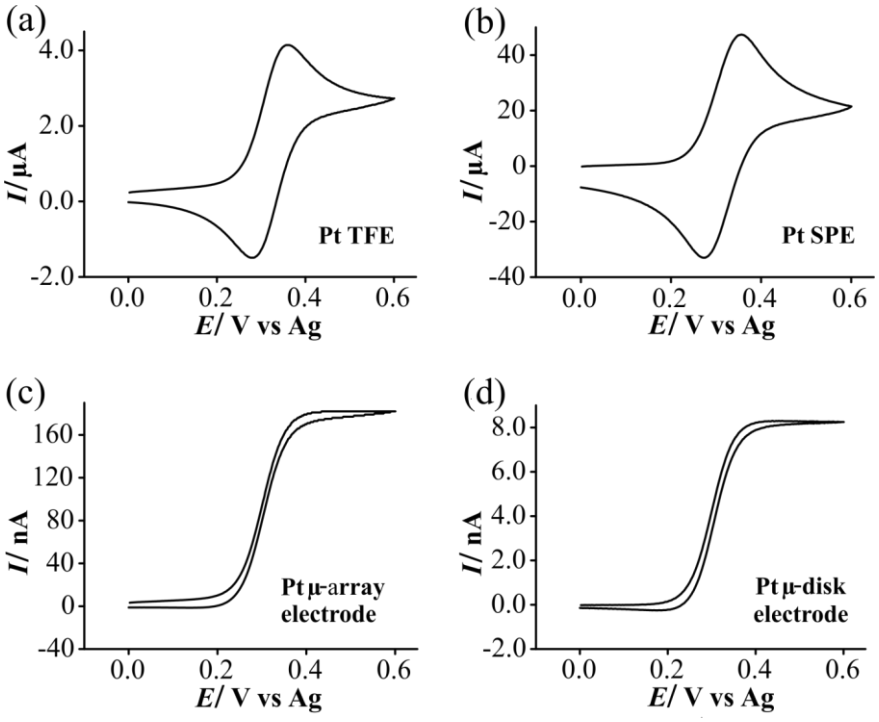

Figure 7.2. Cyclic voltammogram of Fc/Fc^+ redox couple on a Pt (a) TFE, (b) SPE, (c) MATFE, and (d) µ-disk electrode using 1mM ferrocene in acetonitrile with 0.1 M TBAP as an electrolyte at scan rate of 100 mVs^{-1}.

From Figure 7.1, it can be seen very clearly that as the concentration of ammonia increased from 10 ppm to 100 ppm, the current response increased with linearly. Calibration plots (insets to Fig 7.1) showed excellent linearity ($R^2 > 0.99$) for the concentration range studied.

Table 7.1 shows the analytical parameters resulting from the calibration graphs in Figure 7.1. Sensitivities were calculated from the gradient of the line of best fit and limits of detection (LODs) were calculated from three times the standard deviation of the slope of the line of best fit, over the concentration range studied. It is noted that currents were reproducible within ca. 3% when recorded on different days. The limit of detection on the Pt TFE is lower than the Pt SPE probably due the much flatter and purely metal based working electrode compared to the paste mixture. The sensitivities were higher on the larger surfaces, as expected due to the higher current responses. The LODs on all surfaces (2.0 to 9.2 ppm) were much lower than the OSHA PEL for ammonia (25 ppm), and this could further be lowered by studying a lower concentration range,[12] however this is not the focus of this study.

Table 7.1. Analytical parameters (sensitivity and limit of detection, LOD) calculated for ammonia oxidation (10-100 ppm) on different Pt electrodes using linear sweep voltammetry (LSV), differential pulse voltammetry (DPV) and square wave voltammetry (SWV).

Electrode	LSV		DPV		SWV	
	Sensitivity/ $Appm^{-1}$	LOD/ppm	Sensitivity /$Appm^{-1}$	LOD /ppm	Sensitivity / $Appm^{-1}$	LOD / ppm
TFE	1.10×10^{-9}	2.7	4.90×10^{-10}	6.1	9.36×10^{-10}	6.7
SPE	1.55×10^{-8}	9.2	6.80×10^{-9}	6.0	1.29×10^{-8}	5.0
MATFE	4.04×10^{-11}	2.0	1.05×10^{-11}	11.1	2.01×10^{-11}	6.4
µ-disk electrode	1.50×10^{-12}	2.7	3.76×10^{-13}	4.7	7.46×10^{-13}	2.1

7.3.1.2 Differential Pulse Voltammetry

As differential pulse voltammetry (DPV) relies on an alternative way of current sampling, it can give limits of detection roughly one order of magnitude more sensitive than LSV. This is indeed the case for ferrocene and ferricyanide (discussed later), but not the case for ammonia. Figure 7.3 shows differential pulse voltammograms for ammonia oxidation (10-100 ppm) in $[C_2mim][NTf_2]$ on Pt (a) TFE, (b) SPE, (c) MATFE, and (d) µ-disk electrode at a scan rate of 100 mVs^{-1},

along with corresponding calibration graphs of oxidation current (baseline corrected) *vs* ammonia concentration in ppm. The dashed line is the blank voltammogram without ammonia. A peak shaped response was obtained on all surfaces rather than the steady state response for LSV on the micron sized surfaces. As with LSV, the DPV current response increases linearly with concentration of ammonia gas. The oxidation peak current (background subtracted) was plotted against the respective ppm concentrations to obtain calibration graphs. Excellent calibration graphs with a straight line of best fit ($R^2 > 0.99$) were obtained for the concentration range studied. The sensitivity and LOD values obtained from the DPV experiments are shown in Table 7.1. Sensitivities were highest on the larger electrodes, and lowest on the (single) µ-disk electrode. The smaller sensitivities and larger LOD values were obtained on all surfaces as compared to LSV and SWV which can be confirmed from the smaller peak current for DPV response on all surfaces. Interestingly, the current response for DPV was much lower compared for LSV with ammonia oxidation, reflected by the smaller sensitivities and larger LODs.

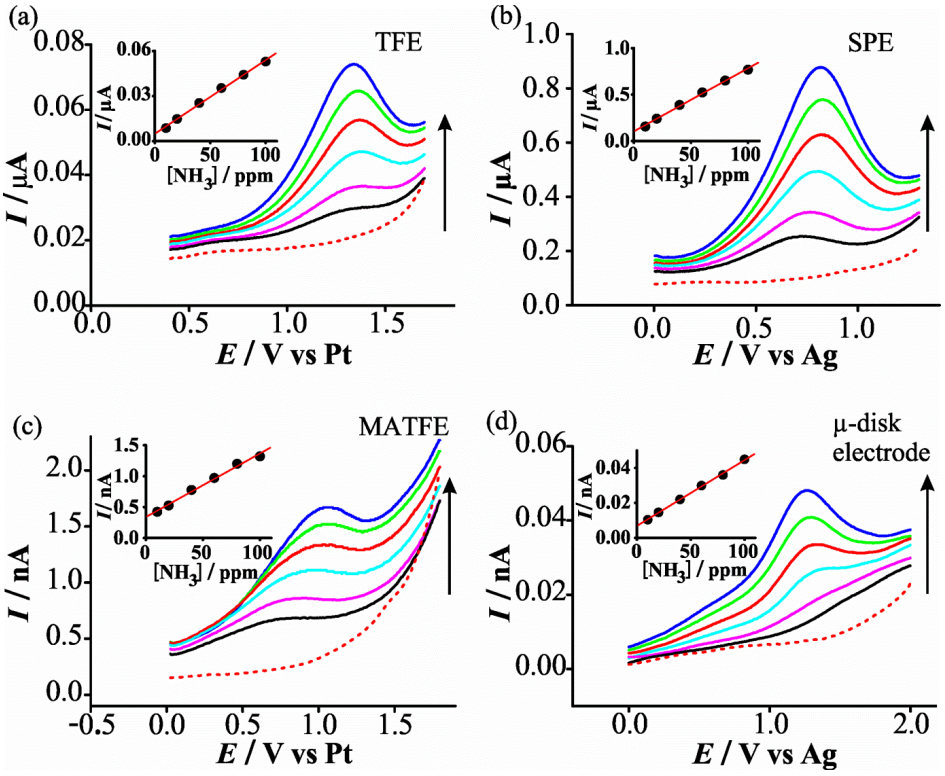

Figure 7.3. Differential pulse voltammetry for the oxidation of ammonia (10-100 ppm) in $[C_2mim][NTf_2]$ on a Pt (a) TFE, (b) SPE, (c) MATFE, and (d) µ-disk electrode at a scan rate of 100 mVs^{-1}. Step potential: 5 mV, modulation amplitude: 50 mV, modulation time: 25 ms, interval time: 50 ms. Dashed line is the response in the absence of ammonia. The insets show calibration plots of peak current (baseline corrected) vs concentration, along with the line of best fit.

In DPV, the capacitive current was found to be larger compared to LSV in [C_2mim][NTf_2], which is contrary to DPV *vs* SWV in protic solvents, possibly due the to slow relaxation of the electrical double layer. In DPV analysis, the current is sampled at the start of pulse called base current (I_b) and at the end of the pulse (pulse current, I_p). The net (or total) current (I_t) is the difference of pulse current and base current ($I_p - I_b$).[3] In the case of ammonia in RTILs, the maximum current contribution of base current appeared when current is sampled at the start of pulse, but due to the slow relaxation of oppositely charged ions, the pulse current is reduced and when the dominant base current is deducted from the pulse current, the net current is decreased consequently, which in turn decreases the sensitivity for DPV analysis of ammonia in RTILs.

7.3.1.3 Square Wave Voltammetry

The square wave parameters were optimized to achieve the highest sensitivity and were found to correspond to an amplitude of 50 mV, a step potential of 5 mV, and a frequency of 20 Hz. By using these values, the sweep rate was kept constant (100 mV/s) in the three voltammetric techniques (LSV, DPV & SWV). Unver these optimized experimental conditions, the current response was measured after saturation of analyte gas at different ammonia concentrations. Fig. 7.4 shows SWV for the oxidation of 10-100 ppm ammonia in [C_2mim][NTf_2] on a Pt (a) TFE, (b) SPE, (c) MATFE, and (d) a µ-disk electrode. The dashed line is the blank voltammogram when ammonia is not present. The insets show the corresponding calibration graphs of oxidation current (baseline corrected) *vs* ammonia concentration. A difference in the oxidation peak potential on each surface is likely due to the unstable and different quasi-reference electrodes. It can be seen in all square wave voltammograms that a greater current response was obtained compared to DPV.

On the large surfaces (TFE & SPE) the current response of SWV is very similar to LSV, but with greater charging current. The capacitive/charging current was found to be the largest for SWV on all surfaces as shown in Figure 7.7, possibly due to the slow relaxation of oppositely charged ions in RTIL as the time to sample the current is small (few milliseconds) compared to DPV.[3, 34] The SWV and DPV current response can be detected very easily even at low concentrations compared to LSV

except on the Pt µ-disk electrode at lower concentrations, where no clear peak shape was observed. The dependence of peak current with concentration of ammonia on all four Pt surfaces shows that the SWV current response increases as the concentration of ammonia gas increase from 10 ppm to 100 ppm in RTIL system. The oxidation peak current (background subtracted) was plotted against the respective ppm concentrations to get calibration graphs with excellent linearity (R^2 > 0.99). The analytical parameters obtained from the SWV are shown in Table 7.1. The sensitivities were highest on the larger electrodes, and lowest on the (single) µ-disk electrode, as observed in case of LSV and DPV. The sensitivities obtained on all surfaces were greater than for DPV but unexpectedly lower than LSV. The LODs obtained for SWV on all surfaces were mostly similar or slightly superior to DPV. For SWV, the LODs on all surfaces (2.1 to 6.7 ppm) were significantly lower than the permissible exposure limit of 25 ppm for ammonia.

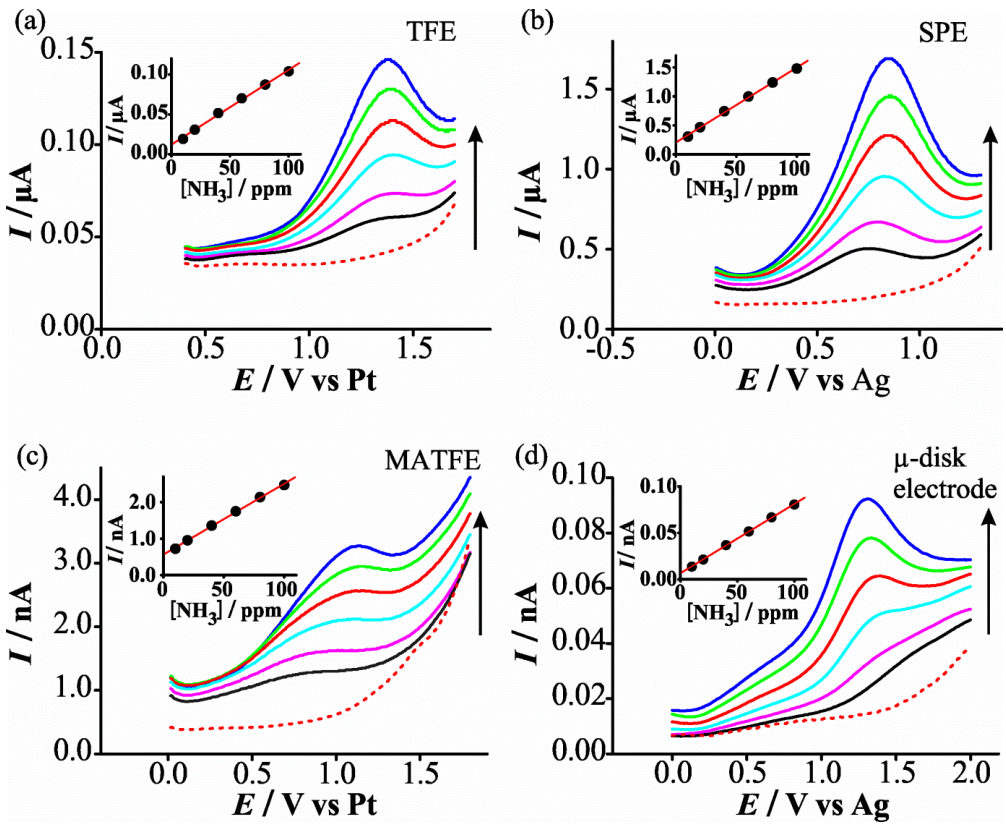

Figure 7.4. Square wave voltammetry for the oxidation of ammonia (10-100 ppm) in $[C_2mim][NTf_2]$ on a Pt (a) TFE, (b) SPE, (c) MATFE, (d) µ-disk electrode at a scan rate of 100 mVs^{-1}. Step potential: 5 mV, amplitude: 50 mV, frequency: 20 Hz. Dotted line is the response in the absence of ammonia. The insets show calibration plots of peak current (baseline corrected) vs concentration, along with the line of best fit.

7.3.2 Comparison of Current Density and Sensitivity

In order to investigate the rate of mass transfer on different size of electrodes, current density (*J*) was calculated for different concentrations of ammonia on all four types of Pt electrodes and plotted *vs* ammonia concentration for all three electrochemical techniques. Figure 7.5 shows current density plots for (a) LSV, (b) DPV and (c) SWV on four different Pt electrodes of varying size in [C_2mim][NTf_2]. The current densities of the Pt TFE (diameter = 1 mm) and Pt SPE (diameter = 4 mm) are very similar to each other, irrespective of the size of the electrode, as the rate of mass transfer is independent of the area of the electrode. [35] In this case, linear diffusion is predominant. As was discussed in chapter 4, the current density on the Pt MATFE and µ-disk electrode is significantly higher than the larger electrodes due to the faster rate of mass transfer (radial diffusion).

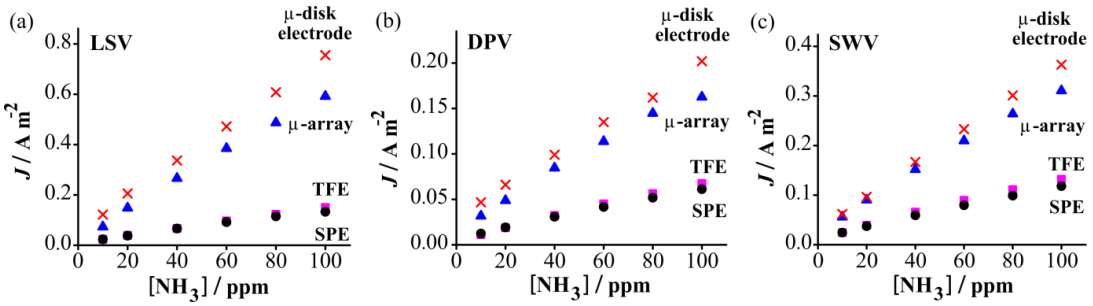

Figure 7.5. Comparison of current density plots for the oxidation of ammonia (10-100 ppm) on a Pt (■) TFE, (●) SPE, (▲) MATFE, and (×) µ-disk electrode in the RTIL [C_2mim][NTf_2], calculated from three different electrochemical techniques (a) LSV, (b) DPV, (c) SWV and plotted together vs ammonia concentration.

In order to compare which voltammetric technique is more sensitive for ammonia oxidation on different types of Pt electrodes in [C_2mim][NTf_2], the calibration graphs for LSV, DPV and SWV were plot together for the four different types of Pt electrodes. Figure 7.6 shows calibration plots for LSV, DPV and SWV for 10-100 ppm ammonia oxidation in [C_2mim][NTf_2] on all four different surfaces. On the macro-surfaces (Figure 7.6 a & b) it can be seen very clearly that LSV is slightly superior to SWV. However, this effect is much more prominent on the micron-sized surfaces, MATFE (Figure 7.6c) and µ-disk electrode (Figure 7.6d). Table 7.1 shows LOD and sensitivity values for all these plots. Not only was LSV found to be more sensitive than DPV and SWV for ammonia in [C_2mim][NTf_2], but also less background charging current was observed. This is a surprising observation and the reasons for this will be explained further in the next two chapters.

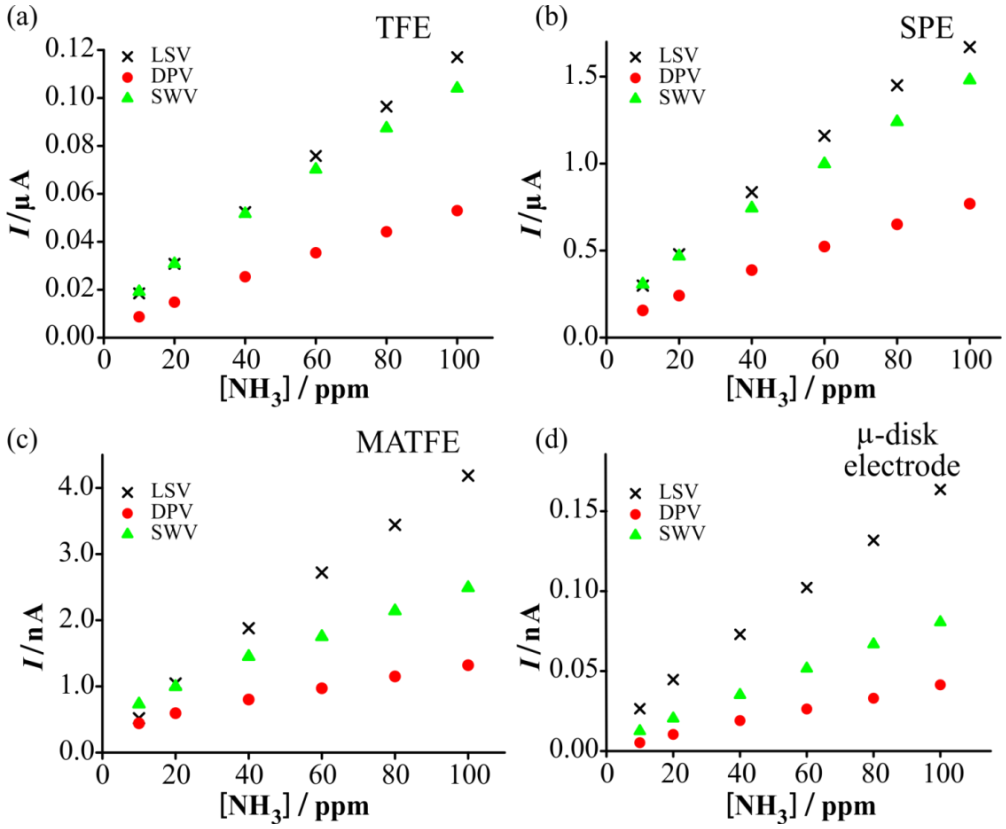

Figure 7.6. Comparison of calibration plots of peak current (baseline corrected) for ammonia oxidation (10-100 ppm) using three different electrochemical techniques LSV (●), DPV (▲), SWV (×), in the RTIL [C_2mim][NTf_2], on four different Pt electrodes: (a) TFE, (b) SPE, (c) MATFE and (d) μ-disk electrode and plot together vs ammonia concentration.

Figure 7.7 shows a plot of the average charging current in [C_2mim][NTf_2] calculated from the blank voltammograms, which is highest for SWV on all surfaces. As charging current directly affects sensitivity, this suggests that SWV will not give rise to more sensitive readings.[3] On Pt microelectrodes and MATFEs, the charging current is quite small due to the smaller areas. From the higher values of the charging current for DPV or, it can be assumed that the rearrangement of the electrical double layer is slower in RTILs than in aqueous system, probably due to the higher viscosity of RTILs. In DPV and SWV, the pulse time is very short, which may lead to greater background currents, as is observed in Figure 7.7.

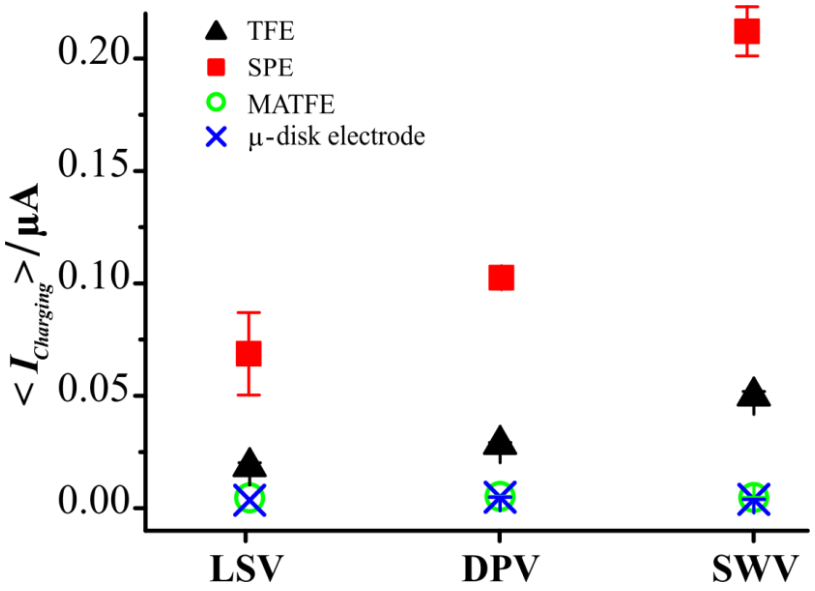

Figure 7.7. Plot of charging current calculated from the blank voltammograms, corresponding to the oxidation peak potential for different ammonia concentrations on all Pt surfaces for three different electrochemical techniques. The error bars show the variation of one standard deviation from the mean.

7.4 Conclusions

LSV, DPV, and SWV was performed to compare which technique is the most sensitive for ammonia sensing in $[C_2mim][NTf_2]$. The calibration graphs obtained for all electrochemical techniques in the concentration range 10-100 ppm were linear, and the limits of detections found on all surfaces (2-11 ppm) were much lower than the permissible exposure limit (25 ppm). Comparatively, LSV was found to be the most sensitive technique, with less background charging current, while DPV was the least sensitive. This result is surprising, since SWV is often the most sensitive technique for many electroanalytical applications. Although it is noted that all electrochemical techniques used in this work are highly suitable for ppm-concentration ammonia detection on disposable electrodes in RTILs, LSV appears to be the best choice for achieving the highest sensitivity.

References

1. R. A. Medeiros, R. C. Rocha-Filho and O. Fatibello-Filho, *Food Chemistry*, 2010, **123**, 886-891.
2. M. S. Krause and L. Ramaley, *Analytical Chemistry*, 1969, **41**, 1365-1369.
3. A. Chen and B. Shah, *Analytical Methods*, 2013, **5**, 2158-2173.
4. C. Krantz-Rülcker, M. Stenberg, F. Winquist and I. Lundström, *Analytica chimica acta*, 2001, **426**, 217-226.

5. G. Hanrahan, D. G. Patil and J. Wang, *Journal of Environmental Monitoring*, 2004, **6**, 657-664.
6. N. A. El-Maali, *Bioelectrochemistry*, 2004, **64**, 99-107.
7. G. A. Junter, *Electrochemical detection techniques in the applied biosciences: Analysis and clinical applications*, Halsted Press, 1988.
8. S. A. Özkan, B. Uslu and H. Y. Aboul-Enein, *Critical reviews in analytical chemistry*, 2003, **33**, 155-181.
9. A. Cavicchioli, M. A. La-Scalea and I. G. R. Gutz, *Electroanalysis*, 2004, **16**, 697-711.
10. S. Mannino and J. Wang, *Electroanalysis*, 1992, **4**, 835-840.
11. J. R. Stetter and J. Li, *Chem. Rev.*, 2008, **108**, 352-366.
12. G. Hussain and D. S. Silvester, *Anal. Chem.*, 2016, **88**, 12453-12460.
13. S. Trasatti and P. Kurzweil, *Platinum Metals Review*, 1994, **38**, 46-56.
14. A. J. Bard and L. R. Faulkner, *Electrochemical Methods, Fundamentals and Applications*, John Wiley & Sons, New York, 1980.
15. C. H. Hamann, A. Hamnett and W. Vielstich, *Electrochemistry, 2nd, Completely Revised and Updated Edition*, Wiley-VCH, Weinheim, 2007.
16. Š. Komorsky-Lovrić and M. Lovrić, *Advances in Analytical Chemistry*, 2013, **3**, 9-13.
17. J. J. O'Dea, J. Osteryoung and R. A. Osteryoung, *Analytical Chemistry*, 1981, **53**, 695-701.
18. J. G. Osteryoung and R. A. Osteryoung, *Analytical Chemistry*, 1985, **57**, 101A-110A.
19. L. Ramaley and M. S. Krause, *Analytical Chemistry*, 1969, **41**, 1362-1365.
20. K. Murugappan and D. S. Silvester, *Sensors and Actuators B: Chemical*, 2015, **15**, 6866-26876.
21. C. Villagrán, C. E. Banks, C. Hardacre and R. G. Compton, *Analytical Chemistry*, 2004, **76**, 1998-2003.
22. M. T. Carter, J. R. Stetter, M. W. Findlay and V. Patel, *ECS Trans.*, 2012, **50**, 211-220.
23. M. T. Carter, J. R. Stetter, M. W. Findlay and V. Patel, *ECS Trans.*, 2014, **64**, 95-103.
24. J. F. M. Oudenhoven, W. Knoben and R. van Schaijk, *Procedia Eng.*, 2015, **120**, 983-986.
25. U. Schroder, J. D. Wadhawan, R. G. Compton, F. Marken, P. A. Z. Suarez, C. S. Consorti, R. F. de Souza and J. Dupont, *New J. Chem.*, 2000, **24**, 1009-1015.
26. D. S. Silvester, A. J. Wain, L. Aldous, C. Hardacre and R. G. Compton, *J. Electroanal. Chem.*, 2006, **596**, 131-140.
27. J. Lee, K. Murugappan, D. W. M. Arrigan and D. S. Silvester, *Electrochim. Acta*, 2013, **101**, 158-168.
28. X. Ji, D. S. Silvester, L. Aldous, C. Hardacre and R. G. Compton, *J. Phys. Chem. C*, 2007, **111** 9562–9572.
29. D. S. Silvester, L. Aldous, C. Hardacre and R. G. Compton, *The Journal of Physical Chemistry B*, 2007, **111**, 5000-5007.
30. M. C. Buzzeo, D. Giovanelli, N. S. Lawrence, C. Hardacre, K. R. Seddon and R. G. Compton, *Electroanalysis*, 2004, **16**, 888-896.
31. I. B. Goldberg, A. J. Bard and S. W. Feldberg, *The Journal of Physical Chemistry*, 1972, **76**, 2550-2559.
32. C. Gabrielli, M. Keddam, N. Portail, P. Rousseau, H. Takenouti and V. Vivier, *The Journal of Physical Chemistry B*, 2006, **110**, 20478-20485.
33. D. M. Oglesby, S. H. Omang and C. N. Reilley, *Analytical Chemistry*, 1965, **37**, 1312-1316.
34. A. J. Bard and L. R. Faulkner, *Electrochemical Methods: Fundamentals and Applications*, John Wiley New York, 2001.
35. M. Ciobanu, J. P. Wilburn, M. L. Krim and D. E. Cliffel, in *Handbook of Electrochemistry*, ed. C. G. Zoski, Elsevier, Amsterdam, 2007, pp. 3-29.

Chapter 8

8. Sensitivity of Voltammetric Techniques for Reversible, Quasi-Reversible and Irreversible Redox Processes

For electroanalysis, square wave voltammetry (SWV) and differential pulse voltammetry (DPV) are often preferred techniques due to their negligible charging current, inherent background subtraction and fast sampling time. They are generally considered to be more sensitive than linear sweep/cyclic voltammetry (LSV/CV). However, in the previous chapter, LSV was found to result in a higher current response for ammonia oxidation in $[C_2mim][NTf_2]$ compared to SWV and DPV. In this chapter, we will describe an investigation into the comparative sensitivity of LSV and SWV for a range different analytes in water, acetonitrile and RTILs using simulation. These analytes were chosen based on their different electrode kinetics. The type of response was ultimately found to depend significantly on the reversibility of the electrochemical process. This chapter therefore first describes the modelling of a simple, one electron transfer reaction for fast reversible, quasi-reversible and irreversible redox processes. The simulated parameters are then employed experimentally to study different analytes in different electrolyte systems.

8.1 Introduction

Over the last few decades, SWV and DPV are extensively used electroanalytical techniques in aqueous or conventional organic solvents due to their high sensitivity and selectivity, low cost, fast sampling time, and negligible capacitive current. These techniques usually give an order of magnitude better sensitivity with higher signal to noise ratios than LSV, where the limits of detection for SWV and DPV are in the nanomolar range, far superior than for LSV.[1, 2] The better sensitivity of SWV and DPV than LSV is due to their pulsing strategies, where the potential of the sample is changed from one potential to another and the current is sampled at two points along the pulse, rather than continuous monitoring of current as a function of time as in LSV. Lei *et al*. employed LSV and SWV for the electrochemical detection of arsenic (As) in aqueous solution on an array of gold nanoparticles made by modifying a

glassy carbon electrode with gold nanoparticle modified multi-walled carbon nanotubes. They found that SWV gives much higher sensitivity ca. 7 times larger than LSV.[3] Roberta *et al*. developed a voltammetric method for the simultaneous determination of phenolic antioxidants in food products on boron-doped diamond electrodes using CV, DPV and SWV and found that SWV is an efficient, effective and sensitive technique to detect different antioxidants from aqueous-ethanolic solutions simultaneously.[4]

Thus, from the literature, SWV is considered as powerful tool for electroanalytical applications[2, 5-8] mechanistic studies,[9-12] and the calculation of electron transfer kinetics.[13-16] It is a large amplitude differential technique in which the potential waveform is composed of a staircase potential ramp modified with symmetrical square wave pulses of short duration. In SWV, two equal magnitude and oppositely directed pulses of amplitude (ΔE_p), are superimposed at regular intervals on a staircase ramp of step potential (ΔE_s), which forms one cycle of a square waveform. The influence of charging current is negligible because both the forward and backward currents are sampled at the end of each pulse during the last few microseconds. The forward current comprises of both faradaic and non-faradaic processes, while the backward current is mainly non-faradaic and thus the resulting total SWV current is the difference of forward and backward, which is mainly just the faradaic process.[2, 17] Thus, due to the square wave shape of potential modulation and fast speed of current sampling, this enables SWV to discriminate the influence of charging current and makes the technique highly sensitive with lower limits of detection. [2, 17-19]

In SWV, the total time taken to complete each square wave cycle is called a cycle period (T) and its reciprocal is termed the SWV frequency ($f = 1/T$) which is a critical time parameter to determine the speed of the experiment and thus analogous to the scan rate in cyclic voltammetry.[17] In SWV, scan rate (v) can be defined as the product of frequency (f) and step potential (ΔE_s) of the potential ramp, ($v = f \times \Delta E_s$). For a fast reversible redox process, the SWV total current is proportional to the square root of square wave frequency; however, for a quasi-reversible process, the SWV net current response is not a linear function of the SWV frequency. In this case, the change in total current response for a quasi-reversible process can be

enhanced by the transformation of the backward component under the influence of increased frequency.[18] Brookes *et al*. developed a model to simulate SWV for reversible, quasi-reversible and irreversible redox processes and compared the simulated data with experimental data for the oxidation of 4-chloronitrobenzene and found that peak current is a linear function of the square root of frequency.[20] Wang *et al*. investigated the electrode kinetics of azobenzene, a quasi-reversible two electron transfer process, on the basis of quasi-reversible maximum (QRM) which can be demonstrated as the parabolic dependence of ratio of SWV total current and frequency *vs* the logarithm of frequency.[16] Thus in SWV, the frequency is the main tool that describes the reversibility of the redox process, reaction mechanism and electrode kinetics.[11, 17, 21, 22] The second important parameter in SWV is the pulse height called SWV amplitude (ΔE_p) which influences the SWV total current response.[17] A literature survey shows that there are very limited studies[23-25] where the amplitude is used as a tool for mechanistic and electrode kinetics.

Recently, Mirceski *et al*. introduced a new approach to study the electrode kinetics of a variety of quasi-reversible electrode mechanisms on the basis of SWV amplitude, named "amplitude-based quasireversible maximum", rather than the classical quasireversible maximum (QRM) where SWV frequency is the main tool to study the reaction kinetics.[25] This approach can be utilised in this chapter.

The reversibility of a redox reaction is based on the rate constant for the electron transfer (k^o) as proposed by Matsuda and Aybe. They used a model to define whether the electrode process is fast reversible, quasi-reversible and irreversible,[26] as follows:[26, 27]

The redox process will be:

Fast reversible if: $k^o \geq 0.3$ cm/s

Quasi-reversible if: $0.3 > k^o > 2\times10^{-5}$ cm/s

Irreversible if: $k^o \leq 2\times10^{-5}$ cm/s

On the basis of rate constant, different theoretical models have been proposed in order to investigate the different parameters of square wave voltammetry.[13, 17, 20, 28-31] O'Dea *et al*. proposed a theoretical model for a simple reversible redox process to

investigate different SWV parameters such as peak shift, peak width, and peak height as a function of rate constant in order to study reversible, quasi-reversible and irreversible processes.[13] They also investigated the electrochemical system by introducing different follow-up mechanisms such as a preceding chemical reaction, following chemical reaction, and catalytic chemical reaction to understand how these mechanisms affect the current response.[13]

In this chapter, a simple, one electron transfer model was proposed on the basis of different rate constants for fast reversible, quasi-reversible, and irreversible redox process and the SWV peak currents were studied as a function of various SWV parameters such as amplitude, frequency and step potential. The optimized SWV parameters are then employed experimentally for different gaseous and dissolved analytes in room temperature ionic liquids (RTILs) including aqueous/organic electrolyte systems on Pt thin-film electrodes for fast reversible, quasi-reversible and irreversible redox natures to study the effect of reversibility on the sensitivity for square wave voltammetry. Finally, the SWV results are compared with LSV and DPV responses for fast reversible, quasi-reversible and irreversible redox process to conclude which technique is more sensitive for a particular analyte. The novelty of this work is that we have optimised the sensitivity of SWV for gaseous analytes in RTILs on thin-film electrode surfaces for the first time. Finally, all this information will help us to determine which electrochemical technique is the most suitable for particular analytes.

8.2 Experimental

8.2.1 Chemical Reagents

All chemicals were commercially available and used as received. Ethanol (EtOH, 99%), acetone (99% purity), sulfuric acid (98% w/w [18.4 M]) and zinc chloride ($ZnCl_2$, 40% w/v, used as a soldering flux for connecting wires with electrodes), ferrocene ($Fe(C_5H_5)_2$, 98 % purity), potassium hexacyanoferrate (III) ($K_3Fe(CN)_6$, ACS reagent, ≥99% purity), and tetra-N-butylammonium perchlorate (TBAP, 98 % purity) were all purchased from Sigma Aldrich. The room temperature ionic liquids (RTILs) 1-ethyl-3-methylimidazolium bis(trifluoromethylsulfonyl)imide ($[C_2mim][NTf_2]$), 1-butyl-3-methylimidazolium bis(trifluoromethylsulfonyl)imide ($[C_4mim][NTf_2]$), 1-butyl-3-methylimidazolium

trifluorotris(pentafluoroethyl)phosphate ([C_4mim][FAP]), 1-butyl-3-methylimidazolium hexafluorophosphate ([C_4mim][PF_6]), N-butyl-N-methylpyrrolidinium bis(trifluoromethylsulfonyl)imide ([C_4mpyrr][NTf_2]), 1-butyl-3-methylimidazolium tetrafluroborate ([C_4mim][BF_4]), 1-hexyl-3-methylimidazolium trifluorotris(pentafluoroethyl)phosphate ([C_6mim][FAP]), were purchased from Merck (Kilsyth, Victoria, Australia) at ultra-high purity electrochemical grade. All RTILs were used as received. Ultrapure water with a resistance of 18.2 MΩcm was prepared by an ultrapure water purification system (Millipore Pty Ltd., North Ryde, NSW, Australia). Acetonitrile (MeCN, >99.8%, Fischer Scientific) was used for washing the electrodes before and after use. Different gas cylinders; ammonia gas (500 ppm, in nitrogen), hydrogen chloride gas (0.2% in nitrogen) and high purity oxygen gas (>99.5%) were purchased from CAC gases (Auburn, NSW, Australia). Hydrogen gas (100%, high purity) was purchased from BOC gases, Welshpool, WA, Australia. Nitrogen gas (for further dilution of NH_3, H_2, HCL & O_2) was obtained from a ≥ 99.99 % high purity, compressed nitrogen cylinder (BOC gases, Welshpool, WA, Australia).

8.2.2 Electrochemical Experiments

All experiments were performed using a PGSTAT101 Autolab potentiostat (Eco, Chemie, Netherlands) interfaced to a PC with Nova 1.10 software, at laboratory room temperature (294±1 K) inside an aluminium Faraday cage present in the fume cupboard to reduce electrical interference. Platinum (Pt) thin-film electrodes (Pt TFEs) from Micrux Technologies, Oviedo, Spain (ED-SE1-Pt) and were employed as the electrode which comprised of a three electrode arrangement, as described in previous chapters. For experiments with aqueous electrolytes, platinum (Pt) conventional macrodisk electrodes (diameter 1.6 μm) from BASi (Indiana, USA) were also employed with an external Ag/AgCl (0.1 M KCl) reference electrode (BASi, Indiana, USA) and a Pt wire (0.5 mm diameter) counter electrode (Goodfellow Cambridge Ltd., UK).

Prior to employing the electrochemical cell for voltammetric experiments, the Pt macrodisk electrode was polished on soft polishing pads (Buehler Illinois) with decreasing size of alumina powder (3 µm, 1 µm and 0.05 µm, Kemet, NSW, Australia). The TFEs were electrochemically activated in 0.5 M H_2SO_4 (aq) by

scanning the potential between -0.21 and +1.3 V (TFE), *vs* stable Ag/AgCl RE and Pt wire RE at a sweep rate of 500 mVs^{-1} for ca. 200 cycles. For this the Pt working along with stable reference and counter electrodes were suspended into a home-made glass cell which contained 2-3 mL of deaerated 0.5M H_2SO_4. After polishing or activation, the electrodes were washed with ultrapure water and dried under a nitrogen stream. For gas experiments, the TFEs were placed into a modified rubber bung by inserting the connecting wires through it so that the electrodes were on one side and connecting wires on the other side of rubber bung. The RTIL (2 µL) was drop-cast on the TFE and the cell was connected directly to the potentiostat through the soldered wires. The electrode with a rubber bung was inserted very gently into one arm of a specially designed glass cell (a modified form of previously reported T-cell)[32-34] whose second tapered joint was closed with a glass stopper. The cell also has two openings – an inlet and outlet for gases. Prior to studying dissolved or gaseous analytes, the cell was purged with nitrogen to remove impurities or dissolved oxygen. When the baseline was stable (after ca. 20 minutes), the analyte gas was introduced into the cell and continuously flowed over the electrode.

8.2.3 Simulation Experiments

In order to investigate the sensitivity of different electrochemical techniques i.e. linear sweep voltammetry (LSV), differential pulse voltammetry (DPV) and square wave voltammetry (SWV) for reversible, quasi-reversible and irreversible redox processes, a simple model was proposed using Digi-Elch7 device (ElchSoft, Germany). For this, two electrochemical techniques were employed. Cyclic voltammetry was first performed at different sweep rates (25-150 mV/s) to study the formal potential (E^o) and peak currents for reversible, quasi-reversible and irreversible redox processes. Square wave voltammetry was performed at different analytical parameters; step potential of 2.5, 5, and 7.5 mV, frequency of 10, 20 and 30 Hz, and amplitude of 25, 50, and 75 mV, to study which set of optimal parameters give the highest sensitivity for all three redox processes. Table 8.1 shows the analytical parameters used for simulation study.

8.2.4 Lab-based Experiments

After simulation, the optimal set of parameters was applied experimentally. For square wave voltammetry, the optimised parameters correspond to a step potential of

5 mV, amplitude of 50 mV, and frequency of 20 Hz to get a well-defined peak shaped voltammogram. Different dissolved species (potassium ferricyanide, ferrocene) and gaseous analytes (hydrogen, hydrogen chloride, oxygen, and ammonia) were studied in aqueous solutions (water), a conventional organic solvent (acetonitrile) and room temperature ionic liquids (RTILs). The reversible redox processes were: (1) 1 mM $K_3Fe(CN)_6$ in water with 0.1 M KCl, (2) 1mM ferrocene in acetonitrile with 0.1 M TBAP, (3) 1mM ferrocene in $[C_2mim][NTf_2]$. The quasi-reversible processes were: (1) 100 % hydrogen, and (2) 100 ppm HCl in $[C_2mim][NTf_2]$, (3) 100 % oxygen gas in water (with 0.1 M KCl), (4) 100 % oxygen gas in acetonitrile (with 0.1 M TBAP) and (5) 100 % oxygen gas in $[C_2mim][NTf_2]$. For an irreversible process, 100 ppm ammonia was studied in seven different RTILs, $[C_2mim][NTf_2]$, $[C_4mim][NTf_2]$, $[C_4mim][FAP]$, $[C_4mim][PF_6]$, $[C_4mim][BF_4]$, $[C_6mim][FAP]$, and $[C_4mpyrr][NTf_2]$. 100 ppm ammonia (irreversible) was also studied in the presence of 1mM ferrocene (fast reversible) to investigate the effect of fast reversible and irreversible redox processes on the sensitivity of three electrochemical techniques.

8.2.5 Gas Mixing System

In order to obtain different concentrations of gases, the desired gas was diluted with nitrogen gas through gas mixing system as reported by Lee et al[34] which consists of two digital flow controllers (0-1.2 L/min, John Morris Scientific, NSW, Australia), one connected with the analyte gas cylinder (NH_3, O_2, H_2, HCl) and the other with a nitrogen cylinder through PTFE tubing via a Swagelok T-joint (Swagelok, Kardinya, WA, Australia). The mixture of both desired gases (H_2/N_2, HCl/N_2, O_2/N_2, NH_3/N_2) was then passed through an additional gas-mixing segment [34] to increase turbulence and to ensure adequate mixing of both gases. The relative flow rates were used to calculate the different concentrations of hydrogen, hydrogen chloride, oxygen, and ammonia, introduced into the T-cell.

8.3 Results and Discussion

In order to study the sensitivity of linear sweep voltammetry (LSV) and square wave voltammetry (SWV) for reversible, quasi-reversible and irreversible redox processes, three simple models were proposed using the simulation program DigiElch. For reversible and irreversible models, a one electron transfer oxidation reaction was

proposed while for the quasi-reversible model, a one electron reduction reaction was proposed, based on the choice of analytes species employed experimentally. For the simulation study, cyclic voltammetry (CV) was performed at different scan rates to study the absolute peak currents, while square wave voltammetry (SWV) was performed to investigate the effect of changing parameters i.e. step potential, amplitude, and frequency on SWV the forward, backward and total currents. From the simulated data, the optimised SWV parameters were applied experimentally to study different dissolved and gaseous analytes in aqueous, organic solvents, and RTILs.

8.3.1 Effect of Square Wave Parameters on Sensitivity Using DigiElch

Figure 8.1 shows the effect of square wave parameters such as step potential, amplitude, and frequency on the absolute currents and ratio of peak currents for SWV *vs* CV for fast reversible, quasi-reversible and irreversible redox processes, simulated using DigiElch. For a fast reversible model (Figure 8.1a), the sensitivity of SWV increased with an increase in amplitude and decreased at higher step potentials. However, an increase in frequency for a constant step potential and amplitude has no effect on the sensitivity. Thus, this information suggests that the sensitivity of SWV for a fast reversible redox process can be enhanced significantly at larger amplitudes and smaller step potentials where the voltammetry gives sharp peaks with larger peak currents.

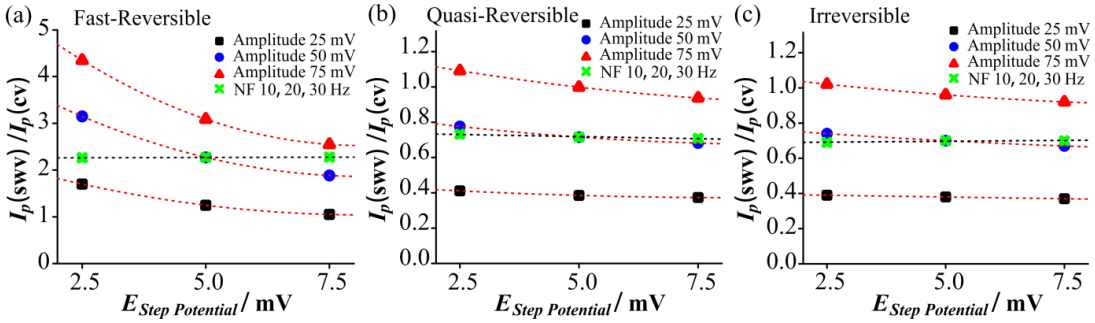

Figure: 8.1. Plots generated from a SWV simulated simple model for (a) fast-reversible, (b) quasi-reversible and (c) irreversible redox processes to explain the effect of SWV step potential, amplitude and frequency on the absolute peak current and the ratio of peak currents for SWV and CV. NF stand for normalized frequency.

For the quasi-reversible model (Figure 8.1b), the currents for SWV increased with an increase of amplitude, however changing step potential had no significant effect at smaller amplitudes (25 mV and 50 mV). Whereas at an amplitude of 75 mV, the

sensitivity of SWV is slightly increased by employing a smaller step potential of 2.5 mV rather than 7.5 mV. Similar to the fast reversible model, the SWV frequency for a quasi-reversible redox process also has no effect on sensitivity at constant amplitude. This information reveals that the sensitivity of a quasi-reversible redox process may be increased at larger amplitudes, and smaller step potentials until a sharp peak shaped wave with a large current is obtained.

For an irreversible model (Figure 8.1c), very similar observations were obtained. However, for the complicated irreversible process of ammonia oxidation in RTILs, involving a multi-electron transfer process followed by a chemical step, this simple model may not provide sufficient information to explain the complex mechanism completely.

8.3.2 Modelling of a Fast Reversible Redox Process

For the simulation of a fast reversible redox process, Figure 8.1a suggests that the highest currents will be obtained with the smallest step potential (2.5 mV) and higher amplitudes. Therefore, simulation of square wave voltammetry was performed at different amplitudes (25, 50 and 75 mV) with a constant step potential of 2.5 mV and frequency of 20 Hz – in order to keep the equivalent scan rate (50 mV/s) the same. Figure 8.2a shows simulated CVs for the model reversible redox couple over a range of scan rates. Conversely, Figures 8.2b-d show SWV for the same system at amplitudes of 25 mV, 50 mV and 75 mV, respectively. Table 8.1 shows the simulation parameters employed in these plots.

Significantly, all SWV plots resulted in total current values (It) larger than the currents for LSV at the equivalent scan rate. Additionally, both the forward current (If) and total peak It values increased as the amplitude was increased. Therefore, the maximum peak current in SWV was twice (at 25 mV amplitude) or four times (at 75 mV amplitude) larger than the peak current observed in LSV. Analysis of the If and backward current (Ib) reveals why this is the case; the forward step of the scan oxidises the species, whereas the backstep has the potential to reduce this oxidised product. The net result is that the total current increases. Furthermore, the reduced oxidised species can now be re-oxidised (increasing If further) and the product is

then re-reduced (increasing It further). This 'positive feedback loop' results in the currents for SWV exceeding those observed by LSV.

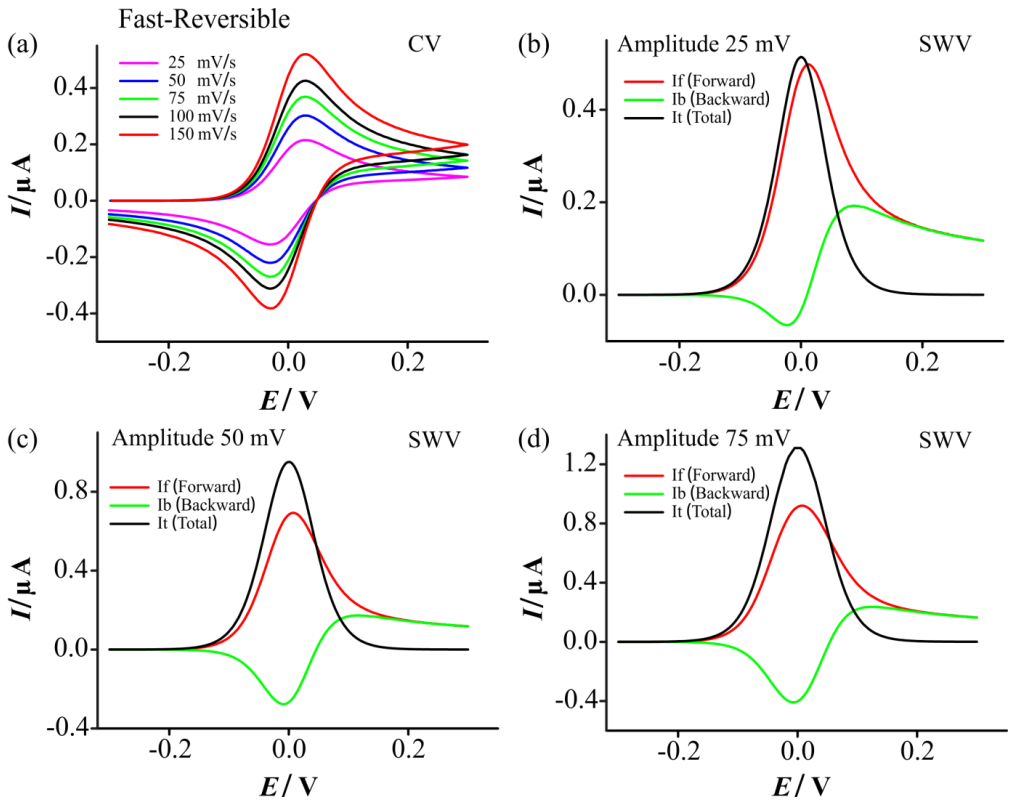

Figure: 8.2. Plots generated from the simulation of a fast-reversible model, (a) CV at scan rate 25, 50, 75, 100, 150 mV/s, and simulated SWV for forward, backward and total currents at amplitudes of (b) 25 mV, (c) 50 mV, and (d) 75 mV. The SWV step potential was 2.5 mV and frequency was 20 Hz. The concentration of oxidative species is 1 mM.

Regarding the significant effect of amplitude upon the current, the overlap between If and Ib is clearly key. At the smallest amplitude (25 mV), at low overpotentials, oxidation is observed for If, whereas for Ib this oxidation product is reduced. However, close to the peak potential and beyond the formal potential (E_f), oxidation occurs during both the forward and backward steps. As a result the effect of the 'positive feedback' is minor, and Ib does not increase It at the peak in current for If. As the amplitude increases, the 'positive feedback' loop is sustained for longer as the backward step has a more reductive potential. This enhances If (positive feedback) and also enhances It (due to significant Ib still being generated at the peak potential for If). Similar observations were observed by Osteryoung et al. who studied the dimensionless net peak current ($\Delta\psi_p$) for square wave voltammetry using various kinetic parameters to investigate the sensitivity of SWV for reversible, quasi-reversible and irreversible analytes.[35]

Table 8.1. Analytical parameters used for the simulation of reversible, quasi-reversible and irreversible redox processes using DigiElch.

Parameters	Fast Reversible	Quasi-Reversible	Irreversible
Charge transfer reaction	$Oxi + e \rightarrow Red$	$Red + e \rightarrow Oxi$	$Oxi + e \rightarrow Red$
Formal potential, E^o / (V)	**0**	**0**	**-0.3**
Transfer coefficient, (α / eV)	0.5	0.5	0.5
Rate of electron transfer, (k_s / cm/s)	**10000**	**1×10^{-4}**	**1×10^{-6}**
Diffusion coefficient, (D_{Oxi} / cm^2/s)	4×10^{-7}	4×10^{-7}	4×10^{-7}
Diffusion coefficient, (D_{Red} / cm^2/s)	4×10^{-7}	4×10^{-7}	4×10^{-7}
Radius of electrode (R / cm)	0.05	0.05	0.05
Initial Conc. C_{init} / mol/L	0.001	0.001	0.001
Geometry of electrode	Disk	Disk	Disk
Diffusion	Semi-infinite 2D	Semi-infinite 2D	Semi-infinite 2D
Start potential, E_{start} / (V)	-0.30	0.30	-0.30
End potential, E_{end} / (V)	0.30	-0.30	0.30

8.3.3 Modelling of a Quasi-Reversible Redox Process

Figure 8.3 shows the modelling of a quasi-reversible redox process using cyclic voltammetry and square wave voltammetry and Table 8.1 shows the simulation parameters employed. Figure 8.3b-d shows the SWV forward, backward, and total currents at different amplitudes from 25 mV to 75 mV with a constant step potential (2.5 mV) and frequency (20 Hz). At an amplitude of 25 mV (Figure 8.3b), the forward current is negative due to the reduction of redox species, whereas the backward current is also negative. This suggests there is not enough overpotential to oxidize the reduced species, and the 'positive feedback loop' described above does not occur (i.e. If is not enhanced and correspondingly It is also not enhanced). As a result, the total current is negative and even smaller than the backward current. As the amplitude increases, the relative size of the backward current gets smaller, resulting in a larger total current. Interestingly, there is a small shoulder in the backward peak towards negative currents (Figure 8.3d) and the reason for this is unknown at present.

Overall, these results reveal that the currents for LSV are always the same or better than SWV. The conventional amplitudes investigated here are insufficient to enhance the SWV performance for quasi-reversible couples. However, larger amplitudes can

be predicted to yield improved SWV currents as suggested by Osteryoung et al.[35] and this will be investigated in more detail in Chapter 9.

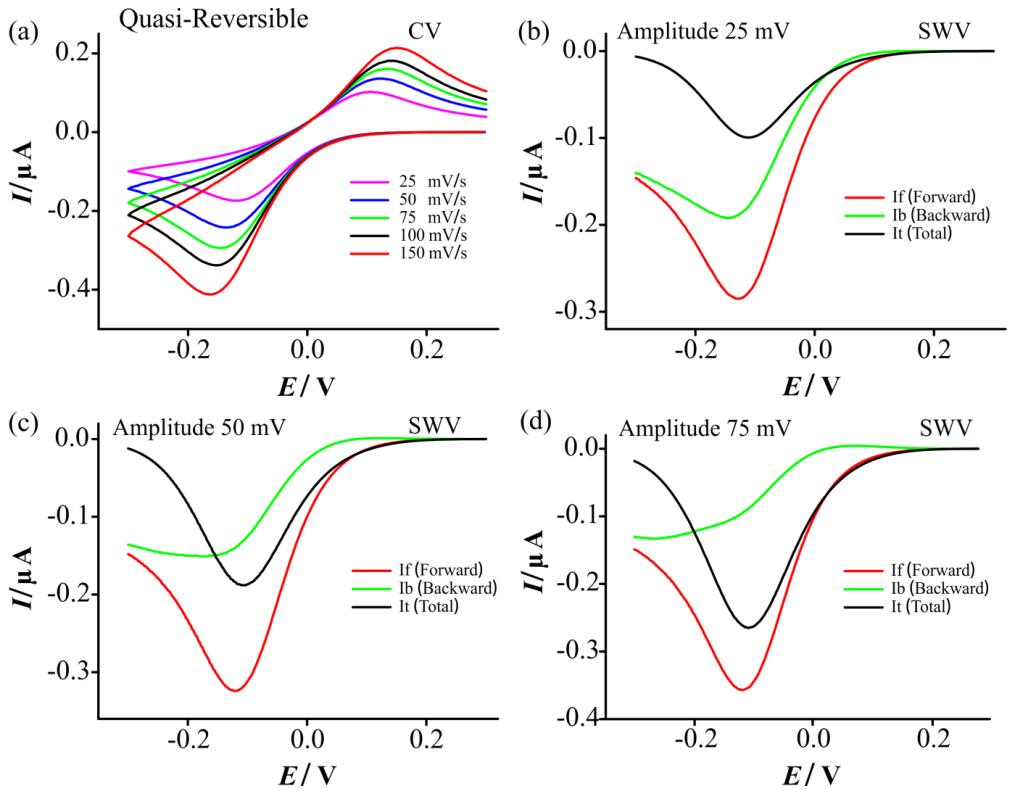

Figure: 8.3. Plots generated from simulation of a quasi-reversible process, (a) CV at scan rate 25, 50, 75, 100, 150 mV/s, and SWV forward, backward and total currents at amplitudes of (b) 25 mV, (c) 50 mV, and (d) 75 mV. The SWV step potential was 2.5 mV and frequency was 20 Hz. The concentration of reductive species is 1 mM.

8.3.4 Modelling of an Irreversible Redox Process

Figure 8.4 shows the plot generated from the simulation of an irreversible redox process for cyclic voltammetry and square wave voltammetry. Table 8.1 shows the modelling parameters employed. In the CV at varying scan rates (Figure 8.4a), the redox species is oxidised during the forward scan but there is no peak in the backward scan due to the very slow rate of electron transfer ($k_s = 10^{-6}$ cm/s) and the negative formal potential employed ($E^o = -0.3$ V). Figures 8.4b-d show the forward, backward, and total currents at varying amplitudes from 25 mV to 75 mV with a constant step potential of 2.5 mV and frequency of 20 Hz.

It can be seen in Figure 8.4 that the forward current is positive due to the oxidation of redox species, whereas the backward current is also positive due to the oxidation of small amount of parent species diffusing towards the interface. There is no redox

species to be reduced at the surface, and thus the 'positive feedback loop' does not occur and the resulting total current is even smaller than the backward current (subtraction of two positive currents).

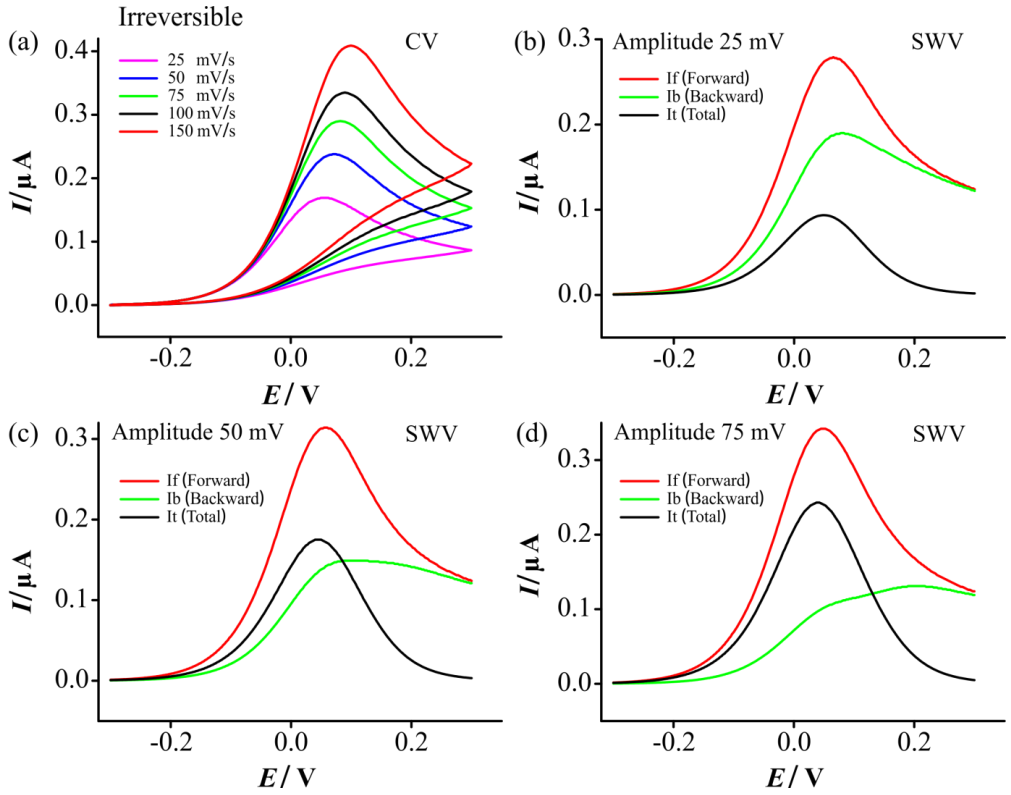

Figure: 8.4. Plots generated from the simulation of an irreversible model, (a) CV at scan rate 25, 50, 75, 100, 150 mV/s, and simulated SWV forward, backward and total currents at amplitudes of (b) 25 mV, (c) 50 mV, and (d) 75 mV. The SWV step potential was 2.5 mV and frequency was 20 Hz. The concentration of oxidative species is 1 mM.

As with the case for a quasi-reversible process, when the amplitude is increased the backward current decreases and the total current is higher. If the amplitude was increased further above 75 mV, it is not expected to improve the backward process due to there being no electrogenerated material available at the electrode surface, The positive current present in the reverse peak at all amplitudes suggests that the sensitivity of SWV for irreversible redox processes cannot be improved due to kinetic limitations.[35] Under such conditions, LSV will always give a higher current response compared to SWV.

8.3.5 Experimental Study of Fast Reversible Redox Processes

In this section, the optimal set of SWV parameters obtained from the simulation data was applied experimentally to study reversible redox species such as $K_3Fe(CN)_6$ and ferrocene in aqueous, organic and RTIL media. For a fast reversible redox process, the simulation study revealed that large amplitude with small step potential gives the highest current response. For the experimental study, it was found that a step potential of 5 mV, amplitude of 50 mV and frequency of 20 Hz was sufficient to yield a sharp peak and also the expected higher current response. These set of parameters were kept the same for all analytes (reversible, quasi-reversible and irreversible redox); corresponding to an equivalent scan rate of 100 mV/s, which was used for all comparative LSV scans.

Figure 8.5 shows a comparison of experimental SWV *vs* LSV for the electrochemical reduction of the reversible redox species, 1 mM $K_3Fe(CN)_6$ in water (with 0.1 M KCl), on a Pt TFE. The reduction of $K_3Fe(CN)_6$ in aqueous media can be represented by the following equation:[36, 37]

$$Fe(CN)_6^{3-} + e^- \rightleftharpoons Fe(CN)_6^{4-} \qquad \textbf{(8.1)}$$

Figure 8.5a shows the SWV forward, backward and total currents, where the forward peak has a large negative current corresponding to the reduction of $Fe(CN)_6^{3-}$, and the backward peak has relatively small positive current, corresponding to the oxidation of electrogenerated $Fe(CN)_6^{-4}$.

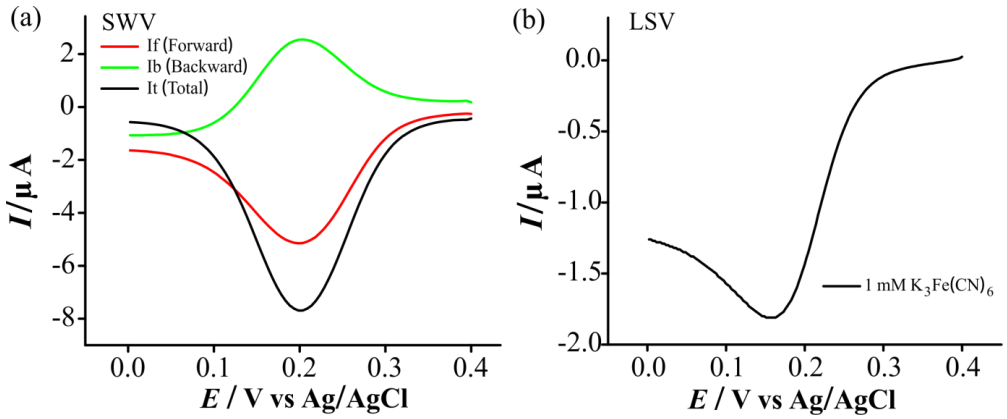

Figure: 8.5. Comparison of experimental voltammetry for a fast-reversible redox species (a) SWV forward, backward and total currents (b) LSV, for 1mM $K_3Fe(CN)_6$ in water with 0.1 M KCl on Pt TFE at a scan rate of 100 mVs^{-1}. The SWV parameters are: step potential of 5 mV, amplitude of 50 mV, frequency of 20 Hz.

The resulting total current is the difference between the forward step and the backward step which gives a large negative current since they are occurring at the same potential. Figure 8.5b shows the LSV current response for the same process at a scan rate of 100 mV/s. It can be seen that the SWV total current is ca. 4 times larger than for LSV. Thus these observations reveal that for a fast reversible redox process, SWV is (experimentally) more sensitive than LSV, as indicated by the prior simulations.

Another example of a reversible redox process is the oxidation of ferrocene (Fc). Fc undergoes a reversible (both kinetically and chemically) electrochemical redox process under standard conditions, due to its large rate constant for electron transfer ($k^o \geq 0.3$ cm/s).[26] Table 8.2 shows the reported diffusion coefficient and rate constant for Fc in an organic solvent and RTIL. Figure 8.6 shows a comparison of experimental SWV *vs* LSV for the oxidation of 1 mM Fc in acetonitrile with 0.1 M TBAP (a and b) and in the RTIL [C_2mim][NTf_2] (c and d). The electrochemical oxidation of ferrocene in organic media or RTILs can be represented by the following equation:[38, 39]

$$[Fe(C_5H_5)_2] \rightleftharpoons [Fe(C_5H_5)_2]^+ + e^- \qquad \textbf{(8.2)}$$

In SWV, the forward peaks have a positive current, corresponding to the oxidation of ferrocene (Fc) to the ferrocenium cation (Fc^+), whereas the backward peak shows negative currents which correspond to the reduction of the ferrocenium cation into ferrocene. The resulting total current is the difference which is therefore a large positive current. The total current is much larger in acetonitrile (Figure 8.6a) than in the RTIL (Figure 8.6c) which is probably due to the faster rate of diffusion of Fc in organic solvents compared to RTILs.[38, 40] During the start of SWV forward, backward and totals currents in RTILs, more significant background (non-Faradaic, capacitive) current is noticed, which is probably due to the higher viscosity of RTILs than organic solvents,[38, 40] where the slow relaxation and high concentration of oppositely charged ions in the double layer region can contribute to significant capacitive current. However, the contribution of capacitive current to the total current response was found to be negligible during the simulation study and was not further studied. Figures 8.6b,d show the corresponding LSV response at a scan rate of 100 mV/s. In both electrolytes, the total current for SWV was superior to LSV, which

reveals that for fast reversible redox processes, SWV always gives a higher current response compared to LSV at the equivalent scan rate.

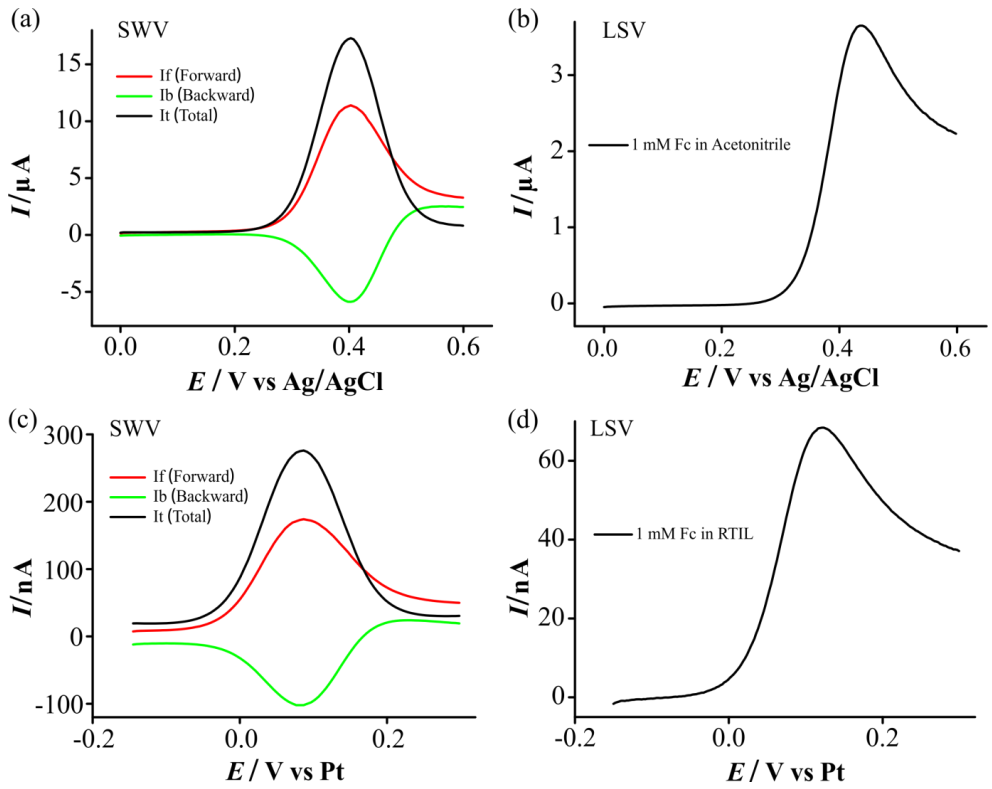

Figure: 8.6. Comparison of experimental square wave voltammetry for fast-reversible redox species. SWV forward, backward and total currents for 1 mM ferrocene in (a) acetonitrile with 0.1 M TBAP and (c) [C_2mim][NTf_2]. (b, d) Corresponding LSV responses on a Pt TFE at a scan rate of 100 mVs^{-1} *vs* Ag/AgCl RE and Pt wire CE, and integrated Pt CE and RE respectively. The SWV parameters are: step potential of 5 mV, amplitude of 50 mV, frequency of 20 Hz.

Table 8.2. Diffusion coefficients (D) and rate constants (k^o) for different redox species. Values were obtained from the literature.

Species	D / (cm^2 s^{-1})	k^o / (cm s^{-1})	References
$Fe(CN)_6^{-3}$ in Water	6.32×10^{-6}	0.21	[41]
Fc in Acetonitrile	2.30×10^{-5}	0.99	[42]
Fc in [C_2mim][NTf_2]	3.35×10^{-7}	0.21	[43]
H^+ in [C_2mim][NTf_2]	2.50×10^{-7}	1.30×10^{-3}	[44]
H_2 in [C_2mim][NTf_2]	5.50×10^{-6}	6.50×10^{-3}	[45]
O_2 in Water	1.60×10^{-5}	-	[46]
O_2 in Acetonitrile	9.20×10^{-5}	1.0×10^{-4} *a	[47]
O_2 in [C_2mim][NTf_2]	7.30×10^{-6}	2.0×10^{-4} *b	[48-50]
$O_2^{\bullet-}$ in [C_2mim][NTf_2]	2.70×10^{-6}	-	[48-50]

*: rate constant was calculated from the simulation of O_2 using Digi-Elch, (a) transfer coefficient 0.8, (b) 0.5.

8.3.6 Electrochemical Study of Quasi-Reversible Redox Species

In this section, the same comparison was performed for quasi-reversible redox couples in RTILs with different kinetics. The analytes chosen for this study were: hydrogen chloride (HCl), hydrogen (H_2) and oxygen (O_2). A discussion will be made on HCl and H_2 first (where ΔE_p is ca. 90-120 mV at 100 mV/s), followed by a discussion on O_2 (where ΔE_p is larger, often 200-300 mV). In all cases, the optimized SWV parameters correspond to a step potential of 5 mV, amplitude of 50 mV, and frequency of 20 Hz.

Figure 8.7a,b shows a comparison of experimental SWV forward, backward, and total currents *vs* LSV for 100 ppm HCl and 100 % H_2 in [C_2mim][NTf_2] on a Pt TFE. These two redox couples possess rate constants on the faster side of the defined range for quasi-reversibility ($0.3 > k^o > 2\times10^{-5}$ cm/s), close to the reversible limit. Therefore the SWV response for such redox species is expected to be quite similar to the reversible process just described. In terms of mechanisms, HCl dissociates in RTILs according to:[51]

$$2HCl_{gas} \rightleftharpoons H^+ + [HCl_2]^- \qquad \textbf{(8.3)}$$

The detection of HCl in RTILs can thus occur through the reduction of H^+ to adsorbed hydrogen (H_{ads}).[51]

$$H^+ + e^- \rightleftharpoons H_{ads} \qquad \textbf{(8.4)}$$

For H_2 in RTILs, the oxidation can be represented by the following equation:[52]

$$\frac{1}{2}H_2 \rightleftharpoons H^+ + e^- \qquad \textbf{(8.5)}$$

Table 8.2 shows the reported rates of electron transfer for H^+ and H_2 in [C_2mim][NTf_2] and their corresponding diffusion coefficients. Figure 8.7a shows the SWV response for 100 ppm HCl in [C_2mim][NTf_2] on a Pt TFE. The forward peak has a negative current as expected, and the backward peak has a positive current, corresponding to the oxidation of adsorbed protons produced in the forward step. The resulting SWV total current is therefore large and negative. Figure 8.7b shows the corresponding LSV response at a scan rate of 100 mV/s. The SWV total current is ca. three times larger than the LSV response, consistent with the results for a fast reversible redox process. For the next analyte species, Figure 8.7c,d shows a

comparison of SWV *vs* LSV for 100 % H_2 in [C_2mim][NTf_2] on a Pt TFE. The forward current is positive, corresponding to the the oxidation of H_2 into protons, whereas the the backward current is negative as a result of the reduction of protons into hydrogen. The resultant SWV total current therefore large and positive; the current is ca. three times higher than the equivalent LSV current (Figure 8.7d). The results for both these redox couples show that they behave quite similar to fast reversible redox processes, where the current response for SWV is far superior to LSV.

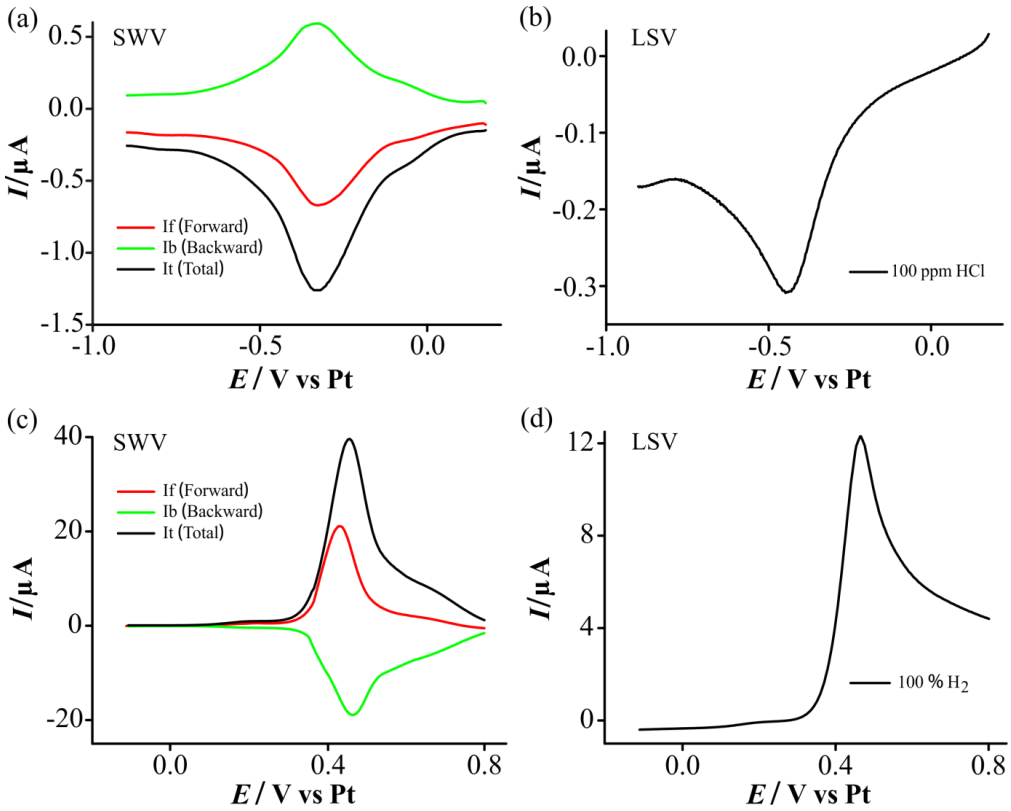

Figure: 8.7. Comparison of voltammetry for reductive and oxidative quasi-reversible redox species. Experimental SWV forward, backward and total currents and LSV (at 100 mVs^{-1}) for (a, b) 100 ppm HCl (c, d) 100 % H_2, on a Pt TFE in [C_2mim][NTf_2]. The SWV parameters are: step potential of 5 mV, amplitude of 50 mV, frequency of 20 Hz.

For a quasi-reversible process with slower kinetics, oxygen (O_2) was chosen. The electrochemical reduction of oxygen in organic and RTIL media is represented by a simple one-electron reduction:[53-56]

$$O_2 + e^- \rightleftharpoons O_2^{\bullet -} \qquad \textbf{(8.6)}$$

The peak to peak separation for the oxygen/superoxide redox couple is relative large (few hundred mV), suggesting that the rate constant is much slower than for H^+

reduction and H_2 oxidation just described. The rate constant for oxygen in acetonitrile and $[C_2mim][NTf_2]$ was calculated by fitting the oxygen voltammetry using DigiElch, and the values are presented in Table 8.2.

In water, the mechanism is more complicated, involving an ECEC mechanism:[54, 56-59]

$$O_2 + 2H^+ + 2e^- \rightarrow H_2O_2 \quad \textbf{(8.7)}$$

$$H_2O_2 + 2H^+ + 2e^- \rightarrow 2H_2O \quad \textbf{(8.8)}$$

The rate constant in water was calculated by simulating the oxygen voltammetry using these two steps. The first step had a rate constant (k^o) of 2.65×10^{-5} cm s^{-1} and a transfer coefficient (α) 0.4 eV. The second step had a rate constant (k^o) of 9.5×10^{-5} cm s^{-1} and a transfer coefficient (α) 0.8 eV. Diffusion coefficients for the redox species O_2, and H_2O_2 were calculated to be 1.6×10^{-5}, and $1.6\times10^{-6,}$ respectively.

Figure 8.8 shows a comparison of experimental SWV *vs* LSV for the reduction of 100 % oxygen in water, acetonitrile, and RTILs. In all media, the backward current (Ib) is negative, despite the fact that the reduction is chemically reversible in acetonitrile and RTILs. This suggests that there is not enough overpotential applied to oxidise the electrogenerated superoxide back to oxygen. Overall, the SWV total current response is therefore smaller than the forward current, and similar to the equivalent LSV response in water and RTILs, and much less than LSV in acetonitrile. This is an important finding and suggests that using SWV for the detection of redox couples with slower kinetics may not be as favourable as using LSV. Based on the results presented in Figure 8.1b, it may be possible to improve the current response for SWV by applying higher amplitudes, and this is the focus of the next chapter.

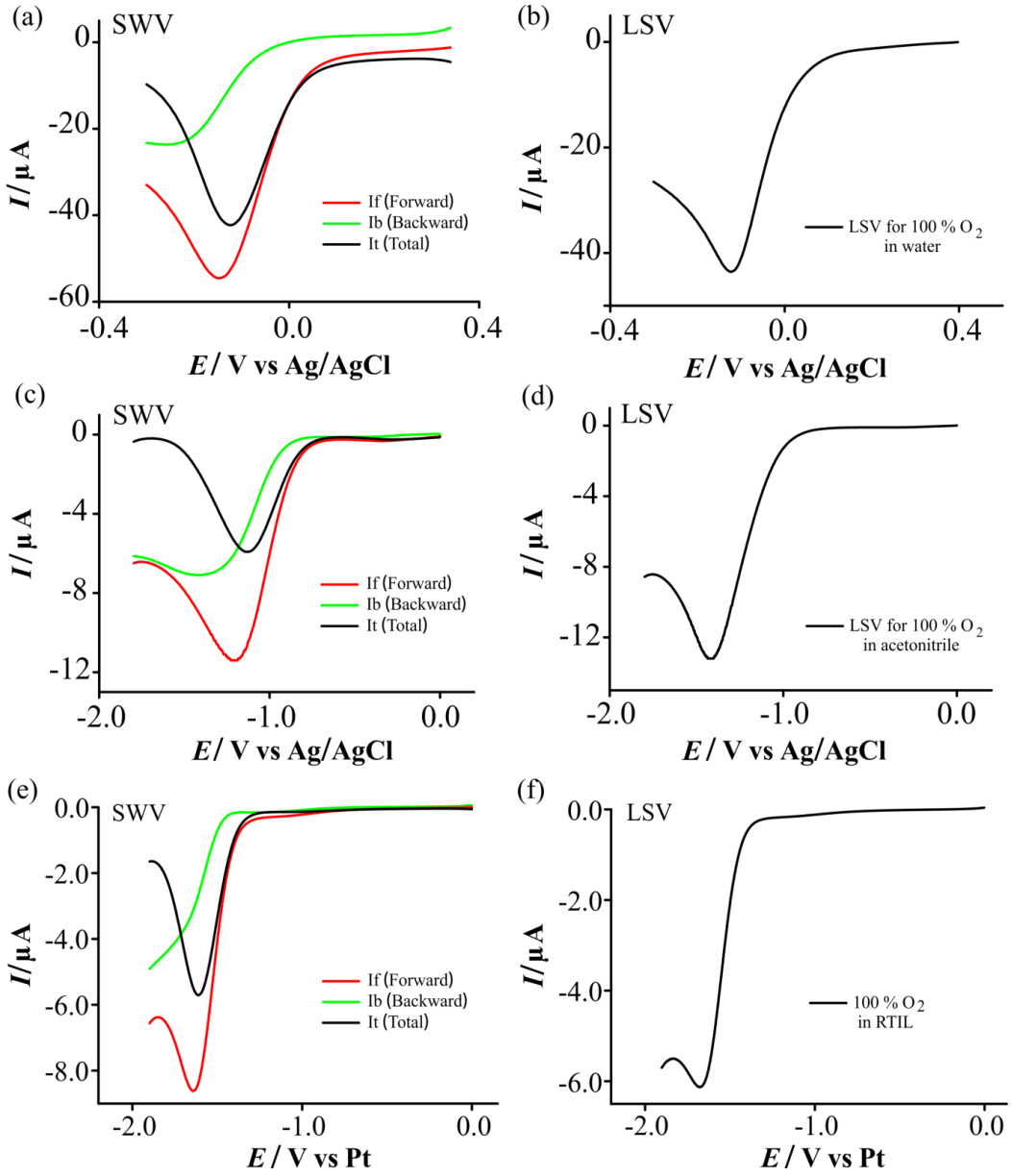

Figure: 8.8. Comparison of voltammetry for the quasi-reversible redox couple oxygen/superoxide. Experimental SWV forward, backward and total currents for 100 % oxygen in (a) water with 0.1 M KCl on a Pt macrodisk electrode (c) acetonitrile with 0.1 M TBAP on a Pt TFE and (e) [C_2mim][NTf_2] on a Pt TFE. Figures (b, d, and f) are the corresponding LSV responses at a scan rate of 100 mVs^{-1}. The SWV parameters are: step potential of 5 mV, amplitude of 50 mV, frequency of 20 Hz.

8.3.7 Electrochemical Study of an Irreversible Redox Species

Finally, having simulated the irreversible scenario earlier in this chapter, and showing that SWV did not give higher currents compared to LSV, it was nethertheless necessary to experimentally investigate if the model was sufficient. In order to do so, ammonia (NH_3) oxidation (irreversible) was studied in seven different RTILs, [C_2mim][NTf_2], [C_4mim][NTf_2], [C_4mim][FAP], [C_4mim][PF_6],

[C_4mim][BF_4], [C_6mim][FAP], and [C_4mpyrr][NTf_2]. The results are only shown for [C_2mim][NTf_2] but appear the same in all RTILs. As described in the previous chapters, the mechanism for ammonia oxidation can be represented by the following equation:[60, 61]

$$NH_3(g) \rightarrow \frac{1}{2}N_2(g) + 3H^+ + 3e^- \qquad \textbf{(8.9)}$$

This process is both chemically and electrochemically irreversible, with an expected rate constant k^o of less than 2×10^{-5} cm/s (although this has not been experimentally determined due to the complicated nature of the follow-up chemistry).

The simulation study for the irreversible model (earlier in this chapter) revealed that the backward component gives a positive current at higer amplitudes. The positive current therefore decreases the sensitivity of SWV. Figures 8.9a,b shows a comparison of the experimental SWV forward, backward, and total currents *vs* LSV for 100 ppm NH_3 in [C_2mim][NTf_2] on a Pt TFE. It is observed that the background-subtracted current response for SWV is smaller than for LSV, incidating that LSV is the superior technique.

In an attempt to show both reversible and irreversible couples on the same graph, ammonia oxidation (irreversible) was studied in the presence of ferrocene (reversible). Figure 8.9c shows the SWV response, and Figure 8.9d shows the corresponding LSV response. It is clearly observed that even when both analytes are present in the same solution, the backward current for ferrocene is negative, and the backward current for ammonia is positive. Overall, the peak is enhanced for ferrocene, but diminished for ammonia compared to the LSV response (Figure 8.9c).

To conclude, it is not possible to improve the current response for SWV for an irreversible redox system. Thus is consistent with literature studies for irreversible redox processes, which show that larger amplitudes have no effect on the sensitivity.[13, 17, 29]

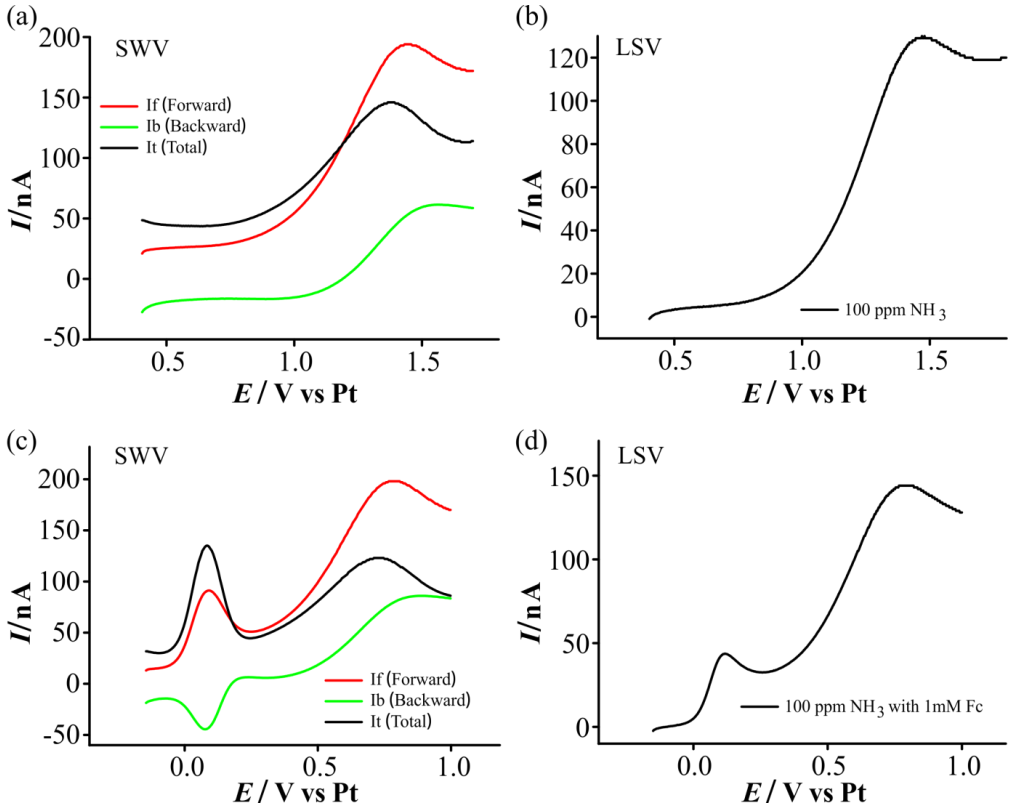

Figure: 8.9. Comparison of experimental voltammetry for an irreversible redox species – ammonia oxidation. SWV forward, backward and total currents for (a) 100 ppm NH_3, (c) 100 ppm NH_3, and 100 ppm NH_3 in the presence of 1mM ferrocene in [C_2mim][NTf_2]. (b, d) shows the corresponding LSV current response at a scan rate of 100 mVs^{-1}. The SWV parameters are: step potential of 5 mV, amplitude of 50 mV, frequency of 20 Hz.

8.4 Conclusions

A simple one electron transfer reaction was modelled successfully for fast reversible, quasi-reversible and irreversible redox processes using the simulation program DigiElch. Different kinetic parameters were studied to investigate the current response of SWV. The optimized kinetic parameters were employed experimentally to study the sensitivity of SWV *vs* LSV for various analytes in water, acetonitrile and RTILs. For fast reversible redox species such as potassium ferricynaide, and ferrocene, SWV gives higher sensitivity than LSV due to the reversible current present in the backward step. For quasi-reversible redox reactions which have a relatively high rate constant, such as the oxidation of H_2 and reduction of protons (for HCl), SWV behaves more like a fast reversible redox process, where SWV is superior to LSV. For a quasi-reversible redox process with a relatively slow rate of electron tranfer kinetics, such as the reduction of oxygen in acetonitrile and RTILs, LSV is only slightly superior to SWV. However, its sensitivity may be improved by

employing a larger amplitude, as will be discussed in the next chapter. For a completely irreversible redox process such as ammonia in RTILs, the SWV response cannot be improved due to the irreversible backward step. In this situation, the preferred voltammetric technique is LSV which gives higher currents compared to SWV.

References

1. C. H. Hamann, A. Hamnett and W. Vielstich, *Electrochemistry, 2nd, Completely Revised and Updated Edition*, Wiley-VCH, Weinheim, 2007.
2. A. Chen and B. Shah, *Analytical Methods*, 2013, **5**, 2158-2173.
3. L. Xiao, G. G. Wildgoose and R. G. Compton, *Analytica Chimica Acta*, 2008, **620**, 44-49.
4. R. A. Medeiros, R. C. Rocha-Filho and O. Fatibello-Filho, *Food Chemistry*, 2010, **123**, 886-891.
5. Š. Komorsky-Lovrić and I. Novak, *Journal of food science*, 2011, **76**.
6. S. A. Özkan, B. Uslu and H. Y. Aboul-Enein, *Critical reviews in analytical chemistry*, 2003, **33**, 155-181.
7. B. Uslu and S. A. Ozkan, *Analytical Letters*, 2011, **44**, 2644-2702.
8. L. Jia, X. H. Zhang, Q. Li and S. F. Wang, *Journal of Analytical Chemistry*, 2007, **62**, 266-269.
9. J. Gonzalez, A. Molina, F. Martinez Ortiz and E. Laborda, *The Journal of Physical Chemistry C*, 2012, **116**, 11206-11215.
10. E. Laborda, A. Molina, Q. Li, C. Batchelor-McAuley and R. G. Compton, *Physical Chemistry Chemical Physics*, 2012, **14**, 8319-8327.
11. A. Molina, J. González, E. Laborda, Y. Wang and R. G. Compton, *Physical Chemistry Chemical Physics*, 2011, **13**, 16748-16755.
12. V. Mirc˘eski, F. Quentel, M. L'Her and C. Elleouet, *The Journal of Physical Chemistry C*, 2007, **111**, 8283-8290.
13. J. J. O'Dea, J. Osteryoung and R. A. Osteryoung, *Analytical Chemistry*, 1981, **53**, 695-701.
14. M. Lovrić and D. Jadreško, *Electrochimica Acta*, 2010, **55**, 948-951.
15. S. A. Trammell, D. Zabetakis, M. Moore, J. Verbarg and D. A. Stenger, *PLOS ONE*, 2015, **9**, e115966.
16. L. Wang, H. Chen, X. Huang and J. Nan, *Electroanalysis*, 2009, **21**, 755-761.
17. V. Mirceski, S. Komorsky-Lovric and M. Lovric, *Square-wave voltammetry: theory and application*, Springer Science & Business Media, 2007.
18. F. Scholz, *Electroanalytical methods*, Springer, 2010.
19. A. J. Bard and L. R. Faulkner, *Electrochemical Methods, Fundamentals and Applications*, John Wiley & Sons, New York, 1980.
20. B. A. Brookes, G. Macfie and R. G. Compton, *The Journal of Physical Chemistry B*, 2000, **104**, 5784-5789.
21. F. E. A. Catunda, M. F. de Araujo, A. M. Granero, F. J. Arévalo, M. G. de Carvalho, M. A. Zón and H. Fernández, *Electrochimica Acta*, 2011, **56**, 9707-9713.
22. A. Y. Tesio, A. M. Granero, H. Fernández and M. A. Zón, *Electrochimica Acta*, 2011, **56**, 2321-2327.
23. S. J. M. Rosvall, M. Sharp and A. Bond, *Journal of Electroanalytical Chemistry*, 2002, **536**, 161-169.

24. S. J. M. Rosvall, M. Sharp and A. M. Bond, *Journal of Electroanalytical Chemistry*, 2003, **546**, 51-58.
25. V. Mirceski, E. Laborda, D. Guziejewski and R. G. Compton, *Analytical Chemistry*, 2013, **85**, 5586-5594.
26. H. Matsuda and Y. Ayabe, *Berichte der Bunsengesellschaft für physikalische Chemie*, 1955, **59**, 494-503.
27. A. M. Bond, *Broadening electrochemical horizons*, Oxford University Press, Oxford, 2002.
28. M. Rudolph, *Journal of Electroanalytical Chemistry*, 2001, **503**, 15-27.
29. Š. Komorsky-Lovrić and M. Lovrić, *Advances in Analytical Chemistry*, 2013, **3**, 9-13.
30. B. A. Brookes and R. G. Compton, *The Journal of Physical Chemistry B*, 1999, **103**, 9020-9028.
31. B. A. Brookes, J. C. Ball and R. G. Compton, *The Journal of Physical Chemistry B*, 1999, **103**, 5289-5295.
32. U. Schroder, J. D. Wadhawan, R. G. Compton, F. Marken, P. A. Z. Suarez, C. S. Consorti, R. F. de Souza and J. Dupont, *New J. Chem.*, 2000, **24**, 1009-1015.
33. D. S. Silvester, A. J. Wain, L. Aldous, C. Hardacre and R. G. Compton, *J. Electroanal. Chem.*, 2006, **596**, 131-140.
34. J. Lee, K. Murugappan, D. W. M. Arrigan and D. S. Silvester, *Electrochim. Acta*, 2013, **101**, 158-168.
35. J. G. Osteryoung and R. A. Osteryoung, *Analytical Chemistry*, 1985, **57**, 101-110.
36. M. A. Dayton, J. C. Brown, K. J. Stutts and R. M. Wightman, *Analytical Chemistry*, 1980, **52**, 946-950.
37. D. K. Nordstrom, *Geochimica et Cosmochimica Acta*, 1977, **41**, 1835-1841.
38. E. I. Rogers, D. S. Silvester, D. L. Poole, L. Aldous, C. Hardacre and R. G. Compton, *The Journal of Physical Chemistry C*, 2008, **112**, 2729-2735.
39. A. M. Bond, T. L. E. Henderson, D. R. Mann, T. F. Mann, W. Thormann and C. G. Zoski, *Analytical Chemistry*, 1988, **60**, 1878-1882.
40. N. G. Tsierkezos, *Journal of Solution Chemistry*, 2007, **36**, 289-302.
41. E. L. Goldstein and M. R. Van de Mark, *Electrochimica Acta*, 1982, **27**, 1079-1085.
42. A. D. Clegg, N. V. Rees, O. V. Klymenko, B. A. Coles and R. G. Compton, *Journal of Electroanalytical Chemistry*, 2005, **580**, 78-86.
43. N. Fietkau, A. D. Clegg, R. G. Evans, C. Villagrán, C. Hardacre and R. G. Compton, *ChemPhysChem*, 2006, **7**, 1041-1045.
44. Y. Meng, L. Aldous, S. R. Belding and R. G. Compton, *Physical Chemistry Chemical Physics*, 2012, **14**, 5222-5228.
45. Y. Meng, L. Aldous, S. R. Belding and R. G. Compton, *Chemical Communications*, 2012, **48**, 5572-5574.
46. M. C. Buzzeo, C. Hardacre and R. G. Compton, *Analytical Chemistry*, 2004, **76**, 4583-4588.
47. Q. Li, C. Batchelor-McAuley, N. S. Lawrence, R. S. Hartshorne and R. G. Compton, *Journal of Electroanalytical Chemistry*, 2013, **688**, 328-335.
48. M. C. Buzzeo, O. V. Klymenko, J. D. Wadhawan, C. Hardacre, K. R. Seddon and R. G. Compton, *J. Phys. Chem. A*, 2003, **107**, 8872-8878.
49. E. E. L. Tanner, L. Xiong, E. O. Barnes and R. G. Compton, *Journal of Electroanalytical Chemistry*, 2014, **727**, 59-68.
50. E. I. Rogers, A. M. O'Mahony, L. Aldous and R. G. Compton, *ECS Transactions*, 2010, **33**, 473-502.
51. K. Murugappan and D. S. Silvester, *Physical Chemistry Chemical Physics*, 2016, **18**, 2488-2494.
52. D. S. Silvester, K. R. Ward, L. Aldous, C. Hardacre and R. G. Compton, *J. Electroanal. Chem.*, 2008, **618**, 53-60.

53. M. E. Peover and B. S. White, *Electrochimica Acta*, 1966, **11**, 1061-1067.
54. P. S. Jain and S. Lal, *Electrochimica Acta*, 1982, **27**, 759-763.
55. R. G. Evans, O. V. Klymenko, S. A. Saddoughi, C. Hardacre and R. G. Compton, *J. Phys. Chem. B*, 2004, **108**, 7878-7886.
56. H. S. Wroblowa, P. Yen Chi and G. Razumney, *Journal of Electroanalytical Chemistry and Interfacial Electrochemistry*, 1976, **69**, 195-201.
57. K. L. Hsueh, D. T. Chin and S. Srinivasan, *Journal of Electroanalytical Chemistry and Interfacial Electrochemistry*, 1983, **153**, 79-95.
58. E. Yeager, *Journal of Molecular Catalysis*, 1986, **38**, 5-25.
59. C. Song and J. Zhang, in *PEM Fuel Cell Electrocatalysts and Catalyst Layers: Fundamentals and Applications*, ed. J. Zhang, Springer London, London, 2008, DOI: 10.1007/978-1-84800-936-3_2, pp. 89-134.
60. X. Ji, C. E. Banks, D. S. Silvester, L. Aldous, C. Hardacre and R. G. Compton, *Electroanal.*, 2007, **19**, 2194 – 2201.
61. X. Ji, D. S. Silvester, L. Aldous, C. Hardacre and R. G. Compton, *J. Phys. Chem. C*, 2007, **111** 9562–9572.

Chapter 9

9. Optimising Square Wave Voltammetry for Oxygen Reduction – A Quasi-Reversible Process

In the previous chapter, it was speculated that the sensitivity of SWV for a quasi-reversible redox process could be improved by employing a larger amplitude. In this chapter, this process is modelled using the simulation program Digi-Elch and the data is fitted to the experimental 100 % oxygen response in an RTIL. Using this model, different SWV parameters were studied to investigate the sensitivity of SWV and work towards more sensitive quantification of O_2. The optimised set of SWV parameters was applied experimentally to study different concentrations of oxygen at three different amplitudes. Finally SWV at three different amplitudes was compared with LSV to investigate the effect of amplitude on the sensitivity of voltammetric techniques for oxygen reduction in RTIL.

9.1 Introduction

The monitoring of oxygen has great importance in many applications such as food quality,[1] medical applications,[2] mining industry,[3] and environmental monitoring.[4] The concentration of oxygen below 18 % by volume is dangerous for human life due to risk of asphyxiation and above 23 % is at a danger of fire.[5] Thus, it is important to monitor oxygen within this range using sensitive and low-cost oxygen monitoring devices such as amperometric gas sensors. The use of non-volatile electrolyte such as room temperature ionic liquids (RTILs) as a sensing media makes the sensor more stable, thus enables the device to work in hot and dry environment.[6, 7]

As discussed in the previous chapter, Mirceski *et al*. introduced a new approach of "amplitude-based quasireversible maximum" rather than the classical quasireversible maximum (QRM) to study the electrode kinetics of a variety of quasi-reversible electrode mechanisms.[8] In this chapter, we will employ a similar approach where the SWV amplitude is used as the main tool to study the sensitivity of SWV for a quasi-reversible redox process. For this, we introduce a one electron transfer model for a quasi-reversible redox reaction with a rate constant (k^o) of 2×10^{-4} cm/s and the simulated data is fitted with experimental data for 100 % oxygen voltammetry in a

room temperature ionic liquid (RTIL). Using a quasi-reversible model, various SWV parameters such as step potential, frequency and amplitude were studied to optimise the SWV parameters. With the best set of SWV parameters, the SWV split currents such as forward, backward and total current response were studied over a range of SWV amplitudes. The best set of three amplitudes is studied experimentally to investigate the influence of amplitude on the current for SWV at different concentrations (10-100 % and 1-10 % oxygen).

9.2 Experimental

9.2.1 Chemical Reagents

All chemicals were commercially available and used as received. The room temperature ionic liquid (RTIL) 1-ethyl-3-methylimidazolium bis(trifluoromethylsulfonyl)imide ($[C_2mim][NTf_2]$) was purchased from Merck KGaA (Kilsyth, Victoria, Australia) at high purity electrochemical grade. Acetone (99% purity), ethanol (EtOH, 99%), sulfuric acid (98% w/w [18.4 M]) and zinc chloride ($ZnCl_2$, 40% w/v, used as a soldering flux for connecting wires with electrodes), were all purchased from Sigma Aldrich. Acetonitrile (MeCN, >99.8%, Fischer Scientific) was used for washing the electrodes before and after use. Ultrapure water with a resistance of 18.2 MΩcm was prepared by an ultrapure water purification system (Millipore Pty Ltd., North Ryde, NSW, Australia). High purity oxygen gas (>99.5%) was purchased from CAC gases (Auburn, NSW, Australia). Nitrogen gas (for further dilution of O_2) was obtained from a ≥ 99.99 % high purity, compressed nitrogen cylinder (BOC gases, Welshpool, WA, Australia).

9.2.2 Electrochemical Experiments

All experiments were performed using a PGSTAT101 Autolab potentiostat (Eco, Chemie, Netherlands) interfaced to a PC with Nova 1.11 software, at laboratory room temperature (294±1 K) inside an aluminium Faraday cage present in the fume cupboard to reduce electrical interference. Platinum (Pt) thin-film electrodes (TFEs), obtained from Micrux Technologies, Oviedo, Spain (ED-SE1-Pt) were used as sensing surfaces, which have a three electrode arrangement, with working, counter and reference electrodes, all made of Pt with 1mm diameter working electrode, on a Pyrex glass substrate.

Before sensing gas experiments, the TFEs were electrochemically activated using 0.5 M H_2SO_4 (aq) *vs* stable Ag/AgCl (0.1 M KCl) reference electrode (BASi, Indiana, USA) and Pt coil counter electrode (Goodfellow, Cambridge Ltd., UK) at a sweep rate of 500 mVs^{-1} for ca. 200 cycles. The electrodes were washed with ultrapure water and dried under a stream of nitrogen. For gas sensing experiments, the TFE electrode was placed into a modified rubber bung and inserted into the glass cell (a modified version of a T-cell).[9-11] 2 µL of RTIL was drop-cast on the TFE. Prior to the introduction of oxygen, the cell was purged with nitrogen to remove dissolved gases and impurities. When the baseline was stable (after ca. 20 minutes), oxygen gas was introduced into the cell and continuously flowed over the electrode.

Three different electrochemical techniques were performed to study oxygen reduction. Cyclic voltammetry (CV) was performed to study the mechanism of 100 % oxygen on Pt TFE in $[C_2mim][NTf_2]$. For the analytical utility and limit of detection (LOD) study, different concentrations were measured between 10-100 % and 1-10 % oxygen using linear sweep voltammetry (LSV) and square wave voltammetry (SWV) to investigate which technique is more sensitive in a gas/ionic liquid system. For LSV and SWV, the potential was scanned between 0.0 V and - 2.1 (depending on the reduction peak potential) to study the reduction peak of oxygen.

In order to get the best sensitivity of SWV for quasi-reversible redox process (oxygen reduction in RTIL) *vs* LSV, simulation was performed for 100 % oxygen CV using the simulation program DigiElch7 (ElchSoft, Germany). The simulated parameters obtained from CV were applied to optimise the SWV which correspond to a step potential of 2.5, 5 and 7.5 mV, amplitude of 50, 100, 150, 200, 300 and 400 mV, and a frequency of 10, 20 and 30 Hz. The optimised SWV parameters were also applied experimentally to study oxygen reduction in $[C_2mim][NTf_2]$. Under the optimized experimental parameters, oxygen voltammetry was performed for different concentration ranges from 10-100 % O_2 and SWV results were studied at three different amplitudes of 50, 150 and 300 mV at constant step potential (2.5 mV) and frequency (20 Hz). To obtain the lowest limits of detection and highest sensitivities for oxygen in ionic liquids, the SWV was also performed at a lower concentration range from 1-10 % O_2 and the results are compared with LSV.

9.2.3 Gas Mixing System

In order to obtain different concentrations of oxygen gas, high purity 100 % oxygen was diluted with nitrogen gas through gas mixing system as reported by Lee et al[11] which consisted of two digital flow controllers (0-1.2 L/min, John Morris Scientific, NSW, Australia), one connected with the analyte gas cylinder (O_2) and other with a nitrogen cylinder through PTFE tubing via a Swagelok T-joint (Swagelok, Kardinya, WA, Australia). The mixture of both desired gases (O_2/N_2) was then passed through an additional gas-mixing segment[11] to increase turbulence and to ensure adequate mixing of both gases. The relative flow rates were used to calculate the different concentrations of oxygen introduced into the T-cell.

9.3 Results and Discussion

9.3.1 Simulation of Oxygen Reduction Using DigiElch

In order to simulate the CV of oxygen reduction, a quasi-reversible one electron transfer model was proposed. The modelled reaction mechanism can be described as below.

$$A + e^- = B \qquad \textbf{(9.1)}$$

Where A is oxygen and B is superoxide. First cyclic voltammetry (CV) was performed experimentally at 100 mV/s and was simulated using DigiElch. Figure 9.1 shows overlaid experimental (black) and simulated (red) cyclic voltammograms for the reduction of oxygen.

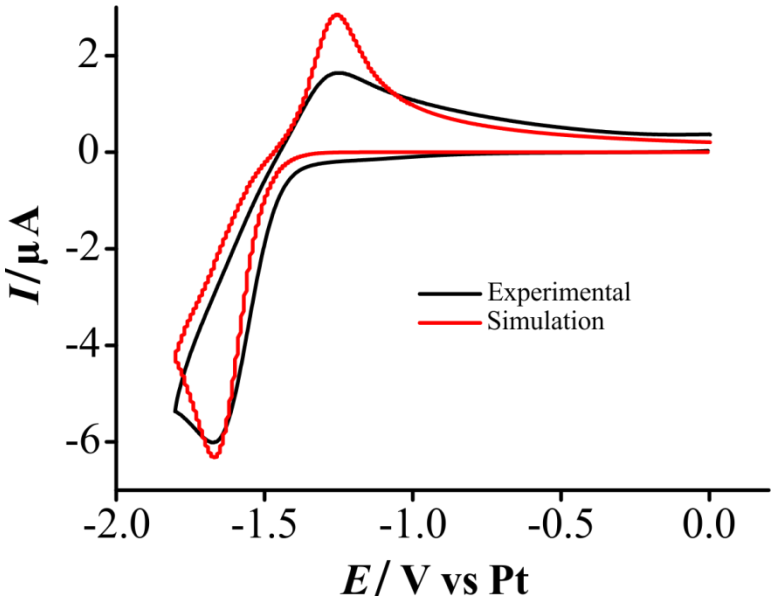

Figure 9.1. Comparison of experimental (black) and simulated (red) CV for the reduction of 100 % O_2 in [C_2mim][NTf_2] on a Pt TFE *vs* integrated Pt CE and RE at a scan rate of 100 mVs^{-1}.

Table 9.1 shows the simulation parameters used to model this process. The simulated model looks the most similar to the experimental CV (in terms of peak to peak separations) when choosing a rate constant for electron transfer (k^o) of 2×10^{-4} cm/s, diffusion coefficients for oxygen, O_2 (Do_2) of 9.3×10^{-6} cm^2/s, and for superoxide, O^{2-} ($Do_2^{\bullet-}$) of 6×10^{-6} cm^2/s. The optimised simulated parameters were then applied to run cyclic voltammetry at different scan rates to study the absolute peak current for oxygen reduction. The diffusion coefficients used for simulation study are similar to those reported in the literature.[12, 13] Fitting of the reverse peak current was not attempted as it was not the focus of this study.

9.3.2 Optimisation of Square Wave Parameters Using DigiElch

To optimise the SWV parameters of step potential, amplitude and frequency, the parameters obtained from the simulation of CV was then applied in square wave voltammetry. A number of SWV scans were run at different sets of SWV parameters such as step potential of 2.5, 5, 7.5 mV, amplitude of 50, 75, 100, 125, 150, 175, 200, 225, 250, 275, 300, 350, 400 mV, and frequency of 10, 20, 30 Hz, while keeping one parameter constant and changing the others. Table 9.1 shows the simulation parameters used to model square wave voltammetry.

Table 9.1. Analytical parameters used in the simulation of SWV for a quasi-reversible redox process using DigiElch.

Parameters	Values	Parameters	Values
Charge transfer reaction	$A + e \rightarrow B$	Start potential, E_{start} / (V)	0.0
Formal potential, E^o / (V)	**-1.45**	End potential, E_{end} / (V)	-1.8
Transfer coefficient, (α / eV)	0.5	Step potential, dE_s / (V)	2.5, 5, 7.5
Rate of electron transfer, (K^o / cm/s)	$\mathbf{2\times10^{-4}}$	Amplitude, E_{sw} / (V)	50-400
Diffusion coefficient, (D_{O2} / cm^2/s)	9.3×10^{-6}	Frequency, f / (Hz)	10, 20, 30
Diffusion coefficient, (D_{O2^-} / cm^2/s)	6×10^{-6}	Scan rate, V / (V/s)	50, 100, 150
Radius of electrode (R / cm)	0.05	Geometry of electrode	Disk
Initial Conc. C_{init} / mol/L	2.7×10^{-3}	Diffusion	Semi-infinite 2D

Figure 9.2 shows a plot of the simulated ratio of absolute peak currents for SWV and CV *vs* step potential at different amplitudes and frequencies. It is noted that at a constant amplitude and frequency, the sensitivity of SWV increases with a decrease in step potential from 7.5 mV to 2.5 mV. Interestingly, SWV frequency has no significant effect on sensitivity at a constant amplitude and step potential. However, the sensitivity of SWV for a quasi-reversible process is increased with the increase of amplitude but this increase was consistent and uniform with different step potentials at smaller amplitudes of 50 mV to 100 mV. As the amplitude is increased above 300 mV, a dominant increase in sensitivity is observed at a smaller step potential of 2.5. Importantly, at the largest amplitude of 400 mV with smaller step potential of 2.5 mV, the sensitivity is ca. 6 times larger than at an amplitude of 50 mV. Thus, this information suggests that the sensitivity of SWV for a quasi-reversible redox process can be enhanced many times by using larger amplitude with a smaller step potential where the SWV gives a sharp peak with a larger current response.

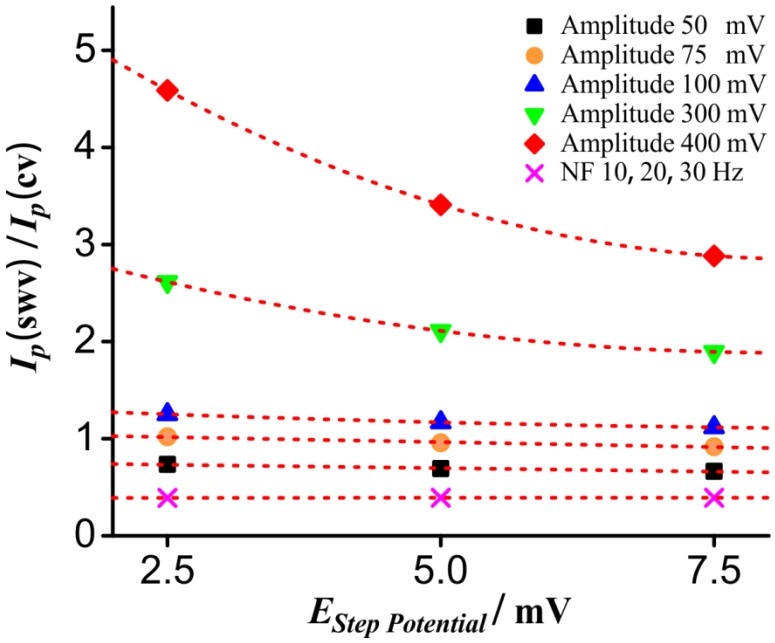

Figure: 9.2. Plot generated from the simulation of a quasi-reversible redox process to investigate the effect of SWV step potential, amplitude and frequency on the ratio of peak current for SWV and CV. NF stands for normalized frequency.

9.3.3 Effect of Changing Square Wave Amplitude for a Quasi-Reversible Redox Process Using DigiElch

In order to investigate the effect of amplitude on the sensitivity of SWV, the quasi-reversible reaction was modelled at different SWV amplitudes while keeping a smaller step potential and constant frequency. Figure 9.3 shows simulated SWV forward, backward, and total current response for the quasi-reversible model at different amplitudes of 50, 100, 150, 200, 300 and 400 mV with a step potential of 2.5 mV and frequency of 20 Hz. In all plots, the forward current (If) corresponds to the reduction of redox species (oxygen), whereas the backward current (Ib) corresponds to the stepping the potential back at the end of the pulse and the total current (It) is obtained from the difference of forward and backward currents (If – Ib).[14] At a smaller amplitude of 50 mV (Figure 9.3a), the forward component is negative due to the reduction of redox species, whereas the backward component is also negative which means that the overpotential is insufficient to drive the reaction in the reverse direction.

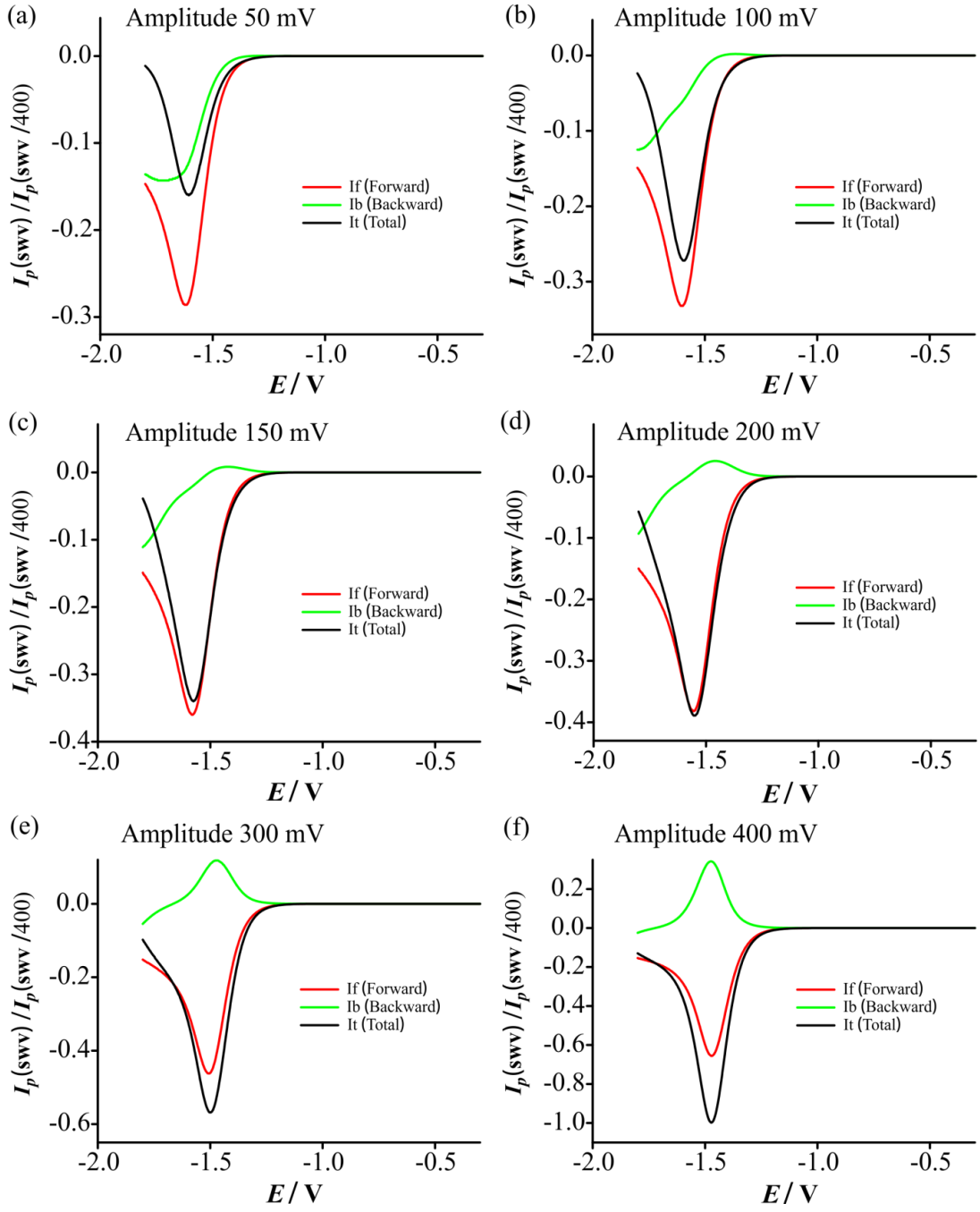

Figure: 9.3. Simulated forward, backward and total currents for 2.7 mM O_2 on a macrodisk electrode (radius = $5x10^{-2}$ m) at a scan rate of 50 mVs^{-1}. The SWV parameters are: step potential of 2.5 mV, amplitude of (a) 50 mV, (b) 100 mV, (c) 150 mV, (d) 200 mV, (e) 300 mV, and (f) 400 mV, frequency of 20 Hz.

As a result, the SWV total current is decreased even smaller than the forward component. Similar observations were reported in the literature when SWV was performed at smaller amplitudes.[8] As amplitudes increase, a similar effect is observed until an amplitude of 300 mV is applied. At this point, a significant backward peak developed (Figure 9.3e) since there is enough overpotential to drive

the backward reaction. However, the peak currents for the forward and backward component are not at the same peak potential, which decreased the SWV total current from the expected value. As the amplitude increased further to 400 mV (Figure 9.3f), a large backward component developed with a prominent peak shaped response which suggests that this larger amplitude provides enough overpotential to drive the quasi-reversible electrode reaction in the backward direction. It is important to note here, at this overpotential, the peak currents for both forward and backward component are at the same peak potential which results in a dominant SWV total current with sharp peak response which is ca. 6 times larger than the 50 mV amplitude (Figure 9.3a).

Figure 9.4 shows the plot generated from the simulated data for SWV amplitude *vs* ratio of peak currents for SWV and CV and normalized SWV absolute current.

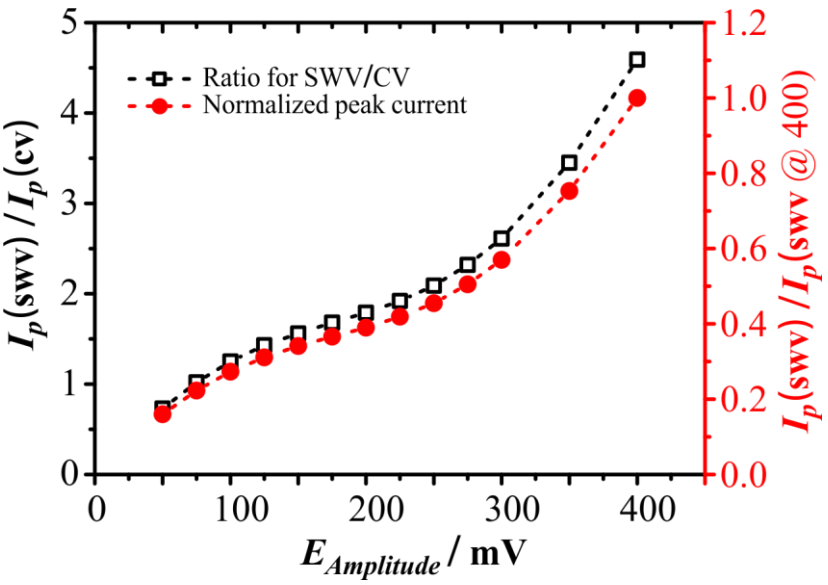

Figure: 9.4. Plot generated from simulated data for effect of square wave amplitude on ratio of peak current for SWV and CV and normalized peak current for 2.7 mM O_2 on disk electrode (radius = $5x10^{-3}$ m) at a scan rate of 50 mVs^{-1}. The SWV parameters are: step potential of 2.5 mV, amplitude of 50, 75, 100, 125, 150, 175, 200, 225, 250, 275, 300, 350, 400 mV, and frequency of 20 Hz.

It can be see that, as the amplitude is increased from 50 mV to 200 mV, both the ratio and absolute peak currents increased proportionally. When the amplitude is increased from 300 mV to 400 mV, a dominant increase in SWV current was observed which confirms that large amplitudes provide sufficient overpotential to drive the backward step.

9.3.4 Experimental Study of Square Wave Amplitude for Oxygen Reduction

Thus, in this section, the sensitivity of SWV with respect to the applied amplitude was studied experimentally for 100 % oxygen reduction in the RTIL on a Pt TFE. Figure 9.5 shows the experimental SWV forward, backward, and total currents for 100 % O_2 reduction in [C_2mim][NTf_2] at different amplitudes of 50, 100, 150, 200, 300 and 400 mV with a step potential of 2.5 mV and frequency of 20 Hz. Figure 9.5a shows the SWV forward, backward and total current responses at a smaller amplitude of 50 mV, where the forward current is large and negative due to the reduction of oxygen. Interestingly, the backward current is also negative which shows that there is not enough overpotential to drive the backward reaction. Thus, the SWV total response was smaller than the forward component. Similar observations were observed when the simulation was performed at smaller SWV amplitudes. At 100 mV amplitude (Figure 9.5b), a small peak was observed in the backward component with a positive current response, showing that this potential allows some superoxide to oxidize but is still not enough to completely oxidise the electrogenerated products. At 200 mV amplitude (Figure 9.5d) a prominent backward peak developed with a sharp current response. However, at a larger amplitude of 300 mV (Figure 9.5e), the peak current for both forward and backward components were at the same peak potential, therefore the resulting SWV total current was ca. 3.5 times larger than the forward current. When the SWV total current at 300 mV was compared with 50 mV amplitude, it was ca. 6.3 times larger, meaning that larger amplitudes provide sufficient overpotential for the oxidation of superoxide into oxygen.

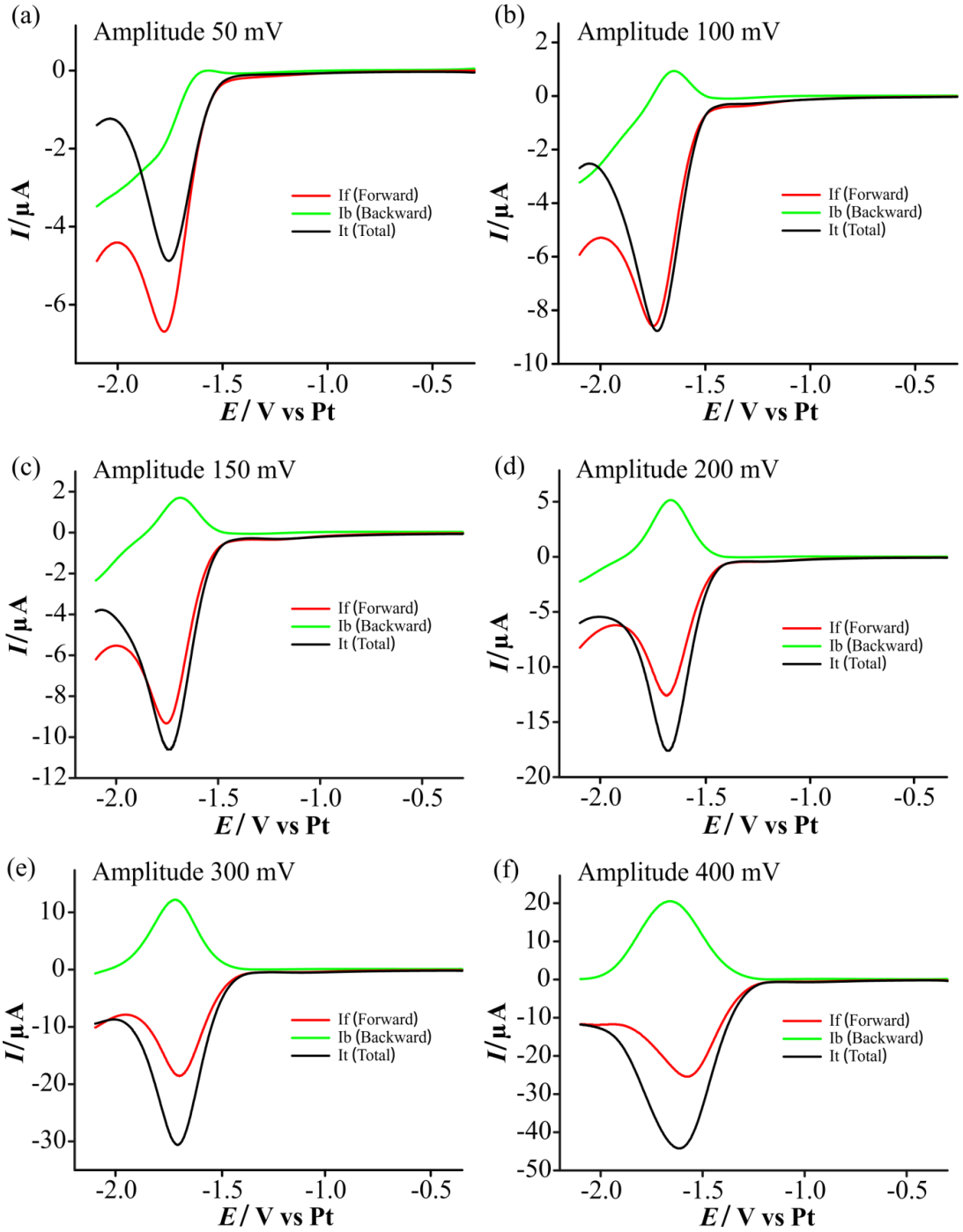

Figure: 9.5. Experimental forward, backward and total currents for 100 % O_2 on a Pt TFE in $[C_2mim][NTf_2]$ at a scan rate of 50 mVs^{-1}. The SWV parameters are: step potential of 2.5 mV, amplitude of (a) 50 mV, (b) 100 mV, (c) 150 mV, (d) 200 mV, (e) 300 mV, and (f) 400 mV, frequency of 20 Hz.

Interestingly, when the amplitude is increased to 400 mV (Figure 9.5f), not only are the peak currents for both forward and backward components increased, but the peaks become more broad, which suggests that 300 mV is the optimum amplitude to get the best SWV response. The peak shape is very simple and it is very easy to get i_p, even automatically. This is important for smarter sensors that can analyse the data

to get lower LODs, and also to realise when interferences are present, whereas LSV is much harder to analyse.

Figure 9.6 shows a plot of SWV amplitude *vs* ratio of peak currents for SWV and CV, along with absolute peak current. Clearly, it can be seen that at smaller amplitudes of 50-150 mV, both the ratio and absolute peak currents for SWV are increased accordingly. However, as amplitude increases from 150 mV to 400 mV, a dominant increase in the SWV response is observed which shows that the potential of the backward component was sufficiently high to reach an overpotential to drive the oxidation of superoxide in the backward step.

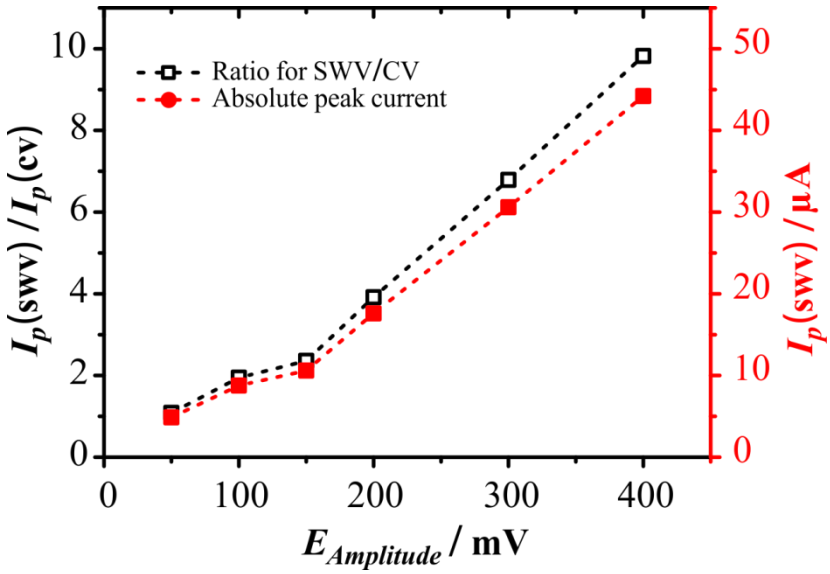

Figure: 9.6. Plot generated from experimental data for the effect of square wave amplitude on ratio of peak current for SWV and CV and absolute current for 100 % O_2 in [C_2mim][NTf_2] on Pt TFE at a scan rate of 50 mVs^{-1} vs integrated Pt CE and RE. The SWV parameters are: step potential of 2.5 mV, amplitude of 50, 100, 150, 200, 300, 400 mV, frequency of 20 Hz.

9.3.5 Square Wave Voltammetry for Oxygen Reduction at Different Concentrations

To investigate the sensitivity of SWV *vs* LSV for oxygen reduction and the effect of amplitude on SWV current response, SWV was performed at amplitudes of 50 mV, 150 mV and 300 mV, with a step potential of 2.5 mV, and frequency of 20 Hz. The SWV total response for 10-100 % O_2 was compared with LSV at a scan rate of 50 mV/s. Figure 9.7 shows a comparison of the voltammetric response for the reduction of 10-100 % O_2 in [C_2mim][NTf_2] on a Pt TFE using (a) LSV and (b-d) SWV at amplitudes of 50 mV, 150 mV, and 300 mV, respectively. The response in the

absence of oxygen is shown as a red dashed line. The insets show the corresponding calibration plots for the reduction of oxygen (background subtracted) *vs* concentration.

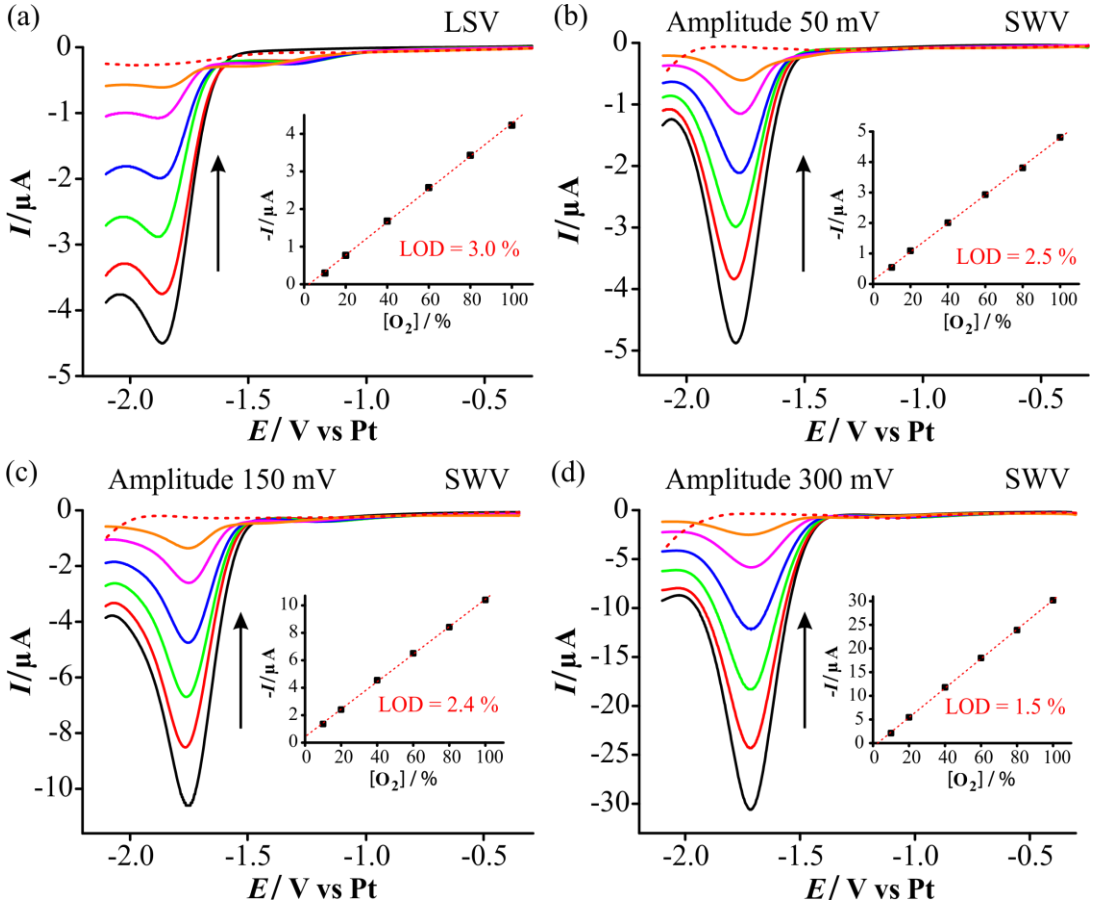

Figure: 9.7. Experimental (a) LSV at a scan rate of 50 mVs^{-1}, (b) SWV at 50 mV amplitude, (c) SWV at 150 mV amplitude and (d) SWV at 300 mV amplitude, for reduction of oxygen at different concentrations (100-10 %) in $[C_2mim][NTf_2]$ on a Pt TFE . Dotted line is the response in the absence of oxygen. The insets show calibration plots of peak current (baseline corrected) *vs* concentration, along with the line of best fit.

For both LSV and SWV, as the concentration of O_2 increases, the current response increases with excellent linearity ($R^2 > 0.999$). All plots show well-defined peak-shaped responses, which are more obvious for SWV at lower concentrations. The most important observation in the SWV response is that at 50 mV amplitude (Figure 9.7b) the current is slightly higher than LSV, whereas at 150 mV amplitude (Figure 9.7c) it was ca. 2.5 times larger. As the amplitude is increased to 300 mV, the SWV response is ca. 7.2 times larger, which suggests that for quasi-reversible redox process, the SWV gives a much higher sensitivity at larger amplitudes; similar findings were reported in the literature.[8, 15, 16]

Table 9.2 shows the analytical parameters (sensitivity, limit of detection, LOD) obtained from the calibration plots in Figure 9.7. The sensitivity values were calculated from the gradient of the line of best fit and limits of detection (LODs) were calculated from three times the standard deviation of the slope of the line of best fit, over the concentration range studied. The sensitivities for SWV were relatively high compared to LSV. For SWV, the sensitivities were higher significantly at larger amplitude, as expected e.g. the sensitivity increases from 47 nA/% to 310 nA/% when the amplitude is increased from 50 mV to 300 mV for the concentration range 10-100 %. A similar effect is observed at the lower concentration range. As the amplitude increases from 50 mV to 300, the LODs were also improved. The lowest LOD (0.19 %) was obtained at larger amplitude for 1-10 % of O_2.

Table 9.2. Analytical parameters obtained from SWV and LSV for the reduction of oxygen (10-100 % & 1-10 %) at different amplitudes of 50, 150 and 300 mV (Figure. 9.7 and 9.8) and the equations of the line of best fit, R^2 values, and LODs.

Technique	$[O_2]$range (%)	Amplitude (mV)	Equation of line of best fit	R^2	LOD (% O_2)
SWV	10-100	50	$4.67\times10^{-8}[O_2] + 1.16\times10^{-7}$	0.9995	2.5
SWV	10-100	150	$1.00\times10^{-7}[O_2] + 4.29\times10^{-7}$	0.9996	2.4
SWV	10-100	300	$3.10\times10^{-7}[O_2] - 8.07\times10^{-7}$	0.9998	1.5
SWV	1-10	50	$4.53\times10^{-8}[O_2] + 2.85\times10^{-8}$	0.9995	0.26
SWV	1-10	150	$1.02\times10^{-7}[O_2] + 2.55\times10^{-8}$	0.9996	0.22
SWV	1-10	300	$2.14\times10^{-7}[O_2] - 3.19\times10^{-8}$	0.9997	0.19
Technique	**$[O_2]$range (%)**	**Scan rate (mVs^{-1})**	**Equation of line of best fit**	**R^2**	**LOD (% O_2)**
LSV	10-100	50	$4.39\times10^{-8}[O_2] - 1.04\times10^{-7}$	0.9993	3.0
LSV	1-10	50	$4.16\times10^{-8}[O_2] - 8.59\times10^{-9}$	0.9994	0.28

Figure 9.8 shows a comparison of the calibration graphs for the two different concentration ranges for LSV and SWV at the three chosen amplitudes. This clearly shows the significant improvement in current response at higher amplitudes.

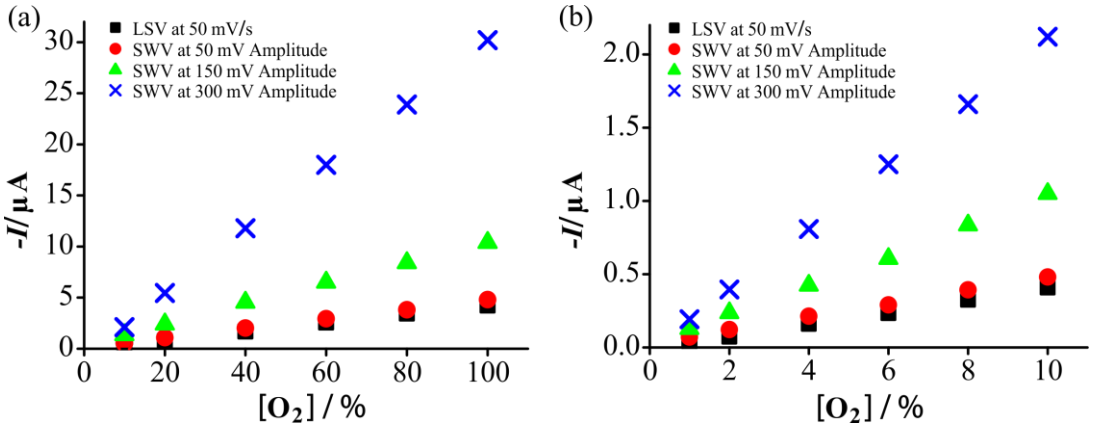

Figure: 9.8. Comparison of calibration plots for LSV and SWV at amplitudes of 50 mV, 150 mV and 300 mV for reduction of oxygen at different concentrations (a) 10-100 % and (b) 1-10 % in $[C_2mim][NTf_2]$ on a Pt TFE.

9.4 Conclusions

In order to improve the sensitivity of SWV for oxygen reduction in $[C_2mim][NTf_2]$, different kinetic parameters such as step potential, amplitude and frequency were varied and modelled to investigate the best set of SWV parameters. A range of different amplitudes were studied successfully to investigate the effect of SWV amplitude on the forward, backward and total currents. The optimized parameters were employed experimentally to study the SWV forward, backward and total currents for 100 % O_2 in $[C_2mim][NTf_2]$ at a wide range of different amplitudes. Three different SWV amplitudes (small, medium and large) were employed at two different concentration ranges (10-100 % and 1-10 %). The sensitivty of SWV was improved significantly with an increase of amplitude. For concentrations of 10-100 % O_2, the SWV was ca. 6.6 times larger at 300 mV amplitude compared to 50 mV and 4.7 times more sensitive for the smaller concentration range. The lowest LOD (0.19 %) was obtained using an amplitude of 300 mV for 1-10 % of O_2. This information shows that enhanced sensitivities can be achieved for quasi-reversible redox processes by increasing the modulation amplitude of SWV. This method can also be applied to other analyte species in addition to oxygen, and is applicable for electroanalysis applications for quasi-reversible redox couples.

References

1. W. A. Hempel, B. D. Papkovsky and P. J. Kerry, *Foods*, 2013, **2**.
2. B. R. O'Driscoll, L. S. Howard and A. G. Davison, *Thorax*, 2008, **63**, vi1.
3. H. Li, X. Mu, Z. Wang, M. Guo, X. Zeng and A. J. Mason, 2013.
4. A. Tengberg, J. Hovdenes, H. J. Andersson, O. Brocandel, R. Diaz, D. Hebert, T. Arnerich, C. Huber, A. Körtzinger, A. Khripounoff, F. Rey, C. Rönning, J. Schimanski, S. Sommer and A. Stangelmayer, *Limnology and Oceanography: Methods*, 2006, **4**, 7-17.
5. , 2016.
6. L. Xiong and R. G. Compton, *Int. J. Electrochem. Sci*, 2014, **9**, 7152-7181.
7. M. C. Buzzeo, C. Hardacre and R. G. Compton, *Analytical Chemistry*, 2004, **76**, 4583-4588.
8. V. Mirceski, E. Laborda, D. Guziejewski and R. G. Compton, *Analytical Chemistry*, 2013, **85**, 5586-5594.
9. U. Schroder, J. D. Wadhawan, R. G. Compton, F. Marken, P. A. Z. Suarez, C. S. Consorti, R. F. de Souza and J. Dupont, *New J. Chem.*, 2000, **24**, 1009-1015.
10. D. S. Silvester, A. J. Wain, L. Aldous, C. Hardacre and R. G. Compton, *J. Electroanal. Chem.*, 2006, **596**, 131-140.
11. J. Lee, K. Murugappan, D. W. M. Arrigan and D. S. Silvester, *Electrochim. Acta*, 2013, **101**, 158-168.
12. M. C. Buzzeo, O. V. Klymenko, J. D. Wadhawan, C. Hardacre, K. R. Seddon and R. G. Compton, *J. Phys. Chem. A*, 2003, **107**, 8872-8878.
13. E. E. L. Tanner, L. Xiong, E. O. Barnes and R. G. Compton, *Journal of Electroanalytical Chemistry*, 2014, **727**, 59-68.
14. A. Chen and B. Shah, *Analytical Methods*, 2013, **5**, 2158-2173.
15. V. Mirceski, S. Komorsky-Lovric and M. Lovric, *Square-wave voltammetry: theory and application*, Springer Science & Business Media, 2007.
16. M. A. Mann, J. C. Helfrick and L. A. Bottomley, *Analytical Chemistry*, 2014, **86**, 8183-8191.

Chapter 10

10. Conclusions and Future Work

In this chapter, the overall conclusions of the work presented throughout this thesis will be summarised. In addition, some future work will also be suggested that could be employed in amperometric gas sensors to further improve their performance for the sensing of toxic gases in room temperature ionic liquids.

10.1 Overall Conclusions

The research presented in this thesis describes the modification of electrode surfaces with materials such as platinum nanoparticles (PtNPs), 3D Pt cauliflower shaped nanostructures, PtNPs modified microchannels. These modified surfaces are incorporated for the sensing of toxic/ambient gases such as ammonia, hydrogen, hydrogen chloride, and oxygen in room temperature ionic liquids (RTILs). Initially, the electrochemical behaviour of ammonia oxidation was investigated in the RTIL $[C_2mim][NTf_2]$ on four different types of planar electrodes, (three commercially available and one modified electrode), all with Pt working electrodes: thin-film electrode (TFE), screen-printed electrode (SPE), micro-array thin film electrode (recessed MATFE), Pt modified micro-array thin film electrode ('filled' MATFE). The results were compared with an "ideal" conventional Pt microdisk (μ-disk) electrode using cyclic voltammetry. The mechanism for ammonia oxidation on all surfaces was the same as on the conventional electrodes. To investigate the analytical utility and limit of detection, four different electrochemical techniques were employed for ammonia oxidation: linear sweep voltammetry (LSV), differential pulse voltammetry (DPV), square wave voltammetry (SWV) and potential-step chronoamperometry (PSCA) over the concentration (10-100 ppm and 0.1-2 ppm) range for ammonia. From all these electrodes, the 'filled' MATFE was found to give the highest currents and LSV was found to be the most sensitive technique. Trace concentrations of ammonia could be detected, with the lowest limit of detection obtained in RTILs to date was 20 ppb which is significantly lower than the permissible exposure limit (25 ppm).

In order to further improve the sensitivity of MATFE, the microholes of the recessed MATFE were decorated with 2D nanostructures and 3D cauliflower shaped Pt deposits and the results were compared with a recessed MATFE. The current density for ammonia oxidation on 3D Pt-cauliflower decorated MATFEs was ca. 4 times larger than recessed MATFEs. To investigate the sensitivity and LOD on all modified MATFEs, different concentrations (10-100 ppm) of ammonia were studied where the highest sensitivity was found on 3D Pt-cauliflower decorated MATFE which is 6.5 times larger than the recessed MATFE. The lowest LOD (0.8 ppm) was found on the 3D Pt-cauliflower decorated MATFE over a (10-100 ppm) concentration range of ammonia. To test the ability of 3D cauliflower decorated microarrays *vs* recessed microarrays for "real-time" analyte detection, potential-step chronoamperometry was performed for 10 ppm ammonia in $[C_2mim][NTf_2]$ where the 3D Pt-cauliflower decorated MATFE gives 12 times higher response compared to the recessed MATFE. All this information was highly encouraging and suggests that the low cost and miniaturized MATFEs can be decorated with 3D Pt-cauliflower shaped nanostructures to detect low concentrations of ammonia with higher sensitivity.

Also in this thesis, the electrochemical oxidation of hydrogen gas was investigated due to its high flammability and explosive nature. For this study, gold macrodisk electrodes were modified successfully with the highly hydrophobic organic molecule, hexadecanethiol (HDT) using polydimethyl siloxane (PDMS) stamps to create Au microchannels. These modified Au microchannels were deposited with PtNPs to form PtNP modified Au microchannels. In order to investigate the sensitivities and LODs for hydrogen oxidation, cyclic voltammetry was performed successfully in $[C_2mim][NTf_2]$ over two concentration ranges (10-100 % and 1-10 %) and the results obtained on PtNP modified Au microchannels were compared with PtNPs modified gold macrodisk electrodes and bare Pt macrodisk electrodes. Two RTILs $[C_2mim][NTf_2]$ and $[C_4mpyrr][NTf_2]$ were also compared in order to investigate which RTIL is best for hydrogen sensing. Excellent linearity was obtained on PtNP modified Au microchannels for both concentration ranges in $[C_2mim][NTf_2]$, whereas on PtNP modified gold and bare Pt electrodes, the gradients deviated at low concentrations and did not pass directly through the origin. The

highest sensitivity and lowest LOD (2.5 %) was obtained on PtNP modified Au microchannels in [C_2mim][NTf_2] for the higher concentration range (10-100 %).

In order to test the ability of PtNP modified Au microchannel electrodes for "real time" hydrogen detection and to measure the response time (t_{90}), long-term chronoamperometry (LTCA) was performed on PtNPs Au microchannels for both concentration ranges and the results were compared with PtNP modified gold and bare Pt electrodes. The highest current-time response was obtained on the PtNPs Au microchannels in [C_2mim][NTf_2] whereas the smallest response was obtained on the bare Pt macrodisk electrode. A very fast response time (2 seconds) was obtained on the PtNP modified Au microchannels, which is ca. 20 times faster than on macrodisk electrodes due to the very small volume of RTIL used in this work. The lowest reported LOD (0.1 %, low concentration range) was obtained on the PtNP modified Au microchannels which is 40 times smaller than the lower explosive limit (4 %). The RTIL [C_4mpyrr][NTf_2] is not the best choice for long-term hydrogen detection due to the large fall off in current after the maximum, especially at higher concentrations. All these investigations are highly encouraging and suggesting that gold surfaces modified with PtNP microchannels can be employed together with RTILs in amperometric devices to produce fast responding, microarray-based hydrogen gas sensors which can detect hydrogen at analytically useful concentrations (40 times lower than the LEL).

In the second half of this thesis, the sensitivity of different electrochemical techniques such as LSV, DPV and SWV were also investigated successfully for fast reversible, quasi-reversible and irreversible redox processes. For this, a one electron transfer redox reaction was modelled using the simulation program Digi-Elch and the optimised set of parameters were employed experimentally to study the sensitivity of all three techniques for different analytes such as potassium ferricynaide, ferrocene, hydrogen chloride, hydrogen, oxygen, and ammonia which have fast reversible, quasi-reversible and irreversible redox nature in different electrolyte systems (water, acetonitrile and RTILs).

For fast reversible redox species such as potassium ferricynaide, and ferrocene, SWV was found to be the most senstive technique over LSV and DPV due to the negative and reversible backward current component.

For quasi-reversible redox processes which have a moderately fast rate of electron transfer in RTIL such as hydrogen and proton (for hydrogen chloride), the sensitivty of SWV was found to be very similar to the fast reversible redox processes, with SWV superior to both LSV and DPV.

For quasi-reversible redox species with have a smaller hetrogeneous rate constant such as oxygen in acetonitrile and RTILs, LSV was found to be slightly superior than the pulse techniques . However, it was demonstrated that the sensitivty of both SWV and DPV for such quasi-reversible redox processes can be enhanced at a larger modulation amplitude. In the case of oxygen reduction (10-100%) in RTILs, the sensitivty of SWV was found to be ca. 6.6 times more superior at an amplitude of 300 mV compared to 50 mV, givingthe lowest calculated LOD (0.19 % for 1-10 % of O_2). When the large modulation amplitude (300 mV) was applied to DPV for oxygen reduction, the sensitivity of DPV response was also increased (ca. 4 times at 10-100 % O_2).

For both chemically and electrochemically irreversible redox species such as ammonia in RTILs, the sensitivity of SWV can not be improved due to the irreversible backward current component. Under these conditions, the preferred electrochemical technique is LSV which gives a higher current response than SWV.

All of the information reported in this thesis can be used to and suggest which electrochemical technique and what electrode surfaces are best for a particular analyte. This can then be employed togather with RTILs in amperometric devices to produce low cost, miniaturized, and fast responding gas sensors which can detect toxic gases at low concentrations with high sensitivity and small limits of detection.

10.2 Future Work

The work presented in this thesis has demonstrated the modification of electrode surfaces for the sensing of toxic gases in RTILs, and has shown the sensitivity of different electrochemical techniques for gaseous analytes on the basis of their electrochemical reversibility. Still more research needs to be done before the commercialization of RTILs in amperometric gas sensors (AGSs). In sensor technology, high sensitivity, miniaturization, and robustness are important issues that

need to be addressed before the successful application of a sensor. In this section, some suggestions will be presented to address these issues.

The sensitivity could be further improved by incorporating high surface area nanostructured materials (e.g. noble metals) such as Pt mesoporous or nanoporous structures due to their large electroactive surface area, excellent sensitivity, and good electronic properties.[1-4] The sensitivity of electrode surfaces could also be improved by employing physically templated electrodeposition of noble metals (e.g. gold, platinum) into anodised aluminium oxide (AAO). This is a commonly used method for physical templating, where platinum or gold nanorods can be grown on electrode surfaces and could aid in sensing applications.[5-7]

Miniaturization and robustness is another major challenge in RTIL based AGSs. To the best of our knowledge, there is only one USA based company named "KWJ engineering" who are actively working to commercialize RTIL based AGSs. A large challenge is the leakage/seepage of RTIL into the electronic circuit/membrane as discussed with Dr Michael Carter (Director of Research at KWJ Engineering) at PRiME 2016, in Honolulu, Hawaii.[8-10] Recently, Lee *et al*. worked towards improving the robustness of miniaturised surfaces by employing polymer/RTIL composites to form gellified electrolytes.[11] They studied oxygen sensing at different orientations (flat, upside, down, sideways) to investigate the robustness and found that the gellified electrolyte is very stable for the electrochemical behaviour of oxygen, significantly better than the neat RTIL. However, as the concentration of polymer is increased in the RTIL mixture, the current response was decreased due to the higher viscosity of the gel and the slower partitioning of the gas.[11] To overcome this effect of Ohmic drop, polymerised ionic liquids (i.e. polyelectrolytes) would be ideal as electrolytes. These types of materials have large conductivity due to the many repeating units of charged species (functionalities), thus not only can thus be expected to give higher electrochemical responses, but the solid state nature of the gel will significantly reduce electrolyte leakage and improve the robustness of AGSs.[12-18]

There are a number of other challenges that need to be addressed before the commercialization of RTIL-based AGSs. One is the use of an unstable reference electrode, especially prevalent in the miniaturized devices employed in this thesis, which is a difficult problem to address in RTILs and is well discussed in the literature.[19] In addition, fouling of electrode surfaces due to the build-up

electrogenerated products (e.g. following the oxidation of ammonia) is another critical challenge that can reduce the lifetime of a sensor. Finally, fast response times, good selectivity in mixed gas environments, high sensor reproducibility, and low cost of sensor devices are key challenges before the practical application of RTIL based amperometric devices. But it is clear from the work in this thesis that RTILs can be considered to be an appropriate (and often superior) replacement to conventional solvents for the sensing of gases.

References

1. A. Walcarius, *Anal. bioanal. chem.*, 2010, **396**, 261-272.
2. Y. Yamauchi, A. Tonegawa, M. Komatsu, H. Wang, L. Wang, Y. Nemoto, N. Suzuki and K. Kuroda, *J. Am. Chem. Soc.*, 2012, **134**, 5100-5109.
3. Z.-j. Wang, Y. Xie and C.-j. Liu, *J. Phys. Chem. C*, 2008, **112**, 19818-19824.
4. A. Walcarius, *Chemical Society Reviews*, 2013, **42**, 4098-4140.
5. B. J. Plowman, S. K. Bhargava and A. P. O'Mullane, *Analyst*, 2011, **136**, 5107-5119.
6. W. Lee and S.-J. Park, *Chemical reviews*, 2014, **114**, 7487-7556.
7. K. Schwirn, W. Lee, R. Hillebrand, M. Steinhart, K. Nielsch and U. Gösele, *ACS Nano*, 2008, **2**, 302-310.
8. M. T. Carter, J. R. Stetter, M. W. Findlay and V. Patel, *ECS Trans.*, 2012, **50**, 211-220.
9. M. T. Carter, J. R. Stetter, M. W. Findlay and V. Patel, *ECS Trans.*, 2014, **64**, 95-103.
10. M. T. Carter, J. R. Stetter, M. W. Findlay, B. J. Meulendyk, V. Patel and D. Peaslee, *ECS Transactions*, 2016, **75**, 91-98.
11. J. Lee, G. Du Plessis, D. W. M. Arrigan and D. S. Silvester, *Analytical Methods*, 2015, **7**, 7327-7335.
12. H. Chen, J.-H. Choi, D. Salas-de la Cruz, K. I. Winey and Y. A. Elabd, *Macromolecules*, 2009, **42**, 4809-4816.
13. S. Mogurampelly, J. R. Keith and V. Ganesan, *Journal of the American Chemical Society*, 2017, **139**, 9511-9514.
14. H. Liu and S. J. Paddison, *Macromolecules*, 2017, **50**, 2889-2895.
15. L. C. Bradley and M. Gupta, *Macromolecules*, 2014, **47**, 6657-6663.
16. U. H. Choi, A. Mittal, T. L. Price, H. W. Gibson, J. Runt and R. H. Colby, *Macromolecules*, 2013, **46**, 1175-1186.
17. A. S. Shaplov, P. S. Vlasov, E. I. Lozinskaya, D. O. Ponkratov, I. A. Malyshkina, F. Vidal, O. V. Okatova, G. M. Pavlov, C. Wandrey, A. Bhide, M. Schönhoff and Y. S. Vygodskii, *Macromolecules*, 2011, **44**, 9792-9803.
18. G. Hussain, A. Robinson and P. Bartlett, *Langmuir*, 2013, **29**, 4204-4213.
19. D. S. Silvester, E. I. Rogers, R. G. Compton, K. J. McKenzie, K. S. Ryder, F. Endres, D. Macfarlane and A. P. Abbott, *Reference Electrodes for use in RTILs, Chapter 11.2 in the book "Electrodeposition from Ionic Liquids"*, Wiley-VCH Verlag GmbH & Co. KGaA, 2008.

Appendix A

Copy Right Permission Certificate for Figure 2.4

Alphasense Ltd

10th August, 2017

Ref:Ghulam Hussain PhD thesis

Alphasense grants Ghulam Hussain permission to use Alphasense figures and performance specifications in his PhD thesis.
T

Yours sincerely,

Dr John Saffell
Technical Director
Alphasense Ltd.

Alphasense Ltd ■ 300 Avenue West, Skyline 120 ■ Great Notley ■ Essex ■ CM77 7AA ■ UK
Telephone: +44 (0)1376 556700 ■ Fax: +44 (0)1376 335899
E-mail: jrs@alphasense.com ■ Website: www.alphasense.com
Registered in England No: 3264282

Appendix B

Published Article

1. 2018-**Ghulam Hussain,** M. Veronica Sofianos, Junqiao Lee, Caitlyn Gibson, Craig E. Buckley, Debbie S. Silvester, "Macroporous Platinum Electrodes for Hydrogen Oxidation in Ionic Liquids", ***Electrochemistry Communication,*** 86, 43-47.
2. 2017-Junqiao Lee, **Ghulam Hussain**, Craig E. Banks, Debbie S. Silvester., "Screen-Printed Graphite Electrodes as Low-Cost Devices for Oxygen Gas Detection in Room Temperature Ionic Liquids", ***Sensors,*** 17, 2734.
3. 2017-**Ghulam Hussain,** Debbie S. Silvester, "Comparison of Voltammetric Techniques for Ammonia Sensing in Ionic Liquids", ***Electroanalysis,*** 29, 1-10.
4. 2016-**Ghulam Hussain,** Debbie S. Silvester, "Detection of sub-ppm Concentrations of Ammonia in an Ionic Liquid: Enhanced Current Density Using 'Filled' Recessed Microarrays", ***Anal. Chem.,*** 88, 12453-12460.

List of Manuscripts in Preparation

5. **Ghulam Hussain,** Leigh Aldous, Debbie S. Silvester, "Growth of 2D Pt-Deposits to Fill the Micro-Holes in Recessed Micro-Array Thin-Film Electrodes: Enhancement of Ammonia Response from 2D Pt-deposits to 3D Pt-Cauliflowers".
6. **Ghulam Hussain,** Mengchen Ge, Chuan Zhao, Debbie S. Silvester, "Fast Responding Amperometric Hydrogen Gas Sensors based on Microcontact Printing in Room Temperature Ionic Liquids".
7. Mengchen Ge, **Ghulam Hussain,** Chuan Zhao, Debbie S. Silvester, "Microcontact Printing Based Amperometric Gas Sensors for Toxic Gases in Room Temperature Ionic Liquids".
8. **Ghulam Hussain,** Leigh Aldous, Debbie S. Silvester, "Comparison of Voltammetric Techniques to Develop Oxygen Sensors in Room Temperature Ionic Liquids: Enhanced sensitivity Using Optimised Square Wave Voltammetry".
9. **Ghulam Hussain,** Leigh Aldous, Debbie S. Silvester, "Sensitivity of voltammetric techniques for Reversible, Quasi-Reversible and Irreversible Redox process".
10. **Ghulam Hussain**, Junqiao Lee, Debbie S. Silvester, "Low-Concentration Detection of Oxygen and Ammonia on Miniaturized and Robust Amperometric Gas Sensors Based on Polymerized Ionic Liquids".

Oral and Poster Presentation

1. **November 2017:** Oral presentation at the **3rd International conference on "Recent Trends in Chemistry" 2017**, Academic Complex, Allama Iqbal Open University, Islamabad, Pakistan.
   Title: "Modification of Electrode Surfaces for the Sensing of Toxic Gases in Room Temperature Ionic Liquids."

2. **July 2017:** Poster presentation at the **RACI Centenary Congress 2017**, Melbourne Convention and Exhibition Centre, Australia.
   Title: "3D Pt-Cauliflower Decorated Microarrays for Ammonia Gas Sensing in Room Temperature Ionic Liquids."

3. **May 2017:** PhD (Final) Seminar at the **Department of Chemistry, Curtin University WA**.
   Title: "Modification of Electrode Surfaces for the Sensing of Toxic Gases."

4. **March 2017:** Online poster presentation at the **RSC Analytical Twitter Poster Conference**.
   Title: "Sub-ppm Detection of Ammonia in Ionic Liquids: Enhanced Current Density Using "Filled" Recessed Microarrays."

5. **October 2016:** Oral and poster presentations at the **PRiME 2016/230th ECS Meeting**, Honolulu, Hawaii, United States of America.
   Title: "Comparison of Voltammetric Techniques for the Electroanalysis of Dissolved Solids and Gases in Water, Acetonitrile and Room Temperature Ionic Liquids (RTILs): Unusual Behaviour for Gases." and "Electrochemical Detection of Low-Concentration Ammonia Gas on Miniaturised Electrodes in Room Temperature Ionic Liquids."

6. **March 2016**: Online poster presentation at the **RSC Analytical Twitter Poster Conference.**
   Title: "Detection of Low-Concentration Ammonia Gas on Miniaturised Electrodes in Room Temperature Ionic Liquids."

7. **December 2015**: Oral presentation at the **23rd RACI Research & Development Topics Conference** in Analytical & Environmental Chemistry, Melbourne University, Australia
   Title: "Low-Concentration Ammonia Gas Detection on Miniaturised Electrodes in Room Temperature Ionic Liquids."

Appendix C

2016-Kagi-Alexander HDR Publication Award, Department of Chemistry, Curtin University

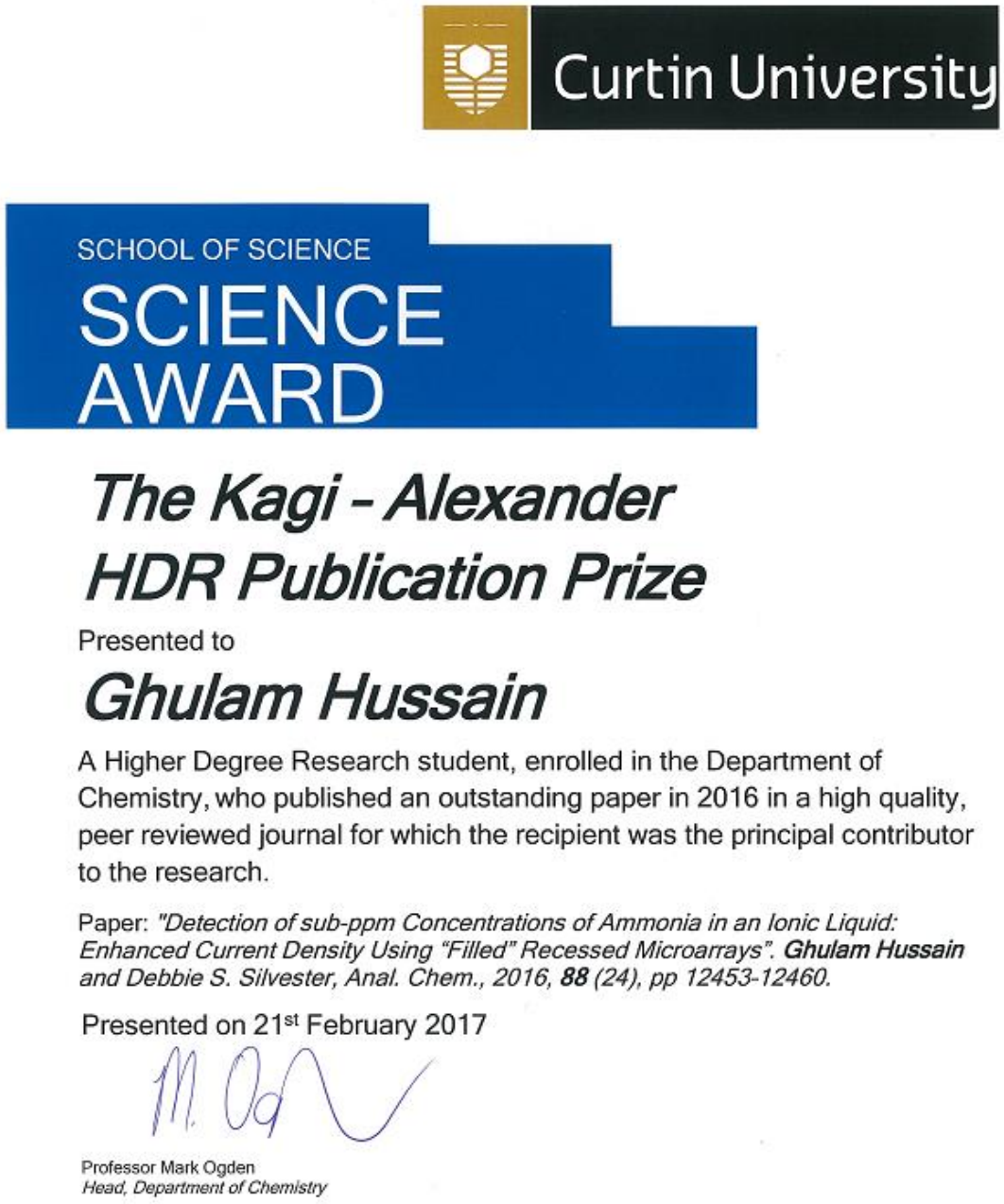

Curtin University

SCHOOL OF SCIENCE

SCIENCE AWARD

The Kagi - Alexander HDR Publication Prize

Presented to

Ghulam Hussain

A Higher Degree Research student, enrolled in the Department of Chemistry, who published an outstanding paper in 2016 in a high quality, peer reviewed journal for which the recipient was the principal contributor to the research.

Paper: *"Detection of sub-ppm Concentrations of Ammonia in an Ionic Liquid: Enhanced Current Density Using "Filled" Recessed Microarrays". **Ghulam Hussain** and Debbie S. Silvester, Anal. Chem., 2016, **88** (24), pp 12453-12460.*

Presented on 21st February 2017

Professor Mark Ogden
Head, Department of Chemistry